博 士 論 文

The Astronomical Seeing at Dome Fuji on the Antarctic Plateau

（南極大陸内陸高原ドームふじにおけるシーイングの性質）

沖 田 博 文

平成 25 年

Thesis

The Astronomical Seeing at Dome Fuji on the Antarctic Plateau

A Dissertation Submitted to Tohoku University
in Partial Fulfillment of Requirements for
the Degree of Doctor of Philosophy in Science

Hirofumi Okita
Astronomical Institute, Graduate School of Science
Tohoku University

February 2014

Abstract

Dome Fuji, the second highest region on the Antarctic plateau, is expected to be one of the best astronomical sites on the Earth. Extremely low temperature at Dome Fuji produces both minimum thermal background and highest atmospheric transmittance on the Earth. In addition the excellent astronomical seeing, which originates from unique meteorological and geographical conditions on the Antarctic plateau, is also expected. However, the seeing measurements at Dome Fuji are yet to be investigated because of both the Antarctic harsh environment and logistical limitations.

Snodar (high-resolition and low minimum sample height sonic rader), PLATO-F (PLATeau Observatory for Dome Fuji), platinum thermometers equipped on the 16-m meteorological mast, AIRT40 (Antarctic Infra-Red Telescope with a 40-cm primary mirror), and two DIMMs (Differential Image Motion Monitor) were developed for the site testings at Dome Fuji, while we used SODAR (SOnic Detection And Ranging), ultrasonic anemometers, and barometer, which were commercially available.

From our observations we found the height of the surface boundary layer at Dome Fuji in fine weather in the Antarctic autumn and winter to be 15.3 $\pm$ 0.8 (statistical) $\pm$ 0.8 (systematic) meters in median. The median absolute deviation (MAD) was 2.7-m. The height of the surface boundary layer remained low and stable for several days. The free-atmosphere and total seeings at Dome Fuji in the Antarctic summer were $0.23'' \pm 0.01''$ (statistical) $\pm$ $0.01''$ (systematic), and $1.1'' \pm 0.1''$ (statistical) $\pm$ $0.1''$ (systematic) in median. MADs were $0.057''$ and $0.47''$, respectively. In addition, the atmospheric convection at the local daytime in the Antarctic summer and autumn was found near the snow surface. It would build the surface boundary layer. The local seeing minimum, which would be caused by the disappearance of the surface boundary layer, was observed at dusk in the Antarctic summer. Based on the study of the refractive-index structure constant, the turbulence strength in the surface boundary layer was two orders of magnitude larger than the atmospheric convection, and four orders of magnitude than the free atmosphere. Assuming constant refractive-index structure constant in each layer, we predict that the seeing is drastically worsen if the telescope height is lower than the surface boundary layer.

This thesis is based on the papers: H. Okita, T. Ichikawa, M. C. B. Ashley, N. Takato, and H. Motoyama (2013). "Excellent daytime seeing at Dome Fuji on the Antarctic plateau," *A&A*, **554**, L5 [50]; H. Okita, N. Takato, T. Ichikawa, C. S. Bonner, M. C. B. Ashley, J. W. V. Storey, and 51^{st} and 52^{nd} JARE Dome Fuji team (2013). "Dome Fuji Seeing –the Summer Results and the Future Winter-over Observations," *Proc. IAU Symposium*, **288**, 25 [52]; H. Okita, T. Ichikawa, T. Yoshikawa, R. G. Lundock, and K. Kurita (2010). "Antarctic Infra-Red Telescope with a 40cm primary mirror (AIRT40): development and improvement," *Proc. SPIE*, **7733**, 62 [51]; C. Murata, T. Ichikawa, R. G. Lundock, Y. Taniguchi, and H. Okita (2008). "A 40-cm infrared telescope in Antarctica," *Proc. SPIE*, **7012**, 79 [49]; and unpublished results.

Contents

Chapter 1

Introduction

1.1 Astronomical motivations to find good seeing sites

Morphology of the galaxies is important to understand the galaxy formation and evolution. By investigating the morphology of the galaxies in the early universe, we can understand when the galaxies were born and how the galaxies evolved. Longer wavelength and higher spatial resolution are needed for the observation of the galactic morphology in the early universe. We considered observations with twice longer wavelength ($2 \sim 4$ μm) and with twice higher spatial resolution limit ($0.3''$) than the current observations.

Longer wavelength and higher spatial resolution observation is difficult for the existing both ground-based and space telescopes. Ground-based observation is limited in the spatial resolution by the Earth's atmosphere. At Mauna Kea in Hawaii, where the world largest telescopes are constructed, the spatial resolution at the wavelength $2 \sim 4$ μm is $\sim 0.5''$. Atmospheric thermal emission and absorption complicate observations with wavelength longer than ~ 2 μm.

Space telescope has no effects from the Earth's atmosphere. However, from the limitation of its mirror size or wavelength range, high spatial resolution observations at $2 \sim 4$ μm wavelength have not performed. For example, Hubble space telescope, which has 2.4-m in diameter primary mirror, can resolve $0.17''$ at 1.6 μm, however it can not observe the wavelength longer than 1.6 μm by technical issue. Spitzer space telescope can observe the wavelength longer than 3.6 μm, however its diameter of the primary mirror is only 0.85-m, thus the spatial resolution at 3.6 μm is only $\sim 1.1''$.

From these reasons, we focus the Antarctic plateau, which is considered to be the best ground-based infrared astronomical site on the Earth.

1.2 Infrared observations at the Antarctic plateau

The sky background at infrared wavelengths on the ground is very bright, compared to that of optical, due to the thermal emission and OH airglow of the Earth's atmosphere. Earth's atmosphere also limits observational wavelengths by its absorption at the infrared range. Therefore ground-based infrared observations are generally difficult.

Antarctic plateau is considered as the best site for ground-based infrared astronomy (Harper 1990; Burton et al. 1994) [17, 24]. An average elevation of the Antarctic plateau is over 3 000-m. An extremely low temperature, for example, -89.2°C was recorded at

Vostok Station on the Antarctic plateau in 1983. Therefore minimum thermal background emission from both the atmosphere and a telescope itself is expected. The Antarctic cold environment enables us the deepest observations at infrared wavelengths. The driest air, which is related to the low temperature and high altitude of the Antarctic plateau, will also give us a merit for high atmospheric transmittance at infrared wavelengths. The Antarctic environment gives us an deepest observations and new observable wavelength windows for infrared astronomy. Thus we have pursued the perspectives of the infrared astronomical observations at the Antarctic plateau.

1.3 Astronomical seeing

The study for the atmospheric turbulence is important for the ground-base astronomy because the turbulence limits the spatial resolution of astronomical targets. The spatial resolution limit due to the atmospheric turbulence is called "Astronomical Seeing," or "Seeing." The full width at half maximum (FWHM) of the point spread function (PSF) with a long exposure time on a large aperture telescope, which is broadened by the atmospheric turbulence, is the definition of the astronomical seeing. The astronomical seeing is usually written in the unit of arcsec as a value at the wavelength of 500 nm and at zenith because the astronomical seeing depends on the wavelength and zenith angle.

1.3.1 Importance of the astronomical seeing

The Rayleigh criterion is generally represented by the theoretical angular resolution limit θ_R of the telescope, which has a diameter D [m], at a wavelength λ [m],

$$\theta_R = 1.22 \, \frac{\lambda}{D} \, , \tag{1.1}$$

where the unit of the angular resolution is in radian. For Subaru telescope, D = 8.2-m, the theoretical resolution is calculated 0.015 arcsec at 500 nm. However, it cannot be realized because of the effect of the atmospheric turbulence. As the atmospheric turbulence broadens PSF to the seeing size, the astronomical seeing set the actual resolution limit. The astronomical seeing at Mauna Kea in Hawaii is $\sim$ 0.7 arcsec. This resolution limit is the same as the Rayleigh limit of a 15-cm diameter telescope. In terms of spatial resolution, Subaru telescope is the same as a telescope with only 15-cm diameter. As such, the astronomical seeing sets a practical limit of the spatial resolution for ground-base astronomy. Therefore finding good astronomical seeing sites is essentially important for ground-based astronomy.

1.3.2 World best astronomical seeing sites

The atmospheric convection by the solar heating, and the mixing of air parcel of different temperature by a wind are the causes of the astronomical seeing degradation. At the top of the high mountains, there is less turbulence caused by the solar heating than at low altitudes. Therefore, to avoid the atmospheric turbulence, some astronomical observatories have been constructed at the top of high mountains (see Table 1.1).

Near the coast, the atmospheric turbulence, which is caused by the solar heating, is smaller than that in the inland because the diurnal variation of the temperature near the

Table 1.1: Astronomical seeing at the world largest telescope sites.

Telescope	Site	Altitude (m)	Seeing ($''$)
Subaru [1]	Mauna Kea, Hawaii	4 200	0.73
VLT [2]	Cerro Paranal, Chili	2 635	0.88
GTC [3]	La Palma, Canary Islands	2 267	0.76
TAO [4]	Cerro Chajnantor, Chili	5 640	0.69
TMT [5]	Mauna Kea 13N, Hawaii	4 050	0.75

References: [1] Uraguchi et al. (2006) [76]; [2] Martin et al. (2000) [44]; [3] Vernin and Muñoz-Tuñón (1994) [78]; [4] Motohara et al. (2008) [46]; [5] Skidomre et al. (2009) [59]

coast is smaller. Thus the good astronomical seeing would be obtained at the mountain peaks near the ocean, or at the coastal mountain range on a continent. These places have a moderating effect on temperature variations (Hardy 1998) [23].

The atmospheric turbulence at upper atmosphere also degrades the astronomical seeing. The jet stream at the troposhere is a main origin of the turbulence. Therefore, relatively weak or no jet stream site is suited for astronomical observations. For example, above the Japanese islands, the strong jet stream, which is the merge of the polar jet and subtropical jet streams, is perpetual, therefore the seeing is poor in general. On the contrary, due to relatively weak subtropical jet stream above the Mauna Kea in Hawaii, the good seeing is expected.

We summarize the astronomical seeing at the world largest telescope sites in Table 1.1. The observatories are located at the best astronomical seeing sites on the Earth. The seeing values in median are corrected at wavelength of 500 nm and at zenith.

1.3.3 Seeing measurement

Astronomical seeing can be measured by using a small telescope. Direct seeing measurements with, e.g., Difference Image Motion Monitor (DIMM: Sarazin & Roddier 1990) [56], and Multi-Aperture Scintillation Sensor (MASS: Tokovinin 1998) [68] have been broadly performed at astronomical observatories and candidates. Astronomical seeing could be also measured from the sum of the turbulence strength in the strata above the site. An acoustic back-scattering sound with SOnic Detection And Ranging (SODAR: Little 1969) [38] is applicable to the measurement of the astronomical seeing without telescope. Temperature measurements in high frequency give the turbulence strength at an height. These methods are described in Chapter 2.

1.4 Earth's atmosphere

In this section we overview the Earth's atmosphere and its turbulence, which affect astronomical observations.

1.4.1 Atmospheric structure

The Earth's atmosphere is a gaseous envelope that surrounds the Earth and extends to several kilometers above the sea level. Based on temperature variations, the Earth's atmosphere is divided into four primary layers (troposphere, stratosphere, mesosphere,

and thermosphere) separated by three isothermal boundaries (tropopause, stratopause, and mesopause). The troposphere is the lowest layer which contains roughly 75% of the Earth's atmosphere mass. Maximum air temperature ($\sim 15°$C) occurs near the ground surface, and the temperature decreases with altitude to $\sim -55°$C (Fig. 1.1). The range of the troposphere is from the ground to 11-km above the sea level at the moderate latitude. The tropopause is an isothermal layer where air temperature remains almost constant at $\sim -55°$C. The tropopause is between 11 and 20-km above the sea level. The stratosphere is the second layer, which the air temperature increases with altitude because the ozone gas absorbs ultraviolet sunlight, thereby creating heat energy. The range of the stratosphere is to $\sim$ 50-km from tropopause.

Figure 1.1 is the model temperature and model pressure profiles referred from the U.S. Standard Atmosphere (1976) in 0 to 32-km (troposphere, tropopause, and lower stratosphere). From the figure, we find that most atmospheric mass is reserved under 20-km above the sea level. Thus the atmospheric turbulence which affects the astronomical seeing is mainly occurred in this range.

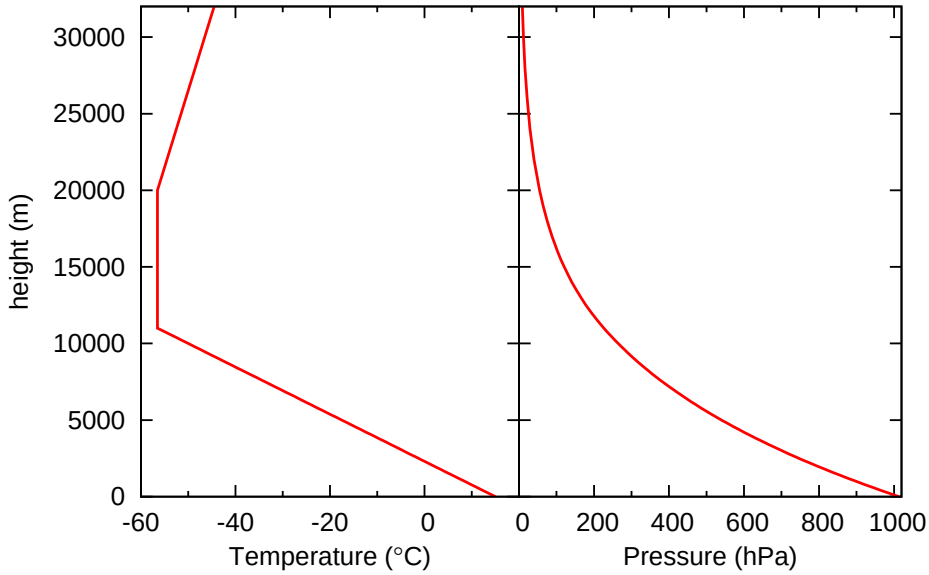

Figure 1.1: Model temperature (left) and model pressure (right) profiles referred from the U.S. Standard Atmosphere (1976).

1.4.2 Atmospheric turbulence

The strength of the atmospheric turbulence which affects the astronomical observation can be explained by the refractive-index structure constant C_n^2. The detailed description for C_n^2 is described in Chapter 2.

C_n^2 profile shows the feature of the atmospheric turbulence at the observation site. C_n^2 profile varies on site, season, and time. If we know C_n^2 profile of the site, the effect to astronomical observations can be predicted.

1.4.3 Model turbulence profile

Here we show some models of the turbulence profile. The most widely used atmospheric turbulence models as a function of altitude is the Hufnagle-Valley model (Hardy 1998; Andrews 2004) [3, 23],

$$\begin{aligned} C_n^2(h) &= 5.94\times10^{-53}\left(\frac{W}{27}\right)^2 h^{10}\exp\left(-\frac{h}{1000}\right) \\ &\quad +2.7\times10^{-16}\exp\left(-\frac{h}{1500}\right) \\ &\quad +A\times\exp\left(-\frac{h}{100}\right)\ , \end{aligned} \tag{1.2}$$

where A is a ground-level value of the refractive-index structure constant, and W is rms wind speed. A and W are defined with

$$\begin{aligned} A &= C_n^2(0) \\ W &= \left\{\left(\frac{1}{15km}\right)\int_{5km}^{20km} dh\ v^2(h)\right\}^{1/2}\ , \end{aligned} \tag{1.3}$$

where $v(h)$ [m s^{-1}] is the wind speed at altitude h [km] above the ground. For example, for H-V 5/7 (Hufnagle-Valley model for the Fried length $r_0 = 5$ [cm] and the isoplanatic angle $\theta_0 = 7$ [micro-radian]), A and W are 1.7×10^{-14} [m$^{-2/3}$] and 21 [ms $^{-1}$], respectively.

Another atmospheric turbulence model is the layered model, e.g., the SLC-Night model (Andrews 2004) [3],

$$\begin{aligned} C_n^2(h) &= 8.4\times10^{-15} && (0<h\le18.5m) \\ &= 2.87\times10^{-12}\ h^{-2} && (18.5<h\le110m) \\ &= 2.5\times10^{-16} && (110<h\le1500m) \\ &= 8.87\times10^{-7}\ h^{-3} && (1500<h\le7200m) \\ &= 2.0\times10^{-16}\ h^{-1/2} && (7200<h\le20000m)\ . \end{aligned} \tag{1.4}$$

The Hufnagle-Valley and SLC-Night both are the models with the strongest turbulence near the ground.

At hight-altitude observatory sites, such as Mauna Kea in Hawaii (4 200-m), atmospheric turbulence has a different character from that at lower elevation sites. There is little turbulence near the surface and turbulence in the troposphere tends to be concentrated in one or two thin layers. The typical model turbulence profile at Mauna Kea is showed in Hardy (1998) [23],

$$\begin{aligned} C_n^2(h) &= 1.63\times10^{-53}h^{10}\exp\left(-\frac{h}{1000}\right) \\ &\quad +1\times10^{-17}\exp\left(-\frac{h}{3000}\right) \\ &\quad +1\times10^{-16}\exp\left\{-\frac{1}{2}\left(\frac{h-6500}{300}\right)^2\right\}\ . \end{aligned} \tag{1.5}$$

Figure 1.2 is the model atmospheric turbulence profiles.

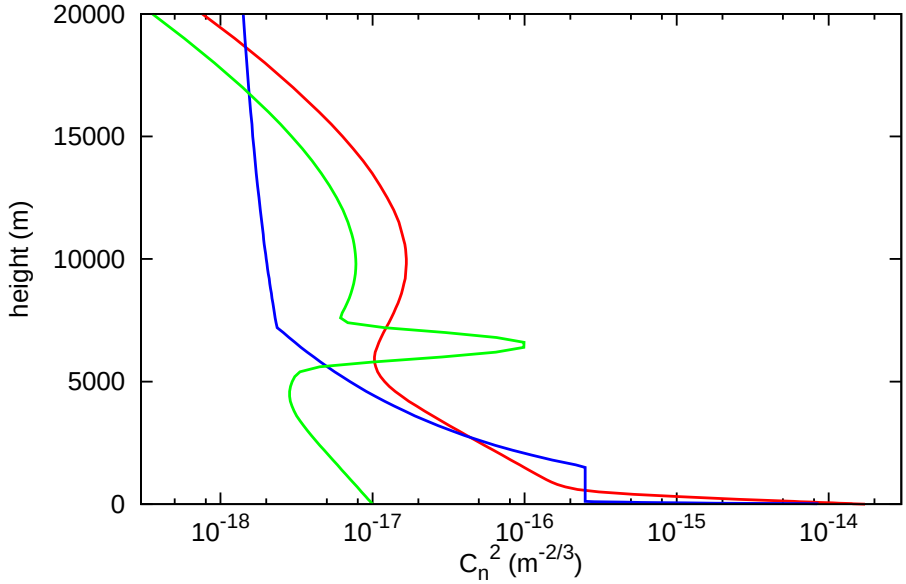

Figure 1.2: Model atmospheric turbulence profiles. Red, blue, and green lines means the Hufnagle-Valley 5/7 model, SLC-Night model, and Mauna Kea model, respectively. We note that the height is above the ground surface level.

1.4.4 Turbulence layer

The atmospheric layer which has a large C_n^2 is called "turbulence layer." The turbulence layer is mainly made by two causes. One is the turbulence layer near the ground, which is influenced by the solar insolation and local geography. The solar insolation makes an atmospheric convection, which is the cause of the atmospheric turbulence. Since the turbulence near the ground is caused by a wind and its friction between the atmosphere and the ground, local geography is important for understanding the turbulence near the ground. Another is the turbulence layer above the upper atmosphere, which is mainly caused by the jet stream. The jet stream is a very strong wind ribbon, which is 9∼16-km above the sea level, just below the tropopause.

During the daytime, the turbulence layer due to the solar heating near the ground is usually the strongest component. At the nighttime, while the surface turbulence is low, the turbulence is caused at higher altitude by wind shear or jet stream (Hardy 1998) [23].

1.4.5 Surface boundary layer and free atmosphere

Atmospheric turbulence, which worsens the seeing, is generally described as the superposition of two components from the observational point of view. The turbulence near the ground is avoidable if its height is sufficiently low and a telescope is constructed above the height. However the turbulence at high altitude is not avoidable. The turbulence layer near the ground is defined as the "surface boundary layer." The height of the surface boundary layer is about several meters to a few hundreds meters. For a moderate latitude astronomical observatory on a mountain top, the height of the surface boundary layer is significantly low, or almost no surface boundary layer.

The layer above the surface boundary layer defines the "free atmosphere." In the upper atmosphere, strong wind shear, such as jet stream, generally makes the seeing worse. Since

astronomical observations in mid-latitude sites are performed through strong wind shear in the upper atmosphere, the seeing at the best mid-latitude sites is $\sim 0.7''$ due to the effect of the free atmosphere.

1.4.6 Turbulence profile on the Antarctic plateau

Turbulence profile above the Antarctica is expected to be very different because of its unique environment. Hufnagle-Valley, SLC-Night, and Mauna Kea models would not fit to the atmospheric turbulence in the Antarctica. Antarctica is one of the coldest regions on the Earth. The surface temperature in the Antarctic region is colder than at any moderate latitudes. In the austral winter there is no sunrise in the Antarctic region, the diurnal variation of the temperature does not occur.

A strong temperature gradient near the snow surface should be caused by the radiative cooling in the Antarctic nocturnal season. This strong temperature gradient with a surface wind will make an atmospheric turbulence near the surface. The astronomical seeing at the surface level, i.e. surface boundary layer seeing, is expected to be worse. The surface of the Antarctic continent is covered with snow, and the ice and snow make the Antarctic plateau inside the continent. As there is no mountain or no valley on the Antarctic plateau, the surface wind will be not affected by the local geography. The katabatic wind is a dominant surface wind in the Antarctic continent. It is caused by the cold and high density air moving from higher elevation to lower along with a plateau slope by the gravity. At the top of the Antarctic plateau, which is called "Dome," no katabatic wind is observed. The height of the surface boundary layer generally increases with growth of wind speed (Bonner et al. 2010a) [13]. Therefore thin surface boundary layer at the dome region is expected.

Above the Antarctica, there is no jet stream in the troposphere. Instead, the polar vortex is in the stratosphere. A typical latitude of the strong polar vortex is north of $\sim 70^\circ$ South (Fig.18 in Saunders et al. 2009) [57]. The height of the polar vortex is over 20-km above the sea level, which is higher than the height of the jet stream in the mid latitude. Since there is little air mass in the upper atmosphere, the impact of the polar vortex for the atmospheric turbulence would be relatively weaker than that of the jet stream. The seeing will be less affected by the polar vortex because it does not depend on the height of the turbulence. Therefore good free-atmosphere seeing is predicted. On the other hand, the stellar scintillation and the isoplanatic angle, which depend on the height of the turbulence, should be affected by the polar vortex. These parameters are introduced in Chapter 2.

From the reasons mentioned above, the "Dome" region on the Antarctic plateau would have thin turbulent surface boundary layer and good free-atmosphere seeing. A good seeing condition can be obtained if telescopes are constructed above the surface boundary layer. Therefore the Antarctic plateau is reasonably expected to be the best astronomical seeing site on the Earth.

1.5 Seeing prediction at the Antarctica

Some numerical simulations were performed for the seeing prediction. Swain & Gallée (2006) [63] calculated the height of the surface boundary layer and the total seeing on the

Antarctic plateau. Saunders et al. (2009) [57] predicted that the free-atmosphere seeing. We summarize them briefly in this section.

1.5.1 Height of the surface boundary layer

Swain & Gallée (2006) [63] simulated the Antarctic atmosphere during the 2004 winter (June, July, and August) using the modèle atmosphérique régional (MAR), which was a regional climate model. C_n^2 profiles were calculated from the vertical temperature gradient and the turbulence kinematic energy. The simulation covered from the surface to the 0.1 hPa pressure level in the vertical dimension with a horizontal resolution of 100-km with 6 hour intervals. The height of the surface boundary layer is the model height at which the atmospheric turbulence kinetic energy is 1% of the lowest height value. The results were 18.5-m at Dome Fuji, 21.7-m at Dome A, and 27.7-m at Dome C, respectively.

They also showed the dependency of the height of the surface boundary layer on the surface wind speed. In the simulation, a weak surface wind brought a low height of the surface boundary layer.

1.5.2 Total seeing

Swain & Gallée (2006) [63] also simulated the total seeing on the Antarctic plateau. The results were shown on the Fig.1 of their paper. The total seeing was predicted $1.3''$ at Dome Fuji, $1.7''$ at Dome A, and $1.3''$ at Dome C, respectively.

1.5.3 Free-atmosphere seeing

Saunders et al. (2009) [57] predicted that the free-atmosphere seeing from the mean wintertime (May-August) over the years 1979-2008 of the NCAR/NCEP reanalysis data, which is a continually updating gridded data representing the state of the Earth's atmosphere, combination between observation and numerical weather prediction. C_n^2 profiles were calculated from the wind speed and the potential temperature gradient from NCAR/NCEP data. They assumed that the wind speed gradient was proportional to the wind speed. C_n^2 profile obtained from NCAR/NCEP data was scaled with the observational profile of Trinquet et al. (2008) [73] at Dome C. The predicted values of the free-atmosphere seeing were $0.209''$ at Dome Fuji, $0.218''$ at Dome A, $0.261''$ at Dome C, and $0.186''$ at South Pole. Free-atmosphere seeing at Dome Fuji was predicted better than at Dome A and Dome C, on the other hand, worse than at South Pole.

The free-atmospheric seeing is considered to depend on the upper atmospheric turbulence, which is caused by the polar vortex in the Antarctica. As the effect of the polar vortex is smaller at higher latitude, it was predicted that the smallest free-atmosphere seeing at South Pole. We summarize predicted and observed seeing on the Antarctic plateau in Table 1.2.

1.6 Seeing measurement on the Antarctic plateau

The Antarctic harsh environment had prevented us measuring the turbulence profile on the Antarctic plateau before 90's. Today, by solving some technical and logistical problems, the astronomical seeing measurements have been performed at various sites on the Antarctic

plateau. Some meteorological simulations were also performed. We describe the details in this section.

1.6.1 South Pole

The first seeing measurement on the Antarctic plateau was carried out at the Amundsen Scott South Pole Station (Loewenstein et al. 1998; Marks et al. 1999; Travouillon et al. 2003a; 2003b) [39, 43, 71, 72]. Marks et al. (1999) [43] used balloon-born micro-thermal probes to profile the temperature structure constant C_T^2 at various height and found that the mean free-atmosphere seeing was $0.37''$. Travouillon et al. (2003a) [71] showed that the atmospheric turbulence was concentrated inside the surface boundary layer sitting bellow $220 \sim 270$-m height on average. Direct measurements of seeing were performed using Differential Image Motion Monitor (DIMM) at the snow surface level, and the results were $1.53 \sim 1.90''$ (Loewenstein et al. 1998; Travouillon et al. 2003b) [39, 72]. Therefore the South Pole was considered not to be suitable for optical/infrared astronomy from the point of the bad seeing near the snow surface. As the surface boundary layer wind is katabatic origin, good seeing near the snow surface is expected at the area with weak wind, such as the top of the Antarctic plateau, i.e., Dome C, Dome A, and Dome Fuji (Marks et al. 2002; 1999) [42, 43].

1.6.2 Dome C

The next seeing measurement in the Antarctic plateau had been carried out at Dome C. Dome C is a local elevation maximum of the Antarctic plateau at 3 250-m elevation and located at the geographical coordinates of $75°06'$ South and $123°21'$ East. Seeing measurements using DIMMs, SOnic Detection And Rangings (SODAR), Multi-Aperture Scintillation Sensors (MASS), and balloons borne microthermal sensors have been performed at Dome C since 2000. Lawrence et al. (2004) [37] reported the winter-time free-atmosphere seeing ($0.27''$) and the height of the surface boundary layer (30-m or lower). Since then, many balloon experiments and DIMMs observations were performed. Eventually the free-atmosphere seeing was found to be $\sim 0.36''$. The height of the surface boundary layer, which produces almost all optical turbulence, was also reported to be $23 \sim 36$-m (Agabi et al. 2006; Aristidi et al. 2005a; 2005b; 2009; Trinquet et al. 2008) [1, 4, 6, 7, 73].

1.6.3 Dome A

Dome A ($80°22'$ South, $77°21'$ East) is the highest peak on the Antarctic plateau at the elevation of 4 093-m. The seeing measurement at Dome A have been carried out with a high-resolution low minimum sample height sonic radar called "Snodar" from 2009 February (Bonner et al. 2010a) [13]. The result of the observations showed that the median height of the surface boundary layer was as low as 13.9-m. The thin surface boundary layer is a merit to build a telescope on a pier to access the free-atmosphere seeing. Although they showed only the thickness of the boundary layer, the free-atmospheric seeing and total seeing from the snow surface at Dome A were unknown yet.

Table 1.2: Astronomical seeing on the Antarctic plateau.

Site	Altitude (m)	SBL height (m)	Total seeing ($''$)	FA Seeing ($''$)
South Pole [1)]	2 835	220 $^{(w)}$ $\sim$ 270 $^{(a,w)}$	1.53 $^{(w)}$ $\sim$ 1.90 $^{(w)}$	0.37 $^{(w)}$
		102 $\pm$ 47 $^{(w)}$	1.75 $\pm$ 0.42 $^{(w)}$	0.186 $^{(w)}$
Dome C [2)]	3 250	23 $\sim$ 36	1.67	0.27 $^{(a)}$ $\sim$ 0.36
		27.7 $^{(w)}$	1.16 $\pm$ 0.68 $^{(w)}$	0.261 $^{(w)}$
Dome A [3)]	4 093	13.9 $^{(a,w)}$	–	–
		21.7 $^{(w)}$	$\sim$ 1.7 $^{(w)}$	0.218 $^{(w)}$
Dome Fuji [4)]	3 810	15.3 $\pm$ 2.7 $^{(a,w)}$	1.1 $\pm$ 0.47 $^{(s)}$	0.23 $\pm$ 0.057 $^{(s)}$
		18.5 $^{(w)}$	$\sim$ 1.3 $^{(w)}$	0.209 $^{(w)}$

Notes: "SBL" and "FA" mean the surface boundary layer and free atmosphere, respectively. The total seeing is the seeing near the snow surface level. Upper line is observational result, and lower line is the predictions (Swain & Gallée 2006 and Saunders et al. 2009) [63, 57], which are the values in the Antarctic winter. Dome A seeings are not available at the time of writing this thesis (February 2014). The superscript $^{(s)}$ $^{(a)}$ $^{(w)}$ mean the results in the Antarctic summer, autumn, and winter. No superscript means the results for all year. The values are median and median absolute deviation (MAD). References: [1)] Loewenstein et al. (1998); Marks et al. (1999); Travouillon et al. (2003a; 2003b) [39, 43, 71, 72]; [2)] Lawrence et al. (2004); Agabi et al. (2006); Aristidi et al. (2005a; 2005b; 2009); and Trinquet et al. (2008) [37, 1, 4, 6, 7, 73]; [3)] Bonner et al. (2010) [14]; and [4)] This thesis.

1.6.4 Dome Fuji

Dome Fuji is located at the geographical coordinates of 77°19′ South and 39°42′ East. The altitude is about 3 810-m, which is one of the local maximum, the second highest region next to Dome A. The annual average temperature at the surface level at Dome Fuji is −54.4°C; the lowest temperature ever recorded is −79.7°C (Yamanouchi et al. 2003) [79]. The Dome Fuji station was constructed for ice-core drilling by the National Institute of Polar Research of Japan (NIPR) in 1995. The winter-over operations were carried out during 1995-1997 and 2003 for ice-core drilling. In the coming decade, NIPR plans to construct a new Dome Fuji station, which will be a permanent winter-over station. Astronomy will be one of the main scientific programs for the new station. To enjoy extremely cold environment at Dome Fuji, we have a plan to construct a 2.5-m mirror infrared telescope named "Antarctic Infra-Red Telescope with 250-cm mirror" (AIRT250).

While the seeing measurement at Dome Fuji had not been performed before 2006, Dome Fuji is predicted to be the best astronomical seeing site among the "Dome" regions of the Anatarctic plateau in the point of the lowest height of the surface boundary layer and the smallest free-atmosphere seeing. However, these simulations would have large uncertainties. For example, the height of the surface boundary layer at Dome A was predicted to be 21.7-m. On the contrary, the site testing found 13.9-m (Bonner et al. 2010a; Swain& Gallée 2006) [13, 63]. There were no astronomical seeing measurements at Dome Fuji before 2006. Direct and quantitative measurement of the atmospheric turbulence at Dome Fuji was required. Here we summarize the astronomical seeing on the Antarctic plateau in Table 1.2.

1.7 The purpose of the thesis

As mentioned above, the Antarctic plateau is considered to have the darkest thermal background and the lowest atmospheric absorption thanks to the cold air and high altitude. In addition the excellent free-atmosphere seeing, which originates from the polar vortex at relatively higher altitude, is also expected on the Antarctic plateau. A weak surface wind brings a low height of the surface boundary layer at the "Dome" regions, which are the highest peaks of the Antarctic plateau. Therefore the Dome regions on the Antarctic plateau are expected to be the best astronomical site on the Earth. Especially, "Dome Fuji" would have the lowest surface boundary layer and the best free-atmosphere seeing. Seeing measurements have been performed or are ongoing at Dome C and Dome A. However, there were no site testings at Dome Fuji dedicated to the seeing.

For the reasons, we planed to carried out the astronomical seeing measurements at Dome Fuji. The purpose of the thesis is to investigate the astronomical seeing and atmospheric structure at Dome Fuji on the Antarctic plateau. For the purpose, we developed the instruments durable in the Antarctic harsh environment, measured the atmospheric turbulence observationally, and evaluated the astronomical seeing based on these observational data.

Chapter 2

Theoretical bases of the turbulence measurements

In this chapter we describe the theoretical bases of the turbulence, following Hardy (1998), Quirrenbach (2000), and Andrews (2004) [3, 23, 54]. Earth's atmosphere affects the optical wave propagation with absorption, scattering, emitting, and refractive index fluctuations, i.e. optical turbulence. We focus on the refractive index fluctuations caused by the atmospheric turbulence.

2.1 Atmospheric turbulence

An atmospheric convection by the solar heating and an mixing of air parcel of different temperature by a wind are almost always occurred in the lower Earth's atmosphere. Since the refractive index of the air parcel depends on its temperature, the distribution of the refractive index varies temporarily and spatially. This phenomena is called "optical turbulence." Intensity and incidence-angle of the rays from an astronomical object for each optical paths are changed with the optical turbulence. Astronomical observations on the ground is always affected by such optical turbulence.

2.1.1 Reynolds number

The properties of fluid flows are characterized by the Raynolds number R_e. If the Raynolds number exceeds the critical value, the fluid flow is changed from laminar to turbulent.

The Reynolds number is defined as

$$R_e = \frac{v\ l}{\nu}\ , \tag{2.1}$$

where v [m s^{-1}] is the characteristic velocity , l [m] the characteristic size of the flow , and ν [m^2 s^{-1}] the kinematic viscosity of the fluid. For air, $\nu \sim 1.5 \times 10^{-5}$ [m^2 s^{-1}]. For the moderate size atmospheric turbulence with $v = 10$ [m s^{-1}] and $l = 15$ [m], the Reynolds number is 1×10^7, which greatly exceeds the critical value of $\sim 2 \times 10^3$. As a result, airflow in the atmosphere is nearly always turbulent.

2.1.2 Kolmogorov model

We assume that the turbulence is homogeneous and isotropic. The mechanical structure of turbulence was investigated by Kolmogorov (1941) [28]. Kolmogorov proposed a model for the velocity of motion in a fluid medium. Kolmogorov assumed that an energy is added to the fluid medium in the form of large-scale disturbance. The energy input occurs by an atmospheric convection with the solar heating, and by mixing of air masses of different temperatures with a wind. This large scale is called "outer scale" L_0. The large scale disturbance breaks down into smaller and smaller structures. The kinetic energy is continually transferred to motions of smaller scale, forming an "energy cascade." The energy cascade continues when the Reynolds number drops below the critical number. After the Reynolds number of the turbulent drops below the critical number, the kinetic energy is dissipated into heat by molecular friction (viscous), and then the turbulence dies away. This small scale is called "inner scale" l_0. The typical value of the outer scale L_0 is a few tens to hundreds of meters. The inner scale l_0 is of order a few millimeters. The scale between l_0 and L_0 is called "inertial range." In the inertial range, the turbulence strength is express as a function of the eddy size l or of the spatial frequency $k = 2\pi/l$. This simple turbulence model was developed by Kolmogorov, and is generally known as "Kolmogorov turbulence."

2.2 Structure and correlation functions

Structure and correlation functions are introduced for quantitative discussion of the atmospheric turbulence. We define a structure function between two components of function $f(x)$ separated by distance r along a coordinate x as follow.

$$D_f(r) \equiv \langle \{f(x) - f(x+r)\}^2 \rangle \tag{2.2}$$

The correlation function between two components of function $f(x)$ separated by distance r along a coordinate x is defined as

$$B_f(r) \equiv \langle f(x+r) f^*(r) \rangle \ . \tag{2.3}$$

The structure function can be written using the correlation function,

$$\begin{aligned} D_f(r) &\equiv \langle \{f(x) - f(x+r)\}^2 \rangle \\ &= \langle f(x)^2 - 2f(x)f(x+r) + f(x+r)^2 \rangle \\ &= \langle f(x)f^*(x) \rangle - 2\langle f(x)f^*(x+r) \rangle + \langle f(x+r)f^*(x+r) \rangle \\ &= 2\{B_f(0) - B_f(r)\} \ , \end{aligned} \tag{2.4}$$

where $\mathrm{B}_f(0)$ is the mean-square value of the function. For most functions, the correlation at larger separation should be zero, i.e., $\mathrm{B}_f(\infty) \to 0$, thus

$$D_f(\infty) = 2B_f(0) \ . \tag{2.5}$$

2.2.1 Velocity structure function for Kolmogorov turbulence

Only two parameters that determine the strength and spectrum of Kolmogorov turbulence are the rate of energy generation per unit mass ϵ_{eng} [J s^{-1} kg^{-1}] or ϵ_{eng} [m^2 s^{-3}], and

the kinematic viscosity ν [m^2 s^{-1}]. We assume that the turbulence is homogeneous and isotropic. Here we define a velocity structure function D_v between two components of velocity separated by distance r along a coordinate x. D_v depends only on r, and can be written as

$$\begin{aligned} D_v(r) &\equiv \langle \{v(x) - v(x+r)\}^2 \rangle \\ &= \alpha \cdot f(r/\beta) \ , \end{aligned} \tag{2.6}$$

where f is a dimensionless function of a dimensionless argument. It is immediately clear that the dimensions of α is velocity squared, and those of β is length. As α and β depend only on ϵ_{eng} and ν, it follows from dimensional analysis that

$$\alpha = \nu^{1/2} {\epsilon_{eng}}^{1/2} \tag{2.7}$$

$$\beta = \nu^{3/4} {\epsilon_{eng}}^{-1/4} \ . \tag{2.8}$$

In addition the structure function must be independent of ν in the inertial range, and therefore the velocity structure function is

$$D_v(r) = \alpha \cdot \left(\frac{r}{\beta} \right)^{2/3} = C_v^2 r^{2/3} \ , \tag{2.9}$$

where C_v^2 is a proportional constant. The unit of C_v^2 is [$m^{4/3}$ s^{-2}]. C_v^2 is named "velocity structure constant." Therefore the turbulence strength can be written only one parameter C_v^2.

2.2.2 Temperature structure function

The atmospheric turbulence, which is caused by the velocity fluctuations, mixes different layers of air and it carries parcels of air with different temperature. Therefore, the temperature fluctuation should follow the Kolmogorov turbulence (Tatarskii 1961) [65],

$$D_T(r) \equiv \langle \{T(x) - T(x+r)\}^2 \rangle = C_T^2 r^{2/3} \ , \tag{2.10}$$

where C_T^2 is named "temperature structure constant." The unit of C_T^2 is [K^2 $m^{-2/3}$].

2.2.3 Refractive-index structure function

The turbulence with different temperature parcels should have different densities or different refractive index n in pressure equilibrium. Therefore, the refractive index structure function is also follow the Kolmogorov turbulence (Tatarskii 1961) [65],

$$D_n(r) \equiv \langle \{n(x) - n(x+r)\}^2 \rangle = C_n^2 r^{2/3} \ , \tag{2.11}$$

where C_n^2 is the refractive index structure constant. The unit of C_n^2 is [$m^{-2/3}$].

The refractive index n can be approximated with pressure P [hPa] and temperature T [K] (Tatarskii 1971) [66],

$$n = 1 + 77.6 \times 10^{-6} \left(\frac{P}{T} \right) \ . \tag{2.12}$$

Therefore

$$dn = -77.6 \times 10^{-6} \left(\frac{P}{T^2} \right) dT \tag{2.13}$$

$$C_n^2 = \left(\frac{77.6 \times 10^{-6} P}{T^2} \right)^2 C_T^2 \ . \tag{2.14}$$

If we know the temperature structure constant C_T^2, temperature T, and pressure P, we can calculate the refractive index structure constant C_n^2.

The power spectral density $\Phi_n(k)$ is calculated from the structure function. Using the Wiener-Khinchin theorem,

$$C_n^2 r^{2/3} = D_n(r) = 2 \int_{-\infty}^{\infty} dk \left\{ 1 - \exp(2\pi i k r) \right\} \Phi_n(k) \ . \tag{2.15}$$

Calculating $\Phi_n(k)$,

$$\Phi_n(k) = \frac{\Gamma(5/3) \sin(\pi/3)}{(2\pi)^{5/3}} C_n^2 k^{-5/3} \tag{2.16}$$

$$\sim 0.033 \ C_n^2 k^{-5/3} \ . \tag{2.17}$$

Therefore, the power spectrum of Kolmogorov turbulence follows $-5/3$ power of the spatial frequency in the inertial range (for one dimension).

2.2.4 Phase structure function

Roddier (1981) [55] gives the phase shift produced by thin turbulence layer of δh as

$$\phi(x) = k \int_{h}^{h+\delta h} dz \ n(x, z) \ , \tag{2.18}$$

where k is the wave number. The phase correlation function and the refractive index correlation function are defined from Eq. (2.3),

$$B_\phi(r) \equiv \langle \phi(x + r) \phi^*(r) \rangle \tag{2.19}$$

$$B_n(r) \equiv \langle n(x + r) n^*(r) \rangle \ . \tag{2.20}$$

From Eq. (2.18), the phase correlation function can be written as

$$B_\phi(r) = k^2 \delta h \int_{-\infty}^{+\infty} dz \ B_n(r, z) \ . \tag{2.21}$$

As δh is much larger than the refractive index fluctuations, the integral is taken from $-\infty$ to $+\infty$.

The phase structure function is expressed as

$$\begin{aligned} D_\phi(r) &= 2\{B_\phi(0) - B_\phi(r)\} \\ &= 2k^2 \delta h \int_{-\infty}^{+\infty} dz \ \{B_n(0, z) - B_n(r, z)\} \\ &= 2k^2 \delta h \int_{-\infty}^{+\infty} dz \ \{B_n(0, z) - B_n(0, 0) + B_n(0, 0) - B_n(r, z)\} \\ &= k^2 \delta h \int_{-\infty}^{+\infty} dz \ \{D_n(r, z) - D_n(0, z)\} \ . \end{aligned} \tag{2.22}$$

Here we use the expression of the refractive index structure function of Eq. (2.11),

$$D_n(r,z) = C_n^2(r^2+z^2)^{1/3} \ . \tag{2.23}$$

Therefore the phase structure function is

$$\begin{aligned} D_\phi(r) &= k^2 C_n^2 \delta h \int_{-\infty}^{+\infty} dz \left\{ (r^2+z^2)^{1/3} - z^{2/3} \right\} \\ &= 2k^2 C_n^2 \delta h \int_{0}^{+\infty} dz \left\{ (r^2+z^2)^{1/3} - z^{2/3} \right\} \\ &= k^2 C_n^2 \delta h \times \frac{1}{3}\frac{6}{5}\frac{\Gamma(1/2)\Gamma(1/6)}{\Gamma(2/3)} r^{5/3} \\ &= 2.914 k^2 \delta h r^{5/3} C_n^2 \ . \end{aligned} \tag{2.24}$$

This expression means that the phase structure function at the output of a thin layer of δh with Kolmogorov turbulence can be written with the refractive index structure constant of C_n^2.

2.3 Turbulence parameters

At first we introduce the coherence function of the phase error separated by distance r. The coherence function of the output of the turbulence layer is defined as

$$\beta_{\phi,\delta h}(r) \equiv \langle \exp\{ i\phi(x) - i\phi(x+r) \} \rangle \ . \tag{2.25}$$

Since the phase shift of $\phi(x)$ follows Gaussian statistics with zero mean, the coherence function can be expressed as

$$\begin{aligned} \beta_{\phi,\delta h}(r) &= \exp\left\{ -\frac{1}{2} \langle |\phi(x) - \phi(x+r)|^2 \rangle \right\} \\ &= \exp\left\{ -\frac{1}{2} D_\phi(r) \right\} \\ &= \exp\left\{ -\frac{1}{2} (2.914 k^2 \delta h r^{5/3} C_n^2) \right\} \ , \end{aligned} \tag{2.26}$$

where we use Eq. (2.24). For astronomical observations, the coherence function at the ground should be integrated all turbulence layer,

$$\beta_{\phi,total}(r) = \exp\left\{ -\frac{1}{2} \int dh \ \sec(\zeta) D_\phi(r) \right\} \tag{2.27}$$

$$= \exp\left[-\frac{1}{2} \left\{ 2.914 k^2 r^{5/3} \sec(\zeta) \int dh \ C_n^2(h) \right\} \right] \ , \tag{2.28}$$

where ζ is the zenith angle of the line of sight. The total coherence function decreases exponentially with 5/3 power of distance r and integral of C_n^2. This expression is fundamentally important for determining the effect of the optical turbulence.

2.3.1 Fried length

Here we study the effect of the turbulence to a star image obtained by an astronomical telescope. The optical transfer function for the whole imaging system $S(r/\lambda)$, i.e. through a telescope and atmosphere, for long exposure is

$$S(r/\lambda) = A(r/\lambda) \cdot T(r/\lambda) \ , \tag{2.29}$$

where r is a diameter of telescope assuming a circular aperture, λ is a wavelength, $A(r/\lambda)$ is atmospheric transfer function, and $T(r/\lambda)$ is telescope transfer function. Fried (1966) [21] introduced the resolving power of a telescope R, which is defined as the integral of the optical transfer function. The resolving power R follows from Eq. (2.29),

$$R = \int d(r/\lambda) \ A(r/\lambda) \cdot T(r/\lambda) \ . \tag{2.30}$$

For a small aperture telescope, turbulence effects are negligible. Thus the resolving power for a diffraction limited telescope with a circular aperture of diameter r is

$$R_S = \int d(r/\lambda) \ T(r/\lambda) = \frac{\pi}{4} \left(\frac{r}{\lambda}\right)^2 \ . \tag{2.31}$$

For a large aperture telescope, the resolving power depends only on turbulence,

$$R_L = \int d(r/\lambda) \ A(r/\lambda) \ . \tag{2.32}$$

Here we define the Fried length r_0, the diameter of a telescope with the same resolving power of the atmospheric turbulence,

$$R_L = \int d(r/\lambda) \ A(r/\lambda) = \frac{\pi}{4} \left(\frac{r_0}{\lambda}\right)^2 \ . \tag{2.33}$$

From Eq. (2.28) the atmospheric transfer function should be written as

$$A(r/\lambda) = \beta_{\phi,total}(r) = \exp\left\{-K \left(\frac{r}{\lambda}\right)^{5/3}\right\} . \tag{2.34}$$

From Eq. (2.33) we obtain

$$\begin{aligned} \frac{\pi}{4} \left(\frac{r_0}{\lambda}\right)^2 &= \int d(r/\lambda) \ \exp\left\{-K \left(\frac{r}{\lambda}\right)^{5/3}\right\} \\ &= \frac{6\pi}{5} \Gamma(6/5) K^{-6/5} \end{aligned} \tag{2.35}$$

or

$$K = 3.44 \left(\frac{r_0}{\lambda}\right)^{-5/3} \ . \tag{2.36}$$

Therefore

$$\begin{aligned} \beta_{\phi,total}(r) &= A(r/\lambda) \\ &= \exp\left\{-3.44 \left(\frac{r}{r_0}\right)^{5/3}\right\} \end{aligned} \tag{2.37}$$

Comparing Eq. (2.28) with Eq. (2.37), we can calculate the Fried length r_0:

$$\begin{aligned} r_0 &= \left\{0.423k^2 \sec(\zeta) \int dh\ C_n^2(h)\right\}^{-3/5} \\ &= 0.185\ \lambda^{6/5} \sec(\zeta)^{-3/5} \left\{\int dh\ C_n^2(h)\right\}^{-3/5} . \end{aligned} \tag{2.38}$$

The Fried length is defined as the diameter of a telescope which is equivalent with the resolving power worsen by the atmospheric turbulence. From Eq. (2.38), we understand that the Fried length depends 6/5 power of wavelength λ, $-3/5$ power of airmass $\sec(\zeta)$, and $-3/5$ power of integration of the refractive index structure constant C_n^2.

2.3.2 Isoplanatic angle

The mean-square wavefront error between two points in the wavefront separated at a distance r is defined by the phase structure function $D_\phi(r)$. An angular anisoplanatism is modeled by two beams incidenting at a telescope pupil and then separate at an angle θ. The separation distance at height h can be written as

$$r(h) = \theta \sec(\zeta) h\ , \tag{2.39}$$

where h is the height of the beam above the telescope and ζ is the zenith angle. Therefore the mean-square anisoplanatic error at angle θ is

$$\begin{aligned} \langle \sigma_\theta^2 \rangle &= D_\phi(r) = D_\phi \left\{\theta \sec(\zeta) h\right\} \\ &= 2.914k^2 \sec(\zeta) \int dh\ C_n^2(h) \left\{\theta \sec(\zeta) h\right\}^{5/3} \\ &= 2.914k^2 \sec(\zeta)^{8/3} \theta^{5/3} \int dh\ C_n^2(h) h^{5/3} \\ &= \left(\frac{\theta}{\theta_0}\right)^{5/3} . \end{aligned} \tag{2.40}$$

θ_0 is defined as

$$\theta_0 = \left\{2.914k^2 \sec(\zeta)^{8/3} \int dh\ C_n^2(h) h^{5/3}\right\}^{-3/5} , \tag{2.41}$$

which is known as the "isoplanatic angle" and is a property of the turbulence distribution.

2.4 Integrated structure function

We study the integration of the phase structure and incident angle structure functions.

2.4.1 Integrated phase structure function

The integrated phase structure function observed at the ground is defined as

$$D_{\phi,total}(r) \equiv \int dh\ \sec(\zeta) D_\phi(r)\ . \tag{2.42}$$

Thus Eq. (2.27) can be expressed as follow.

$$\beta_{\phi,total}(r) = \exp\left\{-\frac{1}{2}D_{\phi,total}(r)\right\} . \tag{2.43}$$

Comparing Eq. (2.37) and Eq. (2.43), we can obtain the integrated phase structure function $D_{\phi,total}(r)$,

$$D_{\phi,total}(r) = 6.88\left(\frac{r}{r_0}\right)^{5/3} . \tag{2.44}$$

The integrated phase structure function is proportional to 5/3 power of the Fried length r_0.

2.4.2 Integrated incident-angle structure function

First, we define the position $\vec{x}$ and distance $\vec{r}$,

$$|\vec{x}| = \sqrt{x^2+y^2} \tag{2.45}$$
$$|\vec{r}| = \sqrt{\xi^2+\eta^2} . \tag{2.46}$$

The incident angle $\alpha(x,y)$ in the x direction can be written with the phase shift $\phi(x,y)$,

$$\alpha_x(x,y) = -\frac{\partial}{\partial x}z(x,y) = -\frac{\lambda}{2\pi}\frac{\partial}{\partial x}\phi(x,y) \tag{2.47}$$
$$\alpha_y(x,y) = -\frac{\partial}{\partial y}z(x,y) = -\frac{\lambda}{2\pi}\frac{\partial}{\partial y}\phi(x,y) . \tag{2.48}$$

Hence the incident-angle correlation functions are

$$\begin{aligned} B_{\alpha_x}(\xi,\eta) &= \langle\alpha(x+\xi,y+\eta)\alpha^*(x,y)\rangle \\ &= -\frac{\lambda^2}{4\pi^2}\frac{\partial^2}{\partial\xi^2}B_\phi(\xi,\eta) \end{aligned} \tag{2.49}$$
$$B_{\alpha_y}(\xi,\eta) = -\frac{\lambda^2}{4\pi^2}\frac{\partial^2}{\partial\eta^2}B_\phi(\xi,\eta) . \tag{2.50}$$

The atmospheric turbulence is homogeneous and isotropic. Therefore,

$$B_{\alpha_x}(\xi,\eta) = B_{\alpha_y}(\eta,\xi) . \tag{2.51}$$

Using Eq. (2.4), the phase structure function is

$$\begin{aligned} D_\phi(\xi,\eta) &\equiv \langle\{\phi(x)-\phi(x+r)\}^2\rangle \\ &= 2\{B_\phi(0,0)-B_\phi(\xi,\eta)\} . \end{aligned} \tag{2.52}$$

Therefore, the correlation functions of the incident angle are

$$B_{\alpha_x}(\xi,\eta) = \frac{\lambda^2}{8\pi^2}\frac{\partial^2}{\partial\xi^2}D_\phi(\xi,\eta) \tag{2.53}$$
$$B_{\alpha_y}(\xi,\eta) = \frac{\lambda^2}{8\pi^2}\frac{\partial^2}{\partial\eta^2}D_\phi(\xi,\eta) . \tag{2.54}$$

For astronomical observations, the correlation functions at the ground should be integrated over all turbulence layers,

$$\begin{aligned} B_{\alpha_x,total}(\xi,\eta) &= \int dh\ \sec(\zeta) B_\alpha(\xi,\eta) \\ &= \frac{\lambda^2}{8\pi^2}\frac{\partial^2}{\partial\xi^2}\int dh\ \sec(\zeta) D_\phi(\xi,\eta) \\ &= \frac{\lambda^2}{8\pi^2}\frac{\partial^2}{\partial\xi^2} D_{\phi,total}(\xi,\eta) \qquad (2.55) \\ B_{\alpha_y,total}(\xi,\eta) &= \frac{\lambda^2}{8\pi^2}\frac{\partial^2}{\partial\eta^2} D_{\phi,total}(\xi,\eta)\ . \qquad (2.56) \end{aligned}$$

From Eq. (2.51),

$$\begin{aligned} B_{\alpha_x,total}(\xi,\eta) &= B_{\alpha_y,total}(\eta,\xi) \qquad (2.57) \\ D_{\alpha_x,total}(\xi,\eta) &= 2\left\{B_\alpha(0,0) - B_\alpha(\xi,\eta)\right\} \\ &= 2\left\{B_\beta(0,0) - B_\alpha(\eta,\xi)\right\} \\ &= D_{\alpha_y,total}(\eta,\xi)\ . \qquad (2.58) \end{aligned}$$

Calculating Eq. (2.55) with Eq. (2.44),

$$\begin{aligned} B_{\alpha_x,total}(\xi,\eta) &= \frac{\lambda^2}{8\pi^2}\frac{\partial^2}{\partial\xi^2}\left\{6.88\ \left(\frac{r}{r_0}\right)^{5/3}\right\} \\ &= \frac{\lambda^2}{8\pi^2}\frac{\partial^2}{\partial\xi^2}\left\{6.88\ (\xi^2+\eta^2)^{5/6} r_0^{-5/3}\right\} \\ &= 0.145\lambda^2 r_0^{-5/3}\left\{(\xi^2+\eta^2)^{-1/6} - \frac{1}{3}\xi^2(\xi^2+\eta^2)^{-7/6}\right\}\ . \qquad (2.59) \end{aligned}$$

For $\eta = 0$, we get the longitudinal correlation (in the direction of the tilt) as a function of the separation $\xi = d$:

$$B_{\alpha_x,total}(d,0) = 0.0968\left(\frac{\lambda}{r_0}\right)^{5/3}\left(\frac{\lambda}{d}\right)^{1/3}\ . \qquad (2.60)$$

For $\xi = 0$, we get the transverse correlation (in a direction perpendicular to the tilt) as a function of the separation $\eta = d$:

$$B_{\alpha_x,total}(0,d) = 0.145\ \left(\frac{\lambda}{r_0}\right)^{5/3}\left(\frac{\lambda}{d}\right)^{1/3}\ . \qquad (2.61)$$

It diverges at the origin, however. According to Sarazin & Roddier (1990) [56], the value at the origin is limited by averaging in the aperture and is expressed with the variance of image motion (Fried 1965; 1975 and Tatarskii 1971) [20, 22, 66],

$$B_{\alpha_x,total}(0,0) = 0.179\left(\frac{\lambda}{r_0}\right)^{5/3}\left(\frac{\lambda}{D}\right)^{1/3}\ , \qquad (2.62)$$

where D is the diameter of a telescope sub-aperture.

Thus the integrated incident-angle structure function for longitudinal direction is

$$\begin{aligned} D_{\alpha_x,total}(d,0) &= \langle\{\alpha(x+d,y) - \alpha(x,y)\}^2\rangle \\ &= 2\left\{B_\alpha(0,0) - B_\alpha(d,0)\right\} \\ &= 2\lambda^2 r_0^{-5/3}(0.179D^{-1/3} - 0.0968d^{-1/3})\ . \qquad (2.63) \end{aligned}$$

The integrated incident angle structure function for transverse direction is

$$\begin{aligned} D_{\alpha_x,total}(0,d) &= \langle\{\alpha(x,y+d)-\alpha(x,y)\}^2\rangle \\ &= 2\left\{B_\alpha(0,0)-B_\alpha(0,d)\right\} \\ &= 2\lambda^2 r_0^{-5/3}(0.179D^{-1/3}-0.145d^{-1/3}) \ . \end{aligned} \tag{2.64}$$

From Eq. (2.58),

$$D_{\alpha_y,total}(d,0) = 2\lambda^2 r_0^{-5/3}(0.179D^{-1/3}-0.145d^{-1/3}) \ . \tag{2.65}$$

The integrated incident angle structure function $D_{\alpha,total}$ is calculated from the diameter of a telescope sub-apertures D, the separation of the sub-apertures d, and the Fried length r_0.

2.5 Effect of the atmospheric turbulence

The atmospheric turbulence degrades the quality of star images in terms of astrometry and photometry. Earth's atmosphere fluctuates star positions and then makes an origin of poor astrometry. Earth's atmosphere also causes intensity fluctuation and it makes photometry less accurate. The former phenomenon is called "astronomical seeing" and the latter is "stellar scintillation." In this section we quantify these astronomical phenomena.

2.5.1 Astronomical seeing

The astronomical seeing ϵ is defined as the full width at half maximum (FWHM) of the point spread function (PSF) spread by the atmospheric turbulence. Fried length r_0, showed in Eq. (2.38), is defined by telescope diameter, which is equivalent with the resolving power worsen by the atmospheric turbulence. The Rayleigh criterion of the angular resolution θ_R for telescope diameter $D = r_0$ and wavelength λ is

$$\theta_R = 1.22\frac{\lambda}{r_0} \ . \tag{2.66}$$

The factor 1.22 is derived from the first zero of the Bessel function. Therefore the astronomical seeing ϵ should be

$$\epsilon < 1.22\frac{\lambda}{r_0} \ . \tag{2.67}$$

Dierickx (1988) calculated the FWHM of the PSF numerically. The astronomical seeing ϵ' at wavelength λ (and zenith angle ζ) is expressed as,

$$\epsilon' = 0.98\ \frac{\lambda}{r_0} \tag{2.68}$$

Here we use Eq. (2.38) for the astronomical seeing ϵ' at wavelength λ and zenith angle ζ,

$$\epsilon' = 5.35\ \lambda^{-1/5}\sec(\zeta)^{3/5}\left\{\int dh\ C_n^2(h)\right\}^{3/5} \ . \tag{2.69}$$

The astronomical seeing depends on $-1/5$ power of wavelength λ, $3/5$ power of airmass $\sec(\zeta)$, and $3/5$ power of integration of the refractive index structure constant C_n^2. The

astronomical seeing is generally defined as the value at $\lambda = 500$ nm and at airmass $\sec(0) = 1$ (i.e. at zenith). Thus we express ϵ the astronomical seeing at 500 nm and at zenith as follows.

$$\epsilon = \left(\frac{500_{nm}}{\lambda}\right)^{-1/5} \left(\frac{1}{\sec(\zeta)}\right)^{3/5} 5.35\ \lambda^{-1/5} \sec(\zeta)^{3/5} \left\{\int dh\ C_n^2(h)\right\}^{3/5} . \quad (2.70)$$

Fried length is also written with the integrated incident-angle structure function expressed in Eq. (2.63) and Eq. (2.64),

$$r_{0,l} = \lambda^{6/5} \left\{2\ (0.179D^{-1/3} - 0.0968d^{-1/3})\right\}^{3/5} D^{-3/5}_{\alpha_x,total}(d,0) \quad (2.71)$$

$$r_{0,t} = \lambda^{6/5} \left\{2\ (0.179D^{-1/3} - 0.145d^{-1/3})\right\}^{3/5} D^{-3/5}_{\alpha_y,total}(d,0)\ . \quad (2.72)$$

Therefore, the astronomical seeing at λ and ζ is calculated from Eq. (2.68),

$$\epsilon_l = \left(\frac{500_{nm}}{\lambda}\right)^{-1/5} \left(\frac{1}{\sec(\zeta)}\right)^{3/5} 0.647\ \lambda^{-1/5} \left\{\frac{D_{\alpha_x,total}(d,0)}{0.179D^{-1/3} - 0.0968d^{-1/3}}\right\}^{3/5} \quad (2.73)$$

$$\epsilon_t = \left(\frac{500_{nm}}{\lambda}\right)^{-1/5} \left(\frac{1}{\sec(\zeta)}\right)^{3/5} 0.647\ \lambda^{-1/5} \left\{\frac{D_{\alpha_y,total}(d,0)}{0.179D^{-1/3} - 0.145d^{-1/3}}\right\}^{3/5} \quad (2.74)$$

It is noted that the astronomical seeing depends on 3/5 power of integrated incident angle structure function $D_{\alpha_x,total}(d,0)$ or $D_{\alpha_y,total}(d,0)$.

2.5.2 Stellar scintillation

Stellar scintillation, or twinkling, is a phenomena of intensity fluctuation of stars caused by the Earth's atmospheric disturbance. It can be easily observed with naked eyes. We introduce its outline briefly because it is beyond the scope of the present thesis.

The stellar scintillation for small intensity fluctuation is defined as the variance of the natural logarithm of the intensity of star light,

$$\sigma_I^2 = \langle(\ln I - \langle \ln I\rangle)^2\rangle\ . \quad (2.75)$$

In Roddier (1981) [55] and Tokovinin (2002) [69], the scintillation index is related to the refractive index structure constant $C_n^2(h)$ by

$$\sigma_I^2 = \int dh\ C_n^2(h)\ Q(h)\ , \quad (2.76)$$

where h is the altitude and $Q(h)$ is a weighting function expressed with the pupil shape. The stellar scintillation depends not only on the atmospheric turbulence but also on the shape of the telescope pupil.

The weight function $Q(h)$ is given by

$$Q(h) = 9.62\lambda^{-2} \int_0^\infty df\ f^{-8/3} \sin^2(\pi\lambda h f^2) A(f) \quad (2.77)$$

$$A(f) = \frac{1}{2\pi} \int_0^{2\pi} d\phi\ |\tilde{W}(f,\phi)|^2\ , \quad (2.78)$$

where f is the spatial frequency.

For a circular aperture of diameter D, $A(f)$ is equal to the square of the Fourier transform of the aperture transmission function normalized at $f = 0$,

$$\tilde{W}(f) = \frac{2J_1(\pi Df)}{\pi Df} \ , \tag{2.79}$$

where J_1 is the first order Bessel function. Thus,

$$A(f) = \left\{ \frac{2J_1(\pi Df)}{\pi Df} \right\}^2 \ . \tag{2.80}$$

For an infinitely small aperture telescope with D, one should set $A(f) = 1$ (Tokovinin 1998) [68]. In this case, which was shown by Roddier (1981) [55], $Q(h)$ is proportional to $h^{5/6}$, and the stellar scintillation is written as

$$\sigma_I^2 \sim 19.2 \ \lambda^{-7/6} \sec(\zeta)^{11/6} \int dh \ h^{5/6} C_n^2(h) \ . \tag{2.81}$$

For an large aperture telescope with D, $Q(h)$ is proportional to h^2. The stellar scintillation can be written as follows (Kenyon et al. 2006; Roddier 1981) [27, 55],

$$\sigma_I^2 \sim 17.3 \ D^{-7/3} \sec(\zeta)^3 \int dh \ h^2 C_n^2(h) \ . \tag{2.82}$$

For an intermediate size telescope, the dependence of $Q(h)$ on h lies between the limiting cases $h^{5/6}$ and h^2 (Tokovinin 1998) [68].

2.6 Methods for the turbulence measurement

We describe the methods for the turbulence measurement. As stated in the previous sections, knowing $C_n^2(h)$ profiles, we can calculate the turbulence parameters, the Fried length r_0 and isoplanatic angle θ_0, and evaluate the atmospheric phenomena of the astronomical seeing ϵ and the stellar scintillation σ_I^2. In this section, we describe optical methods for measuring a turbulence using a small telescope. The turbulence measurements without telescope are also shown.

2.6.1 Differential Image Motion Monitor

Differential Image Motion Monitor (DIMM) was introduced by Sarazin & Roddier (1990) [56]. DIMM is a method to measure the atmospheric turbulence optically by using a small telescope. It is now broadly used for seeing measurement, for example, at the Antarctic plateau, the Greenland Ice Cap, and TMT, GMT, and E-ELT candidate sites (Andersen et al. 2010; Aristidi et al. 2009; Berdja et al. 2011; Dali Ali et al. 2010; Skidmore et al. 2009) [2, 7, 11, 19, 59].

DIMM directly measures the integrated incident angle structure function and converts it to the astronomical seeing. DIMM has two or more sub-apertures with diameter D and separation d. We define the physical positions of two sub-apertures; at (x_1, y_1) and t (x_2=$x_1 + d$, y_2=y_1). Since a wedge prism is attached on one sub-aperture at the entrance pupil of the telescope, DIMM makes two images of the same star on a CCD detector. The star images are focused on the detector; at (x_1', y_1') and at (x_2', y_2'), respectively. To simplify the calculation, we assume that the physical coordinate of sub-aperture is coincident with

the coordinate of the CCD detector (i.e. $x = x'$ and $y = y'$). The dispersion $\sigma^2_{x'}$ [pix^2] of the relative position of two star images on x' axis of the detector is

$$\begin{aligned}\sigma^2_{x'} &= \frac{1}{n-1}\sum_{i=1}^{n}\left\{(x'_1 - x'_2) - (\overline{x'_1 - x'_2})\right\}^2 \\ &\sim p^2_{x'}\ \langle\{\alpha_x(x+d,y) - \alpha_x(x,y)\}^2\rangle \\ &= p^2_{x'}\ D_{\alpha_x,total}(d,0)\ . \end{aligned} \tag{2.83}$$

That on y' axis $\sigma^2_{y'}$ [pix^2] is

$$\begin{aligned}\sigma^2_{y'} &= \frac{1}{n-1}\sum_{i=1}^{n}\left\{(y'_1 - y'_2) - (\overline{y'_1 - y'_2})\right\}^2 \\ &\sim p^2_{y'}\ \langle\{\alpha_y(x+d,y) - \alpha_y(x,y)\}^2\rangle \\ &= p^2_{y'}\ D_{\alpha_y,total}(d,0)\ , \end{aligned} \tag{2.84}$$

where $p_{x'}$ and $p_{y'}$ are the pixel scales [radian/pix] on x' and y' axes on the detector, respectively. n is the measurement number of the star positions.

From Eq. (2.73) and Eq. (2.74), the astronomical seeing at $\lambda = 500$ [nm] at ζ=0 is finally calculated as

$$\epsilon_l = \left\{\frac{61.0\cos(\zeta)}{0.179D^{-1/3} - 0.0968d^{-1/3}}\ \left(\frac{\sigma_{x'}}{p_{x'}}\right)^2\right\}^{3/5} \tag{2.85}$$

$$\epsilon_t = \left\{\frac{61.0\cos(\zeta)}{0.179D^{-1/3}\ -\ 0.145d^{-1/3}}\ \left(\frac{\sigma_{y'}}{p_{y'}}\right)^2\right\}^{3/5}\ , \tag{2.86}$$

in radian. DIMM observations estimate two seeing values of ϵ_l and ϵ_t simultaneously. These two values should be the same if the turbulence is homogeneous and isotropic.

2.6.2 Isoplanatic angle measurement

The instruments that measure refractive turbulence parameters are called the stellar scintillometer or the isoplanometer. The instruments measure the atmospheric turbulence optically with a small telescope. Here we overview the theoretical background.

As shown in Chapter 2.5.2, the weighting function $Q(h)$ of the scintillation index σ^2_I lies between $h^{5/6}$ and h^2. From Eq. (2.41), the isoplanatic angle θ_0 is proportional to $-3/5$ power of the integration of $C^2_n(h)h^{5/3}$. If we observe the stellar scintillation with a "special" shape of the aperture which makes the weighting function of $h^{5/3}$, we can measure the isoplanatic angle directory from the scintillation observation. Loos & Hogge (1979) [40] proposed the circular aperture telescope with $D = 110.3$ or 108.1 [mm] for $Q(h) \propto h^{5/3}$. Krause-Polstorff et al. (1993) [31] showed that the "special" concentric double annular apertures make a weighting function proportional to $h^{5/3}$. Here we examine the weighting function for an annular aperture. We write the annular aperture with an outer diameter of D and inner diameter of αD, the aperture transfer function is written as

$$\tilde{W}(f) = \frac{1}{1-\alpha^2}\left\{\frac{2J_1(\pi Df)}{\pi Df} - \alpha^2\frac{2J_1(\pi\alpha Df)}{\pi\alpha Df}\right\}\ , \tag{2.87}$$

and thus the aperture filtering function for annular aperture is

$$A(f) = \frac{1}{(1-\alpha^2)^2}\left\{\frac{2J_1(\pi Df)}{\pi Df} - \alpha^2\frac{2J_1(\pi\alpha Df)}{\pi\alpha Df}\right\}^2 . \tag{2.88}$$

For the concentric double annular apertures,

$$\begin{aligned} A(f) &= \frac{1}{(1-\alpha_1^2+\alpha_2^2-\alpha_3^2)^2} \\ &\times\left\{\frac{2J_1(\pi Df)}{\pi Df} - \alpha_1^2\frac{2J_1(\pi\alpha_1 Df)}{\pi\alpha_1 Df} + \alpha_2^2\frac{2J_1(\pi\alpha_2 Df)}{\pi\alpha_2 Df} - \alpha_3^2\frac{2J_1(\pi\alpha_3 Df)}{\pi\alpha_3 Df}\right\}^2 \end{aligned} \tag{2.89}$$

In Krause-Polstorff et al. (1993) [31], they used $D = 20.32$ [cm], $\alpha_1 = 0.369$, $\alpha_2 = 0.492$, $\alpha_3 = 0.689$. Ziad et al. (2000) [81] noted that a single annular diameter with $D = 10$ [cm] and $\alpha = 0.4$ is rather close to $h^{3/5}$.

The isoplanatic angle measurement was carried out with the Generalized Seeing Monitor (GSM) and DIMM-θ_0 instruments at Dome C (Aristidi et al. 2005a; Ziad et al. 2008) [4, 80]. Multi Aperture Scintillation Sensor (MASS), which will be descried in Chapter 2.6.3, also measured the isoplanatic angle θ_0 at Dome C and other sites.

2.6.3 Multi Aperture Scintillation Sensor

The astronomical seeing ϵ would not be a sufficient clue to understanding the Earth's atmospheric turbulence because adaptive optics (AO) and interferometry depend on additional atmospheric parameters, such as the isoplanatic angle θ_0 (Hardy 1998) [23]. Photometry and astrometry with high accuracy are also needed for the turbulence profile above the site (Kenyon et al. 2006) [27]. Multi Aperture Scintillation Sensor (MASS) is a powerful tool for advanced site monitoring and testing (Kornilov et al. 2007) [29]. It has been used for site testing at the Antarctic plateau, the Canadian high arctic, TMT, GMT, and E-ELT candidate sites (Lawrence et al. 2004; Steinbring et al. 2013; Schöck et al. 2009; Thomas-Osip et al. 2012; Vázquez Ramió et al. 2012) [37, 58, 61, 67, 77]. MASS is an optical instrument to measure stellar scintillation with a small telescope. Theoretical bases and instrumental properties were described in Tokovinin (1998; 2002), Tokovinin et al. (2003), and Kornilov et al. (2003) [30, 68, 69, 70]. Here we overview MASS theory.

The fluxes I_1 and I_2 are observed simultaneously through two apertures W_1 and W_2. The differential scintillation index $\sigma_{I_d}^2$ is defined as a variance of the natural logarithm of the ratio of the fluxes,

$$\sigma_{I_d}^2 = \left\langle\left(\ln\frac{I_1}{I_2} - \left\langle\ln\frac{I_1}{I_2}\right\rangle\right)^2\right\rangle , \tag{2.90}$$

which corresponds to Eq. (2.76). From Eq. (2.77), Q(h) is given by

$$Q(h) = 9.62\lambda^{-2}\int_0^\infty df\ f^{-8/3}\sin^2(\pi\lambda h f^2)A_d(f) \tag{2.91}$$

$$A_d(f) = \frac{1}{2\pi}\int_0^{2\pi} d\phi\ |\tilde{W}_1(f,\phi) - \tilde{W}_2(f,\phi)|^2 . \tag{2.92}$$

We study the case of the concentric circular aperture. The aperture W_1 is a concentric annular aperture, which has outer diameter D and inner diameter αD. The concentric

circular aperture W_2 has a diameter αD, therefore the apertures can be written as

$$\tilde{W}_1(f,\phi) = \frac{1}{1-\alpha^2}\left\{\frac{2J_1(\pi Df)}{\pi Df} - \alpha^2\frac{2J_1(\pi\alpha Df)}{\pi\alpha Df}\right\} \quad (2.93)$$

$$\tilde{W}_2(f,\phi) = \frac{2J_1(\pi\alpha Df)}{\pi\alpha Df}\ , \quad (2.94)$$

where Eqs. (2.87) and (2.79) are referred. Thus,

$$A_d(f) = \frac{1}{(1-\alpha^2)^2}\left\{\frac{2J_1(\pi Df)}{\pi Df} - \frac{2J_1(\pi\alpha Df)}{\pi\alpha Df}\right\}^2\ . \quad (2.95)$$

$Q(h)$ of the differential scintillation for the concentric circular apertures is practically constant ($Q(h) \propto h^0$) when the Fresnel radius $\sqrt{\lambda h}$ is larger than αD. Thus $\sigma^2_{I_d}$ practically depends on the integral of $C_n^2(h)$. This means that we can directly measure the Fried length r_0, which is caused by the atmospheric turbulence above the height of $h > (\alpha D)^2/\lambda$ from $\sigma^2_{I_d}$. Since ϵ is inversely proportional to r_0, we can also measure ϵ from $\sigma^2_{I_d}$ directly. θ_0 is also measured by MASS directly from a "special" annular aperture (see Chapter 2.6.2).

MASS has four concentric-ring apertures and four photo-multipliers. MASS measures the scintillation indices for each four 4 concentric apertures and therefore, 6 ($= {}_4\mathrm{C}_2$) differential scintillation indices simultaneously. These indices have different waiting function because of different aperture shapes. By comparing these indices with the model turbulence profile, the profile restoration can be performed. Therefore MASS can restore the turbulence profile from the stellar scintillation. For example, MASS restores the turbulence at 0.5, 1, 2, 4, 8, 16-km above the ground (Tokovinin et al. 2003 and Kornilov et al. 2003) [30, 70]. Here we note that MASS has less sensitivity near the ground, i.e. under 0.5-km. The help of DIMM is needed for MASS to measure the optical turbulence between 0 and 0.5-km above the ground.

2.6.4 SOnic Detection And Ranging

Using an acoustic sound wave, we can estimate the temperature structure constant C_T^2 without a telescope. SODAR (SOnic Detection And Ranging, Little 1969) [38] is an instrument to transmit a sound wave and receive its back-scattering. From the back scattering, the turbulence volume, i.e. temperature structure constant C_T^2 can be calculated.

Here we introduce the acoustic scattering cross-section $\sigma_{scat}(h)$ at height h. The cross-section of a turbulent volume is a function of C_v^2 and C_T^2. For an acoustic wave propagation in a turbulent atmosphere, the scattering cross-section was written by Tatarskii (1971) [66],

$$\sigma_{scat}(h) = 0.03\left(\frac{\omega}{c(h)}\right)^{1/3}\cos^2\theta\left\{\frac{C_v^2(h)}{c(h)^2}\cos^2\frac{\theta}{2} + 0.13\frac{C_T^2(h)}{T(h)^2}\right\}\left(\sin\frac{\theta}{2}\right)^{-11/3}\ , \quad (2.96)$$

where ω is the frequency of the acoustic wave in radian per second, θ the scattering angle relative to the original wave vector, $T(h)$ the average temperature of the scattering volume, and $c(h)$ the speed of sound at height h, respectively.

For back-scattering ($\theta = \pi$),

$$\sigma_{scat,\pi}(h) = 0.0039\left(\frac{\omega}{c(h)}\right)^{1/3}\frac{C_T^2(h)}{T(h)^2}\ . \quad (2.97)$$

The cross-section only depends on C_T^2. Therefore an instrument which transmits a sound wave and receives the back scatter sound can measure the temperature structure constant C_T^2. This is the theory of "Sonic Detection And Ranging (SODAR)" (Little 1969) [38].

Little (1969) [38] demonstrated that the acoustic power received at an antenna was related to the scattering cross-section by the SODAR equation,

$$P_r(h) = P_t\ \eta \frac{e^{-2\alpha h}}{h^2} \sigma_{scat}(h) + P_n\ , \tag{2.98}$$

where h is the height of the turbulence volume with scattering cross-section $\sigma_{scat}(h)$, η the system gain, α the atmospheric attenuation constant, and P_t and $P_r(h)$ the transmitted and received powers, respectively. P_n is the noise power. The height of the scattering volume can be calculated from the time of propagation and the speed of sound $c(h)$. The range and sensitivity of SODAR is limited by atmospheric attenuation, $1/h^2$ spreading, and noise. The minimum sampling height of SODAR is restricted by acoustic reverberation within the antenna structure and electrical ringing in the receiver electronics (Bonner et al. 2010a) [13].

The vertical resolution of SODAR, Δh is determined by the length of the transmitted acoustic pulse Δt and the speed of sound c (Bonner et al. 2009) [15],

$$\Delta h = \frac{1}{2} \times c\Delta t\ . \tag{2.99}$$

2.6.5 Temperature structure constant measurement

The temperature structure constant C_T^2 can be measured without telescope. From direct temperature measurement, we can calculate C_T^2, which is written from Eq. (2.10),

$$\begin{aligned} C_T^2 &= \left\langle \{T(x) - T(x+r)\}^2 \right\rangle r^{-2/3} \\ &\sim \frac{1}{n-1} \sum_{i=1}^{n} \{T_i(x) - T_i(x+r)\}^2\ r^{-2/3}\ . \end{aligned} \tag{2.100}$$

C_T^2 can be measured by two methods. One is to use two thermometers. We set two thermometers with separation r, and measure the temperatures simultaneously. Using Eq. (2.100), C_T^2 can be obtained directly.

Another methods is to use an ultrasonic anemometer. The ultrasonic anemometer is an instrument which can measure the three-dimensional wind velocity and temperature simultaneously. Here the wind velocity and the temperature at time of t_i are written as $v_i(x)$ and $T_i(x)$, respectively. If we assume the Taylor's Hypothesis, the temperature structure constant C_T^2 can be written as,

$$C_T^2 \sim \frac{1}{n-2} \sum_{i=2}^{n} \{T_i(x) - T_{i-1}(x)\}^2\ \left\{ (t_i - t_{i-1}) \times \frac{v_i + v_{i-1}}{2} \right\}^{-2/3}\ . \tag{2.101}$$

Thus one ultrasonic anemometer can measure C_T^2 directly. The temperature measurement have to be performed where the Kolmogorov model is applicable ("inertial range"). This means that high frequency temperature measurements (~ 10 [Hz] or higher) are required. From Eq. (2.14) we can convert C_T^2 to C_n^2. Thus, the high frequency and high precise temperature measurements can unveil turbulence strength at the height.

Chapter 3

Observational scheme

As described in Chapter 1, to unveil the spatial resolution limit at Dome Fuji on the Antarctic plateau, we planned to measure the height of the surface boundary layer, total seeing, and free-atmosphere seeing. However, the seeing measurements at Dome Fuji are strongly restricted by the Antarctic logistics. In this chapter, we describe the advantages and disadvantages of each measurement method, explain the limitation by the Antarctic logistics, and show the observational scheme for each expedition.

3.1 Features of each measurement method

3.1.1 DIMM

One of the advantage of DIMM is to directly measure the total seeing. If DIMM is put above the surface boundary layer, the free-atmosphere seeing can be measured directly. DIMM observations are possible with even in the daytime on the Antarctic plateau (Aristidi et al. 2003; 2005a; 2009) [4, 5, 7]. In addition, DIMM system is comparatively light and small (e.g., DF-DIM with $\sim$ 70 kg and $\sim$ 0.3 m^3). On the other hand, C_n^2 profile can not be measured by DIMM observations. Because DIMM measurement needs precise star pointing and tracking on a telescope, it is relatively complicate and difficult.

3.1.2 MASS

An advantage of MASS is that it measures C_n^2 values at 0.5, 1, 2, 4, 8, 16-km above the surface level directly. MASS also directly obtain optical turbulence parameters, such as free-atmosphere seeing and isoplanatic angle. In addition, MASS system is comparatively light and small. However, we can not conduct MASS observations during the daytime because MASS measures a stellar scintillation and the observation should be performed in stable and low background environment. MASS also needs precise star pointing and tracking on a telescope.

3.1.3 SODAR

SODAR measures the turbulence profile without a telescope. It is easy to set up and to start observations on site. SODAR is relatively light and small. On the other hand, SODAR does not measure the turbulence profile near the surface due to the instrument

structure. The accurate calibration is quite important to convert the turbulence profile to C_T^2 value.

3.1.4 Snodar

Snodar (see Chapter 4.3) has the same advantages of SODAR; it measure the turbulence profile without a telescope. Snodar can measure the turbulence profile at nearer snow surface, between 8 and 50-m above the surface, than SODAR. Easy set-up and operation are strong advantages of Snodar. However, Snodar also needs careful calibration to convert the turbulence profile to C_T^2 value. Heavy weight ($\sim$300 kg) and large bulk ($\sim$3 m^3) would be a disadvantage.

3.1.5 Ultrasonic anemometer

The ultrasonic anemometer can measure C_T^2 value directly without a telescope. It is easy to set up and to operate the ultrasonic anemometer on site. The light weight and small size are also its advantage. On the other hand, the ultrasonic anemometer can measure C_T^2 value only at an installation height. Snow removal is needed for winter-over operation because a heater defroster makes a noise for the temperature measurement.

3.2 Logistical limitations

Any activities at Dome Fuji on the Antarctic plateau are restricted by many logistical circumstances. In this section, we list typical logistical limitations. The seeing measurements have to be performed under these logistical conditions.

3.2.1 Access

The Antarctic harsh environment prevents us from frequent accessing to Dome Fuji. We can visit Dome Fuji once a year, only in the Antarctic summer. Japanese Antarctic Research Expedition (JARE) and Dronning Maud Land Air Network (DROMLAN), which is operated by the Antarctic Logistics Center International (ALCI), provide three routes to Dome Fuji. One is the access using the icebreaker "Shirase," helicopters, and snow vehicles. The icebreaker Shirase sails from Fremantle port, Australia to the Antarctic coast near "Syowa" station. It needs about four weeks. After reaching Syowa station, helicopters are used to transport to "S16" milestone on the Antarctic continent. From S16 to Dome Fuji, snow vehicles are used. The journey on snow vehicles needs at least three weeks. In total, about seven weeks are needed to reach Dome Fuji. Although the expedition takes time, it is safest and transport capacity is maximum.

The second route to Dome Fuji is to use DROMLAN aircraft and snow vehicles. DROMLAN provides transportation from Cape Town, South Africa to "Novolazarevskaya" runway near the Russian station on the Antarctic continent using a Russian large transport aircraft. Small aircrafts of DROMLAN fly from Novolazarevskaya runway to "S17" runway near S16 milestone. The flights need at least a week. From S16 to Dome Fuji, snow vehicles are used. The journey on snow vehicles also needs about three weeks. In total, four weeks are needed to reach Dome Fuji.

The third way to go to Dome Fuji is the direct access using only DROMLAN aircrafts. A small DROMLAN aircraft can land on a rough snowfield near Dome Fuji. In total, only a week is needed to go to Dome Fuji. This way takes the least time, however it has the highest risk for life, and the transport capacity is minimum.

3.2.2 Transportation

Almost all cargoes for JARE are shipped on the icebreaker Shirase. Because the icebreaker Shirase sails to Syowa station once a year, we have to transport instruments with careful schedule. Syowa station is located not on the Antarctic continent but on an island. As the Antarctic summer, sea-ice between the island and the continent melts with strong sunlight, the transportation of snow vehicles on ice is not available. Therefore, the cargoes for the Dome Fuji traverse journey, such as snow vehicles, sleds, fuel, foods, and scientific instruments have to be transported from Syowa station to the Antarctic continent in the harsh Antarctic winter.

After the icebreaker Shirase reaches near Syowa station, we can use ship-based helicopters for the transportation. The helicopters can load the cargoes with 2 tons in maximum. Snow vehicle and sleds are the main transporters from S16 milestone to Dome Fuji. One snow vehicle can tow $\sim$ 15 tons. Because $\sim$80% of the cargo is fuel, foods, and some necessaries of life, we can carry a small amount of scientific instruments at one time. For a safety reason, at least two snow vehicles are used for one Dome Fuji traverse journey.

The cargo weight and bulk of DROMLAN air transportation are strongly restricted. DROMLAN is relatively expensive ($\sim$ 100,000 USD for one flight). DROMLAN is usually used for human transportation or for really essential stuff for life.

Dome Fuji traverse journey needs vast preparation. Many supports from Syowa station are essential. Some specialists, i.e. car engineer, welder, carpenter, medical doctor, alpinist, communication operator, are also needed to join the tough journey to Dome Fuji.

3.2.3 Electric power

Electric power for astronomy should be prepared by astronomers at Dome Fuji. During the Antarctic summer, the generators equipped at Dome Fuji station can make $\sim$ 20 kW electric power. However the generators are hard to start up, and actually impossible for unmanned operation. The generators on snow vehicles and portable generators make temporal electric power. The maximum load are $\sim$ 2 kW.

During the Antarctic winter, there are no humans at Dome Fuji at present. There was no electric power available before 2010. Therefore, we constructed PLATO-F (see Chapter 4.2) with the help of University of New South Wales at Dome Fuji in 2011 January. PLATO-F provides $\sim$ 1 kW electric power for a year, though 1 kW is not enough for usual scientific instruments. We save electric power as much as possible for the long operation of instruments.

3.2.4 Communication

Internet communication for astronomy also have been arranged by astronomers at Dome Fuji. Before PLATO-F was equipped, there was no internet communication at Dome Fuji.

Internet communication is available by using the Iridium Satellite Phone Communication on PLATO-F. The service of 128 kbps is available. The communication cost is, however, very expensive ($\sim$ 10 USD/MB).

3.2.5 Human resources

Human resources are really restricted at Dome Fuji. Because of the restriction for transportation, six to fifteen expedition crews are allowed to Dome Fuji at one time. Half of the crews are specialists for logistics. Scientific activities are very limited at Dome Fuji at present. For JARE, many duties are imposed to all crews, including scientists, to live at the Antarctica. About 75% of total visiting duration should be spent for the duties.

3.2.6 Visiting duration

Visiting duration at Dome Fuji is strongly restricted by the Antarctic harsh environment. Therefore the visiting duration is very short in general. There is no winter-over facilities at Dome Fuji at present, we can only stay during the Antarctic summer. The visiting duration is constrained by the schedule of both the voyage of the icebreaker Shirase and the flight of DROMLAN. In the case for using Shirase and snow vehicles, the visiting duration at Dome Fuji is about three weeks. If we access using DROMLAN and snow vehicles, it is about six weeks. The visiting time of the direct access on DROMLAN is restricted by the reason for clew's health. It is allowed for about only a few hours.

3.3 Seeing measurement plans

Ideally, the astronomical seeing measurement should be simultaneously performed with various instruments, which are based on different principles. However, as described above, such simultaneous seeing measurements are currently very restricted at Dome Fuji.

Under the logistical limitations, we planned three measurements to study the astronomical seeing at Dome Fuji; the height of the surface boundary layer with SODAR's and Snodar's turbulence profile, the total seeing with DIMM put on the surface level, and the free-atmosphere seeing with DIMM put on as high as possible. Direct C_T^2 measurement by ultrasonic anemometers was planned for Snodar calibration. We selected not MASS but DIMM for the seeing measurement, because DIMM would work even in daytime on the Antarctic summer. These observations were planned to be performed in the $47^{th}/48^{th}$, $51^{st}/52^{nd}$, and $53^{rd}/54^{th}$ JARE.

3.3.1 $47^{th}/48^{th}$ JARE

The first astronomical site testing at Dome Fuji was performed in the $47^{th}/48^{th}$ JARE. There were no astronomical crews in the campaign, easy observations for some seeing measurements were proposed. Because of the DROMLAN and snow vehicle access, transportation weight and bulk were strongly restricted. From these reasons, we decided to conduct the SODAR observations. There was no electric power during the Antarctic winter, the measurement was scheduled to be performed only in the Antarctic summer.

3.3.2 $51^{st}/52^{nd}$ JARE

We sent two astronomical crews to Dome Fuji in the $51^{st}/52^{nd}$ JARE. We performed seeing measurements with DIMM, which were required for great care on site. Because of no stage or high platform available at Dome Fuji, we put DIMM on the snow surface and to measure the total seeing. The Shirase and snow vehicle access enabled us to carry heavy and large cargoes to Dome Fuji. PLATO-F and Snodar (in total $\sim$ 6 tons) were carried in this campaign. Snodar observations were performed to measure the height of the surface boundary layer. Two ultrasonic anemometers on the 16-m meteorological mast (see Chapter 4.4.2) planned to measure C_T^2 values for Snodar calibration. The electric power and internet communication supplied by PLATO-F enabled the Snodar and ultrasonic anemometers observations after crews left Dome Fuji. We planned whole year measurement for the height of the surface boundary layer by Snodar and ultrasonic anemometer. However, the unmanned and remote DIMM observations were gave up due to technical difficulties.

3.3.3 $53^{rd}/54^{th}$ JARE

We sent two astronomical crews to Dome Fuji in the $53^{rd}/54^{th}$ JARE. The seeing menasurement with DIMM were performed again. Because the 9-m astronomical tower (see Chapter 4.7) was constructed for an infrared observation, we were able to performed the free-atmosphere seeing measurements with DIMM put on the top of the tower. We also planned unmanned and remote whole year observations with DIMM by solving the technical difficulties. However due to power devices failure, we were not able to perform the winter-over observations. The electric power and internet communication were supplied by PLATO-F. The total seeing measurement was not planned on the snow surface because the information was considered to be not important. Snodar, which started the observation in January 2011 but it was stopped by an accident in July, was planned to repair on site and restart the measurement of the height of the surface boundary layer in this campaign.

Chapter 4

Development of the instruments

To investigate the atmospheric turbulence at Dome Fuji, we developed some instruments. In general, the instruments for astronomical site testing are not commercially available. In addition, the instruments for the Antarctica have to work even at -80°C environment. The weight and volume of the instruments should be reduced due to tight logistics limitations. Furthermore there was no electric power nor communication infrastructures at Dome Fuji before we constructed PLATO-F. For these reasons, we developed the instruments, including some infrastructures, by ourselves.

We have some difficulties in the instrumentation for the Antarctica. Since there is significant difference in the environment between the Antarctica and our laboratory (at Sendai in Japan), we should take account of the temperature and sky condition differences, which would make the instrumentation for the Antarctica difficult. For example, we planned to measure the astronomical seeing at daytime using Canopus (α Car, the second brightest star in the sky). However, Canopus is always under the horizon at Sendai. The sky condition at Sendai is much worse than that on the Antarctic plateau. Therefore, the daytime seeing measurement at Sendai would much harder than that on the Antarctic plateau. Actually, no daytime seeing measurements at Sendai were successful.

Snodar, PLATO-F, platinum thermometers equipped on a 16-m meteorological mast, AIRT40 with Tohoku DIMM, and DF-DIMM were developed for the site testing at Dome Fuji. SODAR and ultrasonic anemometers were purchased from commercial companies. The author took part in developing Snodar and PLATO-F at the University of the New South Wales in 2010. Platinum thermometers, a 16-m meteorological mast, and AIRT40 were developed by our group including the author at Tohoku University during 2007–2011. Tohoku DIMM and DF-DIMM were designed, constructed, tested, installed, and operated by the author. We describe the instruments in this chapter below.

4.1 SODAR

SODAR (SOnic Detection And Ranging) is an instrument to measure a back-scattering of a sound wave by the atmospheric turbulence (Little 1969) [38]. Theoretical basis of SODAR is described in Chap. 2.6.4. SODAR can measure turbulence strength profiles, which are proportional to C_T^2 profiles, by emitting a sound and receiving its back-scattering. The calibration is needed to convert the turbulence strength to C_T^2. C_n^2 can be calculated from C_T^2 with Eq. (2.10).

Figure 4.1: Remtech Inc. #PA-1 SODAR without sound cone set at Dome Fuji station in 2006. The backgrounds behind #PA-1 SODAR are the buildings of the station.

4.1.1 Specifications for SODAR

The first astronomical site testing at Dome Fuji was planned in the $47^{th}/48^{th}$ Japanese Antarctic Research Expedition (JARE) in 2006/2007 Antarctic summer. There were no astronomical crews in the campaign, easy observations were required. Because of the DROMLAN and snow vehicles, the transportation weight and bulk were strongly restricted. The generator for the electric power was only operated in the duration of the visit. Thus we planned the measurement for the height of the surface boundary layer using SODAR only in the Antarctic summer. Easy setup and easy operation were also required. On-site calibration for SORAR was gave up because of tight logistical limitation.

4.1.2 Remtech Inc. #PA-1 SODAR

SODAR was required sufficient sensitivity for measuring the turbulence profile. Remtech Inc. #PA-1 SODAR was purchased for the first astronomical site testing at Dome Fuji (Takato et al. 2008) [64]. #PA-1 is a small size Doppler SODAR system measuring remotely a vertical profile of wind speed, direction, thermal stratification and turbulence parameters up to ∼1 000 m. #PA-1 had no modifications for cold environment because it would be used only in the Antarctic summer. The sound cone of #PA-1 was removed for weight saving. The net weight and bulk of #PA-1 are about 78 kg and 0.24 m^3, respectively. Figure 4.1 shows the #PA-1 SODAR at Dome Fuji in 2006.

#PA-1 SODAR emits ∼2 kHz sound with output power of 1 W. Back scattering strength, horizontal wind speed, horizontal wind direction, and vertical wind speed were measured on average of every 15 minute. Some measurement parameters of #PA-1 SODAR are changeable. Initial setup of #PA-1 SODAR was performed by Naruhisa Takato and Fumihiro Uraguchi (Subaru telescope, NAOJ). The author contributed to the data analysis of the SODAR observations.

The minimum sampling height of a SODAR is technically limited due to acoustic revervaration within the antenna structure and electrical ringing in the receiver electronics (Bonner et al. 2010a) [13]. The vertical resolution of SODAR is defined by the length of

the transmitted acoustic pulse and the speed of sound (Bonner et al. 2009) [15]. We set the minimum measurement height of 40-m, maximum height of 1 020-m, and the sampling resolution of 20-m for #PA-1 SODAR.

4.2 PLATO-F

PLATO, the PLATeau Observatory, is a fully automated platform for the Antarctic plateau and provides electrical power and Iridium communication all year (Ashley et al. 2010a; 2010b; 2010c; Hengst et al. 2008; 2010; Lawrence et al. 2008; 2013; Luong-Van et al. 2008; Storey et al. 2012) [8, 9, 10, 25, 26, 35, 36, 41, 62]. PLATO for Dome Fuji, named "PLATO-F" is an evolution of the original PLATO experiment that began operation at Dome A of Chinese Kunlun station in January 2008.

PLATO-F was taken to Dome Fuji by the $51^{st}/52^{nd}$ Japanese Antarctic Research Expedition (JARE) in 2010. PLATO-F arrived at Dome Fuji on 2011 January 12, and began collecting scientific data on 2011 January 17. The observations were stopped on 2011 July 4 by the critical damages on some electric devices. The $53^{rd}/54^{th}$ JARE repaired and replaced some parts of PLATO-F. PLATO-F was restarted on 2013 January 16. It is still running at the time of writing (February 2014).

4.2.1 Specifications of PLATO-F

The second astronomical site testing at Dome Fuji was planned in the $51^{st}/52^{nd}$ JARE in 2010/2011. We scheduled the measurements for the height of the surface boundary layer and for the total seeing by two astronomical crews in the campaign. The Shirase and snow vehicles enabled the transportation of heavy and bulky cargoes. However, helicopter transportation between Shirase and S16 restricted the cargo with maximum weight of 2 tons.

For the full-year, unmanned, and remote site testing, we established the PLATO-F at Dome Fuji to supply electric power and internet communication. Electric power was required as much as possible, and internet communication was also required as fast as possible. Because the next expedition to Dome Fuji would be planned two years later, PLATO-F was required to keep working at least two years.

4.2.2 PLATO-F overview

PLATO-F was designed and built by the University of New South Wales in 2010 under the collaboration between Tohoku University and National Institute of Polar Research in Japan, and University of New South Wales, Macquarie University, Australian Astronomical Observatory in Australia. The author mainly contributed the on-site deploy and repair of PLATO-F at Dome Fuji. The remote operation for PLATO-F has been also performed partly by the author.

Figure 4.2 shows PLATO-F at Dome Fuji in January 2011. PLATO-F consists of two fiberglass modules. The left yellow container is the instrument module, and the right green one is the engine module. The modules are thermally insulated with 200 mm-thick polyurethane foam. The size of each module is that of the ISO standard 10-foot shipping container, and the weight is less than 1.8 t. The size and weight are suit for transportation

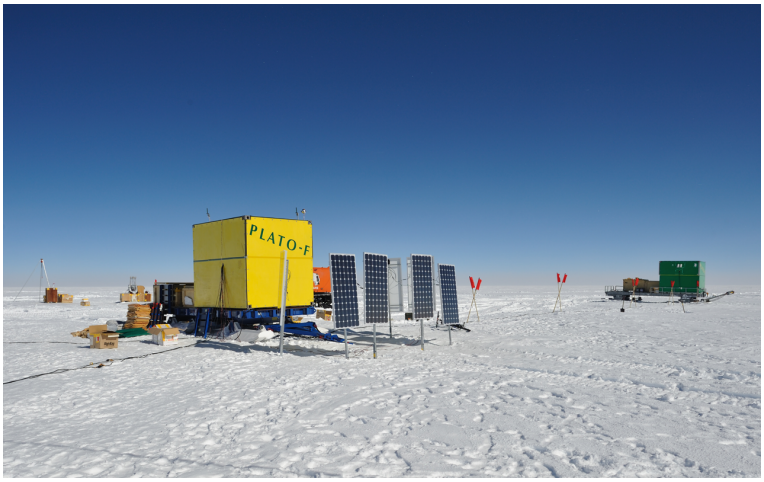

Figure 4.2: PLATO-F at Dome Fuji in January 2011. The left yellow and right green containers are the Instrument Module and Engine Module, respectively. The solar panels are seen in front of the Instrument Module.

by the icebreaker "Shirase," helicopters, and snow vihecles. Some pictures of PLATO-F transportation from Australia to Dome Fuji are shown in Fig. 4.3.

4.2.3 PLATO-F Instrument Module

PLATO-F Instrument Module is designed as a stand-alone unit powered from Engine Module, solar panels, and large capacity butteries. It consists of control, communication, computing, and power electronics. CAN (Controller Area Network) bus is used to connect the modules.

To control PLATO-F two computers are equipped for redundancy. We call them "supervisors." Supervisors are based on PC/104 systems (Parvus ISIS/XL), each with an Iridium satellite modem for the remote operation. Supervisors boot from internal flash disks stood for low temperature and high altitude performance. A readonly operating system (Debian GNU/Linux "Squeeze") is used with to maximize the reliability. Supervisors monitor and control the PLATO-F power distribution, thermal, and engine management subsystems via CAN bus.

Supervisors monitor about 140 analog channels and 96 current-monitored channel for distributing electrical power and heating. All science instruments are operated with either 24 VDC or 110 VAC at 50/60Hz. Supervisors control on/off these outputs. The internal temperature of the Instrument Module is controlled by supervisors using fans that can bring in cold air from outside. Additional fans stir the air to prevent large temperature gradients in the module. Heaters are placed in the crucial places in the module and the battery compartment. The temperature in the Instrument Module is regulated between -20°C and +15°C to avoid the failure.

Each supervisor has an Iridium satellite modem for remote control. In addition, an Iridium OpenPort system provides 128 kbps internet connectivity to the outside world. Status logs and some scientific data are transfered via Iridium. The communication between supervisors and scientific instruments is provided via Ethernet. We can access supervisors and scientific instruments by way of ssh remote login from the University of

Figure 4.3: PLATO-F transportation from Australia to Dome Fuji. Left top; Truck transportation from the University of the New South Wales, Sydney to Fremantle port. Right top; PLATO-F containers on the icebreaker "Shirase." Left bottom; Transportation using a helicopter from Shirase to S16 mailstone on the Antarctic continent. Right bottom; Snow vehicle and sledge transportation from S16 to Dome Fuji.

New South Wales and from Tohoku University.

Solar panels, which are placed near the instrument module, provide an additional electric power with the peak output of 1.3 kW during the Antarctic summer. A bank of LiFePO4 cells provides 20 kWhr of uninterrupted power to the instruments. The batteries also allow for multiple restart and heating of the engines in the Engine Module. Figure 4.4 shows the interior of the PLATO-F Instrument Module in January 2013.

4.2.4 PLATO-F Engine Module

PLATO-F Engine Module provides the primary power source after sunset. The Engine Module contains five #1B30 diesel engines, manufactured by Motorenfabrik Hatz GmbH & Co. KG, six thousand (6 000) liters of Jet-A1 fuel, and power management and control electronics. The Engine Module supplies the electric power of 120 VDC to the Instrument Module. The module is insulated with 200 mm-thick polyurethane foam panels. Appropriate internal temperature is maintained only with the help of the waste heat of the engines.

#1B30 is a compact high efficiency, 350 cc displacement, single cylinder diesel engine. #1B30 was tested in a low pressure chamber at the University of New South Wales to study the starting behavior, efficiency, and thermal performance (Hengst et al. 2008; 2010) [25, 26]. Each engine is run at a fixed speed of ∼2 000 RPM and produces ∼1 kW at 120∼150 VDC. Only one engine is run in the normal operation. Each engine has its

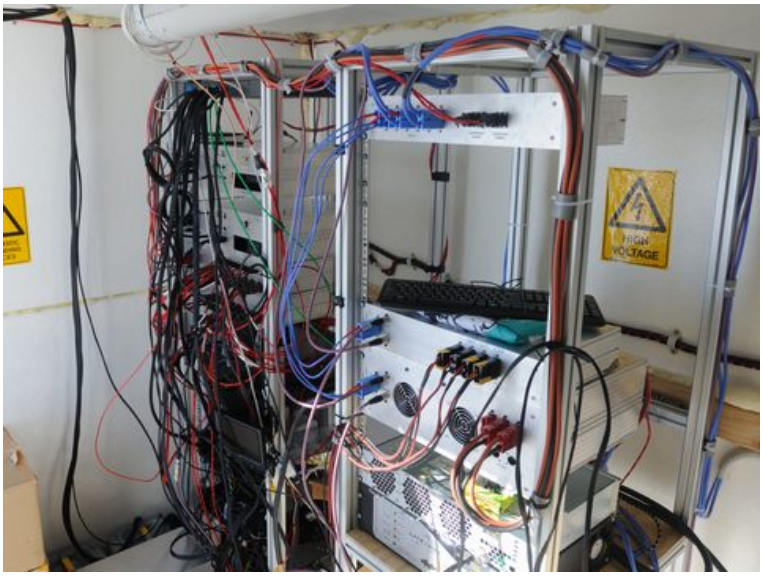

Figure 4.4: Inside of the PLATO-F Instrument Module in January 2013.

Figure 4.5: Inside of the PLATO-F Engine Module in January 2013.

own bulk oil filtration and recirculation system. The oil and fuel pumps are under CAN bus microprocessor control. The engines can be restarted if the internal air temperature is higher than about $-10°C$. Tritium WaveSculptor is used to start the engine by driving current from the 120 VDC bus into the alternator. It is also used to extract the electric power from the alternator. Figure 4.5 shows inside of the PLATO-F Engine Module in January 2013.

4.3 Snodar

Snodar (Surface layer NOn-Doppler Acoustic Radar) is a high-resolution and low minimum sample height sonic rader (SODAR) designed specifically for profiling the surface boundary

layer on the Antarctic plateau (Bonner et al. 2010a; 2010b; 2009; 2008) [13, 14, 15, 16]. Snodar works by sending an intense acoustic pulse into the atmosphere and listening for backscatter. The theory of the operation is the same as that of SODAR.

4.3.1 Specifications of Snodar

Snodar observations were planned in the $51^{th}/52^{nd}$ JARE for measuring the height of the surface boundary layer throughout the year. The transportation with Shirase and snow vehicles allowed us heavily and bulky Snodar in the campaign. PLATO-F was supposed to perform the full-year measurement for the height of the surface boundary layer. On-site calibration was also planned by using ultrasonic anemometers on a meteorological mast. Snodar was required sufficient sensitivity for the measurement of the turbulence profile, higher vertical resolution, and lower minimum height of the sampling than these of SODAR because SODAR had no sensitivity near the snow surface. Full-year, unmanned, and remote Snodar observations demand the electric power and Iridium communication supplied by PLATO-F.

4.3.2 Snodar at Dome Fuji

Snodar was developed and constructed by Colin S. Bonner (the University of New South Wales). Snodar was originally designed for the astronomical site testing at Dome A; our Snodar was a sister model of Dome A Snodar. It is also the result of a scientific collaboration between the universities and institutes in Japan and Australia. The author worked for designing a snow brush to remove snow from the parabola dish, assembling some electric devices, on-site set-upping, and developing a data-reduction method, for the operation at Dome Fuji. A single horn-loaded compression driver as both transmitter and receiver, and an off-axis parabolic dish to collimate the acoustic beam are used for Snodar. Received signal is digitized by a USB sound card. A PC/104 computer performs the signal processing in real time on site. The Iridium communication on PLATO-F allows transferring the results and controlling Snodar remotely. The minimum and maximum sampling height and vertical resolution of Snodar also depend on both device and software setting. We used an acoustic pulses with 5 kHz for Snodar. Figure 4.6 shows Snodar at Dome Fuji in January 2011.

4.4 Meteorological instruments

Meteorological data, such as temperature, wind speed, wind direction, and atmospheric pressure will give more information for understanding the atmospheric conditions near the snow surface at Dome Fuji. Because a strong temperature inversion, which would be caused by the radiative cooling near the snow surface, makes the atmospheric turbulence, meteorological observations would be fundamentally important. Surface wind speed is considered to be correlated with the height of the surface boundary layer (Swain & Gallée 2006, Bonner et al. 2010a) [13, 63]. For the reason, we obtained the meteorological observations at Dome Fuji.

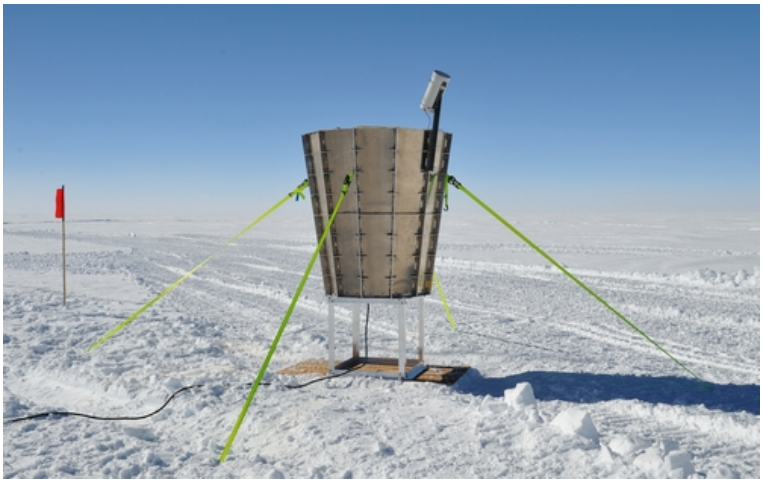

Figure 4.6: Snodar at Dome Fuji in January 2011. The reflector and transducer of Snodar are housed in a sound cone to reduce acoustic noise.

4.4.1 Specifications for meteorological observations

Full-year, unmanned, and remote meteorological observations were planned in the $51^{st}/52^{nd}$ JARE. The electric power and internet communication supplied by PLATO-F were used for the observations. We constructed a meteorological mast at Dome Fuji and put the instruments on the mast for meteorological observations.

The meteorological mast was required as high as possible because higher mast should give us more meteorological informations. To investigate a temperature gradient near the snow surface, thermometers were put on various heights. A direct C_T^2 measurement was used for the Snodar calibration. Wind speed, wind direction, and atmospheric pressure measurements were also required.

4.4.2 Sixteen meter meteorological mast

A meteorological mast with $\sim$ 16-m height was installed by the $51^{st}/52^{nd}$ JARE members. Hereafter we call this mast "16-m meteorological mast." The author took part in the assembling and on-site setting. Figure 4.7 (left) shows the 16-m meteorological mast at Dome Fuji in January 2011.

4.4.3 Platinum thermometers

We used platinum thermometers for the temperature measurement. The platinum thermometers, which were International Standard IEC 60 751, broadly called "Pt100," were supplied by Teijin Engineering Limited. Hand-made double sunshades, made of aluminum, enclose each thermometer to avoid the solar heating (see Fig.4.7 right). The development of the instrument with the platinum thermometers was performed by Takuya Koyama (Tohoku University). The author carried out on-site setup and data reduction for the platinum thermometers.

Six platinum thermometers at height of 0.3, 3.1, 6.5, 9.5, 12.0, 14.4, and 15.8-m were put on the mast. Keyence Co., Ltd. #TR-V550 data logger was used for logging the temperatures. #TR-V550 kept in the thermal control box, which was warmed at $\sim$ 10°C

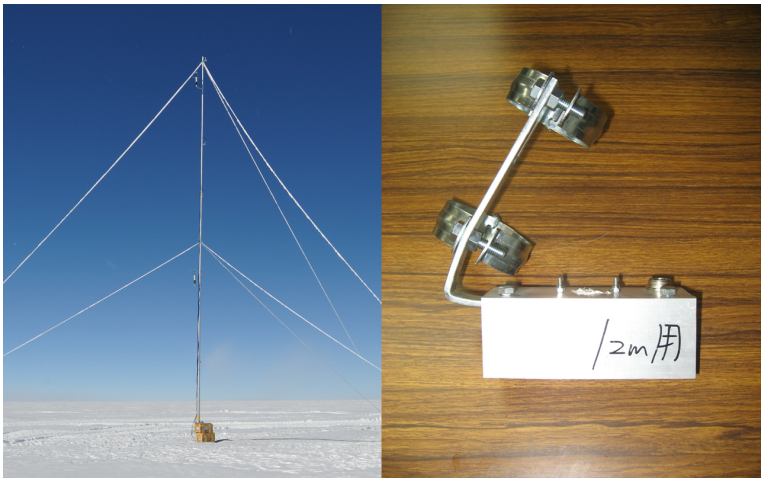

Figure 4.7: Left; 16-m meteorological mast at Dome Fuji. Right; Hand-made double sunshades for platinum thermometer.

by wasted heat and heaters on the snow surface, near the 16-m meteorological mast. #TR-V550 obtained data every two minutes. Observation data were copied to a data server computer inside the PLATO-F Instrument Module, which supplied the electric power and internet communication to #TR-V550.

4.4.4 Ultrasonic anemometers

Ultrasonic anemometers measure ultrasonic sound and convert them to wind speed, wind direction, and sonic temperature. With a fast speed sampling by an ultrasonic anemometer, we can measure C_T^2 value directly. Two ultrasonic anemometers of Model #81000 supplied by R. M. Young Company were used for our site testing. The anemometers were put on the 16-m meteorological mast at the height of 6.1 and 14.4-m above the snow surface. Although it was clearly unsuitable, #81000 anemometers had no modifications for the Antarctic cold environment. The performance evaluation of the #81000 anemometers was performed by Kentaro Kurita. The author carried out on-site setup and and data reduction of the ultrasonic anemometers. Campbell Scientific, Inc. #CR1000 data logger was used with a sampling frequency of 50 Hz. #CR1000 was also kept in the thermal control box on the snow surface near the 16-m meteorological mast. Observation data were transfered to the data server inside the PLATO-F Instrument Module. #81000 anemometers and #CR1000 data logger were also supplied with electric power from PLATO-F.

4.4.5 Barometer

The atmospheric pressure was measured with VAISALA #PTB210 digital barometer inside the thermal control box on the snow surface near the 16-m meteorological mast. We used the #PTB210 barometer without modification for low temperature environment because the barometer should placed inside the thermal control box. We set up #PTB210 to measure the atmospheric pressure between 500 and 1100 hPa. The analogue data was output by voltage range between 0 and 5 V. The conversion from the voltage V [V] to the

pressure P [hPa] is below.

$$P = 600 \times \frac{V}{5} + 500 \tag{4.1}$$

Keyence Co., Ltd. #TR-V550 data logger was used for recording the output voltage of the barometer. The measuring interval was set to every two minutes. The accuracy of the pressure was $\sim \pm 0.1$ hPa from the specification sheet. The atmospheric pressure measurement was planned for Snodar calibration by Kentaro Kurita. The author contributed on site setting and data reduction for the instrument.

4.5 AIRT40

Antarctic Infra-Red Telescope with 40 cm primary mirror (AIRT40) is the first optical/infrared telescope to be deployed at Dome Fuji. AIRT40 is a classical-Cassegrain telescope on a custom-made equatorial mount, which is developed to work under -80°C without heating (Murata et al. 2008; Okita et al. 2010) [49, 51]. AIRT40 was originally developed for pilot infrared observation at Dome Fuji by the Tohoku University Near Infra-Red Camera 2 (TONIC2), and for astronomical seeing measurement by Tohoku DIMM.

4.5.1 Specifications of AIRT40

The $51^{st}/52^{nd}$ JARE planned pilot infrared observation and astronomical seeing measurement with AIRT40 in 2010/2011 Antarctic summer. Shirase and snow vehicles allowed us the transportation of heavily and bulky AIRT40 in this campaign. Although PLATO-F supplied electric power and internet communication all year, we gave up full-year, unmanned, and remote AIRT40 operation due to some technical difficulties. AIRT40 should work under the Antarctic summer temperature. Requirements for AIRT40 were accurate pointing, tracking, and high optical performance. AIRT40 has heavy loading capacity for TONIC2 ($\sim$32 kg). AIRT40 should have high contrast optical systems for the daytime seeing measurement.

4.5.2 AIRT40 overview

AIRT40 is a classical-Cassegrain telescope with a 40 cm mirror in diameter on a custom-made equatorial mount. AIRT40 was developed by the collaboration between IK Technology, Co., Ltd. and Tohoku University. The dedicated efforts of Chihiro Murata made AIRT40 development successful (Murata 2009; Murata et al. 2008) [48, 49]. Then, the author took over the AIRT40 development. The author performed the modifications for the Antarctic environment and performance evaluations for AIRT40. The primary and secondary mirrors of AIRT40 were polished by IK Technology, Co., Ltd. Figure 4.8 is a picture of AIRT40 under development at Tohoku University.

Truss structure of the optical tube minimizes the thermal emission from the telescope itself. The secondary mirror is movable for focusing. The mount of AIRT40 is a fork equatorial made of Aluminum. Right ascension (RA) and declination (DEC) of AIRT40 are controlled with stepping motors. Encoders are not equipped with AIRT40 because no encoders are available at -80°C environment. Teflon (polytetrafluoroethylene, PTFE) covered cables are used for AIRT40. Motors, sensors, and other electric parts, which work at -80°C in the freezer, are used. RA, DEC, and focus motors are controlled with

Figure 4.8: Antarctic Infra-Red Telescope with a 40 cm primary mirror (AIRT40) under assembling in the laboratory at the end of August 2010.

Table 4.1: Technical specifications of AIRT40.

Optical layout	Classical Cassegrain
Primary mirror diameter	400 mm
Focal length of primary mirror	798 mm
Secondary mirror diameter	100 mm
Polisher	IK Technology Co., Ltd.
Diffraction limit	0.31″ @ 500 nm
System Focal length	∼4 800 mm
Mount style	Folk equatorial
Manufacturer	IK Technology Co., Ltd., & Tohoku University
Control	Software on Windows computer
Software developer	Xtron Co., Ltd.

the program on Windows PC developed by Xtron Co., Ltd. Table 4.1 is the technical specifications of AIRT40.

4.5.3 Modifications for the Antarctic environment

AIRT40 has to work under the Antarctic environment. We tested AIRT40 in a freezer of Nihon Freezer Co., Ltd. #CLN-35C, which provides −85°C environment. AIRT40 is too large to put it in the freezer, so that we disassembled AIRT40 to four units: RA motor unit, DEC motor unit, focus unit, and RA shaft unit. If the units work individually at −80°C, AIRT40 should work as a whole in the low temperature. The RA and DEC motors are stepping motors: Oriental Motor Co., Ltd. #CSK564AP-T20. The original grease of the motors were replaced with the Solvay Solexis, Inc. Fombline ZLHT PFPE Grease. The temperature range of the Fombline grease is between −80°C and 200°C in the specification sheet. Since the lowest temperature ever recorded at Dome Fuji was

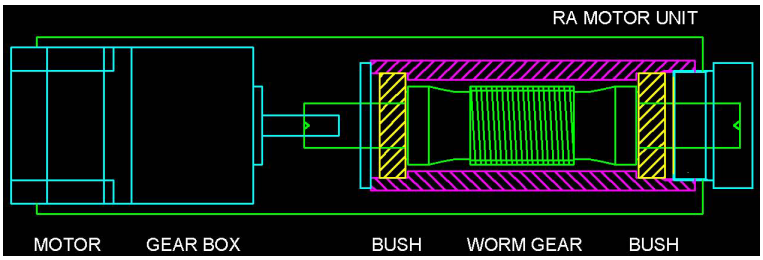

Figure 4.9: Drawing of the RA motor unit. RA motor rotates the worm gear directly. The worm gear supported with two bushes, which are made of gunmetal. Copyright: Okita et al. (2010) [51]

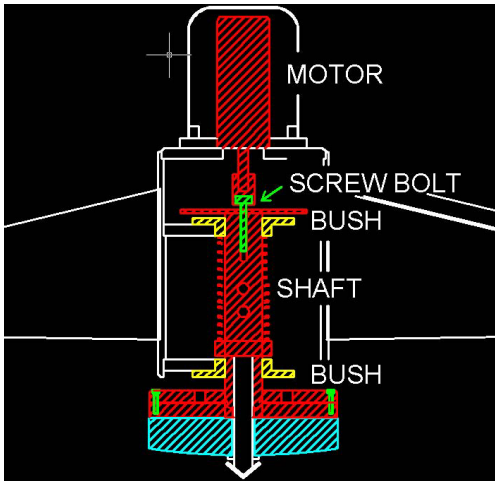

Figure 4.10: Drawing of the focus unit. Shaft and bushes are made of the same steel. Copyright: Okita et al. (2010) [51]

-79.7°C (Yamanouchi et al. 2003) [79], the grease is most suitable for our use. The grease have been used successfully at Dome C, Antarctica (Chihiro Murata, in private communications).

Figure 4.9 is the drawing of the RA motor unit. A worm gear, made of steel, is supported with two bushes, which are made of gunmetal (90% Cu and 10% Sn). Since the space between the worm gear shaft and the bushes decreases and the grease becomes stickier in low temperatures, motor cannot rotate at high speed. If we assume a grease to obey as Newtonian fluid, a maximum motor pulse P which is proportional to rotational velocity, is expressed as a function of temperature T,

$$P(T) \propto T^{\alpha}(T - T_C), \tag{4.2}$$

where T_C is the temperature when the space between the shaft and bushes becomes zero, and α is a viscosity of the grease. We tested the RA motor unit in the freezer. Figure 4.11 shows the result of the cold test. From the cold test, we found that the maximum motor pulse was proportional to the temperature ($\alpha \sim 0$). Therefore, the major cause of the failure of the motor rotation is considered to be the decrease of the space between the shaft and the bushes. The result of the cold test for the DEC motor was roughly as same as the RA one. We re-designed and re-constructed RA and DEC motor units to solve the problem based on these experiments.

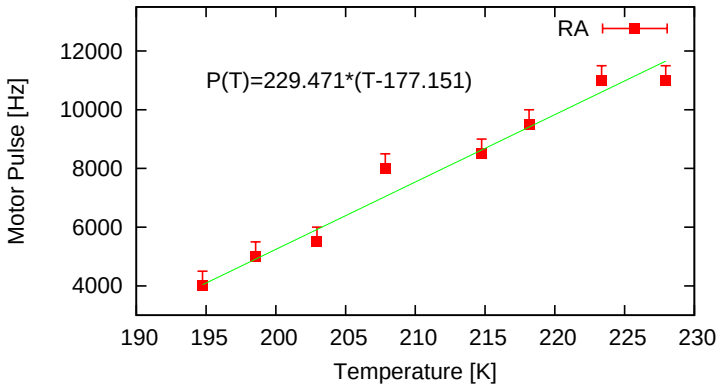

Figure 4.11: Result of the cold test for the RA motor unit. Red filled boxes are the results of the measurement. Green solid line is the best fit. Copyright: Okita et al. (2010) [51]

Figure 4.10 show a drawing of the Focus unit. The secondary mirror was fixed to the shaft and supported by two bushes. Shaft and bushes are made of the same steel. For focusing, the motor rotates the screw bolt to move the secondary mirror up and down. The AIRT40 Focus unit uses a stepping motor #CSK523AP-M30, which is also supplied by Oriental Motor Co., Ltd. The focus motor was also disassembled, de-greased, and greased with the Fombline grease. We tested the focus unit in the freezer and verified that it could move even at -80°C. The result suggests that the space between the shaft and bushes hardly changes if they are made of the same material.

The worm drives of RA and DEC axes reduce the rotation speed of RA and DEC motors. The worm drive units are made of various materials; for example, the worm is made of brass, shaft and bearings made of steel, and housing made of aluminum, etc. Therefore a space between the worm screw and the worm wheel, i.e. "backlash," changes with temperature. The backlash should be adjusted at -80°C, because the motor does not rotate at -80°C, if the backlash adjusted at 20°C.

Finally, we summarize how to make a telescope for the use on the Antarctic plateau.

- Test all components at -80°C environment.
- Use Teflon (polytetrafluoroethylene, PTFE) covered cable.
- Disassemble and degrease all components.
- Use a grease for $-80°$ environment.
- Make a telescope of the same materials.
- Adjust the backlash at low temperature.

4.5.4 Performance evaluations for AIRT40

To evaluate the performance of AIRT40, we calculate the tracking and pointing errors theoretically. The tracking error for equatorial mount is caused by the atmospheric refraction, set up error, and periodic motion. When we track an object A, whose position is (hour angle, declination)=(H_A, δ_A), for m minutes, the tracking error ($\Delta\alpha_{track}$, $\Delta\delta_{track}$)

is written as,

$$\begin{aligned}\Delta\alpha_{track} &= 902.465m \times \left(\frac{\cos\delta_A \sin H_A}{\cos\delta_A \sin H_A - 4.84814\times10^{-6}\epsilon_p \sin H_p \sin\delta_A} - 1\right) \\ &\quad -0.255078m \times \frac{\sin\delta_A \sin L \cos L \cos H_A + \cos\delta_A \cos^2 L}{(\sin\delta_A \sin L + \cos\delta_A \cos L \cos H_A)^2} \\ &\quad +P_0 \times \Big\{ \sin(1.57510m + \phi) - \sin\phi \Big\} \quad , \end{aligned} \tag{4.3}$$

$$\begin{aligned}\Delta\delta_{track} &= -4.37527\times10^{-3}\epsilon_p \; m \times \sin(H_A - H_p) \\ &\quad +0.255078m \times \frac{\sin L \cos L \sin H_A}{(\sin\delta_A \sin L + \cos\delta_A \cos L \cos H_A)^2} \quad , \end{aligned} \tag{4.4}$$

where (H_p, ϵ_p), L, P_0, and ϕ mean the hour angle and the separation of set up error, latitude of the observation site, amplitude and phase of the periodic motion of the telescope, respectively. $\Delta\alpha_{track}$, $\Delta\delta_{track}$, ϵ_p, and P_0 are in arcsec.

The pointing error is caused by the atmospheric refraction, a periodic motion, and a backlash of Dec axis. The lack of orthogonality between RA, DEC, and optical axes of a telescope has also the origin of the pointing error. When AIRT40 is aligned with an object A (hour angle, declination)=(H_A,δ_A), and then points to an object B (H_B,δ_B), the pointing errors of RA and DEC axes ($\Delta\alpha_{point}$, $\Delta\delta_{point}$) are given as,

$$\begin{aligned}\Delta\alpha_{point} &\simeq \epsilon_p \Big\{ \sin(H_B - H_p)\tan\delta_B - \sin(H_A - H_p)\tan\delta_A \Big\} \cos\delta_B \\ &\quad +d \left(\tan\delta_B - \tan\delta_A\right)\cos\delta_B \\ &\quad -t \left(\frac{1}{\cos\delta_B} - \frac{1}{\cos\delta_A}\right)\cos\delta_B \\ &\quad \pm|P_0| \left(\cos\delta_A + \cos\delta_B\right) \\ &\quad +58.3 \times \frac{\sin H_A \cos L}{\sin\delta_A \sin L + \cos\delta_A \cos L \cos H_A} \\ &\quad -58.3 \times \frac{\sin H_B \cos L}{\sin\delta_B \sin L + \cos\delta_B \cos L \cos H_B} \quad , \end{aligned} \tag{4.5}$$

$$\begin{aligned}\Delta\delta_{point} &\simeq \epsilon_p \Big\{ \cos(H_B - H_p) - \cos(H_A - H_p) \Big\} \\ &\quad +58.3 \times \frac{\sin L}{\sin\delta_B \cos\delta_B \sin L + \cos^2\delta_B \cos L \cos H_B} \\ &\quad -58.3 \times \frac{\sin L}{\sin\delta_A \cos\delta_A \sin L + \cos^2\delta_A \cos L \cos H_A} \\ &\quad -58.3 \times \left(\tan\delta_B - \tan\delta_A\right) \\ &\quad \pm 2 \; |B| \quad , \end{aligned} \tag{4.6}$$

where, d means the orthogonalization error between RA and dec axes. The orthogonalization errors between DEC and optical axes is written as t. B means DEC backlash. The unit of $\Delta\alpha_{point}$, $\Delta\delta_{point}$, d, t, and B are arcsec.

We evaluate (H_p, ϵ_p), P_0, d, t, and B of AIRT40 using Eqs. (4.3) $\sim$ (4.6). The observations were performed at Tohoku University from 2008 to 2010. From the test observations, we found $H_p \sim -0.122$ radian, $\epsilon_p \sim 146''$, $P_0 \sim 4.3''$, $d \sim 87''$, $t \sim 320''$, and

$B \sim 86''$. The amplitude of the periodic motion is so small that the stellar image does not run away from the field of view of the Tohoku DIMM (written in Chap. 4.6). However, the pointing error would occur due to the non-orthogonality failure between RA, DEC, and optical axes. Therefore, due to careful assembling and precise alignment for the AIRT40 will be needed for observations at Dome Fuji.

We also evaluated the optical quality of AIRT40. The quality is experimentally evaluated with "Hartmann test". From the observations of stars, the Hartmann constant was found to be $\sim 0.59''$. The quality is sufficient for Tohoku DIMM observations mentioned below.

4.6 Tohoku DIMM

Tohoku University Differential Image Motion Monitor (hereafter we write this "Tohoku DIMM") is the first instrument to measure astronomical seeing at Dome Fuji. Tohoku DIMM was developed based on the University of Tokyo Differential Image Motion Monitor (UT-DIMM: Motohara et al. 2008; 2004; Uraguchi et al. 2004) [46, 47, 74]. The author performed designing, constructing, testing, installing, operating, and data analyzing for Tohoku DIMM. Figure 4.12 is a picture of Tohoku DIMM attached on AIRT40 at Dome Fuji in January 2011.

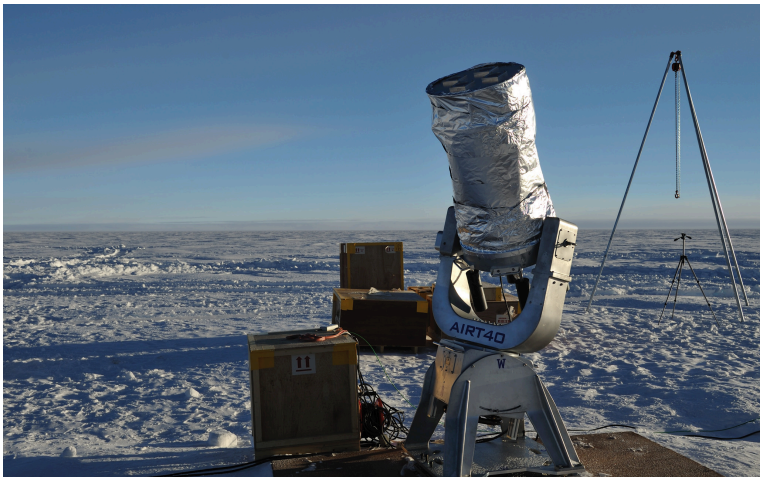

Figure 4.12: Tohoku DIMM attached on AIRT40 at Dome Fuji in January 2011. Aluminum-foil of the optical tube (see Chap. 5.4) enabled us to measure astronomical seeing with reasonable contrast at daytime in the Antarctic summer.

4.6.1 Specifications of Tohoku DIMM

Tohoku DIMM was transported to Dome Fuji in the $51^{st}/52^{nd}$ JARE. Since we sent two astronomical crews to Dome Fuji in this campaign, we succeeded DIMM observations, which were relatively complicate and difficult. AIRT40 was used with Tohoku DIMM. Because of no stage or high platform at Dome Fuji in the campaign, we performed Tohoku DIMM observations at the snow surface to measure the total seeing. Although PLATO-F supplied electric power and internet communication all year, we did not plan full-year,

Table 4.2: Technical specifications of Tohoku DIMM.

Telescope	AIRT40
Subaperture diameter	ϕ 74 mm
Subaperture separation	250 mm
Wedge prism apex angle	$30''$
Wedge prism manufacture	Nitto Optical Co., Ltd.
Camera	Watec WAT-100N
Filter	not used
Observed wavelength	620 nm (peak sensitivity)
Diffraction limit	$2.1''$
Pixel scale	$0.39''$/pix $\times$ $0.46''$/pix
Field pf view	$5.0' \times 3.8'$
Control	UT-DIMM software on Linux

unmanned, and remote Tohoku DIMM observations due to some technical difficulties. Instead, Tohoku DIMM observations were only performed during the Antarctic summer.

Tohoku DIMM required sensitivity enough for the total seeing measurement in daytime, because there was no sunset in the Antarctic summer.

4.6.2 Hardware of Tohoku DIMM

Tohoku DIMM is optimized for AIRT40. Tohoku DIMM had two-pair two-apertures (in total of four apertures) with 74 mm each in diameter and the separation 250 mm. A each aperture is attached a wedge prism with diameter of 80 mm and apex angle $30''$, supplied by Nitto Optical Co., Ltd. Two-pairs two-apertures DIMM can obtain four seeing values simultaneously (horizontal-pair seeing: ϵ_{hl}, ϵ_{ht}, and vertical-pair seeing: ϵ_{vl}, ϵ_{vt}). The advantage of the two-pairs two-apertures DIMM is to get more information for the turbulence.

The detector of Tohoku DIMM is an analog interlace video camera #WAT-100N supplied by Watec Co., Ltd., and can take thirty frames per second. The camera has an electric shutter and manual gain control. We did not use any filter for Tohoku DIMM. Since the peak sensitivity of #WAT-100N is at $\sim$ 620 nm, we assume that the seeing value obtained with Tohoku DIMM is that at 620 nm. The exposure time was set to 0.001 s for the observations. Analog data obtained with #WAT-100N were captured by the analog to digital video converter #ADVC110 supplied by Canopus Co., Ltd. and converted to digital data. Table 4.2 summarizes the technical specifications of Tohoku DIMM.

4.6.3 Software for Tohoku DIMM

Tohoku DIMM was controlled by UT-DIMM software. We modified the UT-DIMM software to optimize for Tohoku DIMM. The software calculates seeing values from digital data. The centers of gravity of the star images were measured in each frame, and the seeing was calculated every 30 frames. As the measurement frequency of Tohoku DIMM depends on the computer performance, seeing values are calculated about each three second.

Table 4.3: Technical specifications of HU-DIMM.

Telescope	Meade LX200GPS-20 with 2× extender with diagonal prism
Focal length	$\sim$ 4 000 mm
Subaperture diameter	ϕ50 mm
Subaperture separation	144
Effective wavelength	620 nm
Camera	Watec WAT-100N
Pixel scale	0.40″/pix × 0.45 ″/pix
Exposure time	0.001 s

Figure 4.13: Simultaneous observations with Tohoku DIMM (inside the astronomical dome) and the Hiroshima University Differential Image Motion Monitor (HU-DIMM) at right side.

4.6.4 Simultaneous observations with HU-DIMM

We carried out simultaneous observations to verify the seeing value of Tohoku DIMM. We borrowed the Hiroshima University Differential Image Motion Monitor (hereafter we write this "HU-DIMM") by courtesy of the Higashi-Hiroshima Observatory (Chiyonobe 2004) [18]. By measuring seeing with Tohoku DIMM and HU-DIMM simultaneously and confirming the consistency, we verified if Tohoku DIMM had some hardware biases and/or software errors. Table 4.3 summarizes the technical specifications of HU-DIMM. Simultaneous observations were performed on the roof of Physics A buildings, Tohoku University on 2008 July 14–15, October 3–4, 9–10, and 13–14. Tohoku DIMM attached on AIRT40 was placed inside an astronomical dome. We put HU-DIMM with the separation of $\sim$ 4 m west of the astronomical dome. Figure 4.13 is a picture of the simultaneous observations at Tohoku University. Vega (α Lyr, V = 0.0 mag.), Alpheratz (α And, V = 2.1 mag.), Deneb (α Cyg, V = 1.3 mag.), and Capella (α Aur, V = 0.1 mag.) were used.

Figure 4.14 and 4.15 are the results of the simultaneous observations. The control computer for HU-DIMM was frequently freezed, anc thus the observations were interrupted

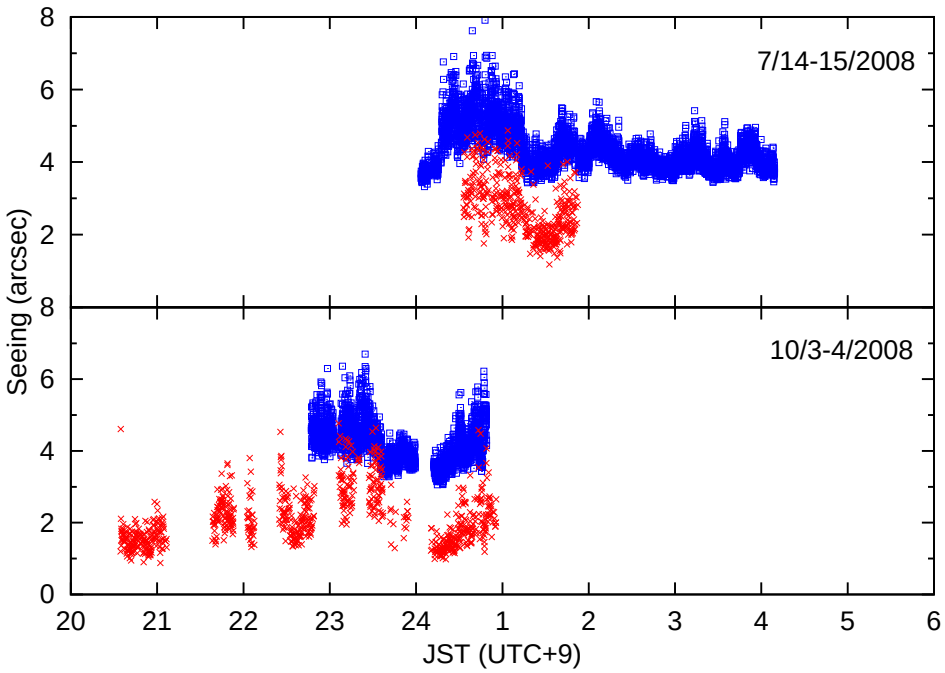

Figure 4.14: Time series seeing obtained with HU-DIMM (red cross) and Tohoku DIMM (blue square) on 2008 June 14–15, and October 3–4. We plots DF-DIMM seeing data with offset of 2″ for clarity.

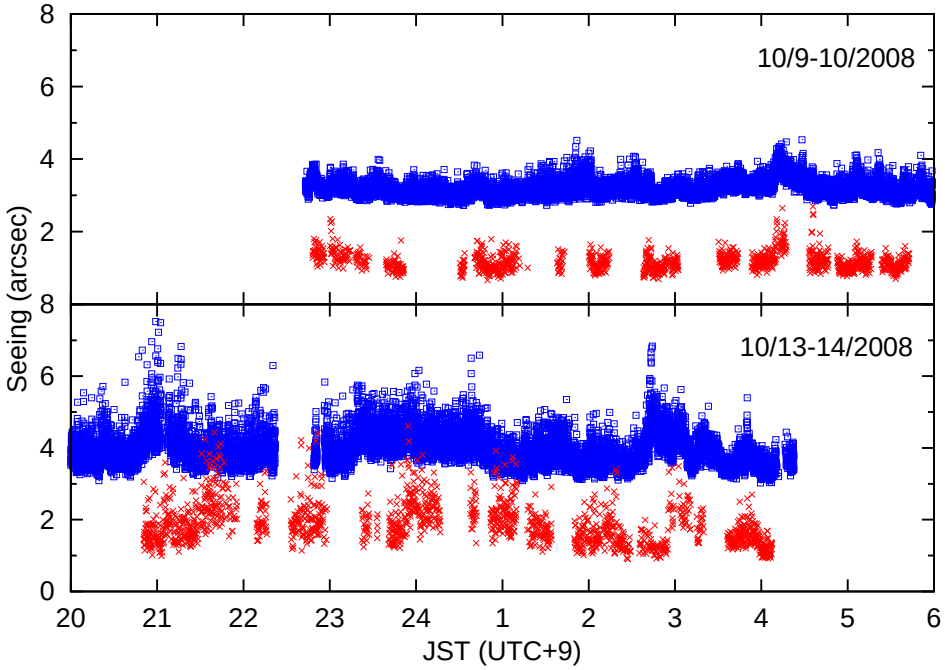

Figure 4.15: Same as Fig. 4.14, but for the period 2011 October 9–10 and 13–14.

sometimes. We found that a clock time of the computer for HU-DIMM was not correct after freezed. Because of the reason, we can not compare the time-variation of the seeing values obtained these two DIMMs.

Instead, the histograms for each night are shown in Fig.4.16. The results are summa-

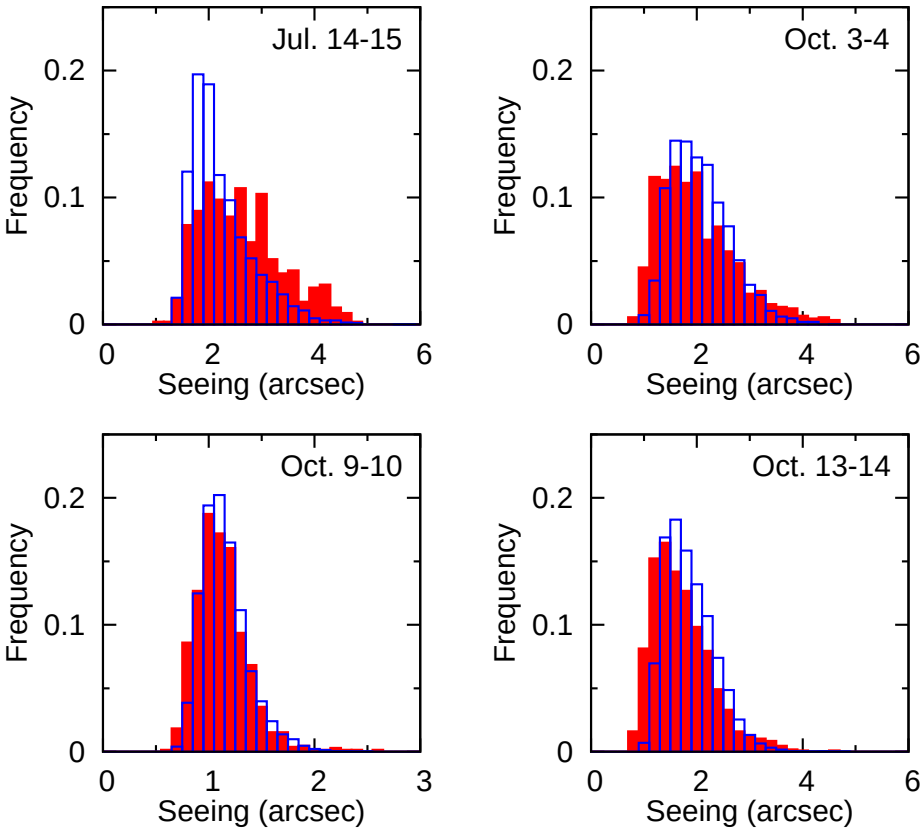

Figure 4.16: Histograms of Tohoku DIMM seeing (Blue blank box) and HU-DIMM (Red filled box) for each night.

rized in Table 4.4. The result indicates that Tohoku DIMM seeing value is consistent with HU-DIMM value within $\sim$ 10% error. As such, Tohoku DIMM had no hardware biases and no software errors on the seeing value.

Table 4.4: Results of the simulteneous observations for Tohoku DIMM and HU-DIMM.

July 14-15	Tohoku DIMM	HU-DIMM
Number of observations	5 481	447
Mean	2.3″	2.7″
Median	2.2″	2.6″

October 3-4	Tohoku DIMM	HU-DIMM
Number of observations	2 887	869
Mean	2.2″	2.1″
Median	2.1″	2.0″

October 9-10	Tohoku DIMM	HU-DIMM
Number of observations	12 433	1 302
Mean	1.2″	1.2″
Median	1.2″	1.1″

October 13-14	Tohoku DIMM	HU-DIMM
Number of observations	9 354	1 057
Mean	2.0″	1.8″
Median	1.9″	1.7″

4.7 Nine meter astronomical tower

To avoid the snow drift and the effect of the atmospheric turbulence by the surface boundary layer near the snow surface, a 9 m astronomical tower was constructed at Dome Fuji.

4.7.1 Background of the 9-m astronomical tower

The $53^{rd}/54^{th}$ JARE planned the third time astronomical site testing at Dome Fuji thuroughout year from 2012/2013 the Antarctic summer. The heavy iron frames of the tower (in total $\sim$ 10 tons) were transported to Syowa station by the icebreaker Shirase in the 53^{rd} JARE campaign, in 2011/2012 the Antarctic summer. In the Antarctic winter in 2012, the 53^{rd} JARE pre-constructed the tower at Syowa station to establish how to construct it in the extremely cold environment. They transported the iron frames of the tower from Syowa station to S16 milestone on the Antarctic continent. Takuya Koyama, who was the first winter-over astronomical crew in JARE, was stayed at Syowa station over winter to prepare astronomical observations and the construction of the tower. A carpenter and medical doctor of the 53^{rd} JARE joined to the Dome Fuji traverse team to construct the tower at Dome Fuji. The 54^{th} JARE members: the author; a carpenter; welder; and engineering scientist, also participated in the team, who flew to S16 on DROMLAN in 2012 November.

The tower was required to be as high as possible. The stage on the tower had to be large enough for AIRT40 and DF-DIMM installation. The tower was required to be stable, so that differential settlement or vibration by wind would be suppressed. The tower had to be constructed as easily as possible. To avoid the astronomical observation time

decreased, the tower should be constructed within the shortest time.

4.7.2 Specifications of the 9-m astronomical tower

The tower was designed by Koei-Densetsu Co., Ltd. Because of the maximum height of the crane of SM106 snow-vehicle ($\sim$ 10 m), we constructed the tower with $\sim$ 9 m high. Hereafter the tower is called as the "9-m astronomical tower." The 9-m astronomical tower is the second highest construction next to the 30-m meteorological tower at "Mizuho" station for JARE on the Antarctic continent. We arrived at Dome Fuji on December 15, 2012 . The construction of the tower was started on December 16. Before the construction of the tower, we made hard snow surface (Koui Kim, in preparation). We finished the construction on December 29.

Figure 4.17 shows the 9-m astronomical tower. The stage size is 5 m length (east-west

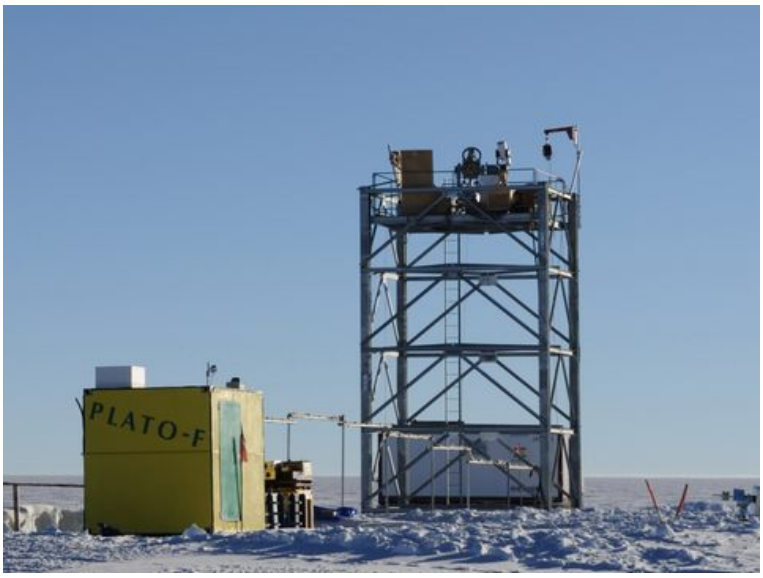

Figure 4.17: Nine meter astronomical tower at Dome Fuji. PLATO-F Instrument Module (left, yellow container) and temporary 20 ft container-module (back of the tower, white container) are also shown.

side) and 4 m width (south-north side). We put AIRT40 on the center of the stage, while DF-DIMM was put on the west side of the stage. A windscreen of 1.8 m $\times$ 2.4 m was also put on the east side of the stage.

Strong wind will cause vibrations of the tower. However, since no wind speed and direction data near the 9 m astronomical tower are available in this campaign, quantitative vibration evaluation was not performed. By the author's naked-eye observations of stars, however, any vibrations were not observed. The differential settlement was measured before and after the construction using a leveling instrument. A Tilt sensor was put on the stage and has continued to measure the differential settlement. Almost no differential settlement was observed (Koui Kim, in preparation).

4.8 DF-DIMM

Dome Fuji Differential Image Motion Monitor (hereafter we write this "DF-DIMM") is the second instrument to measure astronomical seeing at Dome Fuji. DF-DIMM can measure the seeing continuously and autonomously. DF-DIMM was developed and evaluated its performance at Tohoku University. The author performed designing, constructing, testing, installing, operating, and data analyzing for DF-DIMM. Figure 4.18 is a picture of DF-DIMM at Dome Fuji in January 2013.

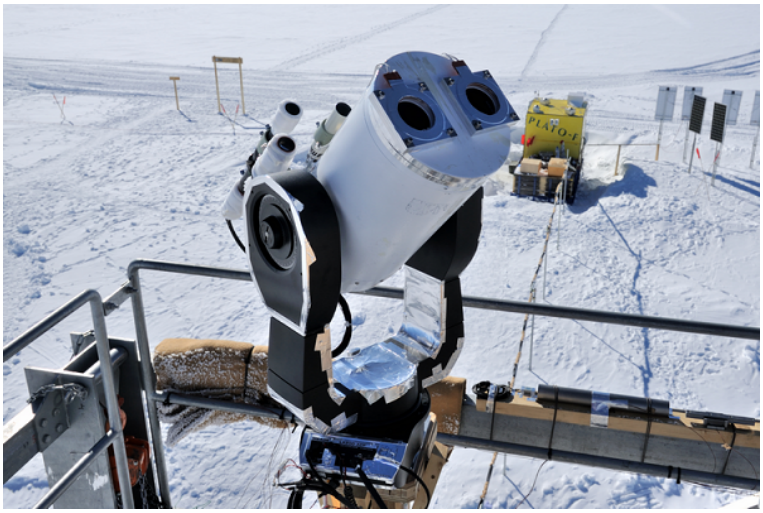

Figure 4.18: DF-DIMM on the 9-m astronomical tower at Dome Fuji, 2013 January. Copyright: Okita et al. (2013a) [50]

4.8.1 Specifications of DF-DIMM

DF-DIMM was designed for measuring the free-atmosphere seeing in the autumn 2012. By using electric power and internet communication supplied by PLATO-F, which was established in the $51^{st}/52^{nd}$ JARE, and by using the 9-m astronomical tower, which will be constructed in the $53^{rd}/54^{th}$ JARE, the free-atmosphere seeing would be measured remotely. Because the icebreaker Shirase in the 53^{rd} JARE was already departed, DF-DIMM had to transport using DROMLAN aircraft in the 54^{th} JARE. This meant that DF-DIMM had to be developed lightly and compactly.

DF-DIMM was required high accuracy of the star position. Unmanned and remotely observations were required in the Antarctic winter. Power and communication consumption for DF-DIM had to be adapted to the capacity of PLATO-F. DF-DIMM also required sensitivity enough for the seeing measurement in the daytime, because there is no sunset in the Antarctic summer.

4.8.2 Hardware of DF-DIMM

DF-DIMM was developed as inexpensively as possible. Inexpensive development was done by using commercial devices. Since the commercial devices, in generally, do not work in the low temperature condition, we tested them in the freezer and improved.

DF-DIMM is based on a 20 cm in diameter Cassegrain telescope, with an CCD camera. The telescope of DF-DIMM was used Meade Instruments Corp., # LX200-8″ ACF

(hereafter we write LX200). LX200 is an automated alt-azimuth mount telescope; it has GPS, tilt, and magnetic sensors. By only using these sensors, i.e., without star alignment, LX200 can point an object with the accuracy of a few degree. In addition, LX200 has a serial communication interface, whose protocol is open, we can easily control remotely LX200 by a computer. Focal length of LX200 is ∼2 000 mm. We used TeleVue Optics, Inc. 90° Everbrite Diagonal to bend the light pass. For a focuser, we used Jim's Mobile, Inc. (JMI) MOTOFOCUS for Meade Cassegrain Telescopes #MFMH. This focuser moves the optical position of the primary mirror for focusing, and can be controlled with LX200 serial command. Too fast for the focuser speed, we added a hand-made electric circuit for speed reducing.

DF-DIMM is a standard two subapertures DIMM; diameter of subapertures are 60 mm and the separation is 140 mm. Each apertures are attached with a wedge prism; diameter of the wedge prism is 80 mm and the apex angle is 30″. The optical tube of LX200 was painted white to minimize the local turbulence inside and around the tube generated by the solar radiation. Unnecessary parts were removed for weight saving. Clearance gaps of the instruments were covered with aluminum foil tape at Dome Fuji

The camera for DF-DIMM was used Santa Barbara Instrument Group, Inc. (SBIG) ST-i Monochrome (Hereafter we write ST-i.) ST-i is not a video camera but a still camera for amateur astronomer. ST-i has high sensitivity detector (maximum quantum efficiency of 55%). ST-i is compact (ϕ31.7 mm × 88.6 mm), light (86 g) , and works only with USB bus power. ST-i has a mechanical shutter and on-chip electronic shutter. We removed the mechanical shutter because it did not work at low temperature. In DIMM observations, we set exposure time of 0.001 s. ST-i takes about six frames per second, depending on the transfer speed of USB 2.0. ST-i is controlled with a software of Nightview[1] (Hroch). The pixel scale with LX200 is ∼ 0.76″/pixel, and the filed of view is ∼ 8.2′ × 6.2′. The accuracy of star positions is discussed in Chap. 4.8.6.

A Narrow-band filter can suppress auroral emissions. Edmund Optics Inc. Fluorescence Bandpass Filters #67013-L was used for this purpose. The center wavelength is ∼ 472 nm, and the band width is ∼ 35nm.

Compulab Ltd. #fit-PC2 is a computer used for controlling LX200 and ST-i. fit-PC2 is compact (101 mm × 115 mm × 27 mm) and it requires only six watts for the operation. We installed Ubuntu 10.04 LST as the operating system. The electrical power required for the operation of DF-DIMM (LX200 telescope, ST-i × 3, and fitPC2 × 3) is ∼ 36-W on average, ∼ 43-W in maximum. DF-DIMM needs total 106-W in maximum including heaters (∼ 47-W) and loss of the AC/DC converter (∼ 16-W).

For transportation, all equipments of DF-DIMM including packing materials were 3 cardboard boxes, volume of 0.30 m^3, weight of 70 kg in total. This small volume and light weight are suited for DROMLAN transportation.

Table 4.5 summarizes the technical specifications of DF-DIMM.

4.8.3 Modifications for the Antarctic environment

Many modifications should made to enable the operation in the Antarctic environment. LX200 and ST-i were disassembled and de-greased. Original cables were replaced to Teflon

[1] http://www.physics.muni.cz/mb/nightview/nightview.html

Table 4.5: Technical specifications of DF-DIMM.

Telescope	Meade LX200-8″ ACF with TeleVue 90° Everbrite Diagonal
Focal length	∼2 000 mm
Subaperture diameter	ϕ60 mm
Subaperture separation	140 mm
Wedge prism apex angle	30″
Filter	Edmund 67013-L
Center wavelength	472 nm
Filter band width	35 nm
Diffraction limit	1.98″
Camera	SBIG ST-i monochrome
Pixel scale	∼0.76″/pix
Field of view	8.2′ × 6.2′
Control	Nightview on fitPC2

Figure 4.19: Left top; Complete disassembling of LX200 for modifying the cold environment. Right top; Motor and electric circuit with heater and polyurethane form (white, wrapping one). Left bottom; "Doughnus-shape" heaters for optical windows. Right bottom; Cold test for LX200 in a freezer.

(polytetrafluoroethylene, PTFE) covered cables. Hand-made USB, RS232C, and Cat5e Ethernet cables of the Teflon covered cables were used.

Machine components were de-greased (Fig. 4.19 top left), and greased with Fomblin ZLHT grease. Bearings were changed to chose of open and non-greased type, and greased with Fomblin ZLHT.

Table 4.6: Technical specifications of NightGuide.

Telescope	Fujifilm HF50HA-1B
Focal length	50 mm
Focal ratio	2.3
Filter	Edmund 67013-L
Wavelength	472 nm
Band width	35 nm
Diffraction limit	5.46″
Camera	SBIG ST-i monochrome
Pixel scale	30.5″/pix
Field of view	5.5° x 4.1°
Control	Nightview on FitPC2

Motors, tilt sensor, and GPS unit of LX200 work at −80°C with 1.7 W rubber heaters and styrene form shield (Fig. 4.19 top right). Wedge prisms were assembled with 3.5 W "doughnus-shape" heaters to prevent from frosting (Fig. 4.19 bottom left). Control computers are put in the thermal control box made of styrene form. By keeping waste heat in the box, the control computers can work at −80°C environment without heater.

The modifications were performed based on the result of cold test. All components were tested in a freezer of Nihon Freezer Co., Ltd. #CLN-35C (Fig. 4.19 bottom right). The freezer can provides −85°C environment. We also performed cold environment evaluations at the Institute of Low Temperature Science, Hokkaido University. We finally confirmed that DF-DIMM worked even in −80°C. Electric power of $\sim$ 47 W in total for heaters was needed.

4.8.4 Finder telescopes

By using tilt, GPS, and magnetic sensors, LX200 can point an object with the accuracy of a few degree. However the field of view of DF-DIMM is only $8.2' \times 6.2'$, and direct pointing would be very difficult. Therefore we mounted wide field of view finders on DF-DIMM.

We developed two finders. One is a finder with wide field of view, named "NightGuide" for the Antarctic winter, and the other is a finder with middle field of view, named "DayGuide" for the Antarctic summer. NightGuide is consist of Fujifilm Corp. #HF50HA-1B C-mount lens (focal length: 50 mm, F/2.3), Edmund Optics Inc. Fluorescence Bandpass Filters #67013-L (center wevelength: 472 nm、band width: 35 nm), and Santa Barbara Instrument Group, Inc. (SBIG) ST-i Monochrome. NightGuide can quickly search a target star. Table 4.6 summarizes the technical specifications of NightGuide. Dayguide is consist of Tomytec Co. Ltd., Pencil BORG #6025 with Tele Vue Optics, Inc. 2.5× Powermates (effective focal length: 438 mm, F/17.5), Edmund Optics Inc. Fluorescence Bandpass Filters #86347-L (center wevelength: 655 nm、band width: 24 nm), and Santa Barbara Instrument Group, Inc. (SBIG) ST-i Monochrome. We used a bandpass filter for DayGuide which transmits longer wavelengths than the filters for DF-DIMM and Nightguide. Longer wavelengths have a benefit for low atmospheric scattering. On the other hand longer exposure is needed due to less efficiency of the detector. To find a star in the Antarctic summer, we used the bandpass filter to suppress auroral

Table 4.7: Technical specifications of DayGuide.

Telescope	Tomytec Pencil BORG 6025 with TeleVue 2.5x Powermate
Focal length	438 mm
Focal ratio	17.5
Filter	Edmund 86347-L
Wavelength	655 nm
Band width	24 nm
Diffraction limit	$6.59''$
Camera	SBIG ST-i monochrome
Pixel scale	$3.49''$/pix
Field of view	0.62° x 0.47°
Control	Nightview on fitPC2

emission and atmospheric scattering light. Pixel scale of DayGuide is $3.5''$/pixel; field of view is $0.62^\circ \times 0.47^\circ$.

In the Antarctic summer, the sun does not set, so that the background is quite bright. If we want to detect a star in the daytime, background has to be reduced than the star image. The number of photons from a star N_{obj}, is proportionate to the square of diameter D of the telescope.

$$N_{obj} \propto D^2 \tag{4.7}$$

On the contrary, the number of photons from diffuse source such as background N_{sky} is proportionate to the square of diameter D of the telescope, the square of the pixel size μ, and inversely proportionate to the square of the focal length f of the telescope.

$$N_{sky} \propto \frac{D^2}{f^2} \cdot \mu^2 \tag{4.8}$$

If we use a telescope with large focal ratio and a detector with small pixel size, we could detect a star image in daytime. As DayGuide is an aperture of 25 mm in diameter and focal ratio of 17.5, and pixel size of 7.4 μm, it can detect stars brighter than ~ 0 mag. with 0.001 s exposure time even in the daytime. Table 4.7 summarizes the technical specifications of DayGuide. The finders solved the problem due to the poor pointing accuracy of DF-DIMM. NightGuide and DayGuide are controlled NightView software on each Compulab Ltd., #fit-PC2s.

4.8.5 Software for DF-DIMM

DF-DIMM was developed for the measurement of the astronomical seeing using Canopus (α Car, V = -0.7 mag, the second brightest star in the sky). Canopus is circumpolar at Dome Fuji, with a zenith angle varying from 25° to 50°, and thus Canopus is suited to continuous observations. Seeing values were calculated, using the equations (13), (14), and (23) of Sarazin & Roddier (1990) [56] with 450 frames taken in about five-minute intervals. The software to calculate the seeing value was developed in C language, AWK, and bash script. Sextractor (Bertin & Arnouts 1996) [12] was used for finding the star positions. Because of many noises in raw images, we took pre-reduction using CFITSIO (Pence 1999) [53] to reduce the noises.

We also developed the softwares, such as pointing, exposure defining, focusing, calculating the focal length, etc. The softwares use Nightviwe, Sextractor, CFITSIO, C language, AWK, and bash script. The finders were controlled with the same softwares. All software were combined in bash script, and run by a crontab of the control computer. If the system power is turned on, DF-DIMM turns up and starts DIMM observations automatically. By the development of DF-DIMM softwares, continuous and fully automatic seeing measurements became possible. Seeing results, telescope logs were compressed and were transfered to Japan via PLATO-F Iridium communication.

4.8.6 Accuracy of star positions

DIMM observation demands a precise measurement of star positions. The resolving power θ_{res} [radian] of a telescope with an aperture diameter D [m] in the wavelength λ [m] is

$$\theta_{res} \sim \frac{\lambda}{D} \ . \tag{4.9}$$

Most photons N_{obj} ($\sim$ 86 %) from a star are detected in the range of the resolving power with the probability distribution of the point spread function (PSF). Photons from background sky N_{sky}, photons from dark noise N_{dark}, and readout noise N_{obs} are also detected on the detector. The accuracy of the star position σ_{pos} can be written using the signal to noise ratio (SNR) as follow.

$$\sigma_{pos} \sim \left(\frac{\lambda}{D}\right) \frac{1}{SNR} \tag{4.10}$$

$$SNR \equiv \frac{N_{obj}}{\sqrt{N_{obj} + N_{sky} + N_{dark} + N_{read}^2}} \tag{4.11}$$

Here we calculate for DF-DIMM case. DF-DIMM has two sub-apertures with diameter $D = 6$ cm and observed at wavelength $\lambda = 472$ nm. Thus the resolving power θ_{res} is $\sim 1.62''$. DF-DIMM observed Canopus (V $= -0.7$ mag.). From the band width (35 nm) of the filter, exposure time of 0.001 s, the efficiency of the telescope 0.6, and the quantum efficiency of the detector 0.53, the number of photons from Canopus N_{obs} is $\sim$ 5400.

A daytime background sky at the wavelength 472 nm is calculated to be $\sim$ 3 mag arcsec^{-2} from the scattering model (Krisciunas et al. 1987; Krisciunas & Schaefer 1991; Krisciunas 1997) [32, 33, 34]. As the pixel scale of DF-DIMM is $\sim 0.76''$/pix, the number of photons from the background sky N_{sky} is calculated to be $\sim$ 180. From the specification sheet of ST-i, the dark noise N_{dark} of $\sim$ 0 e$^-$ and the readout noise N_{read} of 8.6 e$^-$. The SNR can be calculated from the values to be $\sim$ 72. The accuracy of the star position σ_{pos} is $\sim 0.023''$. We note that the PSF obtained from one exposure of DF-DIMM observations is not affected by the atmospheric turbulence because the diameter of DF-DIMM is smaller than the Fried length r_0 and the exposure time is shorter than the coherence time τ_0. From the reason, DF-DIMM can measure star position with the accuracy of $0.023''$ in theory.

In actual case, however, the accuracy of star position detection also depends on a star detection algorithm and the pixel scale of the detector. We verified the accuracy of the star position measurement using artificial stars. The task "mkobjects" of IRAF was used for making artificial stars of the same FWHM and same count of Canopus as obtained with DF-DIM at Dome Fuji. We buried eight artificial stars in each image and used 482 images

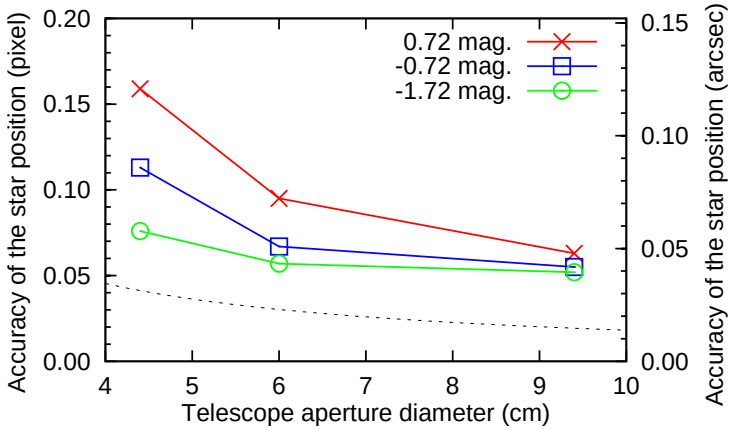

Figure 4.20: Accuracy of the star position using the telescopes diameter D of 4.4, 6.0, and 9.4 cm, and artificial stars of -1.72, -0.72, and 0.72 magnitude. Red cross, blue square, and green circle are the accuracy of the star position determination using -1.72, -0.72, and 0.72 magnitude stars, respectively. Black dot line is the theoretical detection accuracy of the star position with DF-DIMM for Canopus, which is calculated from Eq. 4.10.

for the verification of the accuracy. The star positions were obtained by the Sextractor with the same parameters as those of DF-DIMM observations. From the verification, the accuracy of the position for the artificial stars were found to be ~ 0.067 pixels, or $\sim 0.051''$.

We also simulated the accuracy of the star position using the telescopes diameter D of 4.4, 6.0, and 9.4 cm, and artificial stars of -1.72, -0.72, and 0.72 mag. Figure 4.20 is the results of the simulation.

From Fig. 4.20, the detection accuracy for the fainter stars (0.72, -0.72 mag.) were proportional to $-1/2$ power of diameter D, which is consistent with the theory. On the contrary, for the brightest star the detection accuracy is unchanged 0.05 pixels. The accuracy of the star position would not be smaller than 0.05 pixels even if the telescope diameter is larger, or the star is brighter. This would be caused by less accuracy of Sextractor, and/or less precise the pixel scale for the detector. Conclusively, we verified that the accuracy of the star position for DF-DIMM is $0.023''$ in theory, and $\sim 0.05''$ by the simulation with artificial stars. As the free-atmosphere seeing at Dome Fuji was predicted $0.209''$, we reasonably assumed that DF-DIMM could measure the free-atmosphere seeing with sufficient accuracy.

4.8.7 Simultaneous observation with FE-DIMM

We carried out simultaneous observations at Higashi-Hirosima Observatory to verify the seeing value obtained with DF-DIMM. Higashi-Hiroshima Observatory has the Hiroshima University Faculty of Education Differential Image Motion Monitor (hereafter we call "FE-DIMM"). FE-DIMM is the sister model of the Hiroshima University Differential Image Motion Monitor (HU-DIMM, see Chap. 4.6.4) (Chiyonobe 2004) [18]. By measuring seeing with DF-DIMM and FE-DIMM simultaneously, we can verify if DF-DIMM has some hardware biases and/or software errors.

Table 4.8 summarizes the technical specifications of FE-DIMM. Simultaneous observations were performed at the roof of the Higashi-Hiroshima Observatory. We put DF-DIMM

Table 4.8: Technical specifications of FE-DIMM.

Telescope	Meade LX200GPS-25 with 2x extender wiht diagonal prism
Focal length	$\sim 5\,000$ mm
Subaperture diameter	ϕ50 mm
Subaperture separation	194
Effective wavelength	620 nm
Camera	Watec WAT-100N
Pixel scale	$0.25''$/pix $\times$ $0.28\ ''$/pix
Exposure time	0.001 s

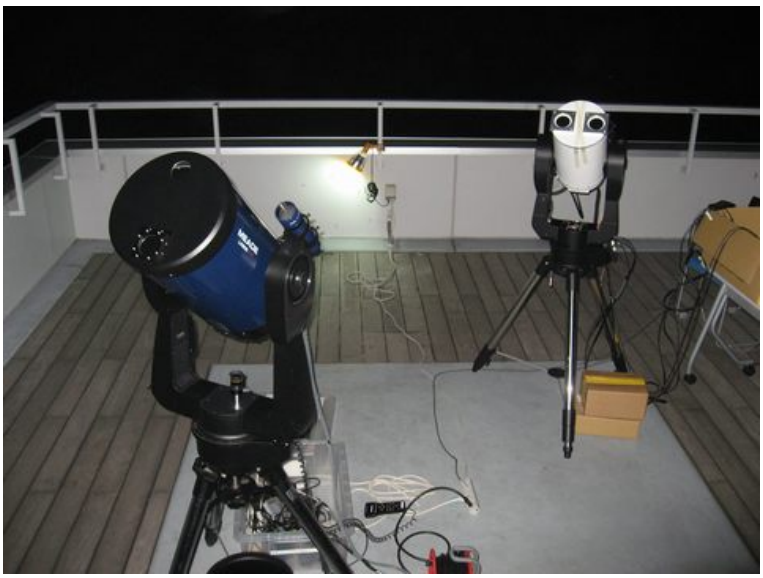

Figure 4.21: Simultaneous observations at Higashi-Hiroshima Observatory. Left dark blue telescope is the Hiroshima University Faculty of Education Differential Image Motion Monitor (FE-DIMM). Right white one is DF-DIMM.

and FE-DIMM on the roof with the separation of $\sim$ 2 m. Figure 4.21 is a picture of the simultaneous observation at Higashi-Hiroshima Observatory.

The effective wavelength of FE-DIMM is 620 nm, while that of DF-DIMM one is 472 nm. We converted the seeing values of DF-DIMM to those at wavelength 620 nm assuming that the seeing value depends on 1/5 power of the wavelength. Hereafter, seeing value in this subsection is discussed at wavelength of 620 nm.

FE-DIMM used Vega (α Lyr, V = 0.0 mag.) to measure seeing. DF-DIMM could not use Vega because of a software problem. Altair (α Aqu, V = 0.9 mag.), Aldebaran (α Tau, V = 1.0 mag.), Capella (α Aur, V = 0.1 mag.) were used for seeing measurements with DF-DIMM. Observations at Higashi-Hiroshima Observatory were carried out from 2012 July 23 to January 27. We succeeded the simultaneous observations on July 24, 25, and 26. Figure 4.22 is the results of the simultaneous observations. From Fig. 4.22, we found that the seeing value obtained from DF-DIMM has the same time-variation with FE-DIMM.

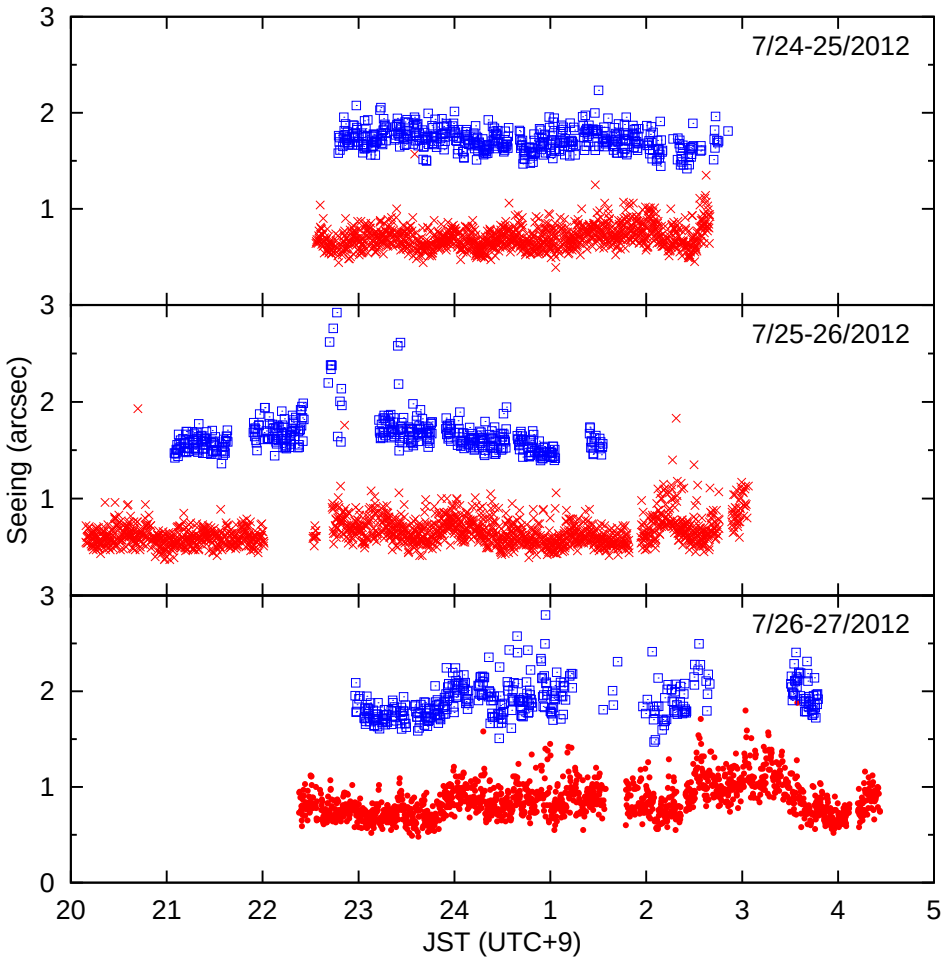

Figure 4.22: Seeings obtained with FE-DIMM (red cross) and DF-DIMM (blue square) during 2012 July 24-27. We plot DF-DIMM seeings with offset of 1″ for clarity.

The statistics for the simultaneous observations are also listed in Table 4.9. Histogram is shown in Fig.4.23 left. The comparison for FE-DIMM and DF-DIMM is also shown in Fig.4.23 right.

From the statistics, DF-DIMM seeing value is consistent with FE-DIMM value within $\sim$ 5% error. From the comparison, the correlation coefficient is $\sim$ 0.63. In summery, from the simultaneous observations, we conclude that DF-DIMM had no hardware biases and no software errors on the seeing values against FE-DIMM and HU-DIMM (see Chap. 4.6.4).

Table 4.9: Statistics for the simultaneous observations at the wavelength of 620 nm.

	DF-DIMM	FE-DIMM
Number of observations	1 778	4 985
Mean	0.73″	0.76″
Median	0.69″	0.73″

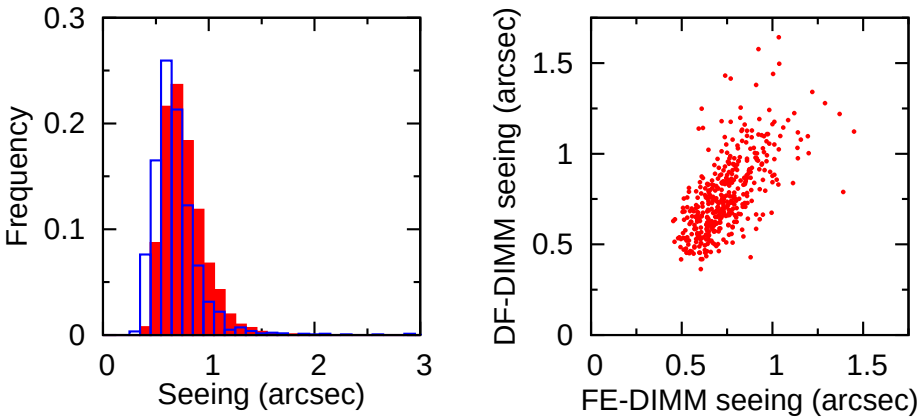

Figure 4.23: Left; Histogram of DF-DIMM seeing (Blue blank box) and FE-DIMM (Red filled box). Right; The comparison between FE-DIMM seeing and DF-DIMM seeing.

Chapter 5

Observations at Dome Fuji

To investigate the spatial resolution limit at Dome Fuji on the Antarctic plateau, we measured the height of the surface boundary layer, the total seeing, and the free-atmosphere seeing using SODAR, Snodar, Tohoku DIMM and DF-DIMM. Meteorological observations wiht platinum thermometers, ultrasonic anemometers, and barometer complement the seeing data for better understanding the atmospheric conditions near the snow surface. This chapter describes the observations at Dome Fuji which were performed in the $47^{th}/48^{st}$, $51^{st}/52^{nd}$, and $53^{rd}/54^{th}$ Japanese Antarctic Research Expedition (JARE).

5.1 SODAR

SODAR gives the height of the surface boundary layer in the Antarctic summer. The observations were successful as planned from 2006 December 21 to 2007 January 7. The electric power of 115 VAC was supplied by the generators deployed at the Dome Fuji Station. As the built-in heater of #PA-1 SODAR produced some noise, we did not use it. No noise source was expected at Dome Fuji, we did not use the sound cone (Takato et al. 2008) [64].

5.2 Snodar

Snodar observations throughout year were planned for measuring the height of the surface boundary layer. Snodar observations were performed from 2011 January 25 to May 13. Since the snow brush to remove the snow from the parabola dish of Snodar did not work, snow accumulation gradually made the measurements difficult. For the reason, Snodar observations were terminated in early May earlier than the plan.

The second Snodar observations were planned for simultaneous observations with DF-DIMM in the $53^{rd}/54^{th}$ JARE in 2012/2013 campaign. Because the repair of PLATO-F took much time, we had no time to fix hardware problems and to remove snow accumulation on the Snodar dish. Therefore we had to give up Snodar observations in the 2012/2013 campaign.

5.3 Meteorological observations

The observations for the meteorological parameters give the data of the atmospheric conditions near the snow surface. We measured temperature, wind speed, wind direction, and atmospheric pressure. The first observations were performed in 2010/2011 campaign. C_T^2 data were obtained Snodar calibration. However the observations ended with the power failure of PLATO-F on 2011 July 4. To repair PLATO-F and to re-start meteorological observations were planned in 2012/2013 campaign, however, the 16-m meteorological mast was found to be fallen. Therefore we gave up the meteorological observations in 2012/2013 season.

5.3.1 Platinum thermometers

The temperature measurements with the platinum thermometers were performed only from 2011 January 21 to July 4. The platinum thermometers were equipped at 0.3 m, 3.1 m, 6.5 m, 9.1 m, 12 m, and 15.8 m on the 16-m meteorological mast. The platinum thermometers at 3.1 m and 6.5 m did not work probably due to a cable disconnection. We tried to fix the problem at the site, but we could not find the disconnection in the "spaghetti cables" inside the thermal comtrol box. The power failure of the PLATO-F was happened, and thus the observation ended on 2011 July 4.

5.3.2 Ultrasonic anemometers

Two ultrasonic anemometers were put on the 16-m meteorological mast at 6.1 m and 14.4 m. The observations were performed from 2011 January 21. Preparation for the ultrasonic anemometers were not enough. From the performance evaluation at Dome Fuji, the accuracy of the #81000 ultrasonics anemometers was found to be ± 0.2°C of the relative temperature, which corresponds to $C_n^2 \sim 1 \times 10^{-13}$ m$^{-2/3}$, with 50 Hz sampling, wind speed $\sim$ 5 m/s, temperature $\sim$ 250 K, and pressure $\sim$ 600 hPa. The noise level of C_n^2 value was the same or larger than the C_n^2 value near the snow surface. Therefore, we finally gave up to use #81000 ultrasonic anemometer for Snodar calibration.

Because #81000 ultrasonic anemometers had no modifications for the Antarctic cold environment, they did not work under ~ -50°C. Sometimes the temperature was gone down below -50°C even in the Antarctic summer. Therefore the wind speed and wind direction data were not reliable. We gave up to use the #81000 ultrasonic anemometer for sampling the wind speed and wind direction. The setting of the data logger was mistaken. Almost all data was lost due to the wrong setting. From these reasons, we concluded that the observations by #81000 ultrasonic anemometers would not be reliable.

5.3.3 Barometer

Atmospheric pressure measurements were performed from 2011 January 21 to June 27 with some data lacks. Although #PTB210 barometer worked well, by the wrong setting of the data logger #TR-V550, we could not measure the pressure under 596-hPa. #PTB210 barometer output pressure data by the voltage between 0 and 5-V. However, #TR-V550 data logger was set the voltage range between 0.8 and 5.1-V. This setting could not log under 0.8-V, thus we could not measure the pressure under 596-hPa (see Eq. (4.1)). Due to the power failure of the PLATO-F, the observation ended on July 4.

5.4 Tohoku DIMM

Tohoku DIMM observations were carried out for measuring the total seeing in the Antarctic summer in 2010/2011 campaign. Tohoku DIMM, attached on AIRT40, was set on the snow surface. The height of the aperture was $\sim$ 2 m above the snow surface. Tohoku DIMM observed Canopus (α Car, V = -0.7 mag, the second brightest star in the sky) to measure the total seeing. Canopus is circumpolar star at Dome Fuji, with a zenith angle varying from 25° to 50°.

At first, we were not able to detect Canopus. The strong scattering light caused by both sky and snow surface was an unexpected obstruct for the observation of Canopus at Dome Fuji in the Antarctic summer. Then we covered the optical tube of AIRT40 using an aluminum-foil (see Fig. 4.12). After this care, we could observe Canopus with reasonable contrast. The observations were performed from 2011 January 25 to January 28. Finally we could measure seeing in total of 14 463 times during the four days observations. The observations were successfully done as planned.

5.5 DF-DIMM

Full-year measurements for free-atmosphere seeing were planned in the 2012/2013 campaign. DF-DIMM was placed on the 9-m astronomical tower. The height of the entrance pupils was $\sim$ 11 m from the snow surface. We observed Canopus continuously for days with reasonable contrast against the daytime sky background in the Antarctic summer from 2013 January 4 to January 23. However, some power devices of DF-DIMM was found to be out of order after finishing the campaign. Although we tried to fix the problem via PLATO-F communication from Japan, we could not fix it. We could not observe the free-atmosphere seeing in the Antarctic autumn, winter, and spring. Simultaneous observations with Snodar were planned in 2012/2013 campaign. However, we have no time to fix some hardware problems of Snodar. Therefore we finally gave up simultaneous observations. In total, we obtained 3 814 seeing estimates; each was calculated with 450 images over a period of about five-minutes in the Antarctic summer season.

5.6 Range and period of the observations

Here we summarize the astronomical site testings at Dome Fuji. Figure 5.1 shows the diagram of the measurement range of the height for each instrument. SODAR and Snodar use acoustic sound to obtain the turbulence profile, and the temperature structure function constant C_T^2. Tohoku DIMM at 2 m and DF-DIMM at 11 m above the snow surface directly give the astronomical seeings at two height. The meteorological parameters, such as temperature and atmospheric pressure were also obtained. Platinum thermometers give the temperature variation between 0.3 m and 15.8 m above the snow surface. Barometer gives the atmospheric pressure at the surface level. Wind speed, wind direction, and C_T^2 value measurement are not available due to the failure.

We also summarize the observation period for each instrument in Fig. 5.2. Full-year and simultaneous observations with Snodar, platinum thermometers, ultrasonic anemometers, barometer were planned. However, due to the snow accumulation, power failure of

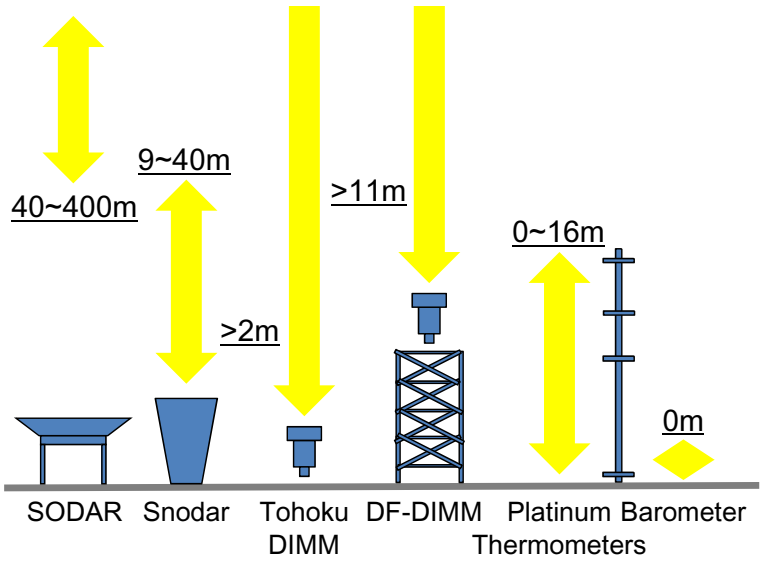

Figure 5.1: Measurement ranges of the height for each instrument.

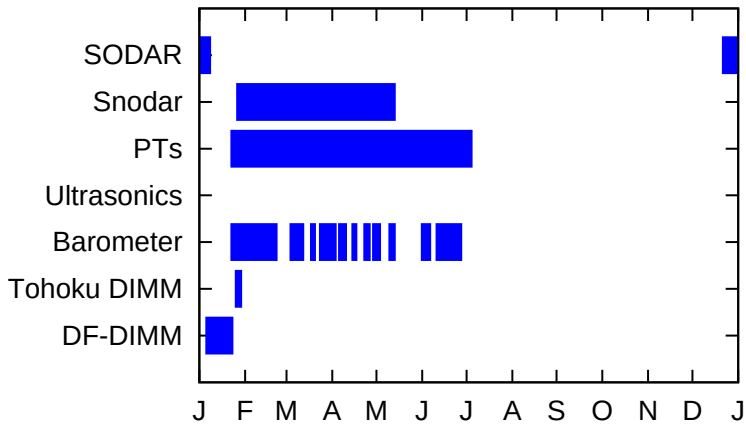

Figure 5.2: Observation periods for each instrument. SODAR observations were carried out during 2006/2007. Snodar, platinum thermometers (Pts), ultrasonic anemometers (Ultrasonics), barometer, and Tohoku DIMM were used in 2011. DF-DIMM was operated in 2013.

PLATO-F, lack of the proper preparation, and wrong setting of data logger, these observations could be partially succeeded. Full-year and simultaneous observations by Snodar and DF-DIMM were also planned, though the observations were not realized due to lack of the working time and hardware troubles. Therefore only limited observation data were obtained.

In this thesis we assume that the general characteristics of the atmosphere at Dome Fuji is not different from year to year. We will discuss the statistical results of the atmosphere, combining the data obtained with different instruments, in different years. For the height of the surface boundary layer, we can discuss the results in the period between the Antarctic summer and winter because we have Snodar data till May 13. For the total and free-atmosphere seeings, we discuss the results in the Antarctic summer.

Figures 5.3 $\sim$ 5.5 shows the sun altitude at Dome Fuji in 2011. From the end of October

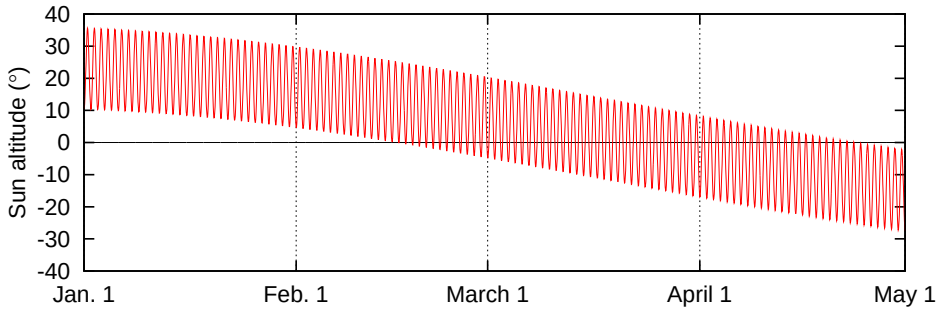

Figure 5.3: Solar altitude at Dome Fuji from January 1 to April 30, 2011. The sun does not set before February 15 (Antarctic summer), and it does not rise after April 25 (Antarctic winter).

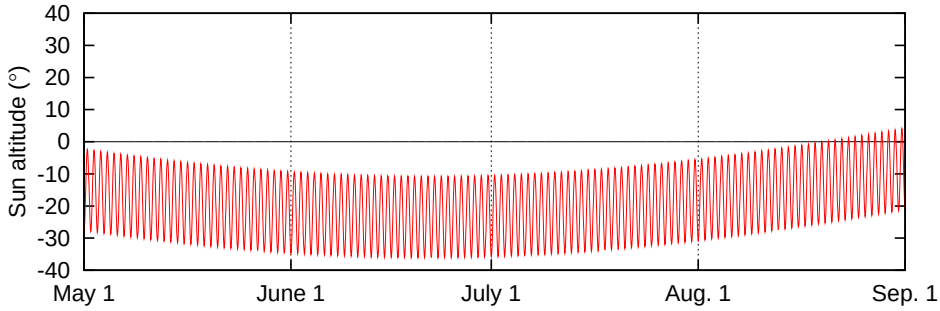

Figure 5.4: Same as Fig. 5.3, but for the period from May 1 to August 31, 2011. The sun does not rise before August 18 (Antarctic winter).

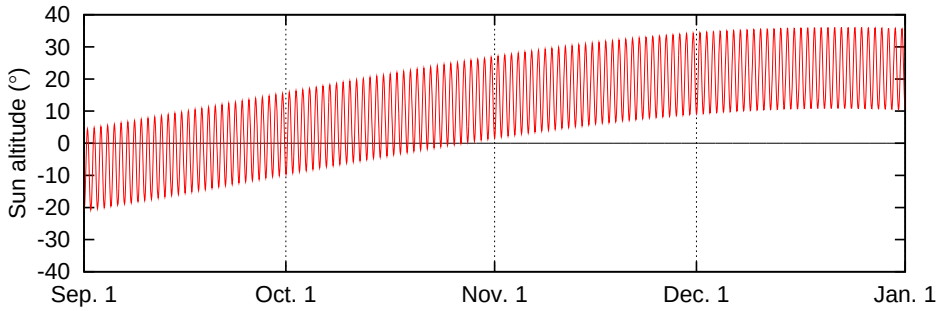

Figure 5.5: Same as Fig. 5.3, but for the period from September 1 to December 31, 2011. The sun does not set after October 28 (Antarctic summer).

to mid February the sun does not set because of the Dome Fuji latitude of 77°19′ South. We call this season as the polar day season, or the "Antarctic summer." On the contrary, the polar night seasons, or the "Antarctic winter" is defined the duration between no sunrise, from end of April to mid August, at Dome Fuji. Between the Antarctic summer and the Antarctic winter is called as the "Antarctic autumn" or "Antarctic spring." SODAR, Tohoku DIMM, and DF-DIMM were operated only in the Antarctic summer, while Snodar, platinum thermometers, and barometer observations were performed from the Antarctic summer to the Antarctic winter.

Chapter 6

Data reduction and error analyses

In this chapter, we analyze the observation data obtained with the instruments to discuss the astronomical seeing at Dome Fuji. Uncertainties and errors for each instrument were also estimated.

6.1 SODAR

Although no SODAR calibrations at Dome Fuji are available, SODAR was calibrated and evaluated by Fumihiro Uraguchi (Uraguchi et al. 2008) [75] at a mid-latitude site. After the site testings at Dome Fuji, #PA-1 SODAR was calibrated at Okayama Astronomical Observatory (OAO), Japan, and settled at Mauna Kea in Hawaii for regular operation. The calibrations were carried out with some micro-thermal sensors put on the 30 m meteorological mast at OAO between May 14 and 23, 2007. Thanks to the calibration, the conversion factor between the temperature structure constant C_T^2 and received signal P_r was found as

$$C_T^2 = 3.0^{+4.7}_{-1.8} \times 10^{-7}\ P_r. \tag{6.1}$$

However, the correlation coefficient is low(~ 0.24). As the large uncertainty is fatal, we gave up the calculation of C_T^2 from the SODAR data. In this thesis, we use SODAR data for the qualitative behavior of the atmospheric turbulence.

Unknown features were found in the observations at OAO and Subaru telescope. The turbulence profiles at OAO, Subaru telescope, and Dome Fuji show similar features at $\sim$ 600 m and $\sim$ 1 000 m. As it is unlikely that the three locations have common characteristics, the features at $\sim$ 600 m and $\sim$ 1 000 m could be caused by the nature inherent to the SODAR we used. To avoid the artificial enhancement, we used SODAR data only below 400 m height. Thus we will discuss the qualitative turbulence profiles between 40 m and 400 m with 20 m resolution for the SODAR data.

6.2 Snodar

Snodar emitted sound wave of 5 000 Hz and sampled the backscatter sound with 96 000 Hz. the received power was calculated by sum 586 samplings. The vertical resolution of Snodar was $\sim$0.9 m, assuming the constant temperature (-60°C) during the observation (Bonner et al. 2010a) [13]. We obtained the turbulence profiles with 30 minute integration to reduce the noise. Figure 6.1 shows two typical received signals.

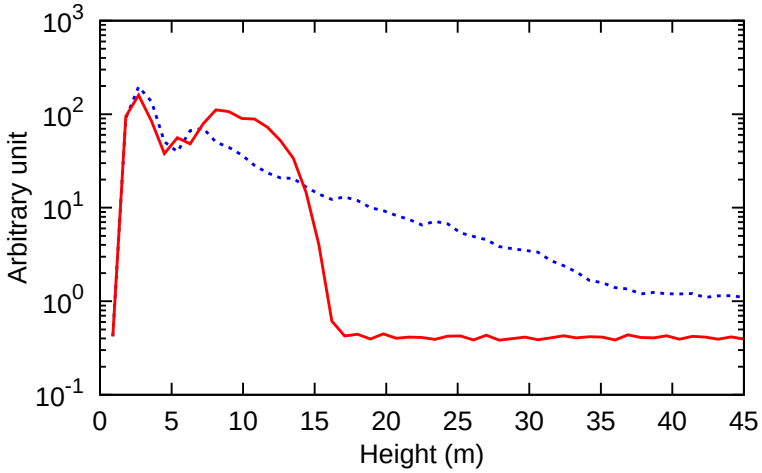

Figure 6.1: Two typical signals received by Snodar at Dome Fuji. Red and blue lines show the 30 minute integration at 12:30-13:00 (UTC+3) on Mar. 12, and at 9:00-9:30 (UTC+3) on Mar. 14, 2011, respectively. The signal strength is in arbitrary unit.

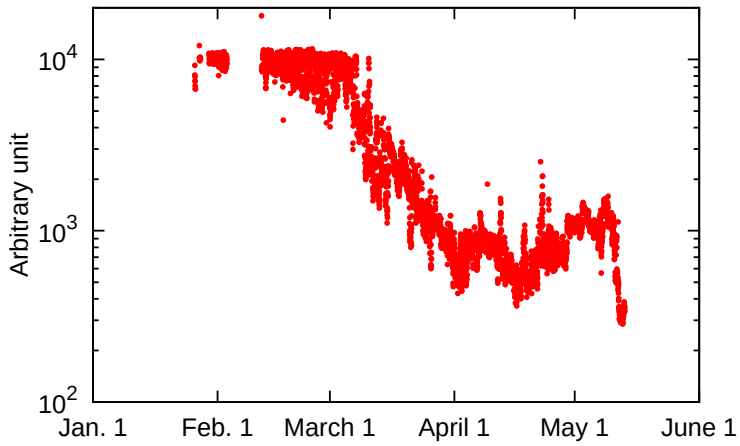

Figure 6.2: Scattered power from the calibration sphere. The signal strength is in arbitrary unit.

The received signals are attenuated with $\exp(-2\alpha h)/h^2$, where h is the height of the scattering volume and α is the atmospheric attenuation coefficient. The signal on March 14 (blue dash line) is fitted with the attenuation curve of h^{-2}, which suggests that the atmospheric turbulence near the snow surface is unchanged. On the other hand, the signal on March 12 (red solid line) dropped two orders of magnitude between 14 m and 17 m, which suggests the turbulence is strongly localized below $\sim$ 15 m. These differences would to be caused due to the weather condition. We discuss this in Chapter 8.1.

6.2.1 Calibration sphere

A calibration sphere is attached on Snodar antenna to measure the efficiency of the system. Figure 6.2 shows the scattered power from the calibration sphere. The scattered power decreased drastically in March, about one tenth of the original value after April. The decrease is considered to be caused by the snow accumulation. Same phenomena were

observed at Dome A (Bonner et al. 2010a) [13]. The decrease of the received signal reduces the signal to noise ratio of the measurement. However, Snodar could observe turbulence variations to some extent even in April and May. Thus we conclude that Snodar successfully measured the turbulence profile from February to May.

6.2.2 Turbulence strength

From the received power P_r, the temperature structure constant C_T^2 can be calculated as a function h using Eqs. (2.97) and (2.98),

$$C_T^2(h) = \frac{h^2 e^{2\alpha h} T^2(h)}{0.0039 \eta P_t k^{1/3}} \{P_r(h) - P_n\} \ , \tag{6.2}$$

where P_n is received noise. P_n should be evaluated in each observation because it strongly depends both on the electric power stability and on ambient conditions. Thus we assume the received noise P_n as the averaged received signals at 40 m or higher above the snow surface.

If we know the atmospheric attenuation α, temperature $T(h)$, coefficiency η, transmitted power P_t, and wave number of the transmitted sound k, we can calculate the temperature structure constant C_T^2. α can obtained with ISO 9613-1 standard (Bonner et al. 2009) [15]. k is 1/5 000. Relative ηP_t is also known from the received power of the calibration sphere. However, the absolute value of ηP_t should be known for correlate calibration. ηP_t could be calibrated with a micro-thermal sensor or an ultrasonic anemometer attached on the meteorological mast. We had planed to calibrate it at Dome Fuji with two ultrasonic anemometers attached at the 16 m meteorological tower. However, the ultrasonic anemometers were found to have no reliability (see Chap. 5.3.2). Therefore we do not discuss the absolute value of the temperature structure constant C_T^2 from the Snodar observations. Instead, we only discuss the relative turbulence strength, which is proportional to C_T^2, in this thesis.

6.2.3 Height of the surface boundary layer

We define the height of the surface boundary layer as the height where the turbulence strength reduces to 1% of its original value (Bonner et al. 2010b) [14]. The minimum sampling height depends on the transducer ringing, antenna reverberation, echoes from fixed objects, and ground clutter. In our case, the minimum sampling height is $\sim$ 9 m. The maximum sampling height of our Snodar is 40 m because we defined the noise with the value at 40 m or higher.

6.2.4 Error analysis for Snodar data

For Snodar analysis, we assume the constant temperature (-60°C) during observations. The assumption introduces less than $\pm$ 5% systematic error in the height and spatial resolution, provided that the actual air temperature is between -80°C and -30°C near the snow surface. We assume the received signal at 40 m or higher above the snow surface as the noise, so that we can not detect the height of the surface boundary layer if it is higher than 40 m. On the other hand, the minimum sampling height of $\sim$9 m would overestimate the height of the surface boundary layer height if it is lower than 9 m.

The statistical error of the height is estimated $\sqrt{1/N}$ percent of the height, where N is the number of measurements. In our case, the height was calculated with the turbulence profiles in each five seconds in 30 minute interval. ($N = 360$). Therefore the statistical error was $\sim 5\%$.

6.3 Platinum thermometers and barometer

Platinum thermometers were calibrated with each other. The dispersion of the thermometers, which would caused by the dispersion of resistance, was $\sim$0.4°C in peak-to-valley. The accuracy of the barometer #PTB210 was relied on the specification sheet ($\pm$ 0.1 hPa). Temperature and atmospheric pressure were logged every two minutes. #TR-V550 data logger saved the data in the binary files. After transfered the files to Japan, we converted to ascii files used the Keyence software on Windows or third party software on Linux. We used the ascii files directly for the temperature analysis.

6.4 Tohoku DIMM

UT-DIMM software was used with some modifications for processing Tohoku DIMM data. The longitudinal seeing ϵ_l and the transverse seeing ϵ_t were calculated using Eqs. (13), (14), and (23) of Sarazin & Roddier (1990) [56] with 30 images taken in each three seconds. The seeing values were then corrected for zenith angle. The effective wavelength of Tohoku DIMM is 620 nm. Since the seeing depends on 1/5 power of the wavelength, we convert the results of Tohoku DIMM to the values at 500 nm. Hereafter, all seeing values for Tohoku DIMM will be discussed at 500 nm.

Tohoku DIMM with two-pair two-aperture DIMM gives four seeing values (ϵ_{hl}, ϵ_{ht}, ϵ_{vl}, and ϵ_{vt}) simultaneously. The values should be the same because the seeing is a scalar quantity. Considering the statistical error, we discarded $\sim$ 1 % of the observations that fell outside the range $0.50 < \epsilon_{hl}/\epsilon_{ht} < 2.0$ and $0.50 < \epsilon_{vl}/\epsilon_{vt} < 2.0$. We averaged four seeings to obtain the seeing value. In total, 14 215 measurements met the criteria. DIMM observation generally has many errors and uncertainties, which are discussed below.

6.4.1 Statistical error

The statistical error of the variance of star position $\sigma_\star^2$ for two-pair two-aperture DIMM is written as $d\sigma_\star^2/\sigma_\star^2 = \sqrt{2/(2N-1)}$, where N is the number of frames used for the variance calculation and the subscript $\star$ represents either longitudinal or transverse. Here we modified Eq. (28) of Sarazin & Roddier (1990) [56] for two-pair two-aperture DIMM. Since for our observations, 30 frames were used to calculate the seeing, the statistical error on the variance was $\sim$ 18%, which corresponds to the seeing error $d\epsilon_\star/\epsilon_\star \propto (d\sigma_\star^2/\sigma_\star^2)^{3/5} \sim$ 11%.

6.4.2 Pixel scale uncertainty

The pixel scale of Tohoku DIMM was calibrated using the diurnal motion of Canopus. The measurement was carried out before the seeing observations. This gave the pixel scales of $0.390'' \pm 0.003''$ per pixel for abscissa and $0.455'' \pm 0.003''$ per pixel for ordinate. The uncertainty contributes $\sim$ 0.7% error in the seeing. The temperature dependence of

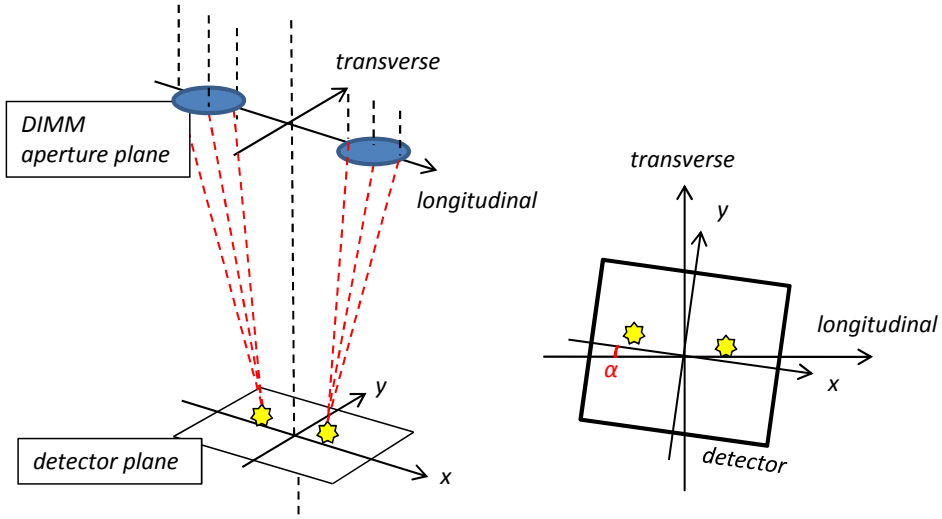

Figure 6.3: Schematics showing the ray trace of a general DIMM. Two subapertures with wedge prisms make two images of the same star on a CCD detector. Copyright: Okita et al. (2013a) [50]

the focal length also affects the pixel scale. We ignore the effect in the present analysis. Therefore the seeing value would have some additional errors due to the focus difference.

6.4.3 Effect of the instrument rotation

To simplify the analysis of DIMM data, the $(x,\ y)$ coordinates of the CCD detector is usually aligned with the longitudinal and transverse DIMM coordinates $(l,\ t)$ defined by Sarazin & Roddier (1990) [56]. If, however, the coordinate frames are misaligned by the angle α and it is ignored in the analysis, the error should be added. Figure 6.3 is the schematics of the coordinates.

Here we write σ_x^2 and σ_y^2 as the variance of the differential motion along the x and y axes, and σ_{xy} as the covariance of x and y. The longitudinal variances of σ_l^2 and transverse variance of σ_t^2 are then

$$\sigma_l^2 = \cos^2(\alpha)\sigma_x^2 + \sin^2(\alpha)\sigma_y^2 - \sin(2\alpha)\sigma_{xy} \quad (6.3)$$

$$\sigma_t^2 = \sin^2(\alpha)\sigma_x^2 + \cos^2(\alpha)\sigma_y^2 + \sin(2\alpha)\sigma_{xy}\ . \quad (6.4)$$

For the precise measurements of the seeing with DIMM, we need in general to transform the $(x,\ y)$ coordinates to $(l,\ t)$ before using the normal DIMM equations. Although Tohoku DIMM would have large α (~ 0.1 radian), we do not correct the instrument rotation effect because we have no σ_{xy} data. Therefore the seeing values obtained with Tohoku DIMM would have large systematic errors due to the instrument rotation ($\sim 7\%$).

6.4.4 Finite exposure effect

Theoretically, DIMM seeing is defined in an infinitely short exposure. Martin (1987) [45] and Soules et al. (1996) [60] discussed the effect of using a finite exposure time. In the case of τ=0.001 s and $w \leq$30 ms^{-1} from Eq. (18) of Soules et al. (1996) [60], our seeing values are underestimated by less than 3 %. Since we have no data of the wind speed in the upper atmosphere, we ignore this effect in the present thesis.

6.4.5 Miscellaneous effects

Readout noise and background noise of the detector also add small biases to the seeing value (Tokovinin 2002) [69]. The local turbulence inside the telescope worsens the observed seeing. Therefore, our results are considered to be an upper limit of the actual seeing. We ignore those effects in the present thesis because of no information of those.

6.5 DF-DIMM

On-site data processing software for DF-DIMM was developed, based on Nightview[1] (Hroch), Sextractor (Bertin & Arnouts 1996) [12], and CFITSIO (Pence 1999) [53]. Seeing values were calculated using Eqs. (13), (14), and (23) of Sarazin & Roddier (1990) [56] with 450 frames taken in about five-minute interval. The seeing estimates were then corrected for zenith angle. Because the observed wavelength of DF-DIMM was 472 nm, we converted the seeing values of DF-DIMM to the values at the wavelength of 500 nm. Hereafter all seeing values for DF-DIMM were discussed with at the wavelength 500 nm.

The longitudinal and transverse seeings should be the same. We discarded ~ 1 % of the observations that fell outside the range $0.50 < \epsilon_l/\epsilon_t < 2.0$. We then averaged ϵ_l and ϵ_t to obtain the seeing value.

6.5.1 Errors and uncertainties

The seeing values measured by DF-DIMM, ϵ_l and ϵ_t, also have errors and uncertainties. The statistical error of the variance of a star position $\sigma_\star^2$ is $d\sigma_\star^2/\sigma_\star^2 = \sqrt{2/(N-1)}$, as shown in Chap. 6.4.1. For DF-DIMM, 450 frames were used in calculating each seeing estimate. As a result, the statistical error on the variance is $\sim 6.7\%$, which corresponds to the seeing error of $d\epsilon_\star/\epsilon_\star \propto (d\sigma_\star^2/\sigma_\star^2)^{3/5} \sim 4\%$.

The pixel scale of DF-DIMM was measured using the diurnal motion of Canopus at Dome Fuji on 2013 January 1. This gives a scale of $0.775'' \pm 0.005''$ per pixel. The uncertainty contributes $\sim 0.8\%$ error in the seeing. The temperature dependence of the focal length also affects the pixel scale; however this effect is negligibly small for our telescope, which moves the primary mirror for focusing. In fact, optical simulations demonstrate that the focal length of DF-DIMM changes less than 0.2% between 20°C and −80°C.

Considering the effect of the instrument rotation effect, it was $\sim 4\%$. Due to the finite exposure effect, the seeing values would be underestimated. Since we have no data of the wind speed in the upper atmosphere, we ignore this effect in the present thesis. Readout noise, background noise make small biases of the seeing value. We discussed those in Chap. 4.8.6 and it was $\sim 0.05''$. It should be subtracted. The local turbulence inside the telescope also add bias to the seeing value. However, since we can not estimate from our observations, we ignore the effect of the local turbulence inside the telescope in the present thesis.

[1] http://www.physics.muni.cz/mb/nightview/nightview.html

Chapter 7

Results

In this Chapter we show the results of the observations at Dome Fuji obtained with SODAR, Snodar, platinum thermometers, barometer, Tohoku DIMM, and DF-DIMM.

7.1 SODAR

SODAR observations were carried out successfully from 2006 December 21 to 2007 January 7. The minimum sampling height of SODAR was set at 40 m. Because of the artificial features at $\sim$ 600 m and at $\sim$ 1 000 m, which were discussed in Chap. 6.1, for the present study we use only the data between 40 m and 400 m with vertical resolution 20 m.

A characteristic turbulence profile is shown in Fig. 7.1. Due to the lack of SODAR calibrations at Dome Fuji and less reliable calibrations at Okayama Astronomical Observatory (OAO), we plot the SODAR results in arbitrary unit. The turbulence profiles for all duration observed with SODAR are shown in Appendix A.

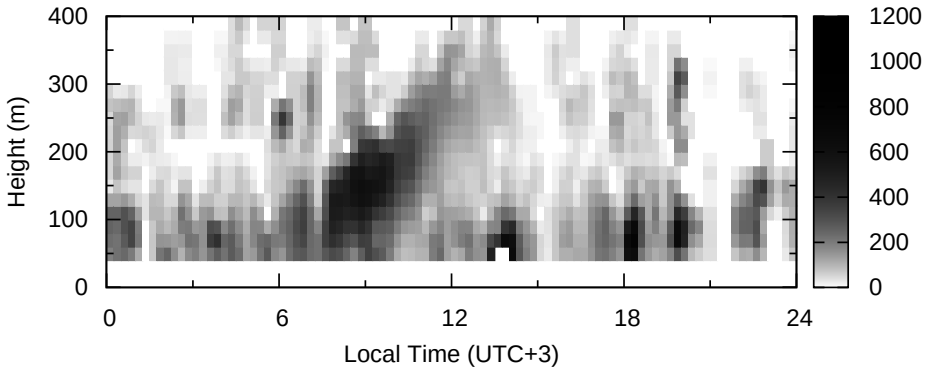

Figure 7.1: Time series of the turbulence strength obtained with SODAR from 00:00 to 24:00 (UTC+3) December 31, 2006. The density bar represents the turbulence strength in arbitrary unit. Under 40 m above the snow surface, SODAR had no sensibility.

From the observations on December 31, strong turbulence rose up from $\sim$ 7 h and reached $\sim$ 350 m height, and it dissipated drastically after $\sim$ 13 h. This daytime turbulence is considered to be the atmospheric convection due to the solar insolation. Since the solar heating is strongest around midnoon in a day, the solar heating makes the atmospheric convection. Turbulence at the local daytime was stronger than at the local nighttime. These phenomena appeared also in other days.

7.2 Snodar

Snodar gives the turbulence profiles from January 26 to May 13, 2011. The characteristic turbulence profiles were shown in Figs. 7.2 $\sim$ 7.4, which were observed on February 23, March 12, and March 14, 2011. On February 23, we found a strong turbulence which rose up from $\sim$ 5 h and dissipated till noon. This would be the atmospheric convection caused by the solar insolation. On the contrary, no atmospheric convection, stable and low height of the surface boundary layer was observed on March 12. There was no clear boundary on March 14. Since the ultrasonic anemometers did not work, Snodar had no calibration. We discuss the Snodar results in arbitrary unit. The turbulence profiles for all duration observed with Snodar are shown in Appendix B.

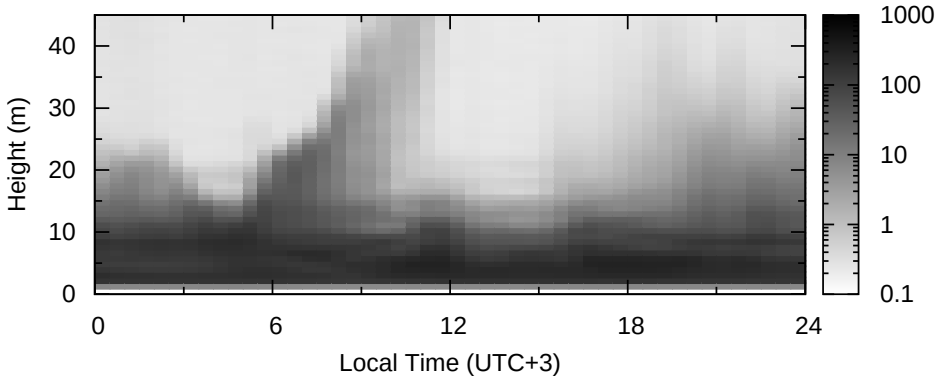

Figure 7.2: Time series of the characteristic turbulence strength obtained with Snodar from February 23 00:00 to 24:00 (UTC+3), 2011. We averaged with 30 minutes observation of the turbulence profiles. The density bar represents the turbulence strength in arbitrary unit. The vertical resolution is 0.9 m.

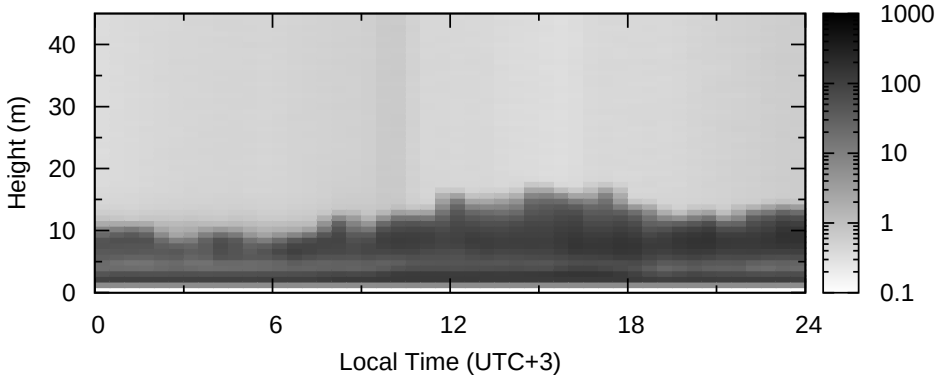

Figure 7.3: Same as Fig. 7.2, but for the period from March 12 00:00 to 24:00 (UTC+3), 2011.

We also show the seasonal characteristic turbulence profiles in Figs. 7.5 $\sim$ 7.8, which were observed on February 2, 12, March 2, and May 3, 2011. In the Antarctic summer, the strong turbulence rose up at the local morning on January 30, 31, and February 12 (Fig. 7.6). On the contrary, on the other days, the turbulence strength and height were unstable (Fig. 7.5). In the Antarctic autumn, as shown in Fig. 7.7, the atmosphere was relatively stabler than that in the Antarctic summer. The turbulence which would be caused by the

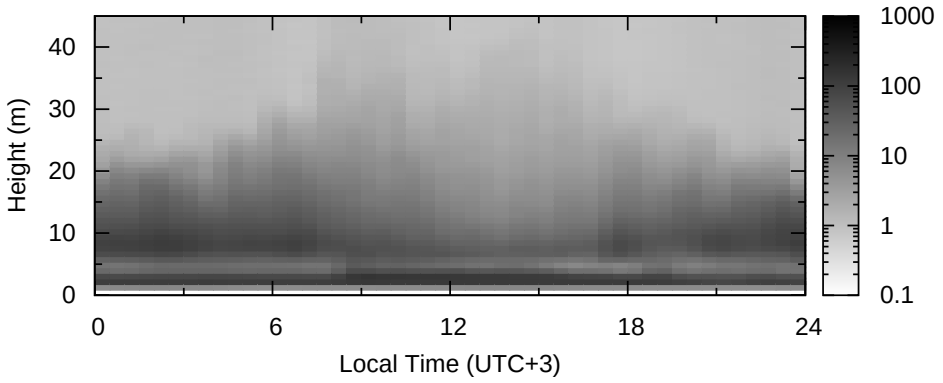

Figure 7.4: Same as Fig. 7.2, but for the period from March 14 00:00 to 24:00 (UTC+3), 2011.

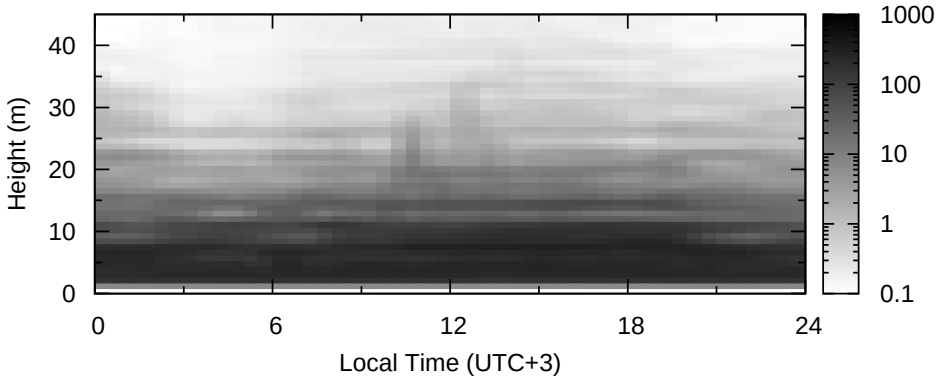

Figure 7.5: Time series of the characteristic turbulence strength obtained with Snodar in the Antarctic summer from February 2 00:00 to 24:00 (UTC+3), 2011. We averaged with 30 minutes observation of the turbulence profiles. The density bar represents the turbulence strength in arbitrary unit. The vertical resolution is 0.9 m.

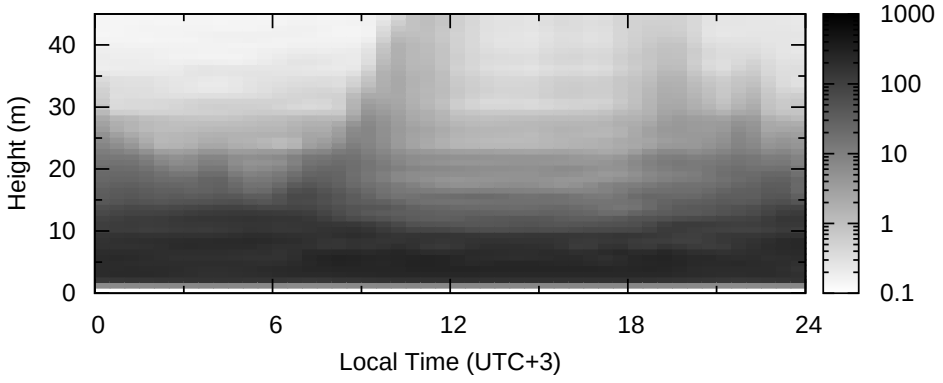

Figure 7.6: Same as Fig. 7.5, but for the Antarctic summer from February 12 00:00 to 24:00 (UTC+3), 2011.

atmospheric convection was shown at the local daytime. In the Antarctic winter, there was no diurnal variation (Fig. 7.8). The turbulence height was low and stable.

The height of the surface boundary layer, which was defined in Chap. 6.2.3, was calculated from the data averaged with 30 minutes observation of the turbulence profiles.

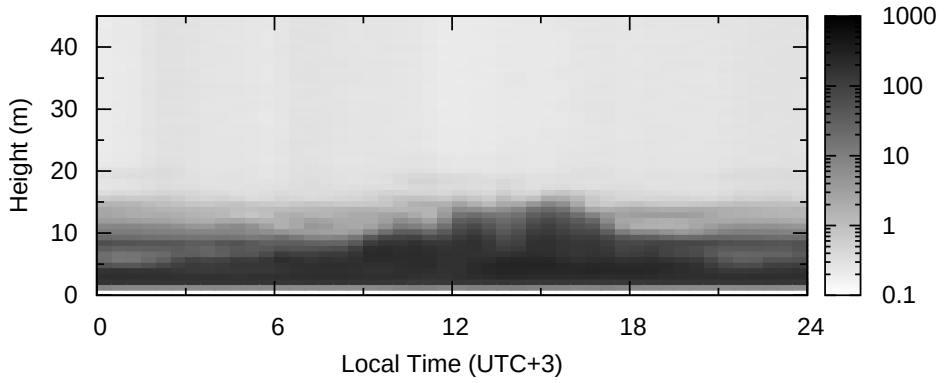

Figure 7.7: Same as Fig. 7.5, but for the Antarctic autumn from March 2 00:00 to 24:00 (UTC+3), 2011.

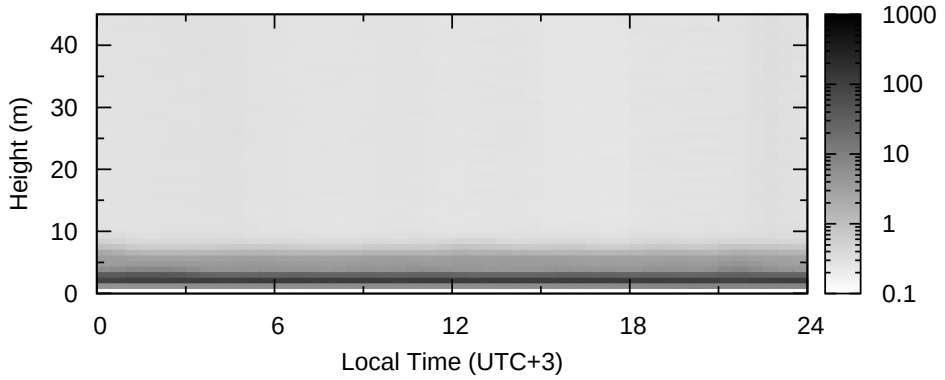

Figure 7.8: Same as Fig. 7.5, but for the Antarctic winter from May 3 00:00 to 24:00 (UTC+3), 2011.

Monthly time series of the height is plotted in Fig. 7.9. From the figure, large variations for each day are discernible in February. However no significant diurnal variation or periodicity are shown in other months. Stable and low height of the surface boundary layer continued for several days in the Antarctic winter.

The histogram and cumulative histogram of the height are shown in Fig. 7.10. Comparing with the cumulative histogram at Dome A (Fig. 6 in Bonner et al. 2010b) [14], the dispersion of the height at Dome Fuji was larger than that at Dome A, which could be due to the weather condition. Table 7.1 shows the monthly height of the surface boundary layer. The mean and median height of the surface boundary layer for entire period were 21.3 m and 17.1 m. The standard deviation (σ) and median absolute deviation (MAD [1]) are 9.0 m and 6.7 m, respectively. The statistical and systematic errors of the height are ±5% and ±5% of the value (discussed in Chap. 6.2.4). We suggest that the large dispersion is due to the weather condition, which will be discussed in Chap. 8.1.

[1]MAD is defined as the median of the absolute deviations from the data's median: 1.4826×median(abs(x−median(x))), where 1.4826 is the scale factor. For normal distribution, MAD equals to one sigma (standard deviation).

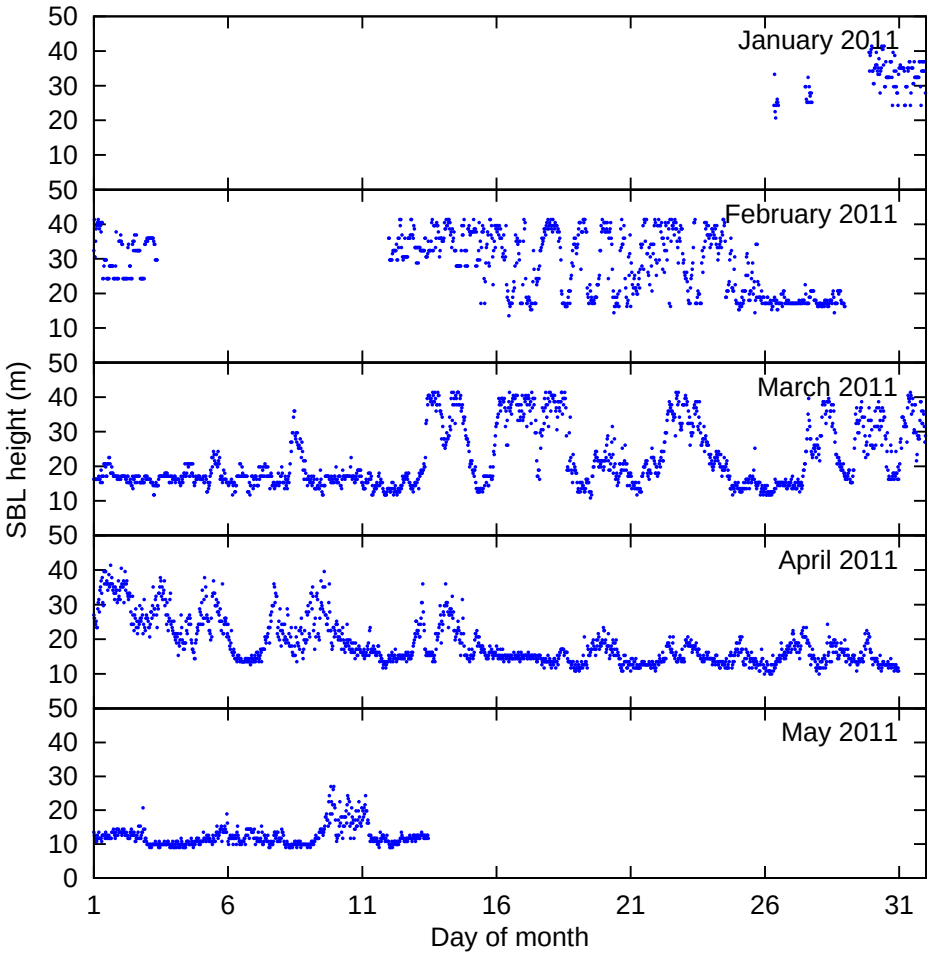

Figure 7.9: Monthly time series of the height of the surface boundary layer observed with Snodar. Each height was calculated from each 30 minute integration.

Table 7.1: The height of the surface boundary layer obtained with Snodar in 2011. (±5% statistical error, ±5% systematic error)

Month	Data availability	Number of 30 minute averages	Mean	σ	Median	MAD
January	8.33 %	124	32.4 m	4.7 m	33.3 m	5.3 m
February	69.3 %	931	28.5 m	8.6 m	29.7 m	12 m
March	100 %	1488	22.1 m	8.7 m	18.0 m	5.3 m
April	100 %	1440	18.6 m	6.4 m	16.2 m	4.0 m
May	40.3 %	599	12.3 m	3.0 m	11.7 m	2.7 m
Total	63.2 %	4582	21.3 m	9.0 m	17.1 m	6.7 m

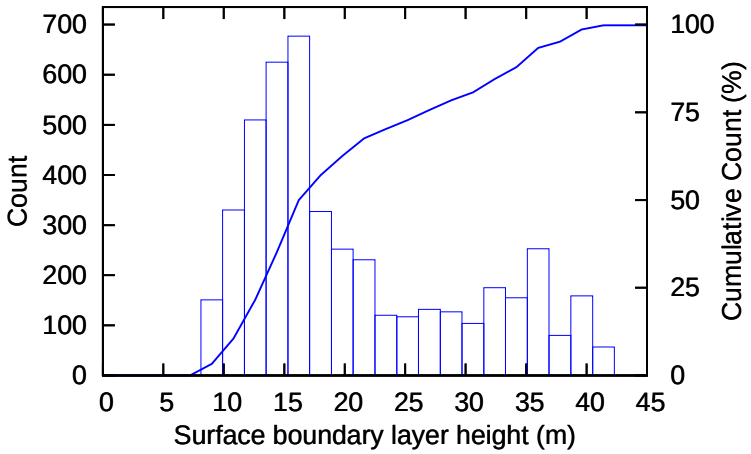

Figure 7.10: Histogram and cumulative histogram of the surface boundary layer height measured with Snodar from January 25 to May 13, 2011.

7.3 Platinum thermometers

Temperature measurements with the platinum thermometers, which were equipped on the 16 m weather mast, were carried out from January 21 to July 4, 2011. The time series of the temperatures at 0.3 m, 9.5 m, 12 m, and 15.8 m are shown in Figs. 7.11 $\sim$ 7.14 for each month. The temperature at 0.3 m above the snow surface had a large diurnal variation by the end of March. The variation is considered to be caused by the solar heating. It disappeared since April, which would be the result of the sun altitude being low. After April the temperature changed in the internal of several days. The time series of the

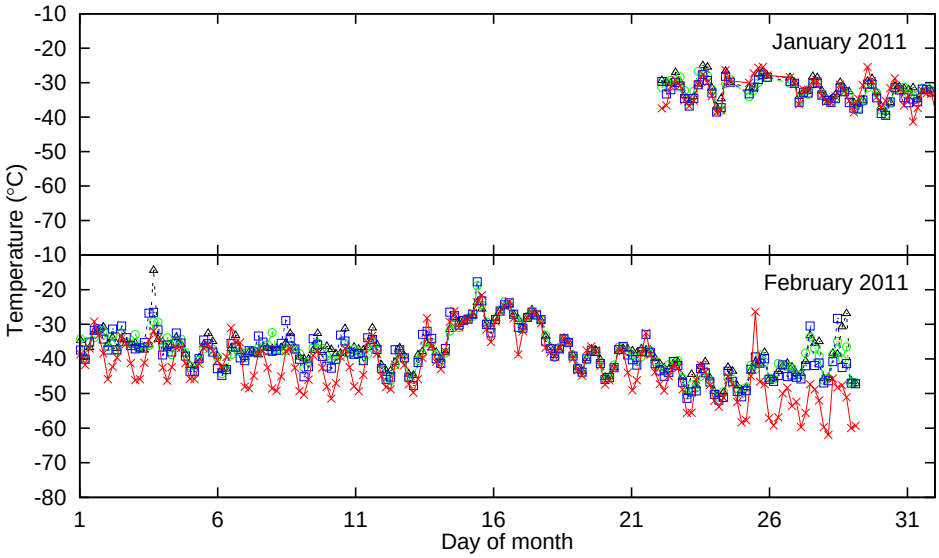

Figure 7.11: Time series of the temperatures (°C) at 0.3 m (red cross), 9.5 m (blue box) 12 m (green circle), and 15.8 m (black triangle) respectively, for the period from January to February, 2011. Temperatures were logged in each two minutes, though we plot each four hours for clarity.

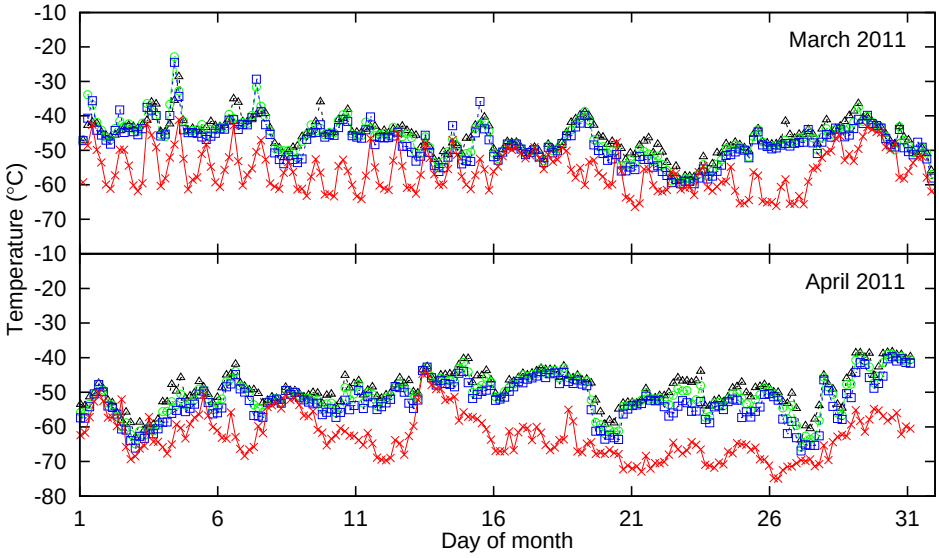

Figure 7.12: Same as Fig. 7.11, but for the period from March to April, 2011.

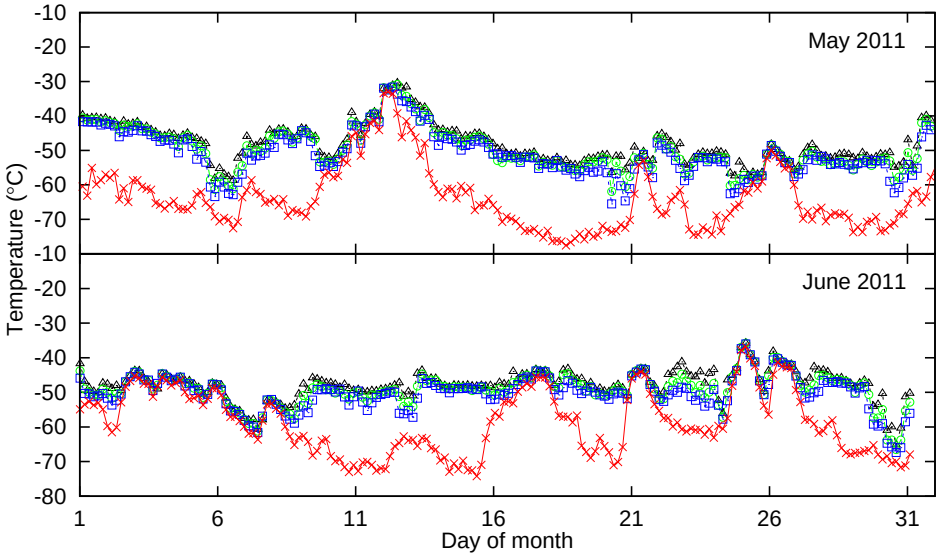

Figure 7.13: Same as Fig. 7.11, but for the period from May to June, 2011.

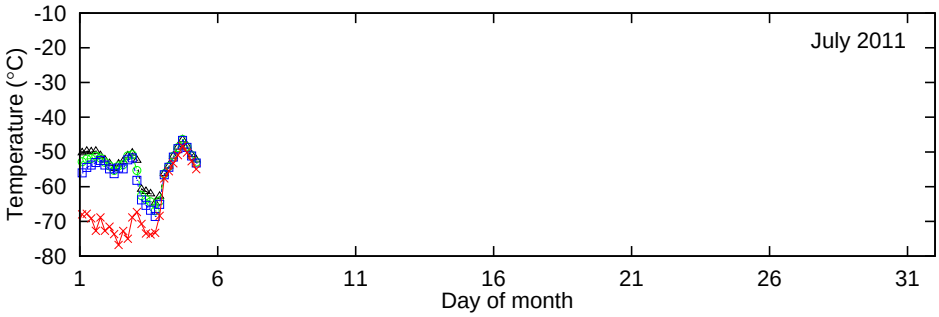

Figure 7.14: Same as Fig. 7.11, but in July, 2011.

temperatures with two minute time resolution for all duration are plotted in Appendix C.1.

Monthly data availability and temperature statistics (mean, minimum, and maximum) for the measurements at 0.3 m, 9.5 m, 12 m, and 15.8 m are given in Table 7.2. The mean temperatures as a function of the height in each month are shown in Fig. 7.15. Mean temperatures (°C) are plotted as a function of the height. Temperatures between 0.3 m and 15.8 m show no large difference and no temperature gradient in January and February. On the other hand, the temperature at 0.3 m was lower than the other heights since March. The temperatures at 9.5 m, 12 m, and 15.8 m show no difference since March. The fact means that a strong temperature gradient arises only near the snow surface in the Antarctic autumn and winter.

Figure 7.16 shows the mean temperatures as a function of month for each height. The temperatures in January and February are relatively higher than those in the other months. The high temperature is considered to be caused by the solar heating in the season. After March the temperature goes down because of weak solar heating in the Antarctic autumn and no solar heating in the Antarctic winter. In the Antarctic winter, the temperature at 0.3 m is clearly lower than the other heights, and very similar to the mean surface temperature during 1995 to 1997 observations. The temperature will drop

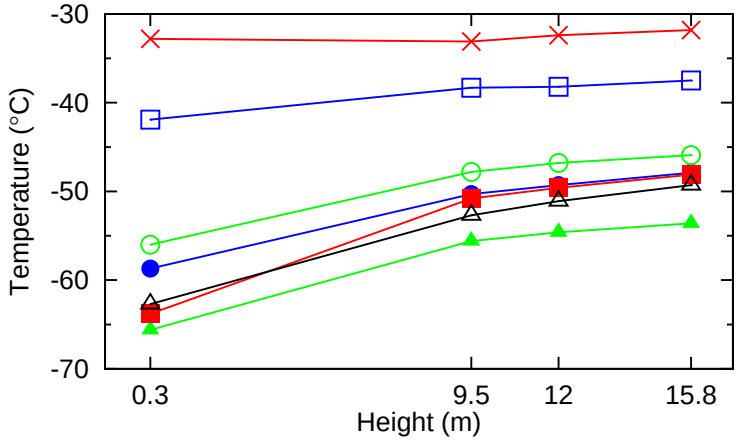

Figure 7.15: Mean temperatures (°C) as a function of the height in January (red cross), February (blue open square), March (green open circle), April (black open triangle), May (red filled square), June (blue filled circle), and July (green filled triangle).

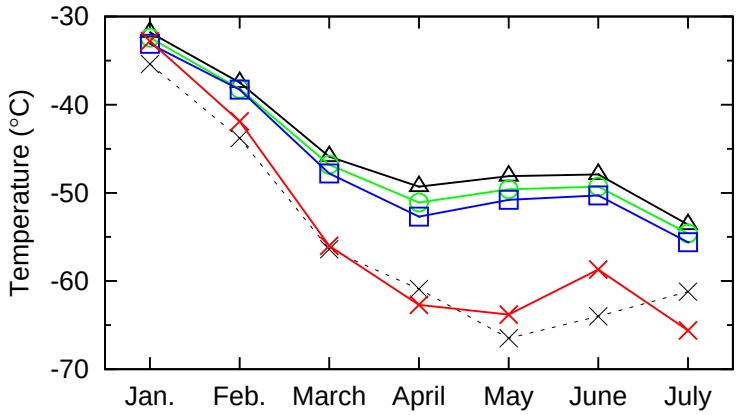

Figure 7.16: Mean temperatures (°C) as a function of month at each height in 2011. Red cross, blue square, green circle, and black triangle mean the mean temperatures at 0.3 m, 9.5 m, 12 m, and 15.8 m above the snow surface, respectively. Dashed cross line is the mean surface temperatures during 1995 to 1997 observations (Yamanouchi et al. 2003) [79].

drastically only in the first ten meters in the Antarctic winter.

The seasonal characteristic temperatures are shown in Figs. 7.17 $\sim$ 7.20, which were observed on February 7, 12, March 2, and May 3, 2011. In the Antarctic summer, diurnal temperature variations for each layer were shown (see Fig. 7.18). These variations would be caused by the solar insolation. Almost half days we observed large temperature difference between at 0.3 m and at the other heights at the local nighttime (January 22, 31, February 1 $\sim$ 4, 6 $\sim$ 11: see Fig. 7.17). In the Antarctic autumn, as shown in Fig. 7.19, the temperature variation at 0.3 m was larger than at other heights. The temperatures at 0.3 m, 9.5 m, and 12 m rose at the local daytime due to the solar insolation. On the other hand, the temperature at 15.8 m hardly changed whole day. In the Antarctic winter, there were no diurnal temperature variations (Fig. 7.20). The temperature at 0.3 m was $\sim$ 20°C colder than those at the other heights.

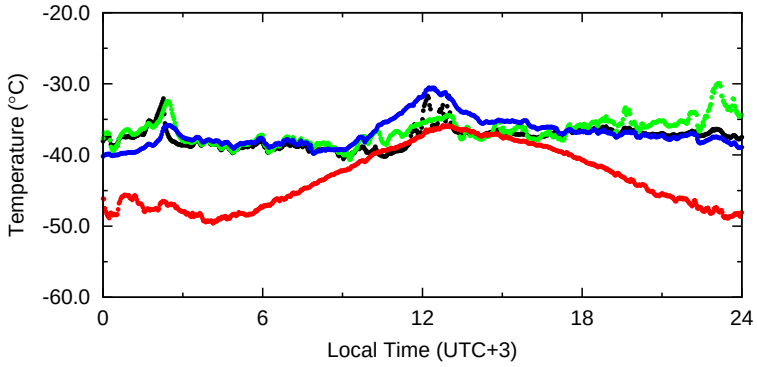

Figure 7.17: Time series of the temperatures (°C) at 0.3 m (red), 9.5 m (blue), 12 m (green), and 15.8 m (black), respectively, with two minute time resolution, in the Antarctic summer from February 7 00:00 to 24:00 (UTC+3), 2011.

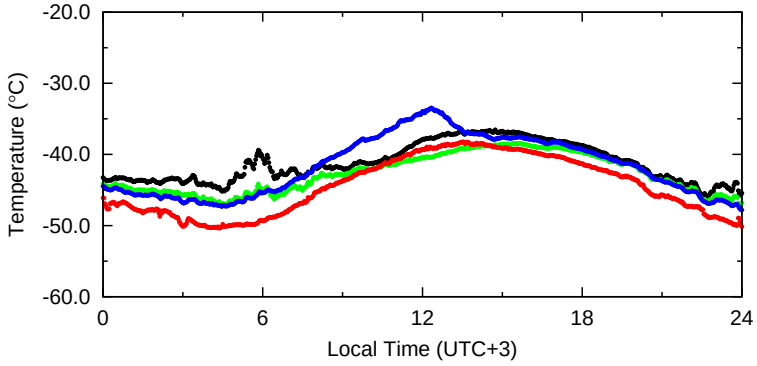

Figure 7.18: Same as Fig. 7.17, but for the Antarctic summer from February 12 00:00 to 24:00 (UTC+3), 2011.

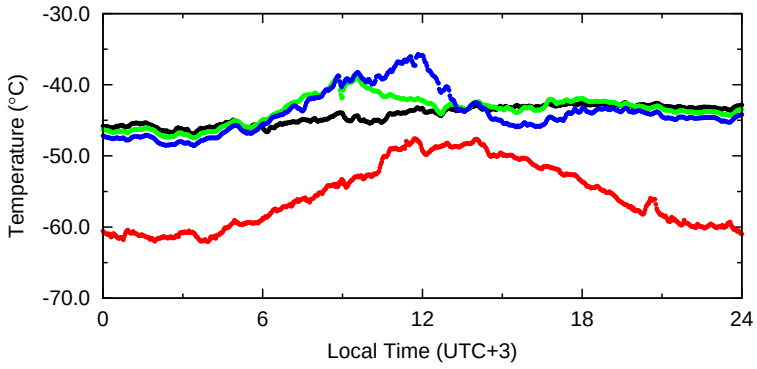

Figure 7.19: Same as Fig. 7.17, but for the Antarctic autumn from March 2 00:00 to 24:00 (UTC+3), 2011.

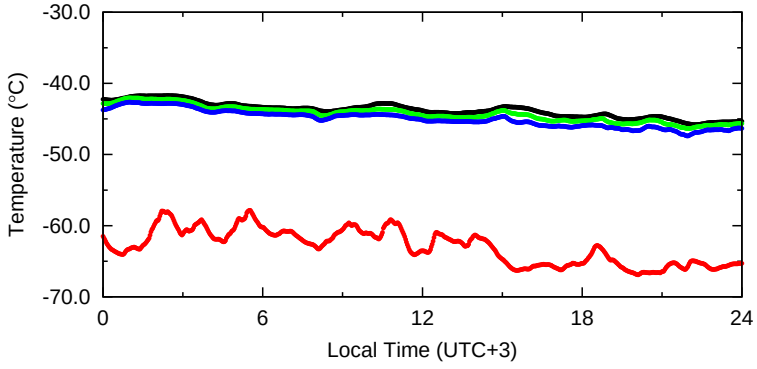

Figure 7.20: Same as Fig. 7.17, but in for the Antarctic winter from May 3 00:00 to 24:00 (UTC+3), 2011.

Table 7.2: Mean, maximum, and minimum temperatures at 0.3 m, 9.5 m, 12 m, and 15.8 m above the snow surface for each month in 2011.

Month	Data	0.3 m			9.5 m			12 m			15.8 m		
	availability	Mean	Max.	Min.	Mean	Max.	Min.	Mean	Max.	Min.	Mean	Max.	Min.
January	29 %	-32.8	-22.2	-43.9	-33.1	-23.2	-40.6	-32.4	-26.3	-40.2	-31.8	-24.1	-39.2
February	100 %	-41.9	-16.2	-62.2	-38.3	-13.1	-53.0	-38.2	-16.0	-52.3	-37.5	-13.2	-51.3
March	100 %	-56.0	-36.5	-67.4	-47.8	-21.6	-61.1	-46.8	-20.8	-60.3	-45.9	-19.1	-59.4
April	100 %	-62.7	-42.6	-76.2	-52.7	-39.3	-67.4	-51.1	-38.7	-66.4	-49.3	-37.6	-65.0
May	100 %	-63.8	-31.5	-78.8	-50.8	-30.6	-66.9	-49.6	-29.9	-64.2	-48.1	-29.3	-60.9
June	100 %	-58.7	-36.7	-74.6	-50.3	-36.0	-67.6	-49.3	-35.8	-66.7	-47.9	-35.8	-65.3
July	14 %	-65.6	-47.2	-76.8	-55.6	-45.9	-69.7	-54.6	-45.7	-68.3	-53.6	-45.6	-65.6
Total	77 %	-55.8	-16.2	-78.8	-47.5	-13.1	-69.7	-46.5	-16.0	-68.3	-45.3	-13.2	-65.6

Now we study the temperature gradient between the height of h_A and h_B, which is defined as

$$\partial T/\partial h \mid_{h_A - h_B} \equiv (T_{h_A} - T_{h_B}) \,/\, (h_A - h_B) \ , \tag{7.1}$$

where $h_A > h_B$. If the temperature gradient is positive, the atmosphere between h_A and h_B is stable. On the other hand, negative temperature gradient means unstable atmosphere in convection. Figures 7.21 $\sim$ 7.24 show the time series of the temperature gradients from 0.3 m to 9.5 m and from 9.5 to 15.8 m for each month. The diurnal variation of the temperature gradient between 0.3 m and 9.5 m was observed by mid-March. The variation would have been caused by the solar heating near the snow surface. After mid-March, the

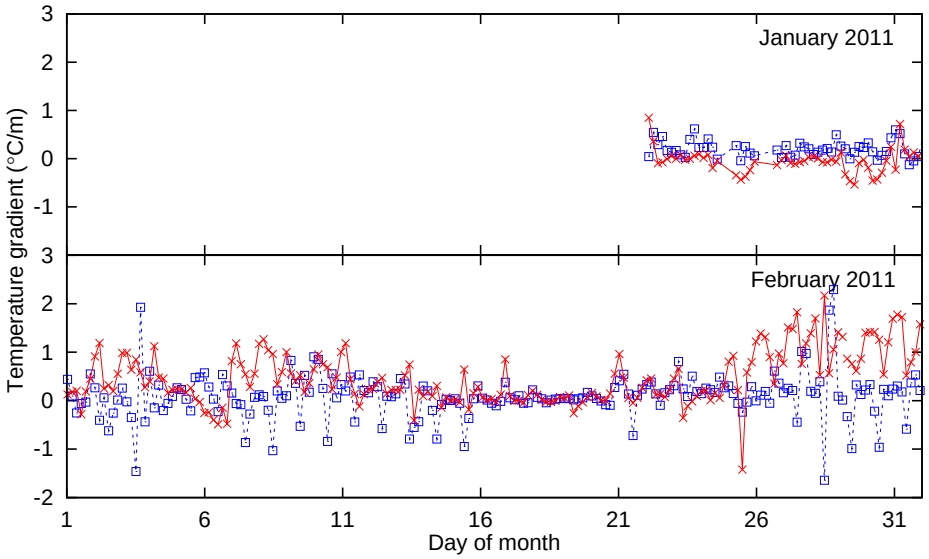

Figure 7.21: Time series of the temperature gradients (°C/m) from 0.3 m to 9.5 m (red cross) and from 9.5 m to 15.8 m (blue square) for the period from January to February, 2011. Temperatures were measured in every two minutes. We plot in each four hours for clarity.

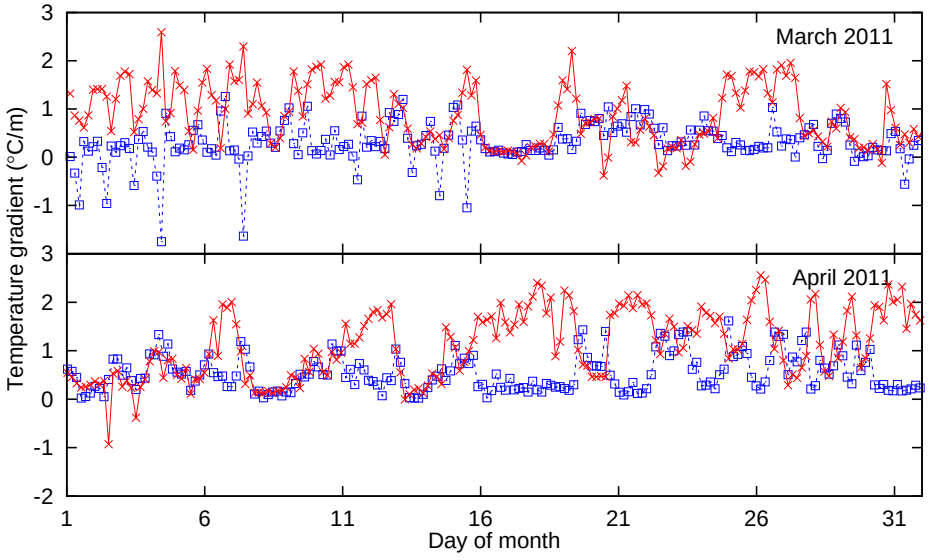

Figure 7.22: Same as Fig. 7.21, but for the period from March to April, 2011.

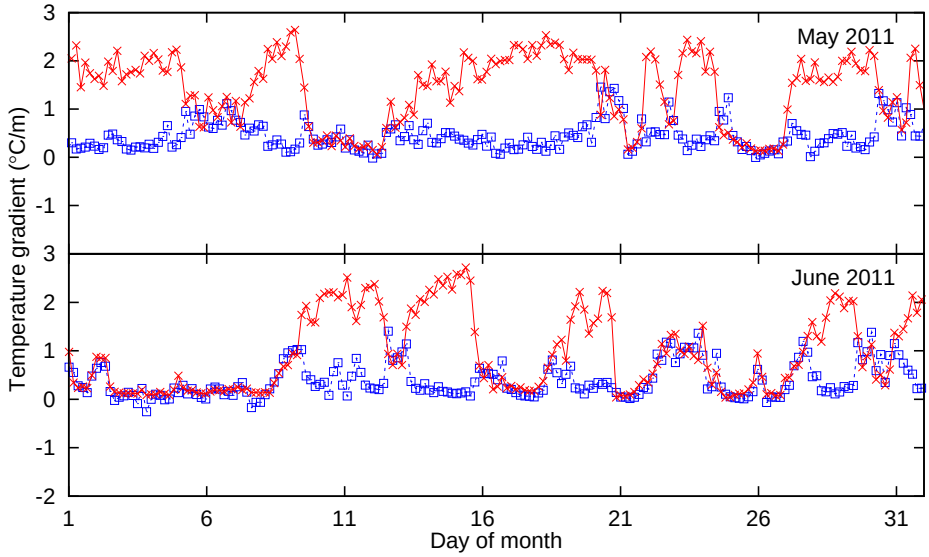

Figure 7.23: Same as Fig. 7.21, but for the period from May to June, 2011.

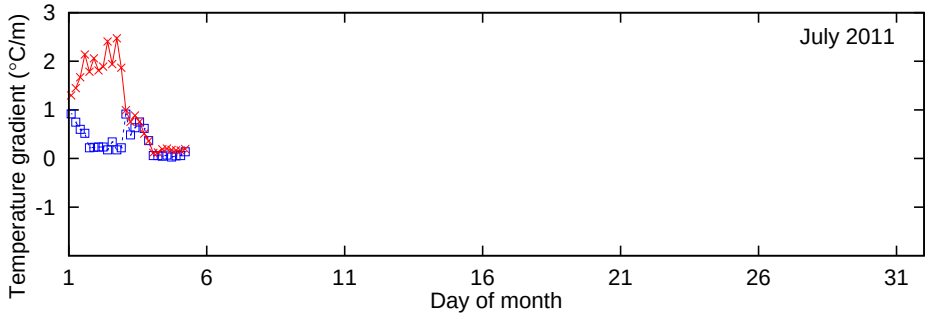

Figure 7.24: Same as Fig. 7.21, but in July, 2011.

temperature gradient varied in the internal of several days. Sometimes the temperature gradient between 0.3 m and 9.5 m became smaller. The phenomena would have been caused in the cloudy or snowfall weather, which prevent radiative cooling. The temperature gradient between 9.5 m and 15.8 m, on the other hand, hardly changed ($\sim$0°C/m) during our observations. The fact suggests that the positive temperature gradient occurs only near the snow surface. The time series of the temperatures gradients with two minute time resolution for all duration are plotted in Appendix C.2.

The seasonal characteristic temperature gradients are shown in Figs. 7.25 $\sim$ 7.28, which were observed on February 7, 12, March 2, and May 3, 2011. In the Antarctic summer, diurnal variations were shown (Figs. 7.25 and 7.26). Almost half days we observed large temperature gradient between 0.3 m and 9.5 m at the local nighttime (January 22, 31, February 1 $\sim$ 4, 6 $\sim$ 11, see Fig. 7.25). The gradient between 9.5 m and 15.8 m became negative at $\sim$ 12 h. The negative gradient would be caused by the solar heating, which made the unstable atmosphere. In the Antarctic autumn, as same in the Antarctic summer, negative gradient between 9.5 m and 15.8 m was also observed at the local daytime (Fig. 7.27). On the other hand, relatively large positive temperature gradient between 9.5 m and 15.8 m was obtained except $\sim$ 15 h. In the Antarctic winter, as shown in Fig. 7.28, a strong positive temperature gradient developed between 0.3 m and 9.5 m.

Almost no temperature gradient was shown between 9.5 m and 15.8 m.

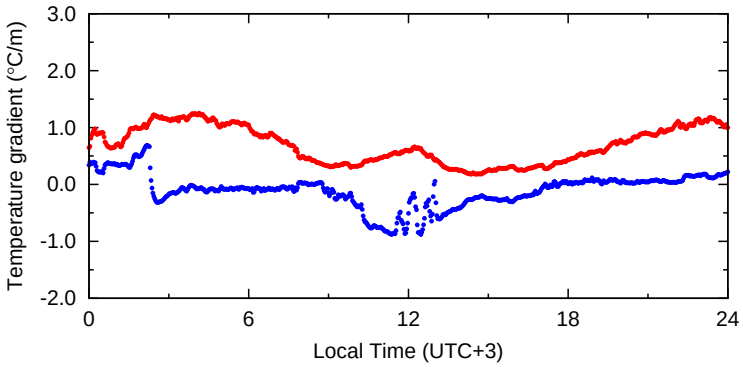

Figure 7.25: Time series of the temperature gradient (°C/m) at 0.3 m (red), 9.5 m (blue), 12 m (green), and 15.8 m (black), respectively, with two minute time resolution, in the Antarctic summer from February 7 00:00 to 24:00 (UTC+3), 2011.

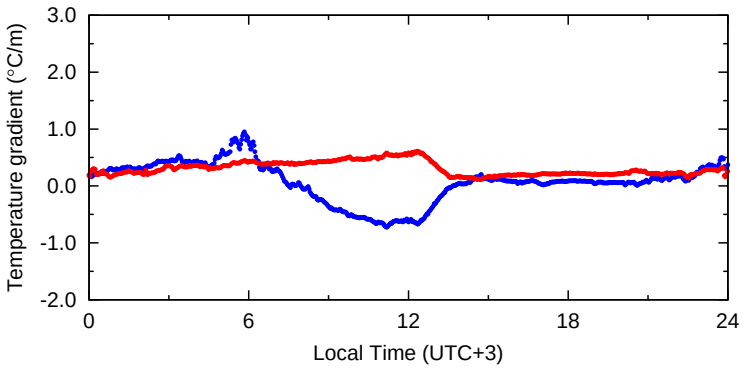

Figure 7.26: Same as Fig. 7.25, but for the Antarctic summer from February 12 00:00 to 24:00 (UTC+3), 2011.

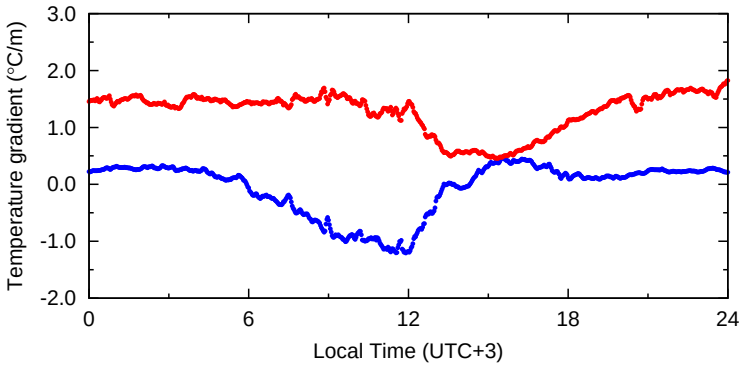

Figure 7.27: Same as Fig. 7.25, but for the Antarctic autumn from March 2 00:00 to 24:00 (UTC+3), 2011.

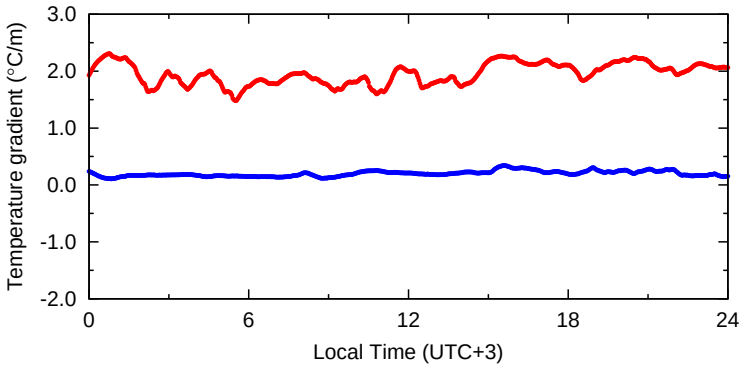

Figure 7.28: Same as Fig. 7.25, but in for the Antarctic winter from May 3 00:00 to 24:00 (UTC+3), 2011.

7.4 Barometer

Atmospheric pressure was measured from January 21 to June 27, 2011 (Some data were lacked due to the wrong setting of the data logger). The time series of the pressure is plotted in Figs. 7.29 ∼ 7.31 for each month. The time series of the atmospheric pressure with two minute time resolution for all duration are plotted in Appendix D. We note that we could not measure the pressure under 596 hPa due to the wrong setting of the data logger (see Chap. 5.3.3).

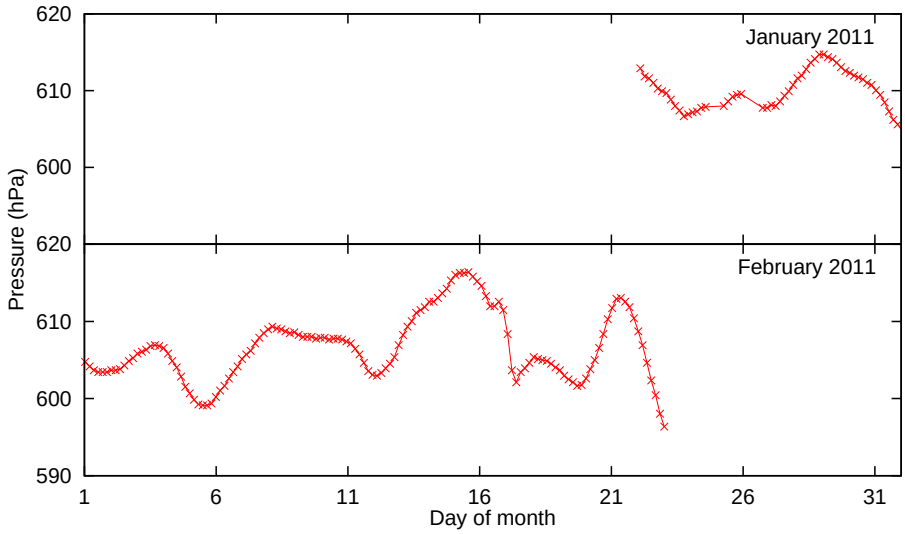

Figure 7.29: Time series of the atmospheric pressure (hPa) for the period from January to February, 2011. Pressure was logged in each two minutes. We plot in each four hours for clarity.

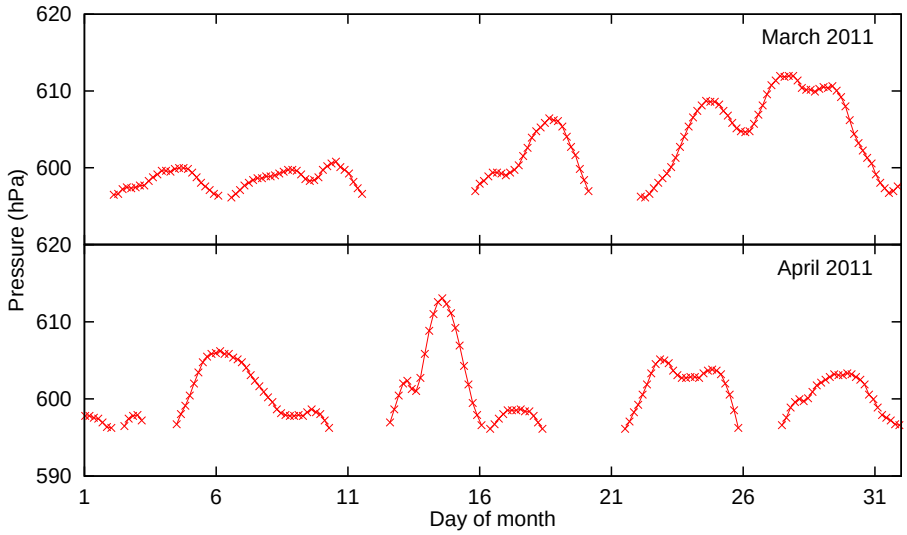

Figure 7.30: Same as Fig. 7.29, but for the period from March to April, 2011.

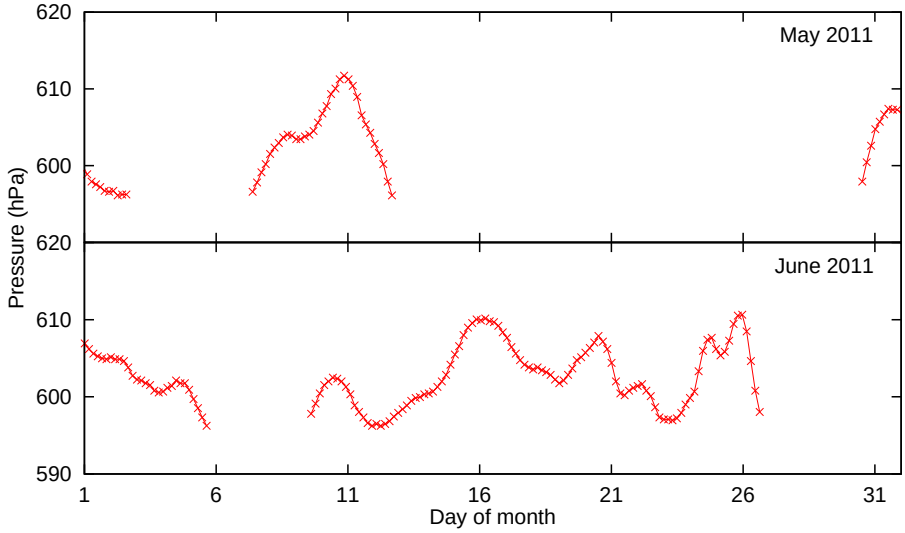

Figure 7.31: Same as Fig. 7.29, but for the period from May to June, 2011.

In the Antarctica plateau, the atmospheric pressure tends to become low when it is fine weather, which is caused by radiative cooling. Therefore, atmospheric pressure can be used as an indicator of the weather condition. The atmospheric pressure showed no significant diurnal variations even in the Antarctic summer. The pressure is supposed to be not sensitive to the temperature. It would slowly change in global meteorology. On the other hand, large variations were observed occasionally (e.g., February 21, April 14), when the local weather condition would have suddenly changed.

7.5 Tohoku DIMM

The seeing measurement with Tohoku DIMM were carried out at 2 m above the snow surface from January 25 to January 28, 2011. The observations were done only for four days, the result of the seeing would have large uncertainties. Figure 7.32 shows the time series of the Tohoku DIMM seeing for each day. The seeing values during the local daytime tended to be smaller than the values during the local nighttime. The seeing had a local minimum of $\sim 0.7''$ near 18 h local time on January 27. A simmilar local minimum at the local dusk has been found at Dome C and been interpreted as due to the disappearance of the surface boundary layer (Aristidi et al. 2005a; 2005b) [4, 6]. The periods with no measurements were due to bad weather and instrumental troubles.

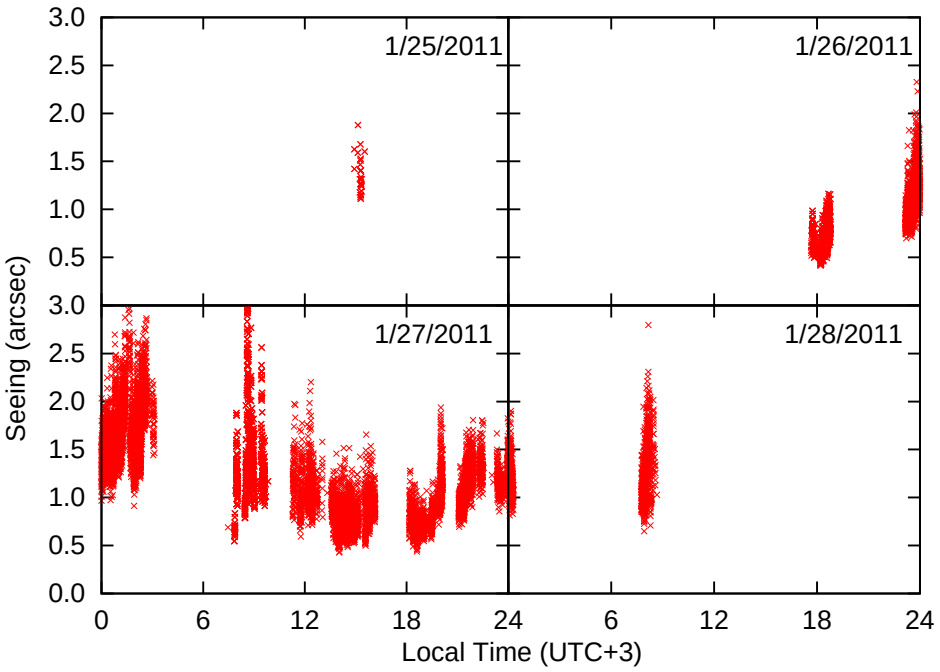

Figure 7.32: Time series of the Tohoku DIMM seeing at the height of 2 m above the snow surface obtained with Tohoku DIMM from January 26 to 28, 2011. The seeing values were converted to the values at the wavelength of 500 nm and at zenith. Copyright: Okita et al. (2013b) [52]

The statistics of the Tohoku DIMM seeing are listed in Table 7.3. The mean and median seeings are $1.2''$ and $1.1''$. σ and MAD are $0.46''$ and $0.46''$. The 25^{th} and the 75^{th} percentiles are $0.81''$ and $1.5''$, respectively. From the studies in Chap. 6.4, Tohoku DIMM seeing has $\pm 11\%$ statistical and $\pm 7\%$ systematic errors in the value. Tohoku DIMM seeing values would have been affected by the strong turbulence near the snow surface, i.e. the surface boundary layer. The histogram and cumulative histogram is plotted in Fig. 7.33.

We also listed the seeing statistics during local daytime (6-18h) and local nighttime (0-6h, 18-24h) in Table 7.3. We will discuss the difference in Chap. 8.4 and Chap. 8.6

Table 7.3: Seeing statistics at 500 nm, at zenith, at 2 m above the snow surface at Dome Fuji during January 25 to 28, 2011. (±11% statistical error, ±7% systematic error)

	All	Daytime	Nighttime
Tohoku DIMM	0-24h	6-18h	0-6h, 18-24h
Mean	1.2″	1.1″	1.4″
Standard deviation	0.46″	0.44″	0.47″
Median	1.1″	0.98″	1.3″
Median absolute deviation	0.46″	0.34″	0.50″
25^{th} percentiles	0.81″	0.79″	0.92″
75^{th} percentiles	1.5″	1.3″	1.6″

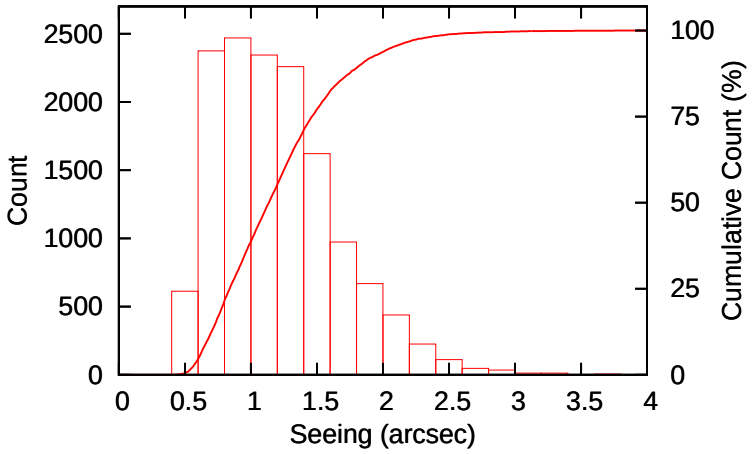

Figure 7.33: Histogram and cumulative histogram of the seeing at 2 m above the snow surface at the wavelength of 500 nm at zenith measured with Tohoku DIMM.

7.6 DF-DIMM

We carried out DF-DIMM observations at 11 m above the snow surface from January 4 to January 23, 2013. In all, we obtained 3 814 seeing data; each is calculated with 450 images taken in each about five minutes. Figures 7.34 $\sim$ 7.37 show the time series of the seeing for each day. It should be noted that seeing ($0.2'' \sim 0.3''$) was observed continuously for several hours only at 11 m above the snow surface. The excellent seeing, ($\leq 0.2''$) was observed for about four hours near local midnight on January 6, 2013. Other excellent seeings ($\leq 0.3''$), were recorded near local midnight on January 11, 15, 21, and 23. Such excellent seeings near local midnight has not been reported in the site testings at Dome C. The seeing has a tendency to have a local minimum of $\sim 0.3''$ near 18 h local time. This is clear in the data for January 6, 7, 9, 15, and 16. A similar local minimum in dusk has been seen both at Dome Fuji with Tohoku DIMM and at Dome C (Aristidi et al. 2005a; 2005b) [4, 6].

The histogram and cumulative histogram of DF-DIMM seeing are plotted in Fig. 7.38. The histogram is expected to consist of two sets of data: those when the telescope is outside the surface boundary layer, and those when the telescope is inside. The long tail of seeing ($\geq 0.4''$) would have been recorded at the latter occasion. We could anticipate that if DF-DIMM is mounted on a higher tower, the fraction of the tail would drop significantly.

The statistics of the seeing 11 m above the snow surface are summarized in Table 7.4. The mean and median seeings at 500 nm are $0.68''$ and $0.52''$. σ and MAD are $0.61''$ and $0.28''$. The 25^{th} and the 75^{th} percentiles are $0.36''$ and $0.78''$, respectively. From the studies in Chap. 6.5, DF-DIMM seeing has $\pm 4\%$ statistical and $\pm 4\%$ systematic errors in the value. We suggest that the large value is due to the poor seeing when the surface boundary layer is above the level of the telescope.

Local daytime (6-18h) and local nighttime (0-6h, 18-24h) seeing statistics are also listed in Table 7.4. The seeing values at the local daytime are larger than those at the local nighttime. It is contrary to the result of the Tohoku DIMM. The statistics will be discussed in Chap. 8.3.

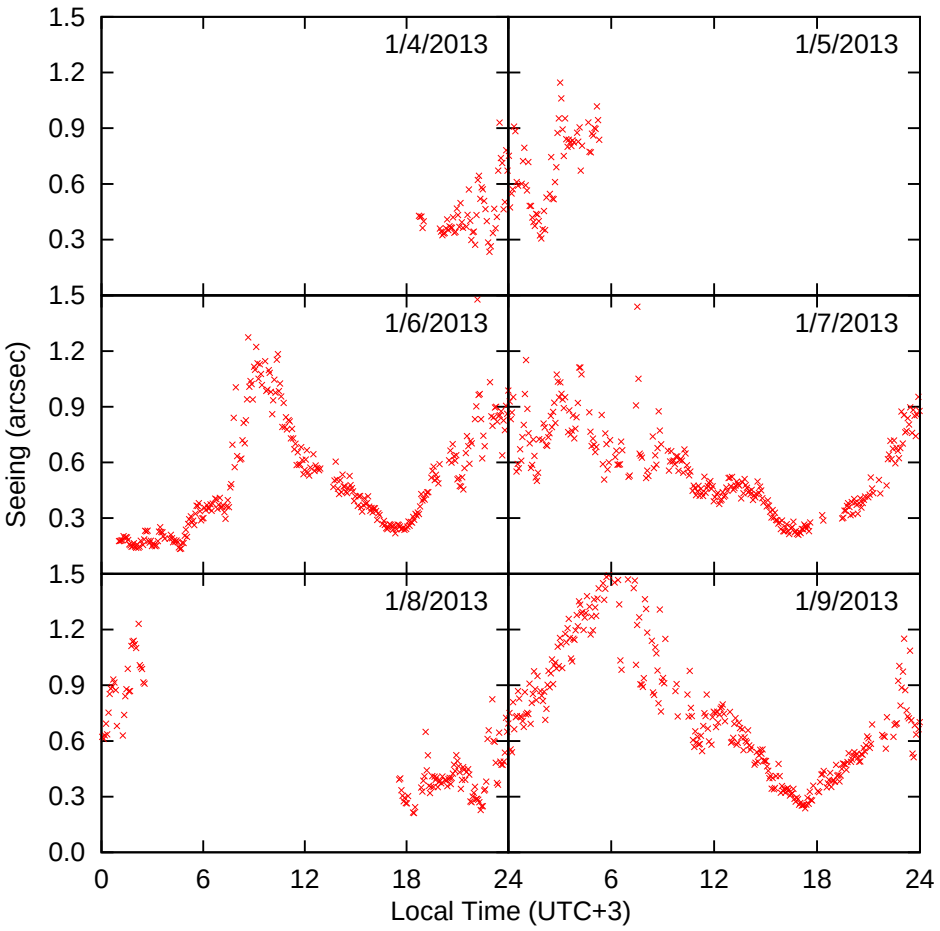

Figure 7.34: Time series of Dome Fuji seeing obtained with DF-DIMM from January 4 to January 9, 2013. The seeing was measured at 472 nm at 11 m above the snow surface. Seeing values are converted to the values at 500 nm and at zenith. We plot the average of the longitudinal and transverse seeings. Copyright: Okita et al. (2013a) [50]

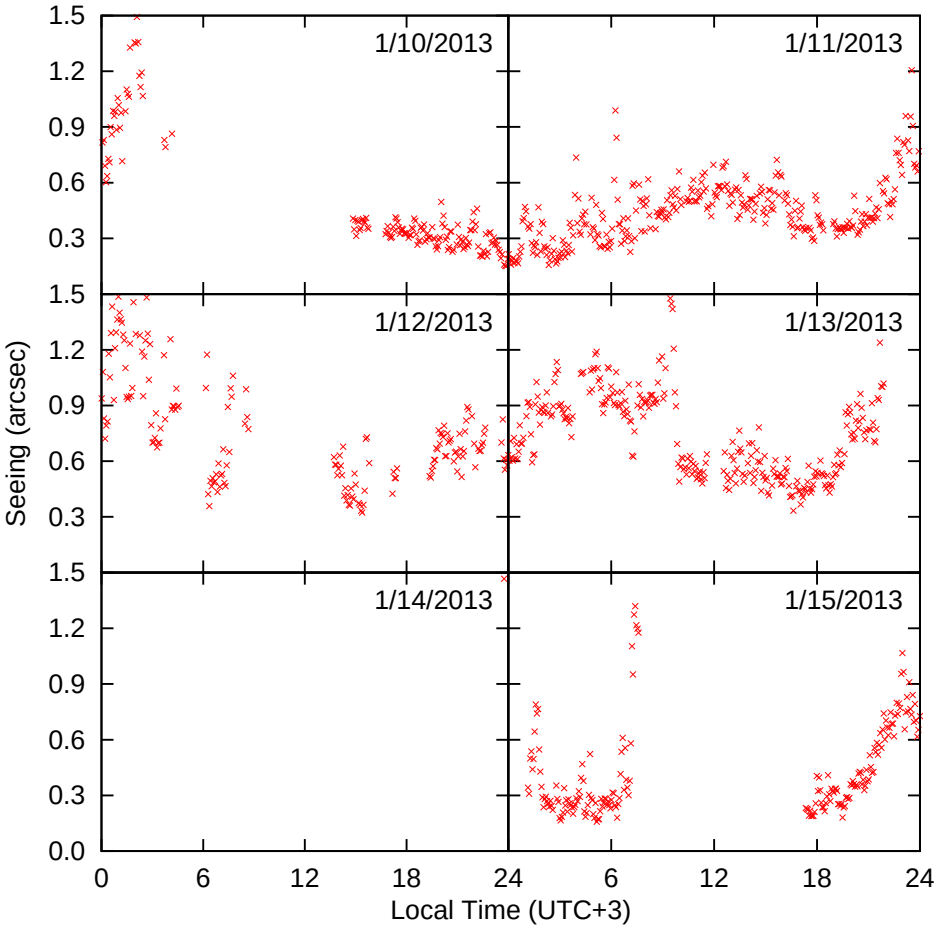

Figure 7.35: Same as Fig. 7.34, but for the period from January 9 to January 15, 2013. Copyright: Okita et al. (2013a) [50]

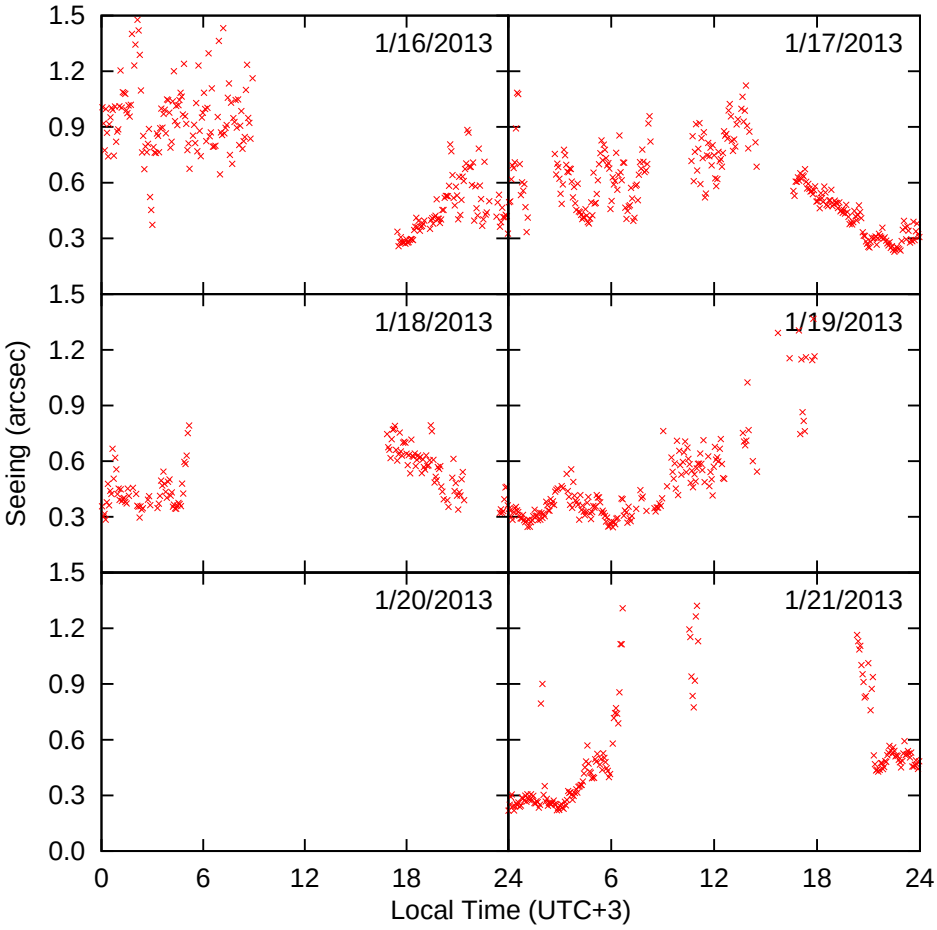

Figure 7.36: Same as Fig. 7.34, but for the period from January 16 to January 21, 2013. Copyright: Okita et al. (2013a) [50]

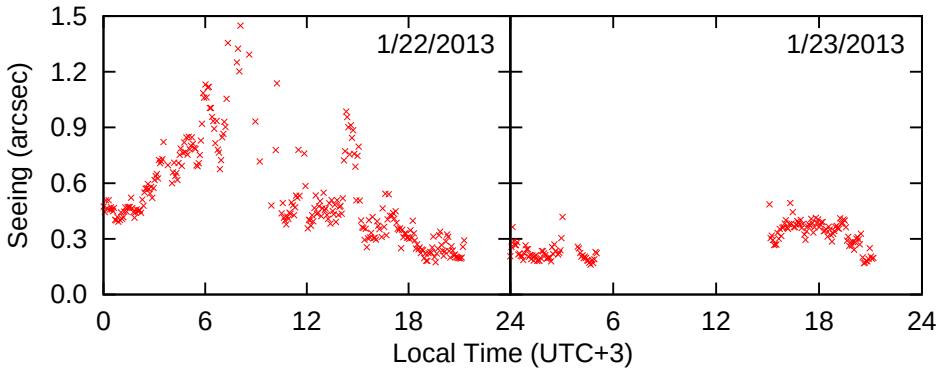

Figure 7.37: Same as Fig. 7.34, but for the period from January 22 and January 23, 2013. Copyright: Okita et al. (2013a) [50]

Table 7.4: Seeing statistics at 500 nm, at zenith, at 11 m above the snow surface at Dome Fuji during January 4 and 23, 2013. (±4% statistical error, ±4% systematic error)

	All	Daytime	Nighttime
DF-DIMM	0-24h	6-18h	0-6h, 18-24h
Mean	0.68″	0.86″	0.55″
Standard deviation	0.61″	0.86″	0.32″
Median	0.52″	0.56″	0.47″
Median absolute deviation	0.28″	0.28″	0.28″
25^{th} percentiles	0.36″	0.41″	0.32″
75^{th} percentiles	0.78″	0.86″	0.74″

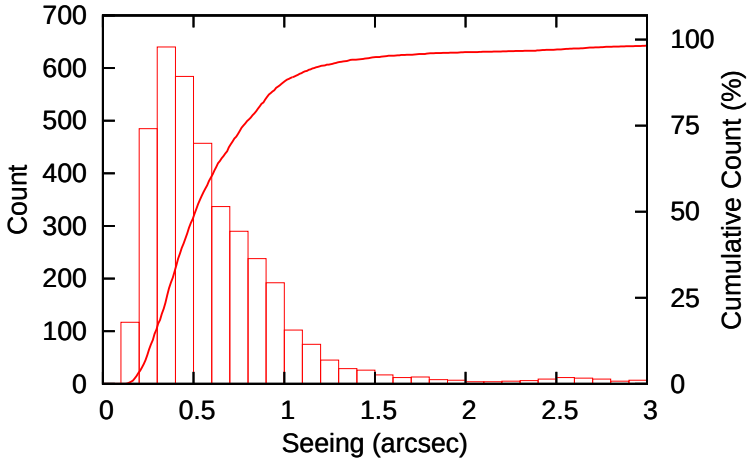

Figure 7.38: Histogram and cumulative histogram of the seeing at 11 m above the snow surface at 500 nm at zenith measured with DF-DIMM from January 4 to 23, 2013. Copyright: Okita et al. (2013a) [50]

Chapter 8

Discussion

8.1 Height of the surface boundary layer

The surface boundary layer was defined as the optical turbulence near the ground (Chap. 1.4.5). On the Antarctic continent, the turbulence will be caused by the temperature gradient and wind near the snow surface (Chap. 1.4.6). The height of the surface boundary layer was also defined in Chap. 6.2.3. The results of Snodar observations, i.e. the mean and median heights of the surface boundary layer for each month, which include all weather conditions, were shown in Table 7.1. The mean and median heights for the entire period of our observation were 21.3 m and 17.1 m, respectively. These results are consistent with the forecast of the simulation (18.5 m, Swain & Gallée 2006) [63]. However, since actual observations would be carried out only under good weather conditions, we focus on the surface boundary layer only in fine weather.

Here we study the temperature gradient in various weather conditions. In fine weather without solar insolation, the atmosphere near the snow surface is cooled by radiative cooling and become stable inversion layer, which has large positive temperature gradient. Conversely the temperature gradient near the snow surface almost disappears in cloudy or snowfall weather because the radiative cooling does not occur. Therefore, by examining the temperature gradient, we could judge the weather condition.

Figure 8.1 is the histogram and cumulative histogram of the temperature gradient between 0.3 m and 9.5 m during the period of Snodar observations. The shape of the histogram appears to be bimodal; one peak is at $0.1^{\circ}\mathrm{Cm}^{-1}$ and another is at $1.5^{\circ}\mathrm{Cm}^{-1}$. A larger temperature gradient would predict the fine weather, and another would suggest the cloudy or snowfall weather conditions. Therefore we assume the fine weather to be the period when the temperature gradient was larger than $0.5^{\circ}\mathrm{Cm}^{-1}$. By using this weather criteria, we could estimate the height of the surface boundary layer only in fine weather.

We note that, as discussed in Chap. 7.3, the characteristic temperature gradients for each season had different features. In the Antarctic winter, as shown in Fig. 7.28, the strong temperature gradient between 0.3 m and 9.5 m was shown. Therefore we consider that we can judge the weather condition with the temperature gradient in the Antarctic winter. In the Antarctic autumn, the large positive temperature gradient between 0.3 m and 9.5 m except at dusk was shown (Fig. 7.27). At dusk, the temperature gradient had a local minimum. The local gradient minimum at dusk would mean the stable atmosphere, which make the local seeing minimum, will be discussed in Chap. 8.5. From our observa-

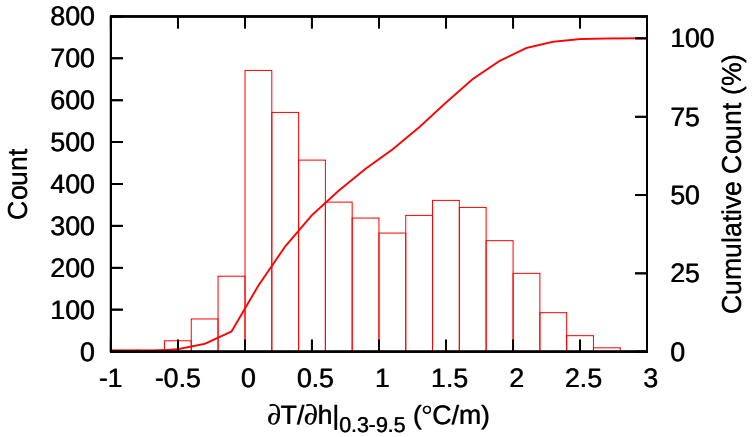

Figure 8.1: Histogram and cumulative histogram of the temperature gradient between 0.3 m and 9.5 m during the period of Snodar observations.

tions, the value of the gradient minimum was $0.5°\mathrm{Cm}^{-1}$ or larger. Therefore we can judge the weather condition by using the criteria $> 0.5°\mathrm{Cm}^{-1}$ even at dusk in the Antarctic autumn. However, at the local daytime in the Antarctic summer, the atmospheric convection would occur due to the solar insolation, which will be discussed in Chap. 8.2. The atmospheric convection was observed on almost all days as the negative temperature gradient between 9.5 m and 15.8 m (Figs. 7.25 and 7.26). The positive temperature gradient between 0.3 m and 9.5 m is considered not to develop due to strong solar heating and relatively weak radiative cooling at the local daytime in the Antarctic summer. Thus the temperature gradient in the Antarctic summer would not suit for the weather criteria. As such, we discuss the height of the surface boundary layer only in the Antarctic autumn and winter in the present thesis.

We also note that we tried to use the atmospheric pressure as a criteria of the weather condition (Figs. 7.29 $\sim$ 7.31). However, the pressure varies with both the local weather condition and the large scale transition. These effects are not distinguishable. Therefore, we do not use the pressure data as the criteria of the weather condition. We also examined the sky images taken with HRCAM to find clear days. HRCAM (High Resolution CAMera) is a digital SLR camera (Canon EOS 50D) equipped with a circular fish-eye lens (Sigma 4.5 mm f/2.8) for all-sky coverage. It was installed on the PLATO-F instrument module. However, both the snow drifting and the auroral emission made the judge of the weather condition difficult. The frost on the camera lens was also an obstacle. As such, we finally gave up using the HRCAM data as a weather criteria. Tohoku DIMM data was also considered to become a verification of the weather condition because the DIMM measurements were performed only in fine weather. However, the simultaneous observations with Tohoku DIMM and Snodar were carried out only four hours. Therefore we did not the use Tohoku DIMM data for the verification of the weather criteria. In addition, the naked-eye cloud-cover measurements were performed during JARE 52^{nd} visiting duration. However, since the simultaneous observations with the cloud-cover measurements and Snodar were only four hours, we did not discus any correlations between them.

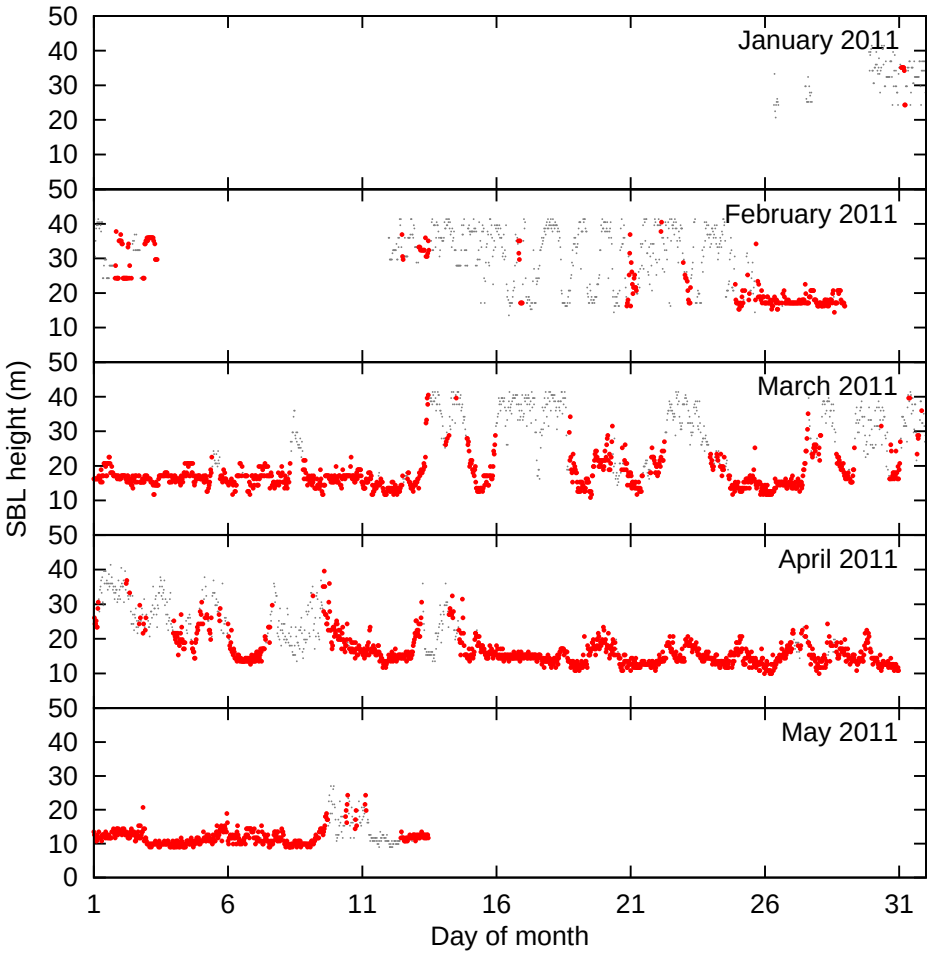

Figure 8.2: Monthly time series of the height of the surface boundary layer obtained with Snodar. Red dots indicate the observations performed with the weather criteria of the temperature gradient > 0.5 °Cm^{-1} (in fine weather), and gray dots indicate those with $<$ 0.5 °Cm^{-1} (in cloudy or snowfall weather).

Figure 8.2 shows monthly time series of the height of the surface boundary layer. We plot the height of the surface boundary layer with the weather criteria of the temperature gradient > 0.5°Cm^{-1}. Figure 8.3 is the histogram and cumulative histogram of the height only in fine weather in the Antarctic autumn and winter, and those for entire period. The mean and median heights of the surface boundary layer in fine weather for each month are listed in Table 8.1. The heights for each season are listed in Table 8.2. The mean and median heights in fine weather in the Antarctic autumn and winter were 16.0 m and 15.3 m. The averaged standard deviation (σ) and median absolute deviation (MAD) are 4.3 m and 2.7 m. The statistical and systematic errors are $\pm 5\%$ and $\pm 5\%$, respectively. The median height (15.3 m) at Dome Fuji is little higher than that (13.9 m) at Dome A (Bonner et al. 2010b) [14], and about half of $23 \sim 36$ m at Dome C (Agabi et al. 2006; Aristidi et al. 2005a, 2005b, 2009; Trinquet et al. 2008) [1, 4, 6, 7, 73]. Figure 8.2 also indicates that the low surface boundary layer stably continues stably for several days.

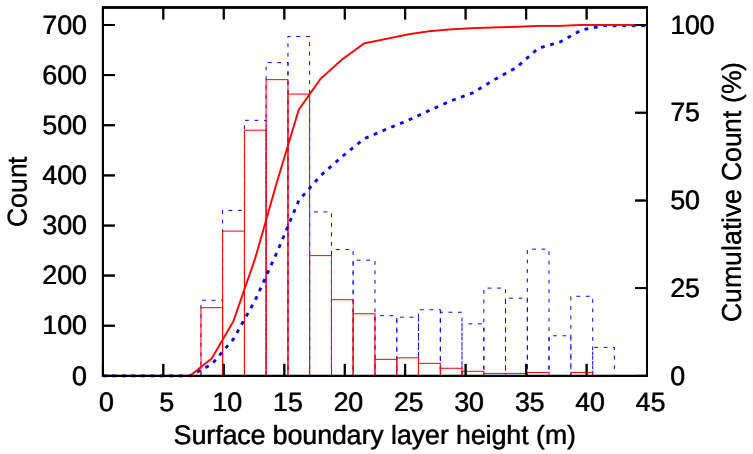

Figure 8.3: Histogram and cumulative histogram of the surface boundary layer height. Red solid line and boxes mean the histogram and cumulative histogram, which are under in fine weather in the Antarctic autumn and winter, and blue dot line and boxes mean those in all weather conditions for entire period.

Table 8.1: Statistics of the surface boundary layer height in fine weather for each month. (±5% statistical error, ±5% systematic error)

Month	Number of observations in fine weather	Mean	σ	Median	MAD
January [1)]	(8)	(32.3 m)	(4.9 m)	(35.1 m)	(0.0 m)
February [1)]	(279)	(22.1 m)	(6.8 m)	(18.0 m)	(2.7 m)
March	972	17.1 m	4.1 m	16.2 m	2.7 m
April	1 076	16.2 m	4.1 m	15.3 m	2.7 m
May	477	11.8 m	2.2 m	11.7 m	1.3 m
Total [1)]	(2 812)	(16.4 m)	(5.0 m)	(15.3 m)	(2.7 m)

Note: [1)] Statistics in January and February would be invalid because the fine weather criteria $> 0.5°\mathrm{Cm}^{-1}$ does not suit in the Antarctic summer (before February 15).

Table 8.2: Statistics of the surface boundary layer height in fine weather for each season. (±5% statistical error, ±5% systematic error)

Season	Number of observations in fine weather	Mean	σ	Median	MAD
Summer [1)]	(383)	(32.8 m)	(4.9 m)	(33.3 m)	(5.3 m)
Autumn	1 989	17.1 m	4.2 m	16.2 m	2.7 m
Winter	737	12.8 m	2.8 m	12.6 m	2.7 m
Autumn and winter	2 726	16.0 m	4.3 m	15.3 m	2.7 m

Note: [1)] Statistics in the Antarctic summer were calculated from the data with all weather conditions.

Now we study the correlation between the height of the surface boundary layer and the temperature gradient between 0.3 m and 9.5 m in the Antarctic autumn and winter. Figure 8.4 shows the correlation for the surface boundary layer height and the temperature

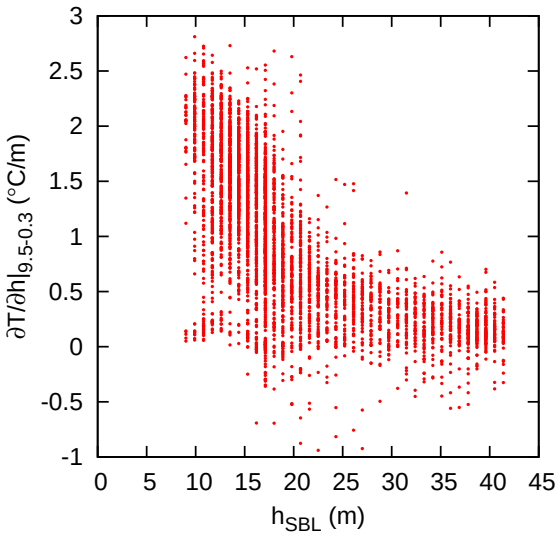

Figure 8.4: Correlation between the height of the surface boundary layer and the temperature gradient between 0.3 m and 9.5 m in the Antarctic autumn and winter.

gradient. The height of the surface boundary layer in the Antarctic autumn and winter was roughly inversely relate to the temperature gradient between 0.3 m and 9.5 m. This correlation would mean the temperature gap inside the temperature inversion layer near the snow surface, i.e. surface boundary layer, to be roughly constant (~ 20°C). Therefore, if we observe the strong positive temperature gradient near the snow surface, low height of the surface boundary layer will be expected.

In summary, we estimated the height of the surface boundary layer in fine weather in the Antarctic autumn and winter to be 15.3 $\pm$ 0.8 (statistical) $\pm$ 0.8 (systematic) m in median. MAD was 2.7 m. The height of the surface boundary layer remained low and stable for several days. The low height of the surface boundary layer is expected when the strong temperature gradient near the snow surface occurs. Since we could judge the weather condition only in the Antarctic autumn and winter, we did not discuss the height in the Antarctic summer. In the case of the Antarctic summer, in general, the height would be thicker due to the atmospheric convection, which will discussed in Chap. 8.2.

It should be noted that, as pointed out by Swain & Gallée (2006) [63] and Bonner et al. (2010a) [13], the height of the surface boundary layer is expected to be correlated with the surface wind speed. Originally we planned to measure the surface wind speed with the ultrasonic anemometers. However the observations were failed due to insufficient preparations. Therefore we do not discuss the correlation from our data.

8.2 Atmospheric convection on the Antarctic plateau

As discussed in Chap. 1.4.6, the surface boundary layer on the Antarctic plateau is built mainly by the strong temperature gradient with the surface wind. In addition, since the solar insolation occurs at the local daytime in the Antarctic summer and autumn, the atmospheric convection would be another cause which builds the surface boundary layer. However, this effect had not been discussed in the previous studies on the Antarctic plateau.

At first we discuss the statistical behavior of the atmospheric turbulence. Figure 8.5 is the diurnal time series of the turbulence profile from 40 m to 400 m above the snow surface measured with SODAR in the Antarctic summer. We stacked the turbulence profiles of the same time. Diurnal variation of the turbulence strength is clearly shown in the figure. The strong turbulence rose up from ∼7 h and reached ∼300 m height at ∼15 h. After reaching 300 m height, the turbulence dissipated rapidly. On the other hand, turbulences were always exist below 100 m height even at the local nighttime.

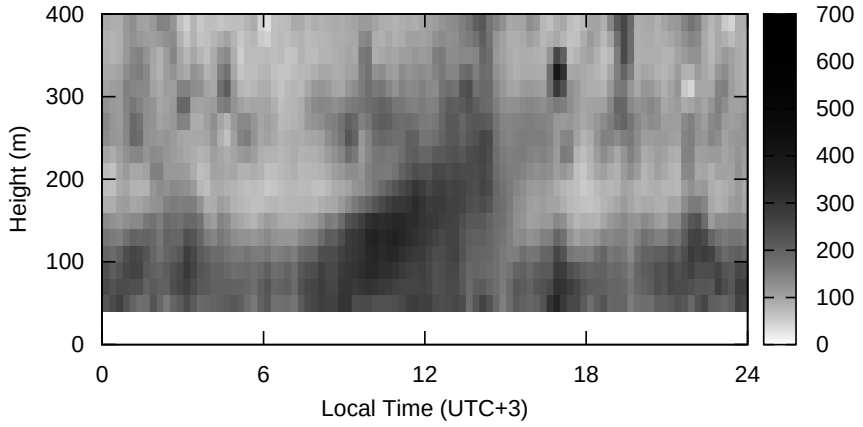

Figure 8.5: Turbulence profile from 40 m to 400 m above the snow surface measured with SODAR in the Antarctic summer 2006/2007. The data at the same time are averaged. The turbulence strength are in arbitrary unit.

Snodar observations also showed the turbulence rising (i.e. atmospheric convection) at the local daytime on several days in the Antarctic summer (see Fig. 7.6). In addition, the negative temperature gradient between 9.5 m and 15.8 m, which means the unstable atmosphere, was observed almost all days at the local daytime in the Antarctic summer (Figs. 7.25 and 7.26). The temperature gradient in the Antarctic autumn, as shown in Fig. 7.27, had same tendency with that in the Antarctic summer. As such, we consider that the atmospheric convection occurs at the local daytime in the Antarctic summer and autumn. The atmospheric convection would be caused by the solar insolation because neither turbulence rising nor negative temperature gradient was observed in the Antarctic winter (Figs. 7.8 and 7.28).

Secondly, we compare the stacked turbulence profile with the stacked DF-DIMM seeing. Figure 8.6 shows the seeing of diurnal time series stacked at the same hour, which were

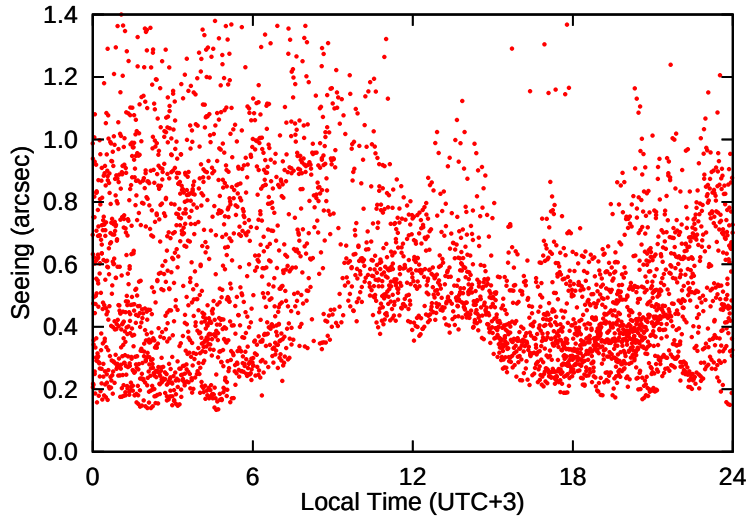

Figure 8.6: All seeing values at the same hours, obtained with DF-DIMM at 11 m above the snow surface during the Antarctic summer.

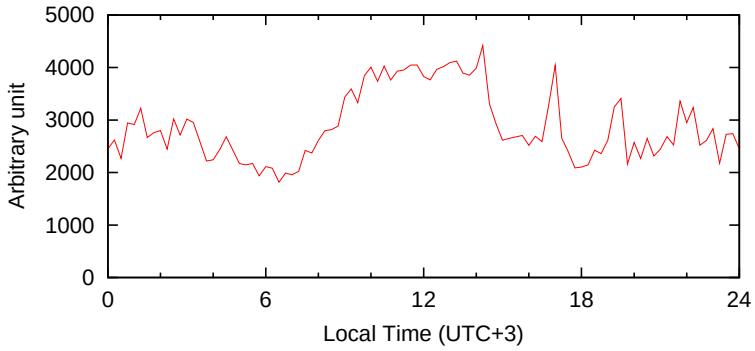

Figure 8.7: Turbulence strength between 40 m and 400 m above the snow surface. All data at the same time are averaged.

obtained with DF-DIMM 11 m above the snow surface from January 4 to January 23, 2013. The lower limit of the stacked DF-DIMM seeing is $\sim 0.2''$ at the local nighttime (0-6 h, 18-24 h) and $\sim 0.4''$ at the local daytime (6-18 h). At the local nighttime in the Antarctic summer, the seeing value near the snow surface would be large by the strong temperature gradient, which was caused by the weak solar insolation and strong radiative cooling, in the surface boundary layer. Therefore the lower limit of the stacked DF-DIMM seeing at the local nighttime can be interpreted to be obtained when the seeing was not affected by the temperature gradient, i.e., when the telescope height was comparatively higher than the surface boundary layer. At the local daytime in the Antarctic summer, however, the lower limit of the stacked DF-DIMM seeing was significantly worse than that at the local nighttime. The difference would be caused by the existence of the atmospheric turbulence at 11 m or higher above the snow surface, which is shown in Fig. 8.5. Figure 8.7 shows the turbulence strength, averaged at the same time, between 40 m to 400 m above the snow surface observed with SODAR. The turbulence between 40 m to 400 m at the local daytime was ~ 1.5 times larger than that at the local nighttime. The difference would be the cause of the degradation for the seeing lower limit.

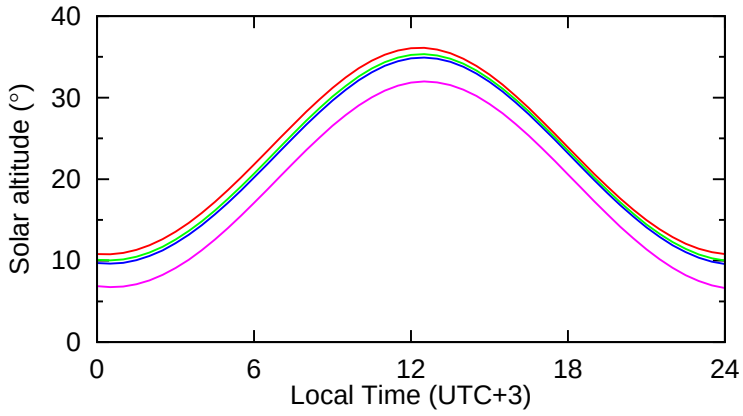

Figure 8.8: Solar altitude on December 21, 2006 (red), January 7, 2007 (blue), January 4, 2013 (green), and January 23, 2013 (magenta), respectively.

We also show the solar altitudes on December 21 2006, January 7 2007, January 4 2013, and January 23 2013 in Fig. 8.8. (SODAR observations were started on December 21, 2006 and ended on January 7, 2007. DF-DIMM observations were started on January 4, 2013 and ended on January 23, 2013.) The solar altitude is different by $\sim 25^\circ$ between midnoon and midnight. At the local daytime in the Antarctic summer, the solar insolation is stronger due to the high solar altitude, and then the atmospheric convection appears. On the contrary, the atmospheric convection does not appear at the local nighttime even in the Antarctic summer because the solar altitude is low enough and therefore the solar insolation is weaker than the radiative cooling. With the same reason, there would be no atmospheric convection in the Antarctic winter because of no solar insolation. Therefore, the surface boundary layer is build by the atmospheric convection at the local daytime in the Antarctic summer. The atmospheric convection at the local daytime in the Antarctic autumn would also occur and it make the seeing value worse.

In summary, from our observations, the atmospheric convection on the Antarctic plateau was found. Since it would be caused by the solar insolation, the atmospheric convection occurs at the local daytime in the Antarctic summer and autumn. In the Antarctic summer, the atmospheric convection makes the lower limit of the seeing observed at 11 m above the snow surface worse ($0.2'' \sim 0.4''$).

8.3 Free-atmosphere seeing in the Antarctic summer

The seeing, which is observed above a certain height, would be larger when the surface boundary layer is higher than the telescope. On the other hand, when it is lower than the telescope, we can get the free-atmosphere seeing. The excellent seeing of $0.2''$, was observed at 11 m above the snow surface at the local midnight on January 6, 2013 (Fig. 7.34), when DF-DIMM supposes to have observed the seeing above the turbulence layer.

Here we discuss the lower limit of the stacked DF-DIMM seeing at the local nighttime (0-6 h, 18-24 h), which is shown in Fig. 8.6. At the local nighttime in the Antarctic summer, the seeing value near the snow surface is expected to be larger due to the strong temperature gradient, which is caused by the weak solar insolation and strong radiative cooling, than the seeing at a local daytime (6-18 h). In fact, Tohoku DIMM seeing ($1.3''$) observed at 2 m above the snow surface at the local nighttime was worse than that ($0.98''$) at the local daytime. However, DF-DIMM seeing observed at 11 m at the local nighttime was $0.47''$ in median, which was better than $0.56''$ at the local daytime. The nighttime DF-DIMM seeing was significantly small compared with the Tohoku DIMM seeing during the same period. This smaller seeing would be owing to the higher telescope location, where the seeing was less affected by the surface boundary layer. As shown in Chap. 8.1, the height of the surface boundary layer in fine weather in the Antarctic autumn and winter was only 15.3 m in median. In other words, the lower limit of the DF-DIMM seeing at the local nighttime can be interpreted to be the observation at the time when the seeing was not affected by the surface boundary layer, i.e., when the telescope height was comparatively higher than the surface boundary layer.

We discuss the free-atmosphere seeing with the DF-DIMM observations. We define the free-atmosphere seeing as the average seeing less than $0.3''$ continuing longer than three hours during the local nighttime (0-6 h, 18-24 h) in the DF-DIMM observations. The free-atmosphere seeing was observed on 1:00-5:30 January 6, 0:00-3:30 January 11, 2:00-6:00 January 15, 0:00-3:30 January 21, and 0:00-5:30 January 23 (see Figs. 7.34 $\sim$ 7.37). Table 8.3 is the free-atmosphere seeing statistics. The histogram and cumulative histogram are plotted in Fig. 8.9. The mean and median are $0.24''$ and $0.23''$. σ and MAD are $0.081''$ and $0.057''$. The statistical and systematic errors are $\pm 4\%$ and $\pm 4\%$, respectively. The median free-atmosphere seeing is good agreement with $0.209''$ of the simulation (Saunders et al. 2009) [57], and better than $0.27'' \sim 0.36''$ at Dome C (Agabi et al. 2006; Aristidi et al. 2009; Lawrence et al. 2004; Trinquet et al. 2008) [1, 7, 37, 73].

The free-atmosphere seeing was measured 287 times. The total number of DF-DIMM observations at the local nighttime was 2 272. Therefore, the provability of 11 m or lower surface boundary layer would $\sim 13\%$ in the Antarctic summer. Low height of the surface boundary layer in fine weather at the local nighttime in the Antarctic summer would be expected.

In summary, we observed the excellent seeing at Dome Fuji at the local nighttime in the Antarctic summer. This excellent seeing is considered to be obtained when the height of the surface boundary layer is lower than the telescope height. In this condition, we can observe the free-atmosphere seeing with DF-DIMM observations at 11 m above the snow surface. The free-atmosphere seeing at Dome Fuji in the Antarctic summer was estimated $0.23'' \pm 0.01''$ (statistical) $\pm$ $0.01''$ (systematic) in median. MAD was $0.057''$. Since the DF-DIMM observations were performed only in the Antarctic summer, we could

Table 8.3: Free-atmosphere seeing statistics in January, 2013. (±4% statistical error, ±4% systematic error)

Date / hour	Number of observations	Mean	σ	Median	MAD
6 / 1:00-5:30	62	0.19″	0.042″	0.18″	0.036″
11 / 0:00-3:30	51	0.26″	0.085″	0.23″	0.059″
15 / 2:00-6:00	58	0.26″	0.067″	0.25″	0.045″
21 / 0:00-3:30	54	0.29″	0.12″	0.26″	0.025″
23 / 0:00-5:30	62	0.22″	0.044″	0.21″	0.032″
Total	287	0.24″	0.081″	0.23″	0.057″

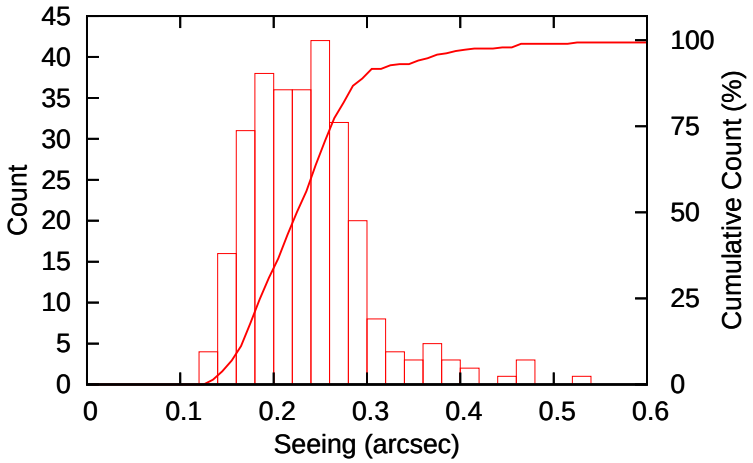

Figure 8.9: Histogram and cumulative histogram of the free-atmosphere seeing on the days in Table 8.3.

not discuss the free-atmosphere seeing in the Antarctic winter. In general, the wind speed of the polar vortex in the Antarctic autumn and winter is faster than that in summer, the free-atmosphere seeing would be worse.

8.4 Total seeing in the Antarctic summer

The turbulence in the surface boundary layer and the free atmosphere compose the total seeing. Tohoku DIMM was put on the snow surface and observed the seeing at 2 m above the snow surface. Therefore the seeing obtained with Tohoku DIMM is considered to be the total seeing. Since the Tohoku DIMM observations were performed during the Antarctic summer, we discuss the total seeing at Dome Fuji only in the Antarctic summer. From Table 7.3, the mean and median total seeings at Dome Fuji in the Antarctic summer were found to be $1.2''$ and $1.1''$, respectively. These values are similar to the total seeings at Dome C (mean $1.06''$, median $0.95''$), which were observed at 3 m above the snow surface in the Antarctic summer (Aristidi et al. 2009) [7].

The total seeing ($1.1''$) is significantly worse than the free-atmosphere seeing ($0.23''$). Therefore the seeing is considered to degrade drastically by the turbulence in the surface boundary layer. At the local daytime (6-18 h) in the Antarctic summer, solar insolation produces the atmospheric convection and makes the seeing worse (as discussed in Chap. 8.2). On the other hand, as discussed in Chap. 8.3, the seeing is degraded by the strong temperature gradient at the local nighttime (0-6 h, 18-24 h). The Tohoku DIMM seeing at the local daytime was $0.98''$ in median, and that at the local nighttime was $1.3''$, respectively (Table 7.3). The results suggest that the turbulence by the temperature gradient was stronger than that by the atmospheric convection near the snow surface. On the other hand, the DF-DIMM seeing at the local daytime ($0.56''$) in median was larger than the value ($0.47''$) at the local nighttime (Table 7.4). The difference can be interpreted to be caused by the difference of the turbulence layer height. The atmospheric convection was formed below 300 m only at the local daytime (as shown in Fig. 8.5). In contrast, in Figs. 7.21 $\sim$ 7.24, the temperature gradient is found to have appeared only near the snow surface. Since DF-DIMM was put at 11 m above the snow surface, the DF-DIMM seeing would not have been very affected by the temperature gradient. Therefore the nighttime DF-DIMM seeing was better than the daytime seeing.

In summery, we estimated the total seeing at Dome Fuji in the Antarctic summer to be $1.1'' \pm 0.1''$ (statistical) $\pm 0.1''$ (systematic) in median. MAD was $0.46''$. Although Tohoku DIMM observations were performed only in the Antarctic summer. Aristidi et al. (2009) [7] reported the total seeing, which was observed at 3 m above the snow surface, all year (summer median $0.95''$, winter $2.37''$). The worse seeing would be due to the stronger temperature gradient in the Antarctic winter. With the same reason, the total seeing at Dome Fuji in the Antarctic winter would be worse than that in the Antarctic summer.

8.5 Local seeing minimum at dusk

We discuss the seeing at dusk in the Antarctic summer. The local minimum ($\sim 0.7''$) of the seeing value near 18 h was observed at 2 m above the snow surface with Tohoku DIMM on January 27, 2011 (see Fig. 7.32). The local minimum ($\sim 0.3''$) near 18 h at 11 m was also observed with DF-DIMM on January 6, 7, 9, 15, and 16, 2013 (Figs. 7.34 $\sim$ 7.36). The seeing distributions shown in Fig. 8.6 also indicate no large seeing values at dusk (16 $\sim$ 20 h). A similar local minimum at dusk in the Antarctic summer was seen at Dome C (Aristidi et al; 2005a, 2005b) [4, 6].

The local seeing minimum at dusk is considered to be caused by the disappearance of the surface boundary layer (Aristidi et al. 2005a; 2005b) [4, 6]. At the local daytime in the Antarctic summer, the surface boundary layer is caused by the atmospheric convection (as discussed in Chap. 8.2). At the local nighttime in the Antarctic summer, the seeing becomes worse due to the strong positive temperature gradient, which is main cause of the surface boundary layer (Chap. 1.4.6). At the transition period of dusk and dawn, since neither atmospheric convection nor strong positive temperature gradient is considered, no surface boundary layer is expected. Thus the seeing would be small at the transition period of dusk and dawn in the Antarctic summer.

From SODAR and Snodar observations, for example we were shown in Figs. 7.1 and 7.6, rising of the strong turbulence was observed at the local daytime in the Antarctic summer. At the local daytime in the Antarctic summer, negative temperature gradient between 9.5 m and 15.8 m was observed, which meant the atmospheric convection (Figs. 7.25 and 7.26). At the local nighttime in the Antarctic summer, large positive temperature gradient between 0.3 m and 9.5 m was observed on almost half days. At dusk and dawn in the Antarctic summer, rising of the strong turbulence was not observed. Zero or small positive gradients between 0.3 m and 9.5 m were observed. These results mean no surface boundary layer at dusk and dawn in the Antarctic summer. Our results agreed with the previous considerations.

Now we consider why the seeing minimum occurred only at dusk. At dusk in the Antarctic summer, the solar insolation becomes weaker, and balances with the radiative cooling on the snow surface. The condition makes stable atmosphere at dusk, which would result in good seeing. After the condition, the snow surface will become gradually colder by radiative cooling, and the temperature gradient become gradually stronger as well. Thus the seeing becomes worse again. On the contrary, in the case of dawn, however, the solar insolation heats the snow surface against the radiative cooling. As a result, warmed air rises from the snow surface and it induces the atmospheric convection. Since the atmospheric convection gradually destroys the strong positive temperature gradient near the snow surface in this period, the strong positive temperature gradient and atmospheric convection coexist at dawn in the Antarctic summer. Therefore, the atmosphere would be unstable at dawn. As a result, the local seeing minimum is observed only at dusk. Figure 8.10 is the schematics of the temperature distribution in the Antarctic summer.

The difference between dusk and dawn was also observed with SODAR. The atmospheric convection rose gradually at dawn, and then it dissipated rapidly at dusk (Fig. 8.5). The turbulence strength between 40 m and 400 m above the snow surface (Fig. 8.7), increased gradually at dawn, while it decreased rapidly at dusk. This difference of the turbulence change is considered to make the local minimum at dusk and no minimum at

dawn.

We also discuss the local seeing minimum at dusk in the Antarctic autumn. Since the surface boundary layer is caused by the atmospheric convection at the local daytime and caused by the strong positive temperature gradient at the local nighttime in the Antarctic autumn, the local seeing minimum at dusk would be expected also in the Antarctic autumn. Figure 7.27 shows the atmospheric convection at the local daytime and the strong positive temperature gradient except $\sim$ 15 h. The local minimum of the temperature gradient between 0.3 m and 9.5 m was observed at dusk. This gradient minimum would mean the weakest surface boundary layer at dusk in the Antarctic autumn. Therefore the seeing in the Antarctic autumn will have a local minimum at dusk. Since the coexistence of the atmospheric convection and the strong positive temperature gradient was clearly shown in the figure, the local seeing minimum would not be expected at dawn in the Antarctic autumn.

In summary, we found the local minimum of the seeing at dusk in the Antarctic summer from both Tohoku DIMM and DF-DIMM observations. The local seeing minimum at dusk is considered to be caused by the disappearance of the surface boundary layer. Since temperature gradient and atmospheric convection are considered to coexist at dawn, the local seeing minimum would not occur at that period. In the Antarctic autumn, the local seeing minimum at dusk would be expected.

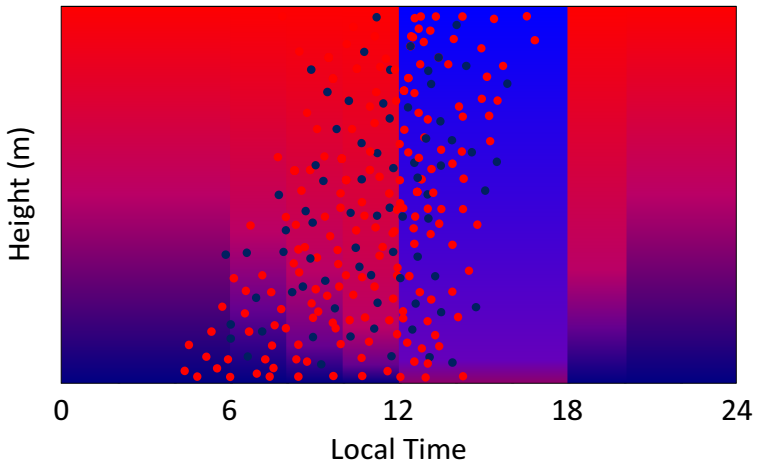

Figure 8.10: Schematics of the temperature distribution in the Antarctic summer. Dots and background gradations represent air parcels and temperature gradient, respectively. The color of them means the temperature difference (redder is hotter, and bluer is colder). At dusk, since there are no atmospheric convection and no temperature gradient. On the other hand, the temperature gradient and atmospheric convection coexist at dawn.

8.6 Estimation of the turbulence strength

In this section we roughly estimate the refractive-index structure constant C_n^2 in each layer. Total seeing ϵ can be represented as the sum of turbulent components with 5/3 power,

$$\epsilon^{5/3} = \epsilon_{FA}^{5/3} + \epsilon_{CZ}^{5/3} + \epsilon_{SBL}^{5/3} \ , \tag{8.1}$$

where subscript FA, CZ, and SBL mean the free atmosphere, the atmospheric convective zone, and the surface boundary layer, respectively. The relation between seeing ϵ and the refractive-index structure constant C_n^2 is written in Eq. (2.69). We can estimate the refractive-index structure constant C_n^2 in each turbulence component by calculating the seeing degradation caused in each layer.

Firstly, we study the contribution in the free atmosphere. Since the free atmosphere, i.e. seeing above the surface boundary layer was $0.23''$, the contribution can be calculated using Eq. (2.69),

$$\int_{h_{SBL}}^{h_{TOP}} C_n^2 dh = 5.9 \times 10^{-14} \ \ [m^{1/3}] \ , \tag{8.2}$$

where h_{SBL} and h_{TOP} mean the height of the surface boundary layer and the height at which C_n^2 decreases significantly to a background level. The median h_{SBL} on the fine weather was 15.3 m (Chap. 8.1). Since h_{TOP} was not measured in our observations, we assume h_{TOP} at Dome Fuji as the same value at Dome C, which is 10 km above the snow surface (Trinquet et al. 2008) [73]. We can make a rough estimate of C_n^2 in this layer, $C_{n,\ FA}^2$, assuming a constant C_n^2 in the free atmosphere,

$$C_{n,\ FA}^2 \sim 10^{-18} \ \ [m^{-2/3}] \ . \tag{8.3}$$

This is almost the same order of the background level (see Fig. 1.2). The result shows no significant turbulence in the free atmosphere.

Secondly, we elucidate the contribution to the total seeing by the atmospheric convection at the local daytime in the Antarctic summer. The difference between the lower limits of the seeing at the local daytime and at the local nighttime could be caused by the presence or absence of the atmospheric convection. Since the lower limit of the daytime and nighttime seeing at 11 m above the snow surface were $0.4''$ and $0.2''$, the contribution of the atmospheric convection is $0.3''$ calculated from Eq. (8.1). Thus the contribution of the atmospheric convection is,

$$\int_{h_{SBL}}^{h_{AC}} C_n^2 dh = 9 \times 10^{-14} \ \ [m^{1/3}] \ , \tag{8.4}$$

where h_{AC} means the upper height of the atmospheric convection. It is found to be ~ 300 m from the SODAR observations (Chap. 8.2).

The atmospheric convection can also be estimated from the median value of the seeing observations at 11 m above snow surface. The difference between the median seeing at the local daytime and at the local nighttime could be caused by the presence or absence of the atmospheric convection. From the median seeing at the local daytime ($0.56''$) and at the local nighttime ($0.47''$), the contribution of the atmospheric convection was $0.25''$. Thus the contribution of the atmospheric convection is,

$$\int_{11m}^{h_{AC}} C_n^2 dh = 6.8 \times 10^{-14} \ \ [m^{1/3}] \ . \tag{8.5}$$

This result is in agreement with the previous estimation of Eq. (8.4). We can make a rough estimate of C_n^2 in the convective zone $C_{n,\ CZ}^2$, assuming a constant C_n^2 in the atmospheric convective zone,

$$C_{n,\ CZ}^2 \sim 10^{-16} \ \ [m^{-2/3}] \ . \tag{8.6}$$

$C_{n,\ CZ}^2$ is two orders of magnitude larger than $C_{n,\ FA}^2$.

Thirdly, we obtain the refractive-index structure constant near the snow surface. Here we assume that the atmospheric turbulence structure was same on average in 2011 and 2013. Since the median seeing during nighttime at 2 m and 11 m above the snow surface were $1.3''$ and $0.47''$, the contribution of the atmospheric turbulence in this range is calculated to be $1.2''$ from Eq. (8.1). Therefore the turbulence in the range during nighttime is,

$$\int_{2m,\ Night}^{11m} C_n^2 dh = 8.7 \times 10^{-13} \ \ [m^{1/3}] \ . \tag{8.7}$$

The daytime turbulence is also obtained from the daytime median seeings. While daytime median seeing $0.98''$ at 2 m and $0.56''$ at 11 m above the snow surface, the contribution of the atmospheric turbulence is $0.73''$. The turbulence at the local daytime is,

$$\int_{2m,\ Day}^{11m} C_n^2 dh = 4.0 \times 10^{-13} \ \ [m^{1/3}] \ . \tag{8.8}$$

The turbulence strength is changed by factor two between the local daytime and the local nighttime. At the local nighttime, the turbulence strength was relatively strong, due to the strong temperature gradient near the snow surface.

Next we make a rough estimate of C_n^2 between 2 m and 11 m. At the local daytime, the atmospheric turbulence in this range is caused by the atmospheric convection. On the other hand, turbulence at the local nighttime is caused by the strong temperature gradient with the surface wind. C_n^2 in the surface boundary layer is estimated from the turbulence strength,

$$C_{n,\ SBL}^2 \sim 10^{-14} \ \ [m^{-2/3}] \ . \tag{8.9}$$

The value is $\sim 10^2$ times larger than $C_{n,\ CZ}^2$, and $\sim 10^4$ times larger than $C_{n,\ FA}^2$.

Finally, we calculate the expected seeing value as a function of the height from the snow surface, assuming constant C_n^2 in each layer. We use $C_{n,\ FA}^2$ 5.9×10^{-18}, $C_{n,\ CZ}^2$ 2.3×10^{-16}, daytime $C_{n,\ SBL}^2$ 4.4×10^{-14}, and nighttime $C_{n,\ SBL}^2$ 9.7×10^{-14} $[m^{-2/3}]$. Figure 8.11 is the seeing expected from $C_{n,\ FA}^2$, $C_{n,\ CZ}^2$, and $C_{n,\ SBL}^2$ integrated from a telescope height to the upper atmosphere. The seeing values between 11 m and 15.3 m are interpolated. The total seeing at the local daytime in the Antarctic summer is degraded by the atmospheric convection. It is also worsen by the temperature gradient with the surface wind at the local nighttime in the Antarctic summer. The seeing value was degraded drastically when the telescope was below the surface boundary layer.

The order estimations suggest that the turbulence strengths in the layers are different by a few orders. From our findings, it would be advised that the telescope should be constructed at the place least higher than the surface boundary layer.

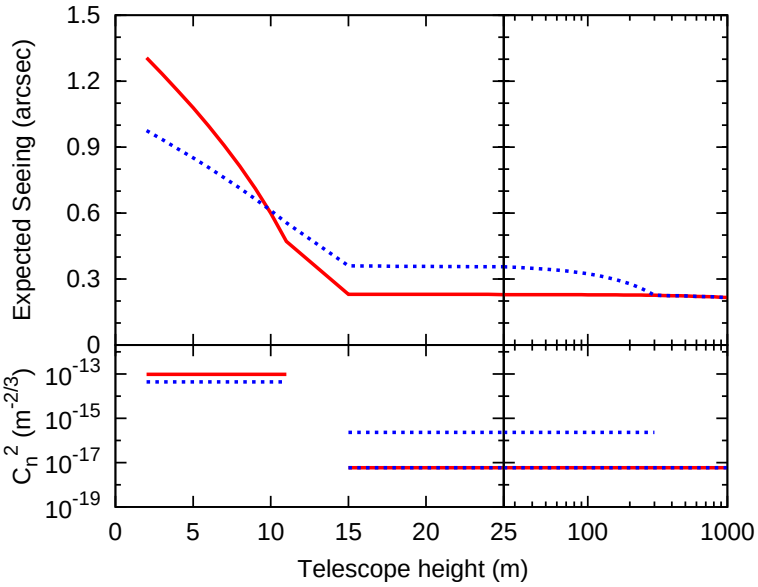

Figure 8.11: Expected seeing as a function of telescope height from the snow surface. Red solid line means the expected seeing without the atmospheric convection, e.g., as at the local nighttime in the Antarctic summer. Blue dot line means the expected seeing at the local daytime in the Antarctic summer. The seeing values between 11 m and 15.3 m are interpolated.

Chapter 9

Future prospects

In this chapter we discuss the necessary additional site testings and the future prospects for enjoying the excellent seeing at Dome Fuji.

9.1 Additional site testings

From our observations, we investigated the height of the surface boundary layer in fine weather in the Antarctic autumn and winter, the free-atmosphere seeing in the Antarctic summer, and the total seeing in the Antarctic summer. However, the surface wind speed, the free-atmosphere seeing in the Antarctic winter, the total seeing in the Antarctic winter, and the turbulence profile in the upper atmosphere at Dome Fuji are unknown yet. Then we propose some additional observations written below. (At the time of writing this thesis, February 2014, the campaigns to go to Dome Fuji has been canceled.)

9.1.1 Surface wind speed

As pointed out by Swain & Gallée (2006) [63] and Bonner et al. (2010a) [13], the height of the surface boundary layer is correlated with the surface wind speed. However, this correlation has not been confirmed yet. We planned to measure the surface wind speed simultaneously with Snodar in the 2010/2011 campaign, but we failed the measurements due to the insufficient preparations of the ultrasonic anemometers. If we can know the surface wind speed, the height of the surface boundary layer would roughly estimated. This is very helpful for site testings at the Antarctic plateau.

9.1.2 Free-atmosphere seeing in the Antarctic winter

From our observations, we obtained the free-atmosphere seeing at Dome Fuji in the Antarctic summer to be $0.23'' \pm 0.01''$ (statistical) $\pm 0.01''$ (systematic) in median. However, we could not discuss the free-atmosphere seeing in the Antarctic winter because our observations were performed only in the summer. In general, the wind speed of the polar vortex in the Antarctic winter is faster than that in the summer, the free-atmosphere seeing would be worse. To know the effect of the polar vortex in the Antarctic winter, the seeing measurements in the Antarctic winter are required.

9.1.3 Total seeing in the Antarctic winter

We estimated the total seeing at Dome Fuji in the Antarctic summer to be $1.1'' \pm 0.1''$ (statistical) $\pm$ $0.1''$ (systematic) in median. However, since Tohoku DIMM observations were performed only in the Antarctic summer, we have no informations about that in the Antarctic winter. Aristidi et al. (2009) [7] reported that the total seeing at Dome C in the Antarctic winter was worse than that in the Antarctic summer. This was because of the stronger temperature gradient in the Antarctic winter. With the same reason, the total seeing at Dome Fuji in the Antarctic winter would be worse than that in the Antarctic summer. To understand the behavior of the total seeing in the Antarctic winter, additional seeing measurements are required.

9.1.4 Turbulence profile in the upper atmosphere

We observed Dome Fuji seeings with Differential Image Motion Monitors (DIMM). Based on the observations, we obtained the free-atmosphere seeing and total seeing in the Antarctic summer. However, DIMM has no resolution for the turbulence height, so that the turbulence profile in the upper atmosphere has not been understood yet. Since the seeing has no dependency on the turbulence height, the turbulence profile in the upper atmosphere is not important. On the other hand, the stellar scintillation depends on $5/6 \sim 2$ power of the turbulence height (as written in Chap. 2.5.2). Accurate photometry is necessary for the study of the turbulence profile. For the adaptive optics and the interferometric observations, understanding of the turbulence profile in the upper atmosphere is important because these observations are strongly affected by the turbulence. Multi Aperture Scintillation Sensor (MASS) is one of the instruments to investigate the turbulence profile in the upper atmosphere (see Chap. 2.6.3). MASS restores the turbulence at 0.5, 1, 2, 4, 8, 16-km above the snow surface and gives the free-atmosphere seeing and the isoplanatic angle directly. Therefore, MASS should be used for the future additional site testings at Dome Fuji.

9.2 Astronomical observations at Dome Fuji

For ground-base astronomical observations, good seeing is important for high spatial resolution and deep imaging. Low surface boundary layer is helpful to construct and maintain a telescope. The stability of the surface boundary layer would make astronomical observations more efficient and precise.

Our observations unveiled the height of the surface boundary layer at Dome Fuji in fine weather in the Antarctic autumn and winter. The free-atmosphere seeing total seeing at Dome Fuji in the Antarctic summer were also clarified. The height of the surface boundary layer in fine weather in the Antarctic autumn and winter was expected 15.3-m in median, which is the second lowest value ever record in the Antarctic plateau. The height 15.3-m is sufficiently low for constructing an astronomical observatory. The free-atmosphere seeing and total seeing in the Antarctic summer were $0.23''$ and $1.1''$ in median, respectively. The free-atmosphere seeing of $0.23''$ is one of the best values on the Earth. These facts indicate that if a telescope is constructed at 15.3-m or higher above the snow surface, we can perform astronomical observations with excellent seeing of $0.23''$ at Dome Fuji.

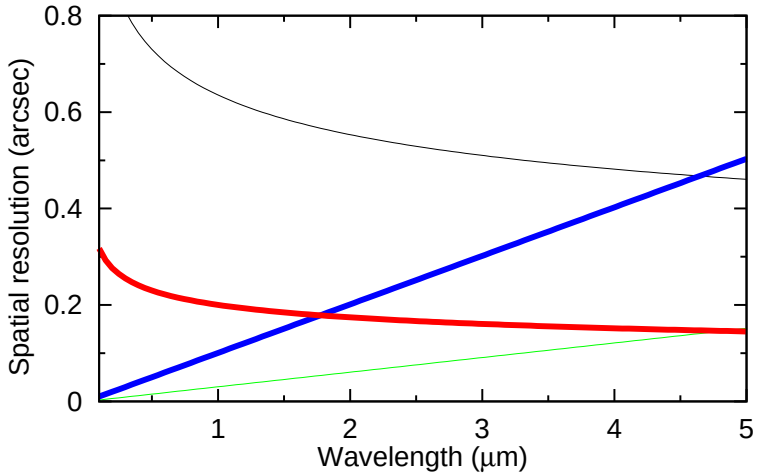

Figure 9.1: Wavelength dependency of the spatial resolution. Red bold line and black narrow lines mean the seeing limit 0.23″ for Dome Fuji and 0.73″ for Mauna Kea in Hawaii. Blue bold and green narrow lines are the Rayleight limits for AIRT250 with 2.5-m mirror and for Subaru telescope with 8.2-m mirror, respectively.

Tohoku University and the Consortium for the Antarctic Astronomy of Japan have proposed "Antarctic Infra-Red Telescope with a 250-cm mirror" (AIRT250) at Dome Fuji to enjoy infrared observations behind dark thermal background and low atmospheric absorption. The free-atmosphere seeing of 0.23″ at Dome Fuji also give us additional advantages in terms of both the high spatial resolution and precise photometry with AIRT250.

Figure 9.1 shows the wavelength dependency of the spatial resolution. It is calculated with 0.23″ seeing at 500 nm with 1/5 power low of the wavelength dependency. We also show the case of Subaru telescope at Mauna Kea in Hawaii (D= 8.2-m and $\epsilon = 0.73''$).

9.2.1 Infrared observations

For the infrared astronomical observations, the excellent free-atmosphere seeing at Dome Fuji has a strong advantage. Thanks to the excellent seeing at Dome Fuji, the diffraction of AIRT250 limits the spatial resolution at the wavelength longer than 1.6 μm. This means that at 1.6 μm or longer wavelengths, AIRT250 can enjoy the same spatial resolution of the Hubble Space Telescope with a 2.4-m mirror. Compared with the Subaru telescope without adaptive optics, AIRT250 has much higher spatial resolution at the wavelength of 4.4 μm or shorter.

The scientific motivation of the thesis is to find a good seeing site for understanding the galactic morphology in the early Universe. We can carry out the observations with twice higher spatial resolution ($\sim 0.3''$) than the current observatories. In the case of AIRT250, we will get 0.24″ spatial resolution at K-band (2.4μm), and 0.36″ at L-band (0.36μm).

9.2.2 Optical observations

For the optical astronomical observations, the excellent free-atmosphere seeing at Dome Fuji also brings a great advantage. At the wavelength shorter than 1.6 μm, the spatial resolution of AIRT250 is limited by the seeing. Adaptive optics can improve the spatial resolution at the near-infrared wavelengths. However, due to the technical difficulties, it

has not been applied to the optical wavelength ($< 0.9\ \mu$m). Therefore the spatial resolution at the optical wavelengths practically depends on the seeing at the site. AIRT250 at Dome Fuji can enjoy the good spatial resolution of $0.23''$ at optical wavelength, which is about one third of the spatial resolution at Mauna Kea in Hawaii. However, we should take care of the auroral emissions for the optical observations at Dome Fuji.

Chapter 10

Conclusions

Dome Fuji on the Antarctic plateau is one of the best astronomical sites on the Earth for the infrared astronomy in terms of dark thermal background and low atmospheric absorption. In addition the excellent astronomical seeing on the Antarctic plateau, which originates from unique meteorological and geographical conditions, is also expected. However, the seeing measurements at Dome Fuji were not performed because of the harsh environment and logistical limitation. Therefore, we developed the instruments durable in the Antarctic harsh environment, adapted the logistical limitations, and evaluated the seeing based on the observational data.

Snodar, PLATO-F, platinum thermometers equipped on the 16-m meteorological mast, AIRT40 with Tohoku DIMM, and DF-DIMM were developed for the site testings at Dome Fuji. We used SODAR, ultrasonic anemometers, and barometer, which are commercially available. SODAR observations in 2006/2007 and Snodar observations in 2011 were performed to investigate the turbulence profile above the snow surface. The platinum thermometers measured temperatures near the snow surface in 2011. Tohoku DIMM and DF-DIMM measured the astronomical seeing at 2-m and 11-m above the snow surface in the Antarctic summer, 2011 and 2013, respectively.

From Snodar and platinum thermometers observations, the height of the surface boundary layer in fine weather in the Antarctic autumn and winter was found 15.3 $\pm$ 0.8 (statistical) $\pm$ 0.8 (systematic) meters in median. The median absolute deviation (MAD) was 2.7-m. The height is a few meters higher than at Dome A (13.9-m), and about half of 23 $\sim$ 36-m at Dome C. The low surface boundary layer continues stably for several days. SODAR, Snodar, platinum thermometers, and DF-DIMM observations unveiled the existence of the atmospheric convection, which would occur in the local daytime in the Antarctic summer and autumn due to the solar insolation. The phenomenon was not discussed in the previous site testings on the Antarctic plateau. The atmospheric convection makes the lower limit (0.2″ to 0.4″) of the seeing observed at 11-m above the snow surface. DF-DIMM observations clarified the free-atmosphere seeing in the Antarctic summer to be 0.23″ $\pm$ 0.01″ (statistical) $\pm$ 0.01″ (systematic) in median. MAD was 0.057″. The excellent free-atmosphere seeing is consistent with the simulation (0.209″), and even better than that (0.27″ $\sim$ 0.36″) at Dome C. The seeing value is smallest ever recorded for ground-based astronomy on the Earth. Tohoku DIMM showed the total seeing in the Antarctic summer to be 1.1″ $\pm$ 0.1″ (statistical) $\pm$ 0.1″ (systematic) in median. MAD was 0.47″. The daytime total seeing is in good agreement with that at Dome C (0.95″

in median). Local seeing minimum at dusk in the Antarctic summer was also observed with both Tohoku DIMM and DF-DIMM. The local seeing minimum at dusk was also observed at Dome C. This phenomenon would be caused by the disappearance of the surface boundary layer at the time. From the roughly estimation of the refractive-index structure constants: the free atmosphere, the atmospheric convective zone, and the surface boundary layer were obtained to be $\sim 10^{-18}$, $\sim 10^{-16}$, and $\sim 10^{-14}$ $m^{-2/3}$, respectively. The turbulence strength dropped two orders of magnitude between the atmospheric convective zone and the free atmosphere, and dropped four orders of magnitude between the surface boundary layer and the free atmosphere. Assuming constant refractive-index structure constant in each layer, we also estimated the seeing value as a function of the height from the snow surface, and found that the seeing was drastically worsen if the telescope was in the surface boundary layer.

We studied the height of the surface boundary layer in fine weather in the Antarctic autumn and winter, the free-atmosphere seeing in the Antarctic summer, and the total seeing in the Antarctic summer. The atmospheric convection, local seeing minimum at dusk, turbulence strength at each layer were also discussed. Finally we summarize our findings of the present thesis as follows.

- The height of the surface boundary layer at Dome Fuji in fine weather in the Antarctic autumn and winter was 15.3 $\pm$ 0.8 (statistical) $\pm$ 0.8 (systematic) meters in median. MAD was 2.7-m. The height of the surface boundary layer remained low stable for several days.

- The atmospheric convection arose in the local daytime in the Antarctic summer and autumn, and it built the surface boundary layer.

- The free-atmosphere seeing at Dome Fuji in the Antarctic summer was $0.23'' \pm 0.01''$ (statistical) $\pm$ $0.01''$ (systematic) in median. MAD was $0.057''$.

- The total seeing at Dome Fuji in the Antarctic summer was $1.1'' \pm 0.1''$ (statistical) $\pm$ $0.1''$ (systematic) in median. MAD was $0.47''$.

- The disappearance of the surface boundary layer made the local seeing minimum at dusk in the Antarctic summer.

- The turbulence strength in the surface boundary layer by two orders of magnitude of the atmospheric convection, and by four orders of magnitude of the free atmosphere.

Acknowledgments

First of all, I would like to thank my supervisor, Prof. Takashi Ichikawa. Prof. Ichikawa gave me great opportunities to go to the Antarctica. I greatly thank Dr. Naruhisa Takato, Prof. Michael C. B. Ashley, and Prof. John W. V. Storey who gave me many invaluable advices and comments for my research. I would also like to thank all of members of the 47^{th}, 48^{th}, 51^{st}, 52^{nd}, 53^{rd}, and 54^{th} Japanese Antarctic Research Expeditions for their great supports.

I acknowledge Dr. Kentaro Motohara for his helpful supports for development of Tohoku-DIMM. I am also thankful to Fumihiro Uraguchi, for set-up and calibrations for SODAR. Dr. Koji Kawabata, Dr. Hiroshi Akitaya, Dr. Kiyoshi Sakimoto, and Dr. Ryosuke Itoh, who are members of Higashi-Hiroshima Observatory, gave me friendly supports for calibration of DF-DIMM.

This research is fully/partially supported by the National Institute of Polar Research through Project Research No. KP-12, Japan Society for the Promotion of Science Grants-in-Aid for Scientific Research Number 18340050 and 23103002, the Mitsubishi Foundation, the Australian Research Council and Australian government infrastructure funding managed by Astronomy Australia Limited. Cold test was carried out under the Joint Research Program of the Institute of Low Temperature Science, Hokkaido University. I appreciate the Sasakawa Scientific Research Grant from The Japan Science Society, and Tohoku University International Advanced Research and Education Organization for scholarships and research expenses.

Finally, I would like to thank my parents Fumio Okita and Takako Okita. I would also like to express my supreme thank to my wife Kanako who married me even though I was still a student.

Bibliography

[1] A. Agabi, E. Aristidi, M. Azouit, E. Fossat, F. Martin, T. Sadibekova, J. Vernin, and A. Ziad. First Whole Atmosphere Nighttime Seeing Measurements at Dome C, Antarctica. PASP, 118:344–348, Feb. 2006.

[2] M. I. Andersen, K. Pedersen, and A. N. Sørensen. Site testing on the Greenland Ice Cap. *Highlights of Astronomy*, 15:634–635, Nov. 2010.

[3] L. C. Andrews. *Field Guide to Atmospheric Optics*. SPIE The International Society for Optical Engineering, 2004.

[4] E. Aristidi, A. Agabi, E. Fossat, M. Azouit, F. Martin, T. Sadibekova, T. Travouillon, J. Vernin, and A. Ziad. Site testing in summer at Dome C, Antarctica. A&A, 444:651–659, Dec. 2005.

[5] E. Aristidi, A. Agabi, J. Vernin, M. Azouit, F. Martin, A. Ziad, and E. Fossat. Antarctic site testing: First daytime seeing monitoring at Dome C. A&A, 406:L19–L22, July 2003.

[6] E. Aristidi, K. Agabi, M. Azouit, E. Fossat, J. Vernin, T. Travouillon, J. S. Lawrence, C. Meyer, J. W. V. Storey, B. Halter, W. L. Roth, and V. Walden. An analysis of temperatures and wind speeds above Dome C, Antarctica. A&A, 430:739–746, Feb. 2005.

[7] E. Aristidi, E. Fossat, A. Agabi, D. Mékarnia, F. Jeanneaux, E. Bondoux, Z. Challita, A. Ziad, J. Vernin, and H. Trinquet. Dome C site testing: surface layer, free atmosphere seeing, and isoplanatic angle statistics. A&A, 499:955–965, June 2009.

[8] M. C. B. Ashley, G. Allen, C. S. Bonner, S. G. Bradley, X. Cui, J. R. Everett, L. Feng, X. Gong, S. Hengst, J. Hu, Z. Jiang, C. A. Kulesa, J. S. Lawrence, Y. Li, D. M. Luong-Van, M. J. McCaughrean, A. M. Moore, C. Pennypacker, W. Qin, R. Riddle, Z. Shang, J. W. V. Storey, B. Sun, N. Suntzeff, N. F. H. Tothill, T. Travouillon, C. K. Walker, L. Wang, J. Yan, H. Yang, D. G. York, X. Yuan, X. Zhang, Z. Zhang, X. Zhou, and Z. Zhu. The PLATO observatory: robotic astronomy from the Antarctic plateau. *Highlights of Astronomy*, 15:627–629, Nov. 2010.

[9] M. C. B. Ashley, G. Allen, C. S. Bonner, S. G. Bradley, X. Cui, J. R. Everett, L. Feng, X. Gong, S. Hengst, J. Hu, Z. Jiang, C. A. Kulesa, J. S. Lawrence, Y. Li, D. M. Luong-van, M. J. McCaughrean, A. M. Moore, C. Pennypacker, W. Qin, R. Riddle, Z. Shang, J. W. V. Storey, B. Sun, N. Suntzeff, N. F. H. Tothill, T. Travouillon, C. K. Walker, L. Wang, J. Yan, H. Yang, J. Yang, D. G. York, X. Yuan, X. Zhang, Z. Zhang,

X. Zhou, and Z. Zhu. PLATO-a robotic observatory for the Antarctic plateau. In L. Spinoglio and N. Epchtein, editors, *EAS Publications Series*, volume 40 of *EAS Publications Series*, pages 79–84, 2010.

[10] M. C. B. Ashley, C. S. Bonner, J. R. Everett, J. S. Lawrence, D. Luong-van, S. McDaid, C. McLaren, and J. W. V. Storey. Future development of the PLATO Observatory for Antarctic science. In *Society of Photo-Optical Instrumentation Engineers (SPIE) Conference Series*, volume 7735 of *Society of Photo-Optical Instrumentation Engineers (SPIE) Conference Series*, July 2010.

[11] A. Berdja, G. Prieto, and J. E. Thomas-Osip. First results from optical turbulence measurements at Cerro Las Campanas in 2010. MNRAS, 416:553–558, Sept. 2011.

[12] E. Bertin and S. Arnouts. SExtractor: Software for source extraction. A&AS, 117:393–404, June 1996.

[13] C. S. Bonner, M. C. B. Ashley, S. G. Bradley, X. Cui, L. Feng, X. Gong, J. S. Lawrence, D. M. Luong-van, Z. Shang, J. W. V. Storey, L. Wang, H. Yang, J. Yang, X. Zhou, and Z. Zhu. Snodar: 2009 performance at Dome A, Antarctica. In *Society of Photo-Optical Instrumentation Engineers (SPIE) Conference Series*, volume 7733 of *Society of Photo-Optical Instrumentation Engineers (SPIE) Conference Series*, July 2010.

[14] C. S. Bonner, M. C. B. Ashley, X. Cui, L. Feng, X. Gong, J. S. Lawrence, D. M. Luong-van, Z. Shang, J. W. V. Storey, L. Wang, H. Yang, J. Yang, X. Zhou, and Z. Zhu. Thickness of the Atmospheric Boundary Layer Above Dome A, Antarctica, during 2009. PASP, 122:1122–1131, Sept. 2010.

[15] C. S. Bonner, M. C. B. Ashley, J. S. Lawrence, D. M. Luong-Van, and J. W. V. Storey. Snodar: An acoustic radar for atmospheric turbulence profiling with 1m resolution. *Acoustics Australia*, 37:47–51, Aug. 2009.

[16] C. S. Bonner, M. C. B. Ashley, J. S. Lawrence, J. W. V. Storey, D. M. Luong-Van, and S. G. Bradley. Snodar: a new instrument to measure the height of the boundary layer on the Antarctic plateau. In *Society of Photo-Optical Instrumentation Engineers (SPIE) Conference Series*, volume 7014 of *Society of Photo-Optical Instrumentation Engineers (SPIE) Conference Series*, Aug. 2008.

[17] M. Burton, D. K. Aitken, D. A. Allen, M. C. B. Ashley, M. G. Burton, R. D. Cannon, B. D. Carter, G. S. Da Costa, M. A. Dopita, M. L. Duldig, P. G. Edwards, P. R. Gillingham, P. J. Hall, A. R. Hyland, P. J. McGregor, J. R. Mould, R. P. Norris, E. M. Sadler, C. H. Smith, J. Spyromilio, and J. W. V. Storey. The scientific potential for astronomy from the Antarctic Plateau. *Proceedings of the Astronomical Society of Australia*, 11:127–150, Aug. 1994.

[18] S. Chiyonobe. "Development a seeing monitor and seeing measurement at a candidate site for Hiroshima University 1.5 m in diameter telescope (広島大学 1.5m 望遠鏡移設地シーイングのモニター装置開発と測定)", Feb. 2004. Bachelor's thesis, Physical Science, Faculty of Science, Hiroshima Univesity.

[19] W. Dali Ali, A. Ziad, A. Berdja, J. Maire, J. Borgnino, M. Sarazin, G. Lombardi, J. Navarrete, H. Vazquez Ramio, M. Reyes, J. M. Delgado, J. J. Fuensalida, A. Tokovinin, and E. Bustos. Multi-instrument measurement campaign at Paranal in 2007. Characterization of the outer scale and the seeing of the surface layer. A&A, 524:A73, Dec. 2010.

[20] D. L. Fried. Statistics of a Geometric Representation of Wavefront Distortion. *Journal of the Optical Society of America (1917-1983)*, 55:1427–1431, Nov. 1965.

[21] D. L. Fried. Optical Resolution Through a Randomly Inhomogeneous Medium for Very Long and Very Short Exposures. *Journal of the Optical Society of America (1917-1983)*, 56:1372, Oct. 1966.

[22] D. L. Fried. Differential angle of arrival - Theory, evaluation, and measurement feasibility. *Radio Science*, 10:71–76, Jan. 1975.

[23] J. W. Hardy. *Adaptive Optics for Astronomical Telescopes*. Oxford University Press, July 1998.

[24] D. A. Harper. Infrared astronomy in Antarctica. In D. J. Mullan, M. A. Pomerantz, and T. Stanev, editors, *American Institute of Physics Conference Series*, volume 198 of *American Institute of Physics Conference Series*, pages 123–129, Jan. 1990.

[25] S. Hengst, G. R. Allen, M. C. B. Ashley, J. R. Everett, J. S. Lawrence, D. M. Luong-Van, and J. W. V. Storey. PLATO power: a robust low environmental impact power generation system for the Antarctic plateau. In *Society of Photo-Optical Instrumentation Engineers (SPIE) Conference Series*, volume 7012 of *Society of Photo-Optical Instrumentation Engineers (SPIE) Conference Series*, Aug. 2008.

[26] S. Hengst, D. M. Luong-Van, J. R. Everett, J. S. Lawrence, M. C. B. Ashley, D. Castel, and J. W. V. Storey. A small, high-efficiency diesel generator for high-altitude use in Antarctica. *International Journal of Energy Research*, 34:827–838, July 2010.

[27] S. L. Kenyon, J. S. Lawrence, M. C. B. Ashley, J. W. V. Storey, A. Tokovinin, and E. Fossat. Atmospheric Scintillation at Dome C, Antarctica: Implications for Photometryand Astrometry. PASP, 118:924–932, June 2006.

[28] A. Kolmogorov. The Local Structure of Turbulence in Incompressible Viscous Fluid for Very Large Reynolds' Numbers. *Akademiia Nauk SSSR Doklady*, 30:301–305, 1941.

[29] V. Kornilov, A. Tokovinin, N. Shatsky, O. Voziakova, S. Potanin, and B. Safonov. Combined MASS-DIMM instruments for atmospheric turbulence studies. MNRAS, 382:1268–1278, Dec. 2007.

[30] V. Kornilov, A. A. Tokovinin, O. Vozyakova, A. Zaitsev, N. Shatsky, S. F. Potanin, and M. S. Sarazin. MASS: a monitor of the vertical turbulence distribution. In P. L. Wizinowich and D. Bonaccini, editors, *Adaptive Optical System Technologies II*, volume 4839 of *Society of Photo-Optical Instrumentation Engineers (SPIE) Conference Series*, pages 837–845, Feb. 2003.

[31] J. Krause-Polstorff, E. A. Murphy, and D. L. Walters. Instrument comparison - Corrected stellar scintillometer versus isoplanometer. Appl. Opt., 32:4051–4057, July 1993.

[32] K. Krisciunas. Optical Night-Sky Brightness at Mauna Kea over the Course of a Complete Sunspot Cycle. PASP, 109:1181–1188, Oct. 1997.

[33] K. Krisciunas and B. E. Schaefer. A model of the brightness of moonlight. PASP, 103:1033–1039, Sept. 1991.

[34] K. Krisciunas, W. Sinton, K. Tholen, A. Tokunaga, W. Golisch, D. Griep, C. Kaminski, C. Impey, and C. Christian. Atmospheric Extinction and Night-Sky Brightness at Mauna-Kea. PASP, 99:887, Aug. 1987.

[35] J. S. Lawrence, G. R. Allen, M. C. B. Ashley, C. Bonner, S. Bradley, X. Cui, J. R. Everett, L. Feng, X. Gong, S. Hengst, J. Hu, Z. Jiang, C. A. Kulesa, Y. Li, D. Luong-Van, A. M. Moore, C. Pennypacker, W. Qin, R. Riddle, Z. Shang, J. W. V. Storey, B. Sun, N. Suntzeff, N. F. H. Tothill, T. Travouillon, C. K. Walker, L. Wang, J. Yan, J. Yang, H. Yang, D. York, X. Yuan, X. G. Zhang, Z. Zhang, X. Zhou, and Z. Zhu. The PLATO Antarctic site testing observatory. In *Society of Photo-Optical Instrumentation Engineers (SPIE) Conference Series*, volume 7012 of *Society of Photo-Optical Instrumentation Engineers (SPIE) Conference Series*, Aug. 2008.

[36] J. S. Lawrence, M. C. B. Ashley, and J. W. V. Storey. Autonomous observatories for the Antarctic plateau. In M. G. Burton, X. Cui, and N. F. H. Tothill, editors, *IAU Symposium*, volume 288 of *IAU Symposium*, pages 6–14, Jan. 2013.

[37] J. S. Lawrence, M. C. B. Ashley, A. Tokovinin, and T. Travouillon. Exceptional astronomical seeing conditions above Dome C in Antarctica. Nature, 431:278–281, Sept. 2004.

[38] C. G. Little. Acoustic methods for the remote probing of the lower atmosphere. In *Proceedings of the IEEE*, volume 57, pages 571–578, Apr. 1969.

[39] R. F. Loewenstein, C. Bero, J. P. Lloyd, F. Mrozek, J. Bally, and D. Theil. Astronomical Seeing at the South Pole. In G. Novak and R. Landsberg, editors, *Astrophysics From Antarctica*, volume 141 of *Astronomical Society of the Pacific Conference Series*, page 296, 1998.

[40] G. C. Loos and C. B. Hogge. Turbulence of the upper atmosphere and isoplanatism. Appl. Opt., 18:2654–2661, Aug. 1979.

[41] D. M. Luong-Van, M. C. B. Ashley, J. R. Everett, J. S. Lawrence, and J. W. V. Storey. PLATO control and robotics. In *Society of Photo-Optical Instrumentation Engineers (SPIE) Conference Series*, volume 7019 of *Society of Photo-Optical Instrumentation Engineers (SPIE) Conference Series*, Aug. 2008.

[42] R. D. Marks. Astronomical seeing from the summits of the Antarctic plateau. A&A, 385:328–336, Apr. 2002.

[43] R. D. Marks, J. Vernin, M. Azouit, J. F. Manigault, and C. Clevelin. Measurement of optical seeing on the high antarctic plateau. A&AS, 134:161–172, Jan. 1999.

[44] F. Martin, R. Conan, A. Tokovinin, A. Ziad, H. Trinquet, J. Borgnino, A. Agabi, and M. Sarazin. Optical parameters relevant for High Angular Resolution at Paranal from GSM instrument and surface layer contribution. A&AS, 144:39–44, May 2000.

[45] H. M. Martin. Image motion as a measure of seeing quality. PASP, 99:1360–1370, Dec. 1987.

[46] K. Motohara, T. Aoki, S. Sako, T. Soyano, M. Doi, M. Tanaka, T. Tanabe, T. Handa, N. Mitani, T. Minezaki, T. Miyata, K. Kawara, K. Kohno, K. Tarusawa, Y. Yoshii, L. Bronfman, M. T. Ruiz, F. Uraguchi, and N. Takato. Seeing environment at a 5640m altitude of Co. Chajnantor in northern Chile. In *Society of Photo-Optical Instrumentation Engineers (SPIE) Conference Series*, volume 7012 of *Society of Photo-Optical Instrumentation Engineers (SPIE) Conference Series*, Aug. 2008.

[47] K. Motohara, M. Doi, T. Soyano, M. Tanaka, K. Kohno, T. Miyata, N. Takato, and F. Uraguchi. University of Tokyo DIMM: a portable DIMM for site testing at Atacama. In A. L. Ardeberg and T. Andersen, editors, *Society of Photo-Optical Instrumentation Engineers (SPIE) Conference Series*, volume 5382 of *Society of Photo-Optical Instrumentation Engineers (SPIE) Conference Series*, pages 648–655, July 2004.

[48] C. Murata. "Development a 40-cm infrared telescope for the Antarctica (南極 40cm 赤外線望遠鏡の開発)". Master's thesis, Astronomical Institute, Graduate School of Science, Tohoku University, Mar. 2009.

[49] C. Murata, T. Ichikawa, R. G. Lundock, Y. Taniguchi, and H. Okita. A 40-cm infrared telescope in Antarctica. In *Society of Photo-Optical Instrumentation Engineers (SPIE) Conference Series*, volume 7012 of *Society of Photo-Optical Instrumentation Engineers (SPIE) Conference Series*, Aug. 2008.

[50] H. Okita, T. Ichikawa, M. C. B. Ashley, N. Takato, and H. Motoyama. Excellent daytime seeing at Dome Fuji on the Antarctic plateau. A&A, 554:L5, June 2013.

[51] H. Okita, T. Ichikawa, T. Yoshikawa, R. G. Lundock, and K. Kurita. Antarctic Infra-Red Telescope with a 40cm primary mirror (AIRT40): development and improvement. In *Society of Photo-Optical Instrumentation Engineers (SPIE) Conference Series*, volume 7733 of *Society of Photo-Optical Instrumentation Engineers (SPIE) Conference Series*, July 2010.

[52] H. Okita, N. Takato, T. Ichikawa, C. S. Bonner, M. C. B. Ashley, J. W. V. Storey, and 51st and 52nd JARE Dome Fuji team. Dome Fuji Seeing -the Summer Results and the Future Winter-over Observations. In *IAU Symposium*, volume 288 of *IAU Symposium*, pages 25–28, Jan. 2013.

[53] W. Pence. CFITSIO, v2.0: A New Full-Featured Data Interface. In D. M. Mehringer, R. L. Plante, and D. A. Roberts, editors, *Astronomical Data Analysis Software and Systems VIII*, volume 172 of *Astronomical Society of the Pacific Conference Series*, page 487, 1999.

[54] A. Quirrenbach. Observing Through the Turbulent Atmosphere. In P. R. Lawson, editor, *Principles of Long Baseline Stellar Interferometry*, page 71, 2000.

[55] F. Roddier. The effects of atmospheric turbulence in optical astronomy. *Progress in optics. Volume 19. Amsterdam, North-Holland Publishing Co., 1981, p. 281-376.*, 19:281–376, 1981.

[56] M. Sarazin and F. Roddier. The ESO differential image motion monitor. A&A, 227:294–300, Jan. 1990.

[57] W. Saunders, J. S. Lawrence, J. W. V. Storey, M. C. B. Ashley, S. Kato, P. Minnis, D. M. Winker, G. Liu, and C. Kulesa. Where Is the Best Site on Earth? Domes A, B, C, and F, and Ridges A and B. PASP, 121:976–992, Sept. 2009.

[58] M. Schöck, S. Els, R. Riddle, W. Skidmore, T. Travouillon, R. Blum, E. Bustos, G. Chanan, S. G. Djorgovski, P. Gillett, B. Gregory, J. Nelson, A. Otárola, J. Seguel, J. Vasquez, A. Walker, D. Walker, and L. Wang. Thirty Meter Telescope Site Testing I: Overview. PASP, 121:384–395, Apr. 2009.

[59] W. Skidmore, S. Els, T. Travouillon, R. Riddle, M. Schöck, E. Bustos, J. Seguel, and D. Walker. Thirty Meter Telescope Site Testing V: Seeing and Isoplanatic Angle. PASP, 121:1151–1166, Oct. 2009.

[60] D. B. Soules, J. J. Drexler, B. F. Draayer, F. D. Eaton, and J. R. Hines. Exposure-Time Effects on Differential r0 Measurements. PASP, 108:817, Sept. 1996.

[61] E. Steinbring, M. Millar-Blanchaer, W. Ngan, R. Murowinski, B. Leckie, and R. Carlberg. Preliminary DIMM and MASS Nighttime Seeing Measurements at PEARL in the Canadian High Arctic. PASP, 125:866–877, July 2013.

[62] J. W. V. Storey, M. C. B. Ashley, Y. Augarten, C. S. Bonner, M. G. Burton, L. Bycroft, J. R. Everett, J. S. Lawrence, D. Luong-Van, S. McDaid, C. McLaren, and G. Summers. The PLATO Robotic Antarctic observatory design and development program. In *Astronomical Society of India Conference Series*, volume 7 of *Astronomical Society of India Conference Series*, page 97, 2012.

[63] M. R. Swain and H. Gallée. Antarctic Boundary Layer Seeing. PASP, 118:1190–1197, Aug. 2006.

[64] N. Takato, F. Uraguchi, H. Motoyama, K. Fukui, M. Taguchi, T. Ichikawa, Y. Taniguchi, and C. Murata. Preliminary evaluation of dome fuji as a possible site for an infrared astronomical observatory -sodar measurement of atmospheric turbulence in the boundary layer in antarctic summer-. *Antarctic record*, 52:182–192, June 2008.

[65] V. I. Tatarskii. *Wave Propagation in Turbulent Medium.* McGraw-Hill, 1961.

[66] V. I. Tatarskii. *The effects of the turbulent atmosphere on wave propagation.* Israel Program for Scientific Translations, 1971.

[67] J. E. Thomas-Osip, G. Prieto, A. Berdja, K. W. Cook, S. Villanueva, D. L. Depoy, J. L. Marshall, J. P. Rheault, R. D. Allen, and D. W. Carona. Characterizing Optical Turbulence at the GMT Site with MooSci and MASS-DIMM. PASP, 124:84–93, Jan. 2012.

[68] A. Tokovinin. A new method of measuring atmospheric seeing. *Astronomy Letters*, 24:662–664, Sept. 1998.

[69] A. Tokovinin. From Differential Image Motion to Seeing. PASP, 114:1156–1166, Oct. 2002.

[70] A. Tokovinin, V. Kornilov, N. Shatsky, and O. Voziakova. Restoration of turbulence profile from scintillation indices. MNRAS, 343:891–899, Aug. 2003.

[71] T. Travouillon, M. C. B. Ashley, M. G. Burton, J. W. V. Storey, P. Conroy, G. Hovey, M. Jarnyk, R. Sutherland, and R. F. Loewenstein. Automated Shack-Hartmann seeing measurements at the South Pole. A&A, 409:1169–1173, Oct. 2003.

[72] T. Travouillon, M. C. B. Ashley, M. G. Burton, J. W. V. Storey, and R. F. Loewenstein. Atmospheric turbulence at the South Pole and its implications for astronomy. A&A, 400:1163–1172, Mar. 2003.

[73] H. Trinquet, A. Agabi, J. Vernin, M. Azouit, E. Aristidi, and E. Fossat. Nighttime Optical Turbulence Vertical Structure above Dome C in Antarctica. PASP, 120:203–211, Feb. 2008.

[74] F. Uraguchi, K. Motohara, M. Doi, N. Takato, A. Miyashita, T. Tanabe, S. Oyabu, and T. Soyano. Simultaneous seeing measurements at Atacama. In J. M. Oschmann, Jr., editor, *Society of Photo-Optical Instrumentation Engineers (SPIE) Conference Series*, volume 5489 of *Society of Photo-Optical Instrumentation Engineers (SPIE) Conference Series*, pages 218–226, Oct. 2004.

[75] F. Uraguchi, N. Takato, I. Iwata, H. Koyano, and Y. Mikami. First results from turbulence profiling with SODAR at Subaru Telescope. In *Society of Photo-Optical Instrumentation Engineers (SPIE) Conference Series*, volume 7012 of *Society of Photo-Optical Instrumentation Engineers (SPIE) Conference Series*, Aug. 2008.

[76] F. Uraguchi, N. Takato, A. Miyashita, and T. Usuda. The DIMM station at Subaru Telescope. In *Society of Photo-Optical Instrumentation Engineers (SPIE) Conference Series*, volume 6267 of *Society of Photo-Optical Instrumentation Engineers (SPIE) Conference Series*, July 2006.

[77] H. Vázquez Ramió, J. Vernin, C. Muñoz-Tuñón, M. Sarazin, A. M. Varela, H. Trinquet, J. M. Delgado, J. J. Fuensalida, M. Reyes, A. Benhida, Z. Benkhaldoun, D. G. Lambas, Y. Hach, M. Lazrek, G. Lombardi, J. Navarrete, P. Recabarren, V. Renzi, M. Sabil, and R. Vrech. European Extremely Large Telescope Site Characterization. II. High Angular Resolution Parameters. PASP, 124:868–884, Aug. 2012.

[78] J. Vernin and C. Muñoz-Tuñón. Optical seeing at La Palma Observatory. 2: Intensive site testing campaign at the Nordic Optical Telescope. A&A, 284:311–318, Apr. 1994.

[79] T. Yamanouchi, N. Hirasawa, M. Hayashi, S. Takahashi, and S. Kaneto. Meteorological characteristics of antarctic inland station, dome fuji (scientific paper). *Memoirs of National Institute of Polar Research. Special issue*, 57:94–104, mar 2003.

[80] A. Ziad, E. Aristidi, A. Agabi, J. Borgnino, F. Martin, and E. Fossat. First statistics of the turbulence outer scale at Dome C. A&A, 491:917–921, Dec. 2008.

[81] A. Ziad, R. Conan, A. Tokovinin, F. Martin, and J. Borgnino. From the Grating Scale Monitor to the Generalized Seeing Monitor. Appl. Opt., 39:5415–5425, Oct. 2000.

Appendix A

SODAR results

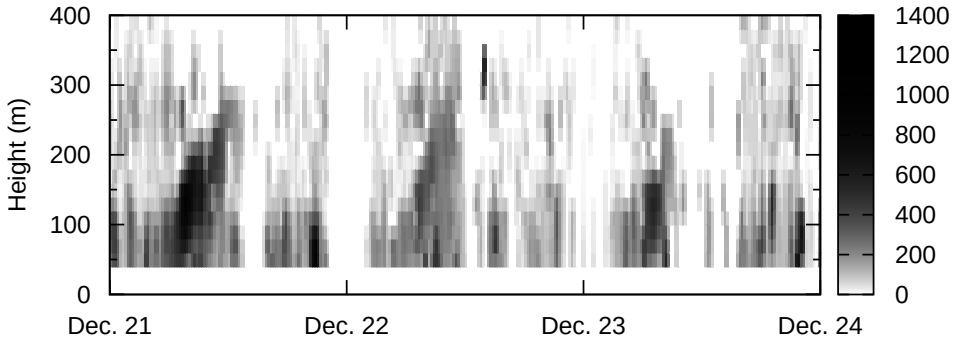

Figure A.1: Time series of the turbulence strength obtained with SODAR from December 21 00:00 (UTC+3) to December 23 24:00, 2006. The density bar represents the turbulence strength in arbitrary unit. Under 40 m above the snow surface, SODAR had no sensibility.

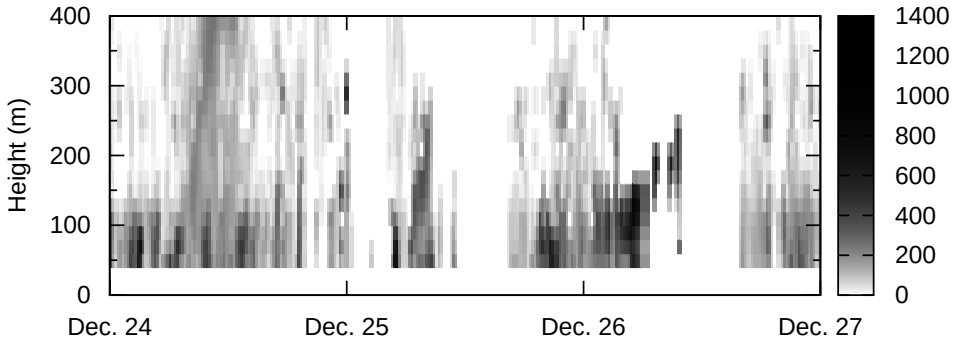

Figure A.2: Same as Fig. A.1, but for the period from December 24 00:00 (UTC+3) to December 26 24:00, 2006.

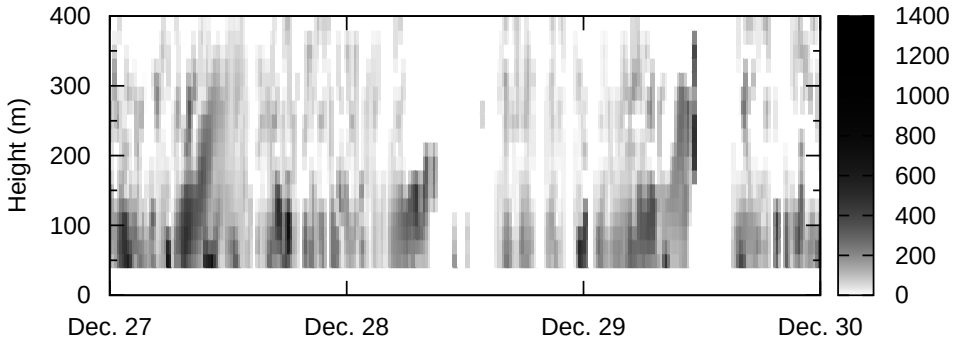

Figure A.3: Same as Fig. A.1, but for the period from December 27 00:00 (UTC+3) to December 29 24:00, 2006.

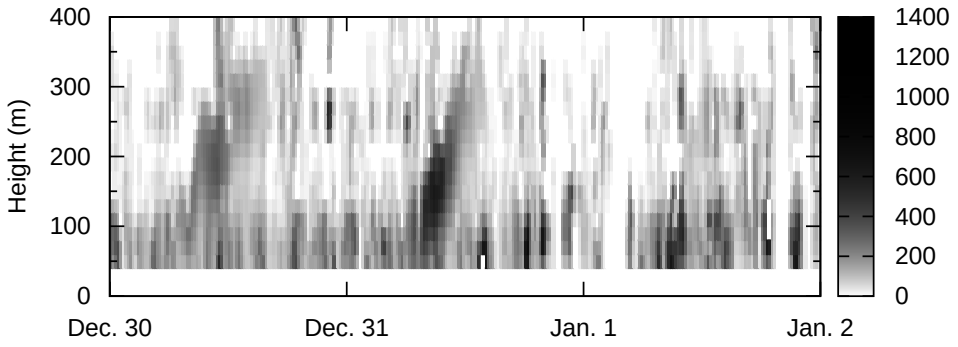

Figure A.4: Same as Fig. A.1, but for the period from December 30 00:00 (UTC+3), 2006 to January 1 24:00, 2007.

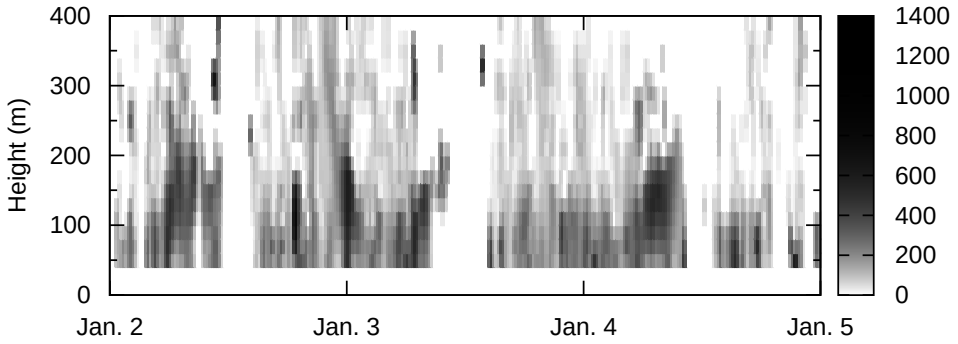

Figure A.5: Same as Fig. A.1, but for the period from January 2 00:00 (UTC+3) to January 4 24:00, 2007.

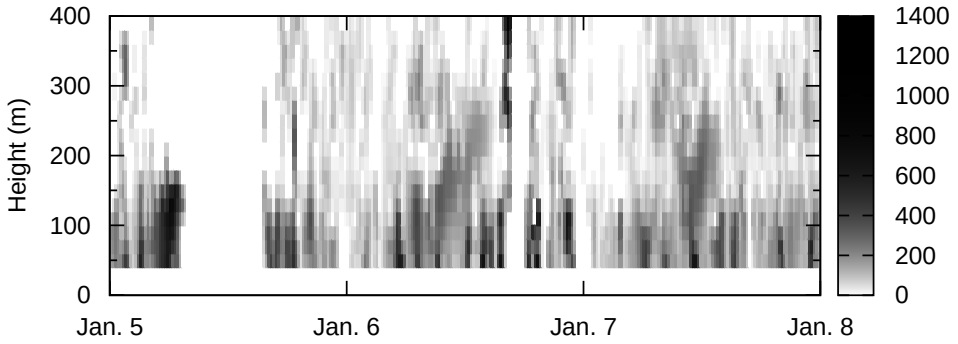

Figure A.6: Same as Fig. A.1, but for the period from January 5 00:00 (UTC+3) to January 7 24:00, 2007.

Appendix B

Snodar results

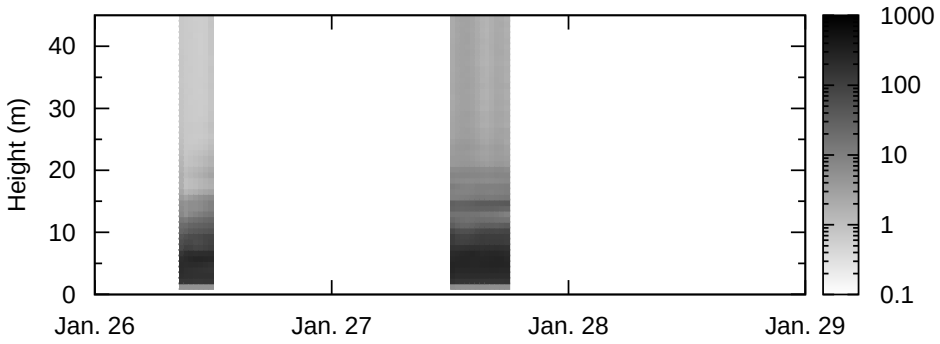

Figure B.1: Time series of the turbulence strength obtained with Snodar from January 26 00:00 (UTC+3) to January 28 24:00, 2011. The density bar represents the turbulence strength in arbitrary unit. The vertical resolution is 0.9 m.

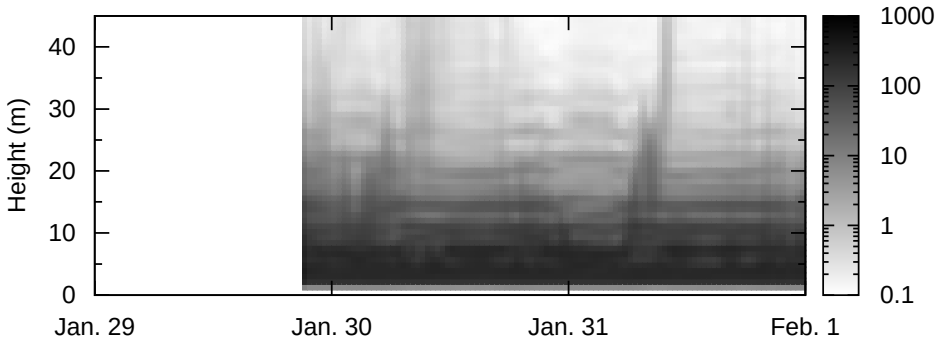

Figure B.2: Same as Fig. B.1, but for the period from January 29 00:00 (UTC+3) to January 31, 2011.

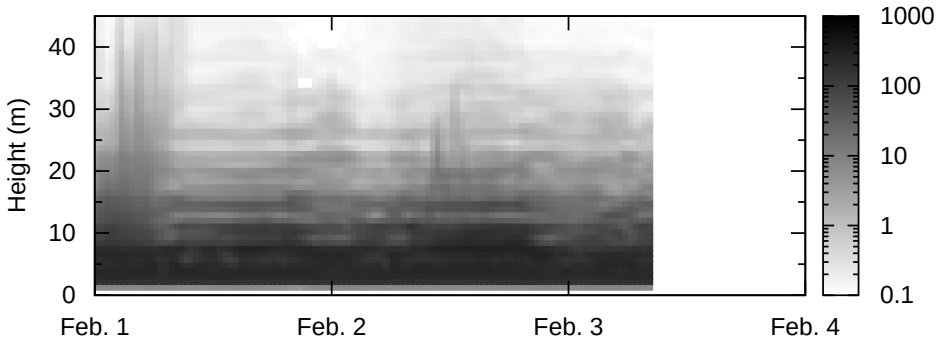

Figure B.3: Same as Fig. B.1, but for the period from February 1 00:00 (UTC+3) to February 3 24:00, 2011.

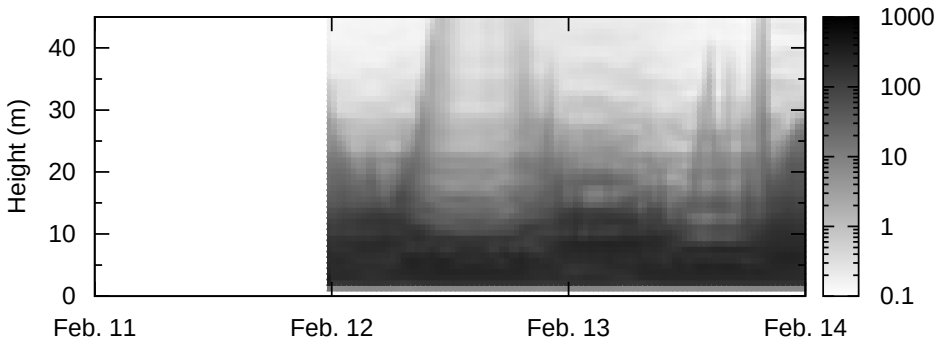

Figure B.4: Same as Fig. B.1, but for the period from February 11 00:00 (UTC+3) to February 13 24:00, 2011.

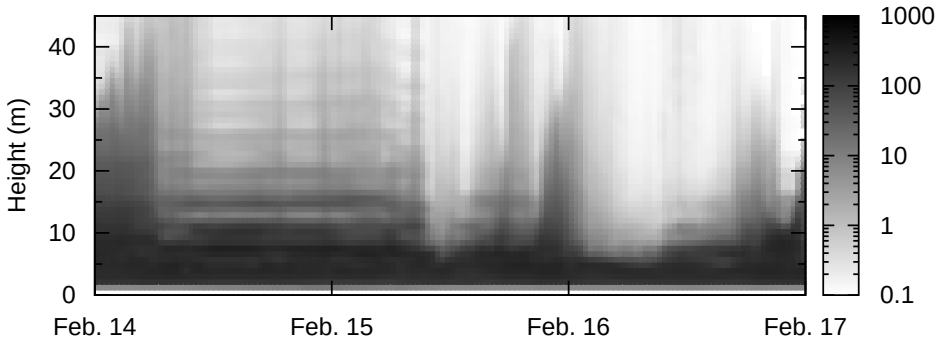

Figure B.5: Same as Fig. B.1, but for the period from February 14 00:00 (UTC+3) to February 16 24:00, 2011.

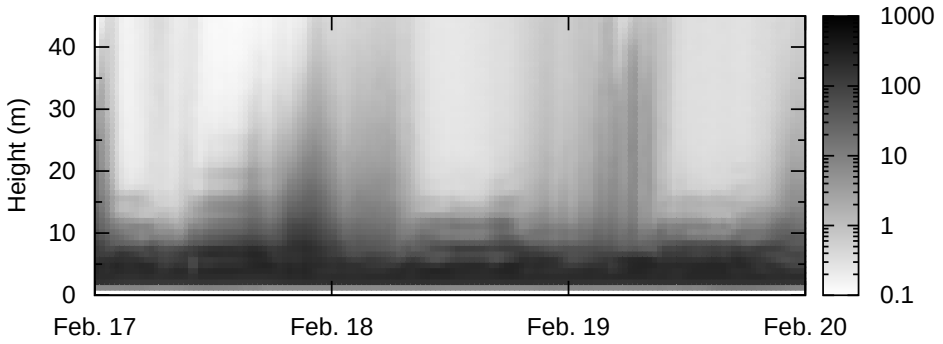

Figure B.6: Same as Fig. B.1, but for the period from February 17 00:00 (UTC+3) to February 19 24:00, 2011.

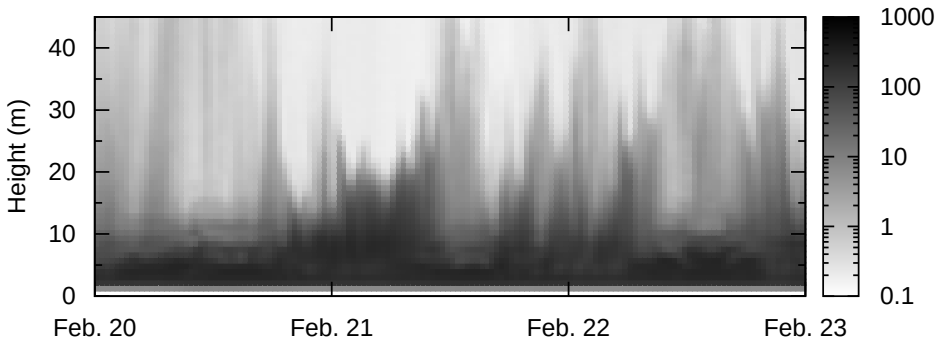

Figure B.7: Same as Fig. B.1, but for the period from February 20 00:00 (UTC+3) to February 22 24:00, 2011.

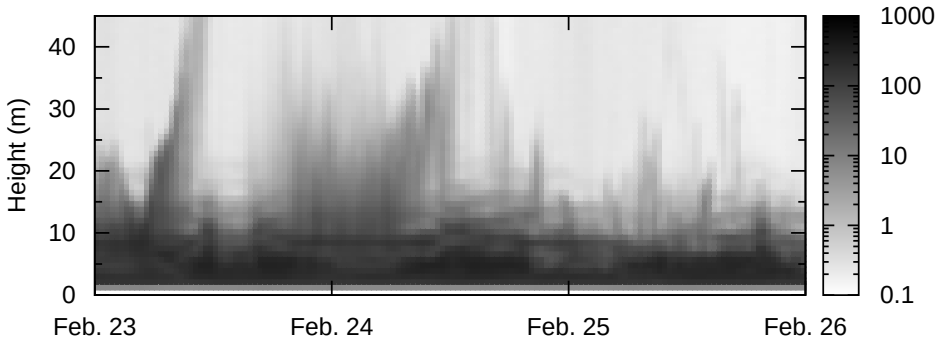

Figure B.8: Same as Fig. B.1, but for the period from February 23 00:00 (UTC+3) to February 25 24:00, 2011.

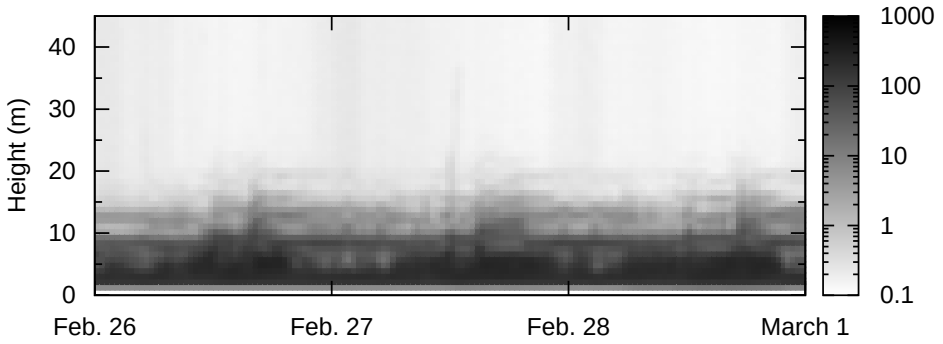

Figure B.9: Same as Fig. B.1, but for the period from February 26 00:00 (UTC+3) to February 28 24:00, 2011.

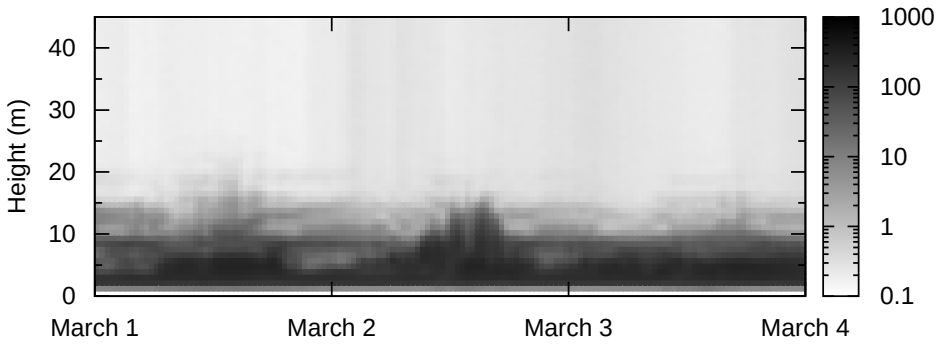

Figure B.10: Same as Fig. B.1, but for the period from March 1 00:00 (UTC+3) to March 3 24:00, 2011.

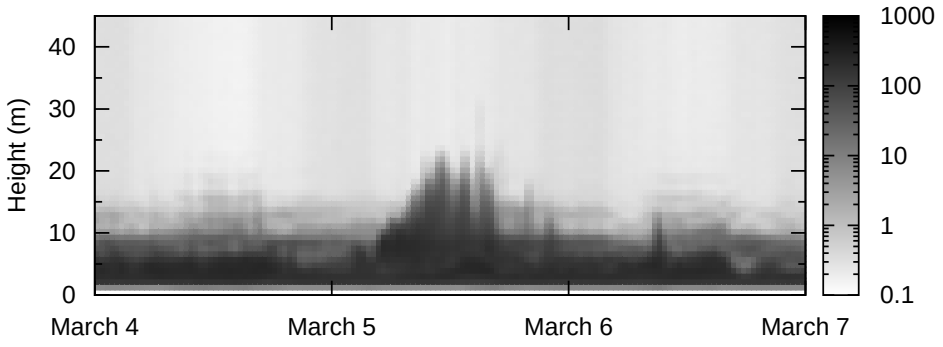

Figure B.11: Same as Fig. B.1, but for the period from March 4 00:00 (UTC+3) to March 6 24:00, 2011.

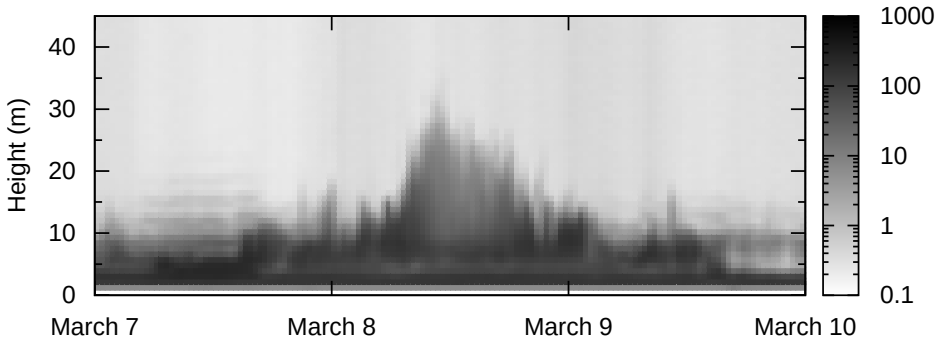

Figure B.12: Same as Fig. B.1, but for the period from March 7 00:00 (UTC+3) to March 9 24:00, 2011.

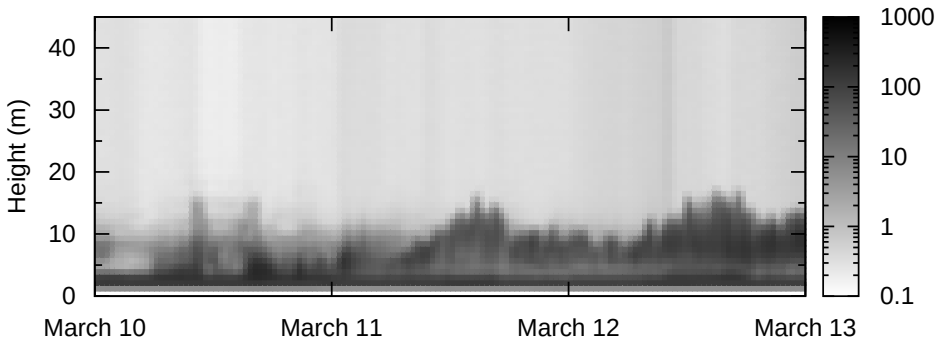

Figure B.13: Same as Fig. B.1, but for the period from March 10 00:00 (UTC+3) to March 12 24:00, 2011.

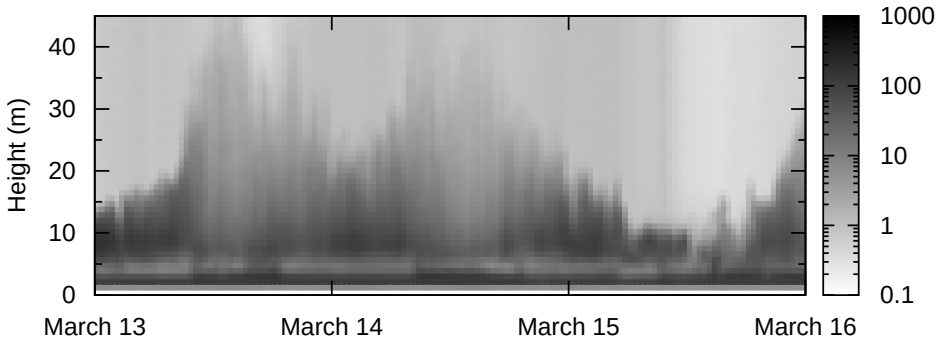

Figure B.14: Same as Fig. B.1, but for the period from March 13 00:00 (UTC+3) to March 15 24:00, 2011.

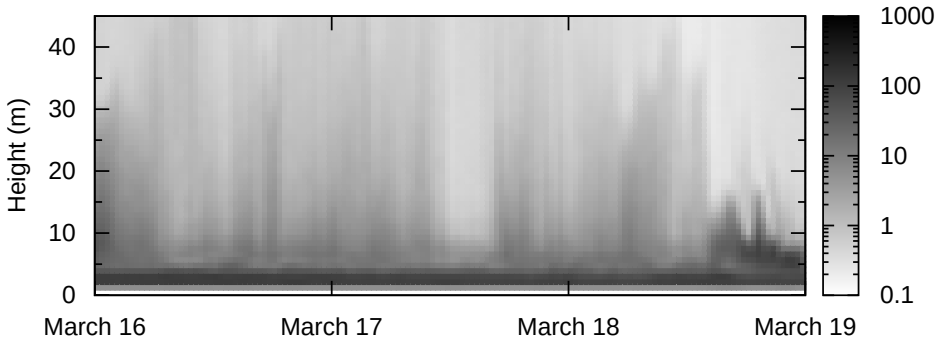

Figure B.15: Same as Fig. B.1, but for the period from March 16 00:00 (UTC+3) to March 18 24:00, 2011.

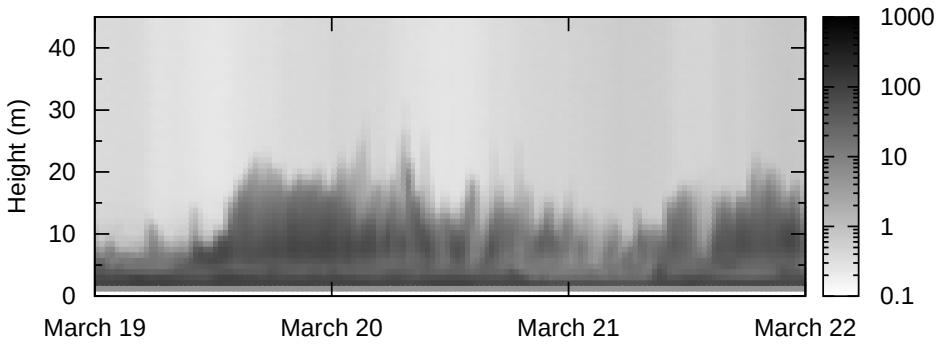

Figure B.16: Same as Fig. B.1, but for the period from March 19 00:00 (UTC+3) to March 21 24:00, 2011.

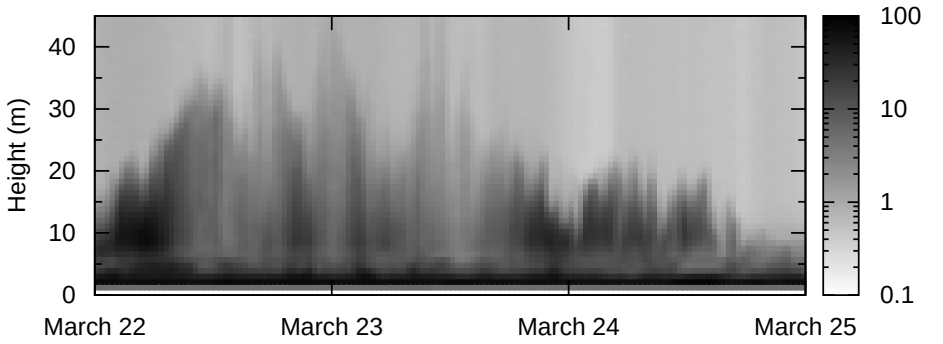

Figure B.17: Same as Fig. B.1, but for the period from March 22 00:00 (UTC+3) to March 24 24:00, 2011.

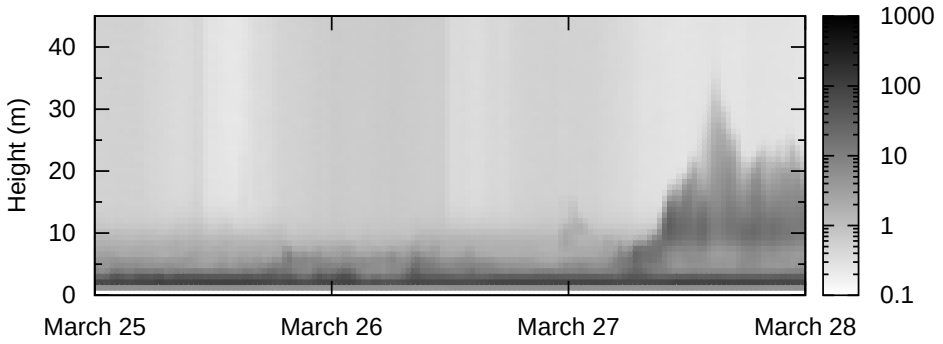

Figure B.18: Same as Fig. B.1, but for the period from March 25 00:00 (UTC+3) to March 27 24:00, 2011.

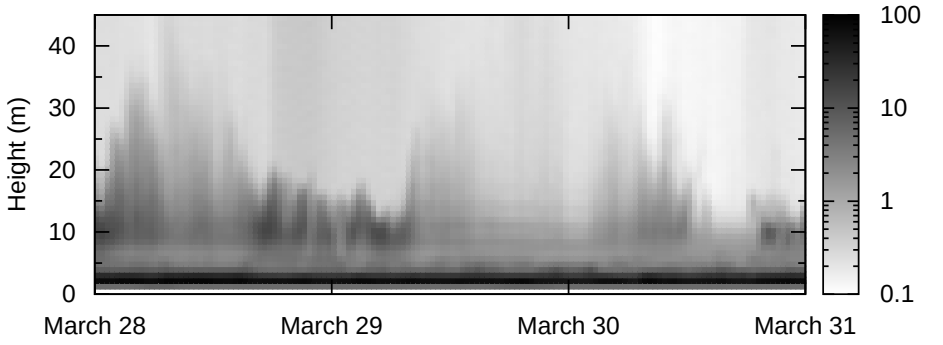

Figure B.19: Same as Fig. B.1, but for the period from March 28 00:00 (UTC+3) to March 30 24:00, 2011.

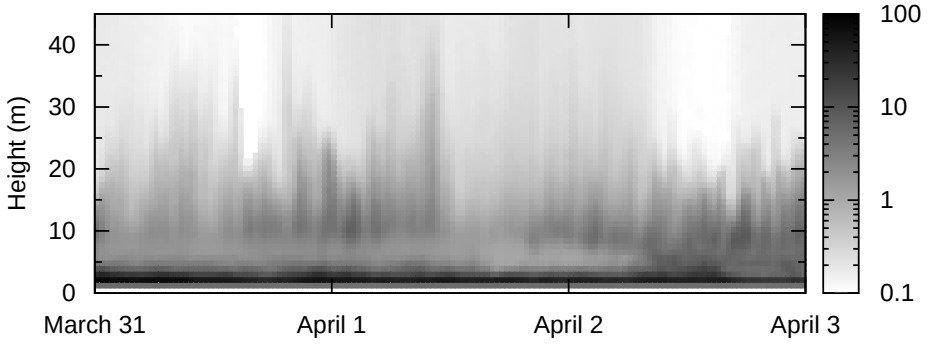

Figure B.20: Same as Fig. B.1, but for the period from March 31 00:00 (UTC+3) to April 2 24:00, 2011.

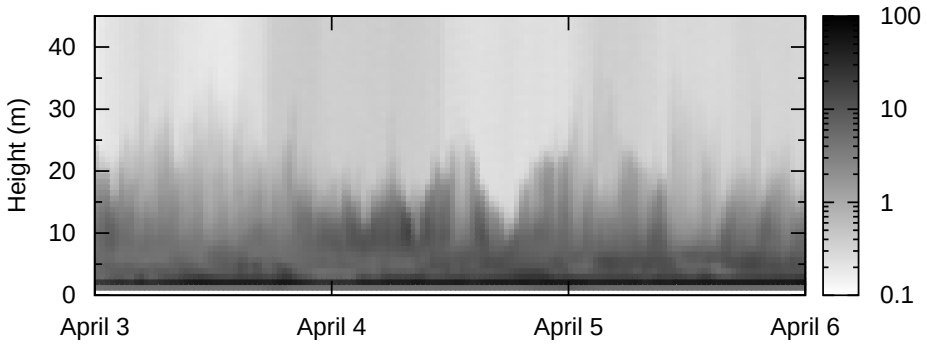

Figure B.21: Same as Fig. B.1, but for the period from April 3 00:00 (UTC+3) to April 5 24:00, 2011.

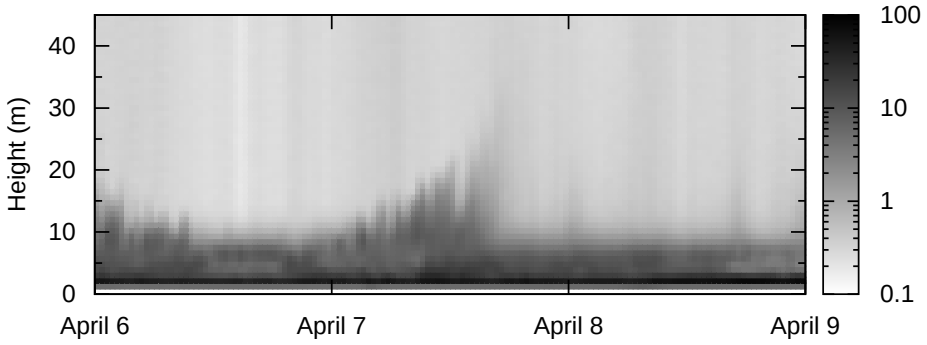

Figure B.22: Same as Fig. B.1, but for the period from April 6 00:00 (UTC+3) to April 8 24:00, 2011.

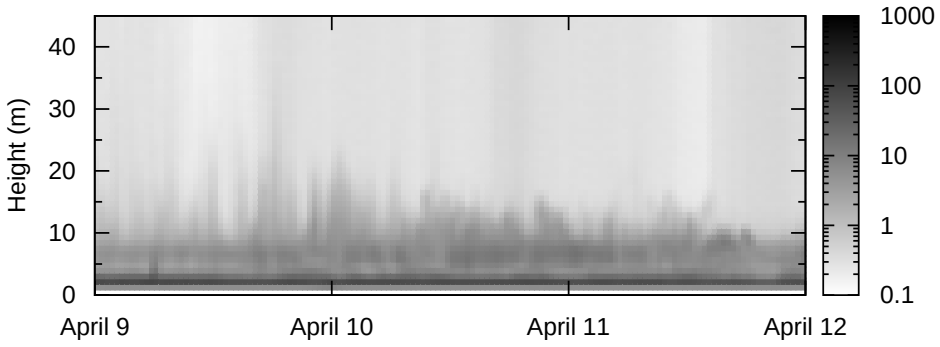

Figure B.23: Same as Fig. B.1, but for the period from April 9 00:00 (UTC+3) to April 11 24:00, 2011.

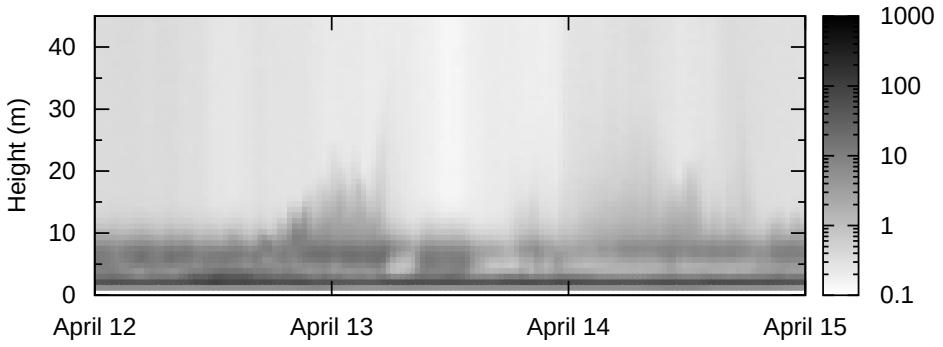

Figure B.24: Same as Fig. B.1, but for the period from April 12 00:00 (UTC+3) to April 14 24:00, 2011.

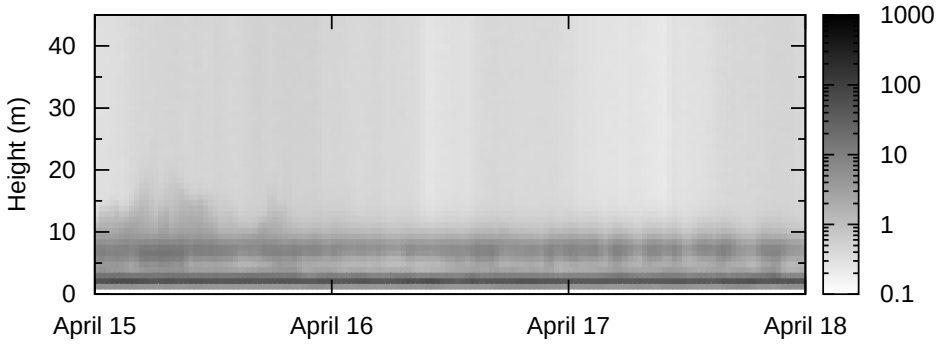

Figure B.25: Same as Fig. B.1, but for the period from April 15 00:00 (UTC+3) to April 17 24:00, 2011.

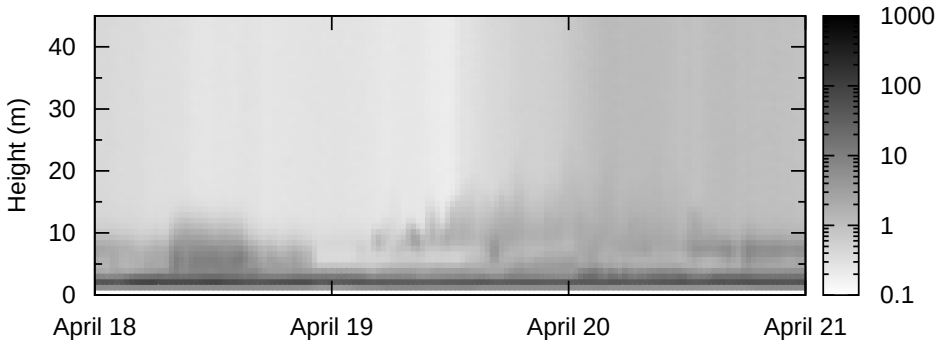

Figure B.26: Same as Fig. B.1, but for the period from April 18 00:00 (UTC+3) to April 20 24:00, 2011.

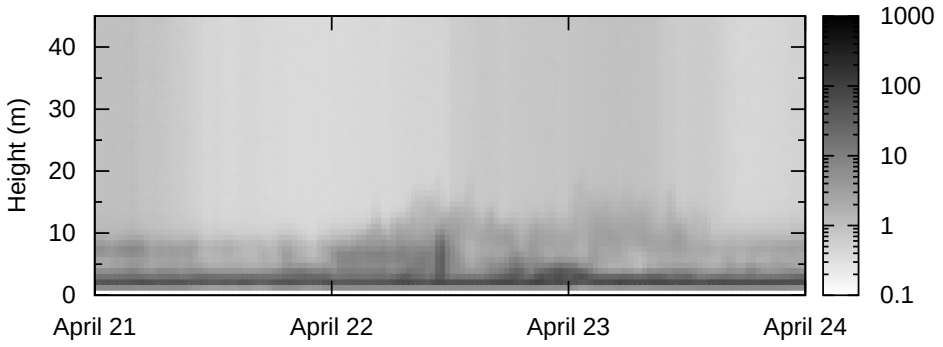

Figure B.27: Same as Fig. B.1, but for the period from April 21 00:00 (UTC+3) to April 23 24:00, 2011.

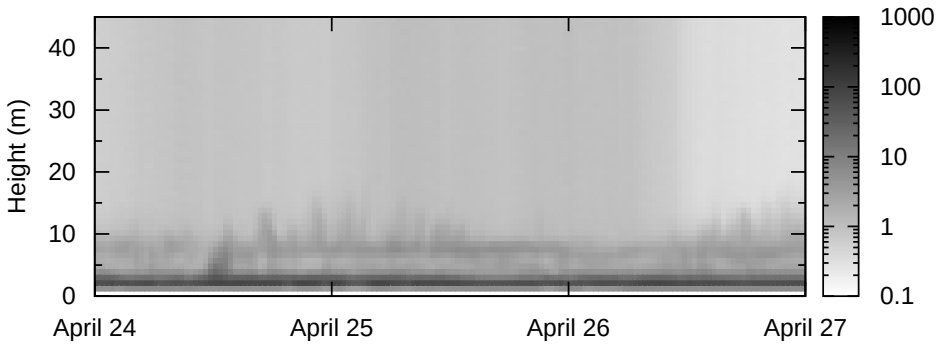

Figure B.28: Same as Fig. B.1, but for the period from April 24 00:00 (UTC+3) to April 26 24:00, 2011.

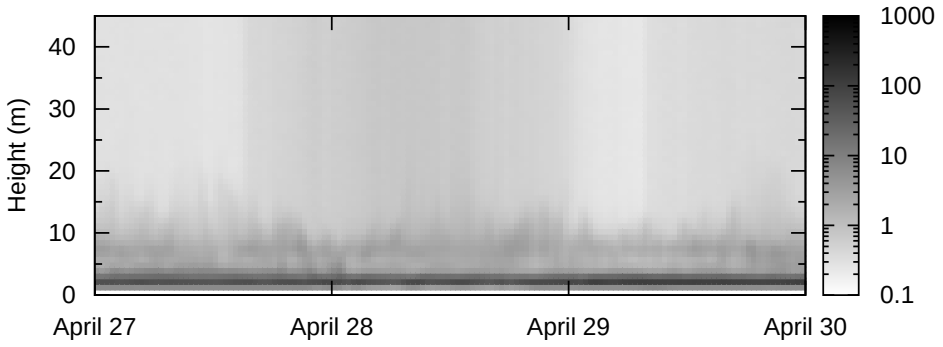

Figure B.29: Same as Fig. B.1, but for the period from April 27 00:00 (UTC+3) to April 29 24:00, 2011.

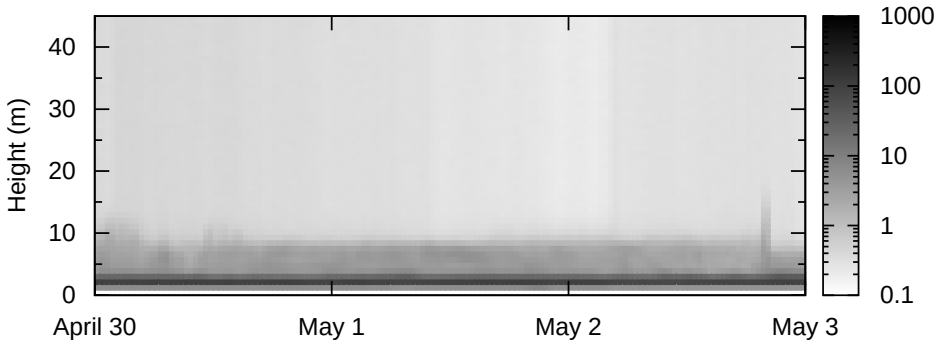

Figure B.30: Same as Fig. B.1, but for the period from April 30 00:00 (UTC+3) to May 2 24:00, 2011.

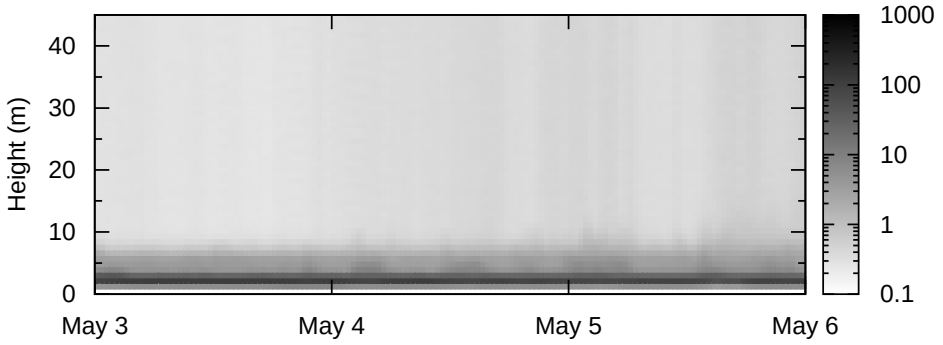

Figure B.31: Same as Fig. B.1, but for the period from May 3 00:00 (UTC+3) to May 5 24:00, 2011.

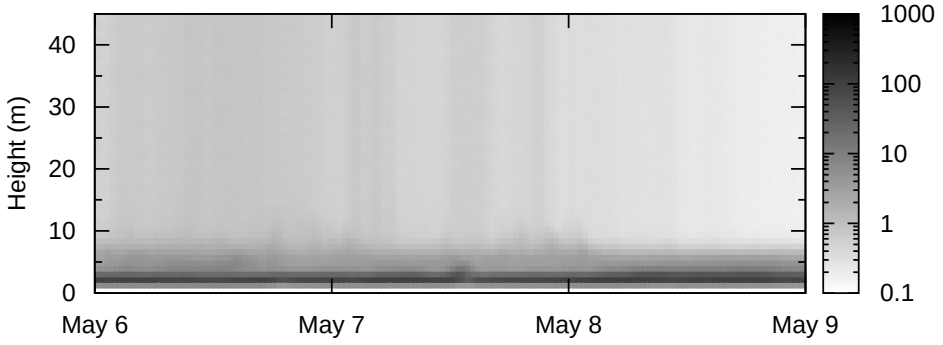

Figure B.32: Same as Fig. B.1, but for the period from May 6 00:00 (UTC+3) to May 8 24:00, 2011.

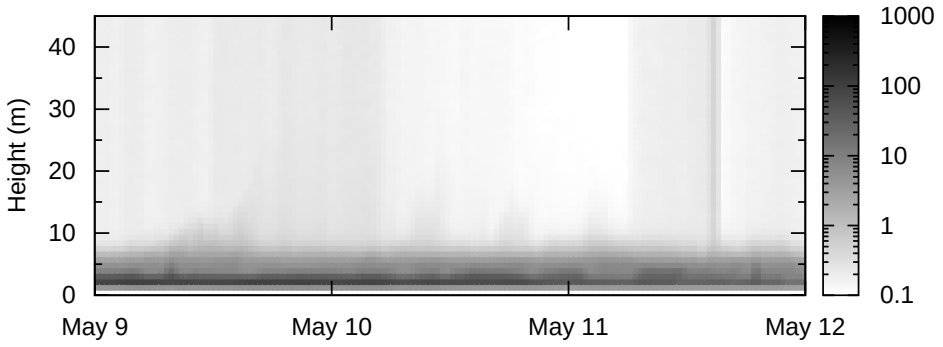

Figure B.33: Same as Fig. B.1, but for the period from May 9 00:00 (UTC+3) to May 11 24:00, 2011.

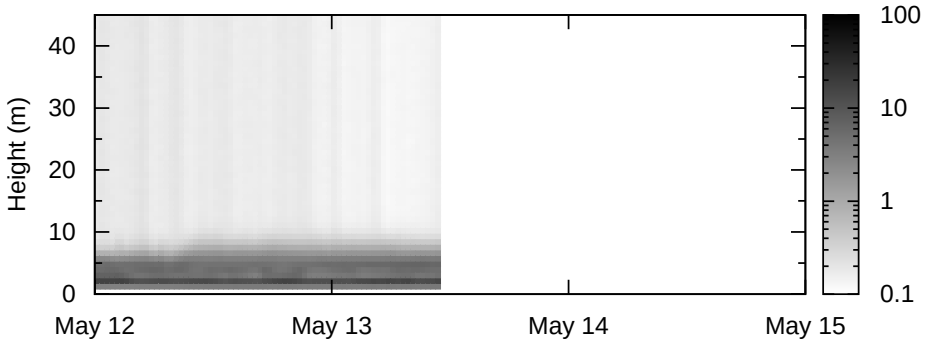

Figure B.34: Same as Fig. B.1, but for the period from May 12 00:00 to May 14 24:00, 2011.

Appendix C

Platinum thermometers results

C.1 Temperatures

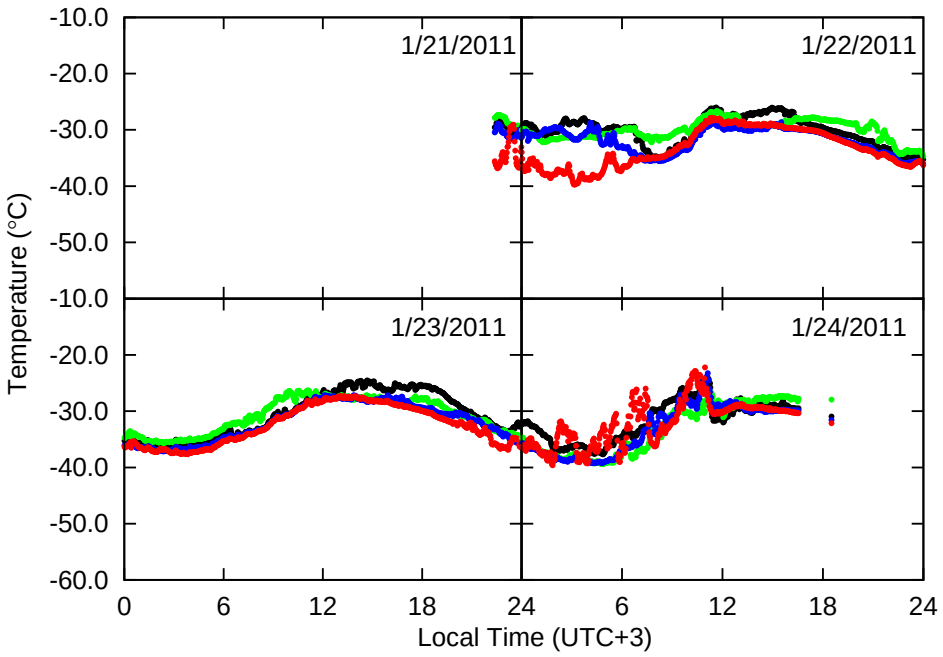

Figure C.1: Time series of the temperatures (°C) at 0.3 m (red), 9.5 m (blue), 12 m (green), and 15.8 m (black), respectively, with two minute time resolution for the period from January 21 00:00 (UTC+3) to January 24 24:00, 2011.

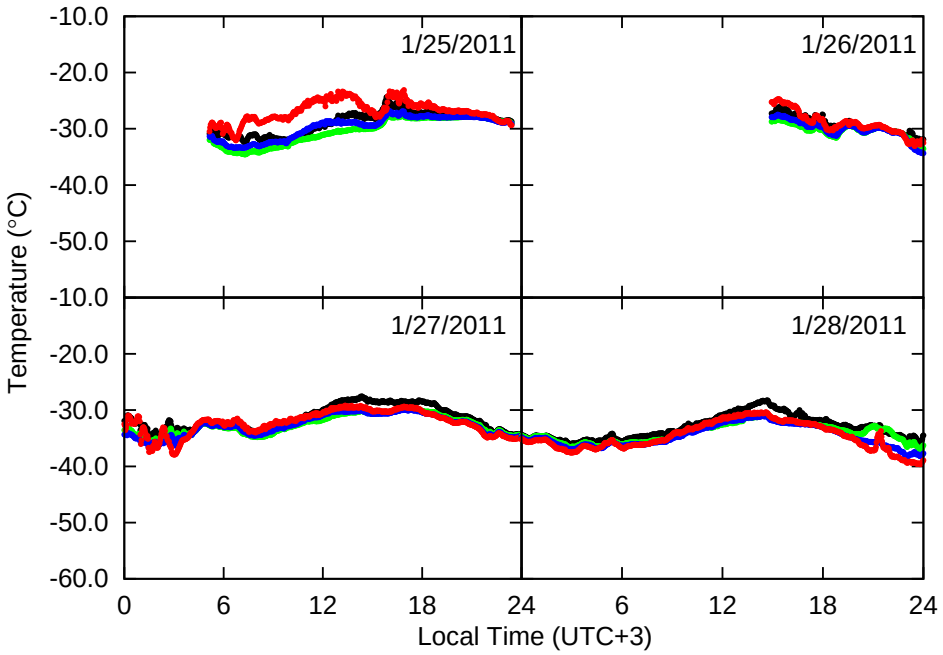

Figure C.2: Same as Fig. C.1, but for the period from January 25 00:00 (UTC+3) to January 28 24:00, 2011.

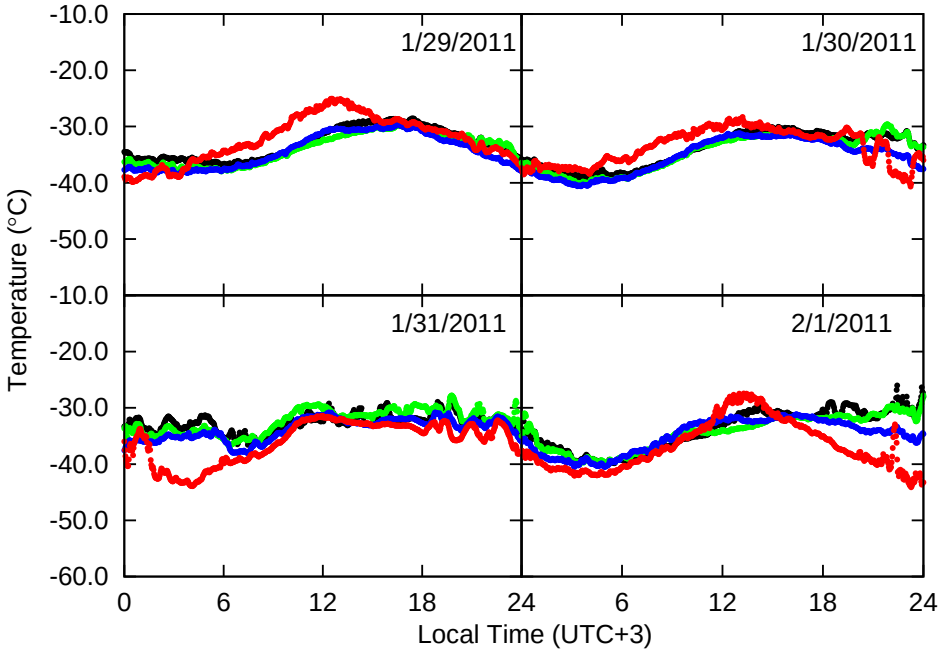

Figure C.3: Same as Fig. C.1, but for the period from January 29 00:00 (UTC+3) to February 1 24:00, 2011.

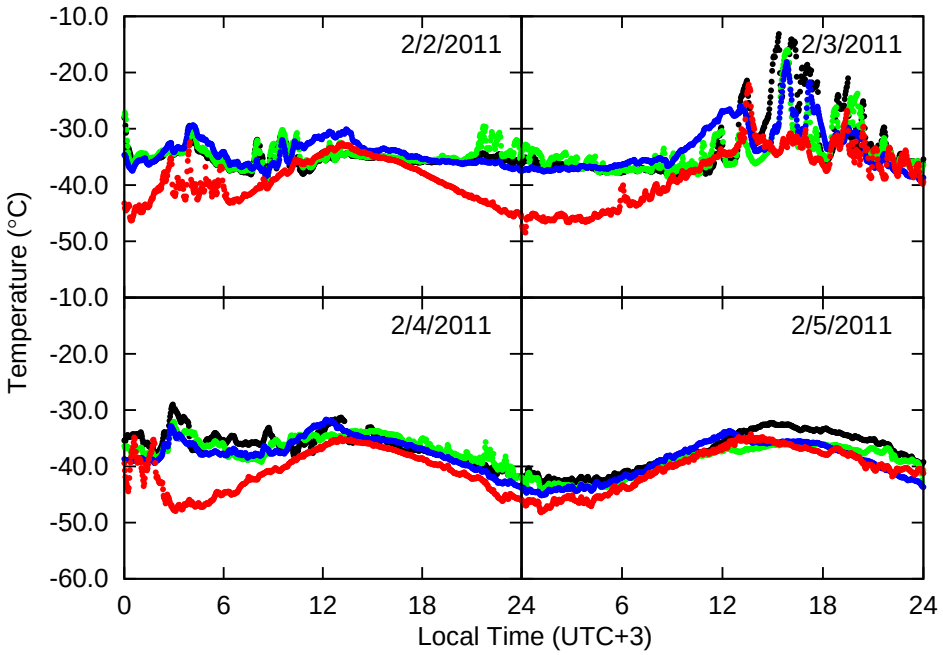

Figure C.4: Same as Fig. C.1, but for the period from February 2 00:00 (UTC+3) to February 5 24:00, 2011.

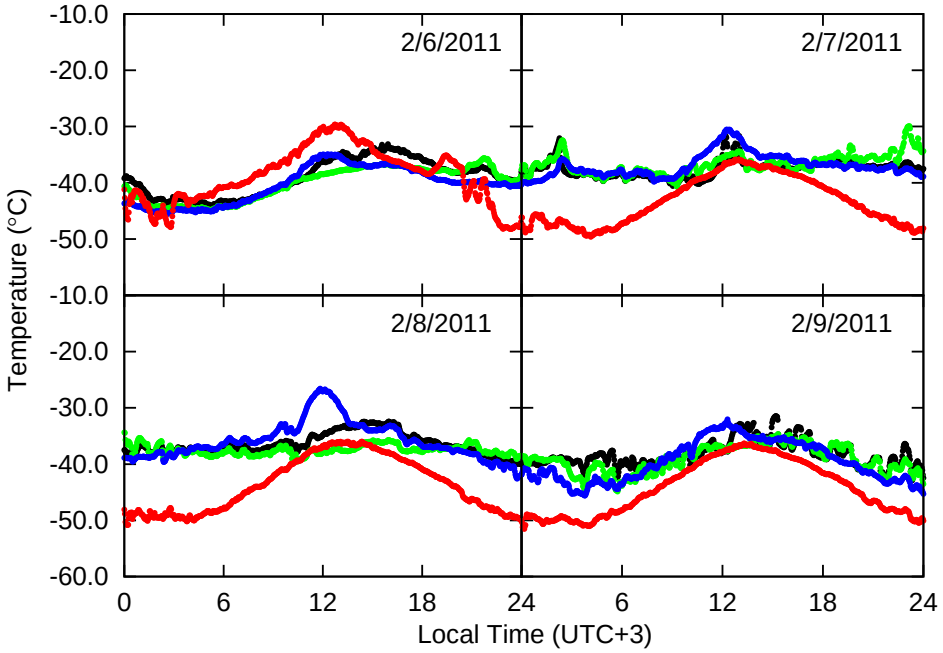

Figure C.5: Same as Fig. C.1, but for the period from February 6 00:00 (UTC+3) to February 9 24:00, 2011.

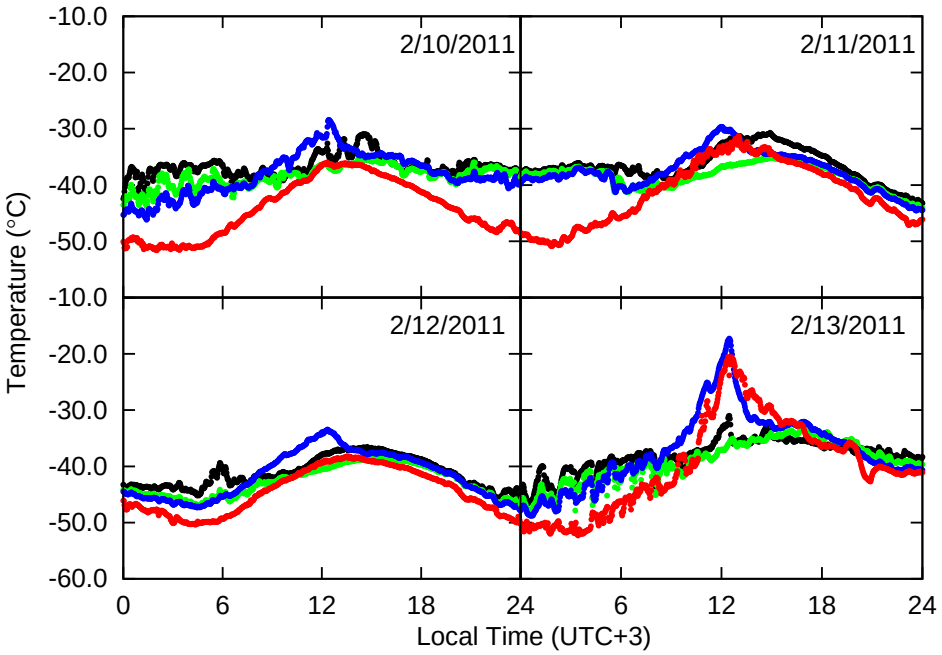

Figure C.6: Same as Fig. C.1, but for the period from February 10 00:00 (UTC+3) to February 13 24:00, 2011.

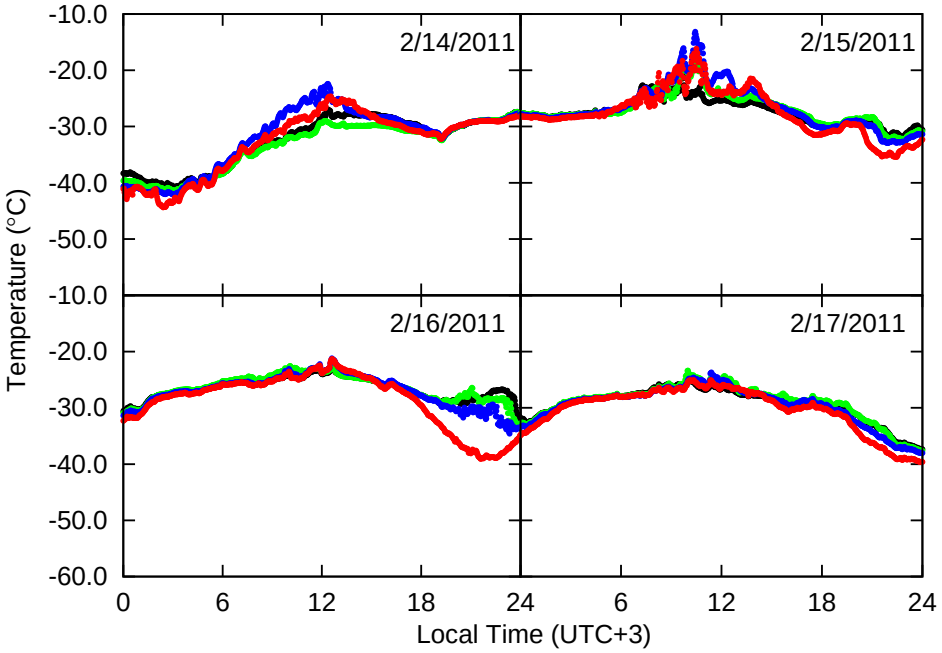

Figure C.7: Same as Fig. C.1, but for the period from February 14 00:00 (UTC+3) to February 17 24:00, 2011.

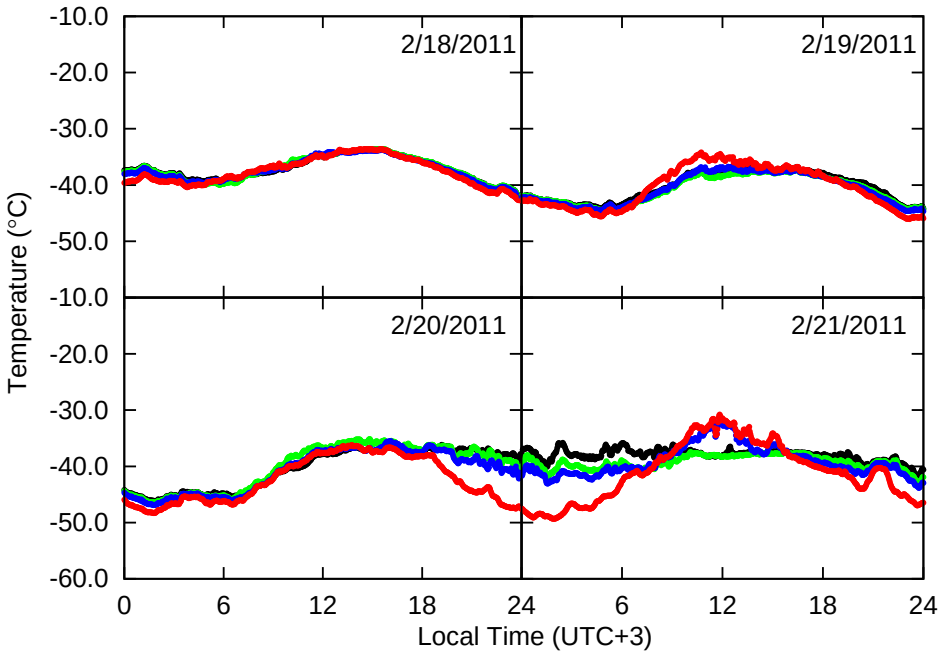

Figure C.8: Same as Fig. C.1, but for the period from February 18 00:00 (UTC+3) to February 21 24:00, 2011.

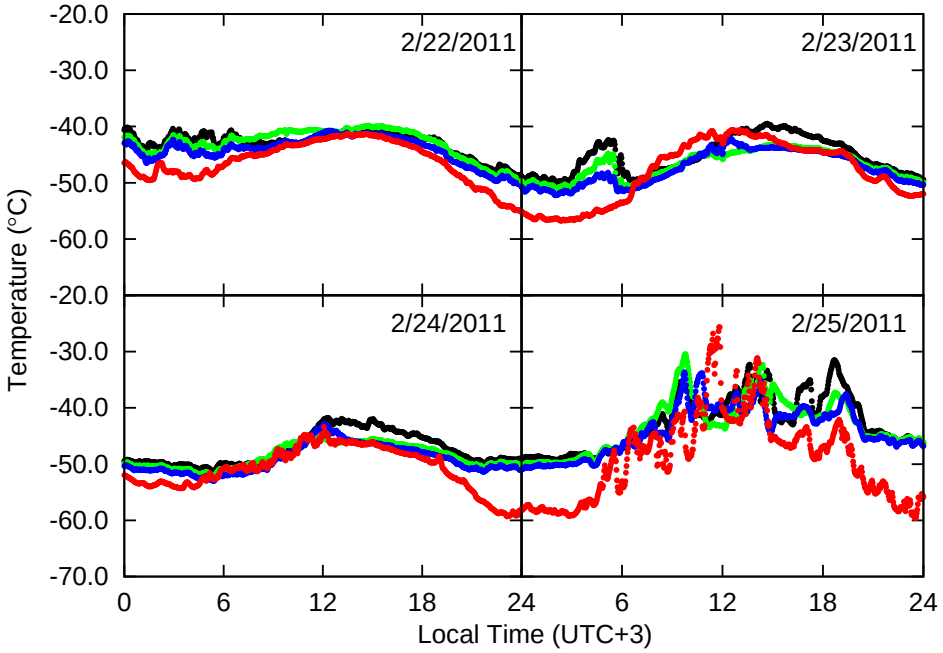

Figure C.9: Same as Fig. C.1, but for the period from February 22 00:00 (UTC+3) to February 25 24:00, 2011.

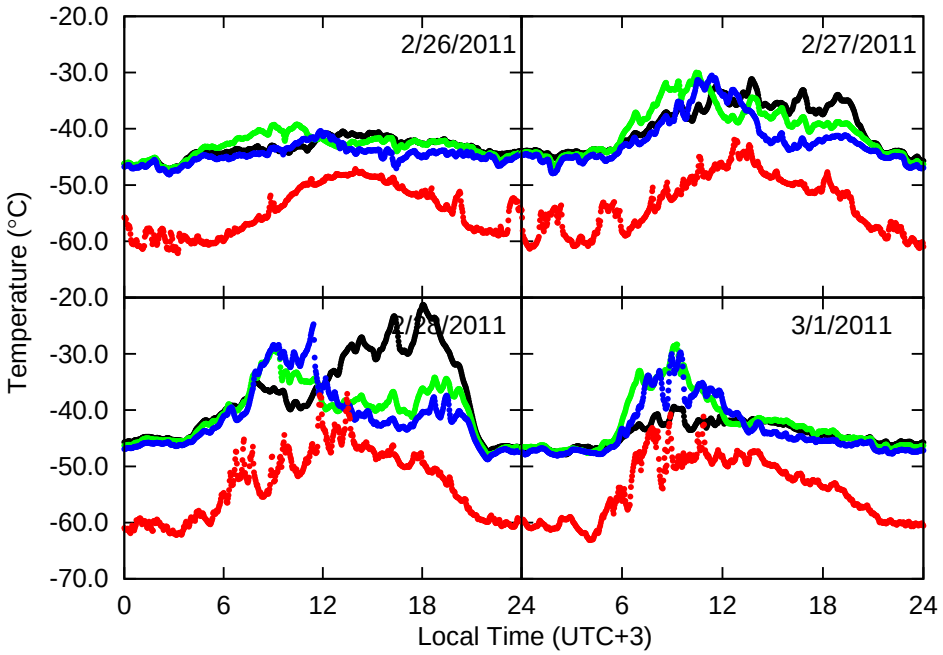

Figure C.10: Same as Fig. C.1, but for the period from February 26 00:00 (UTC+3) to March 1 24:00, 2011.

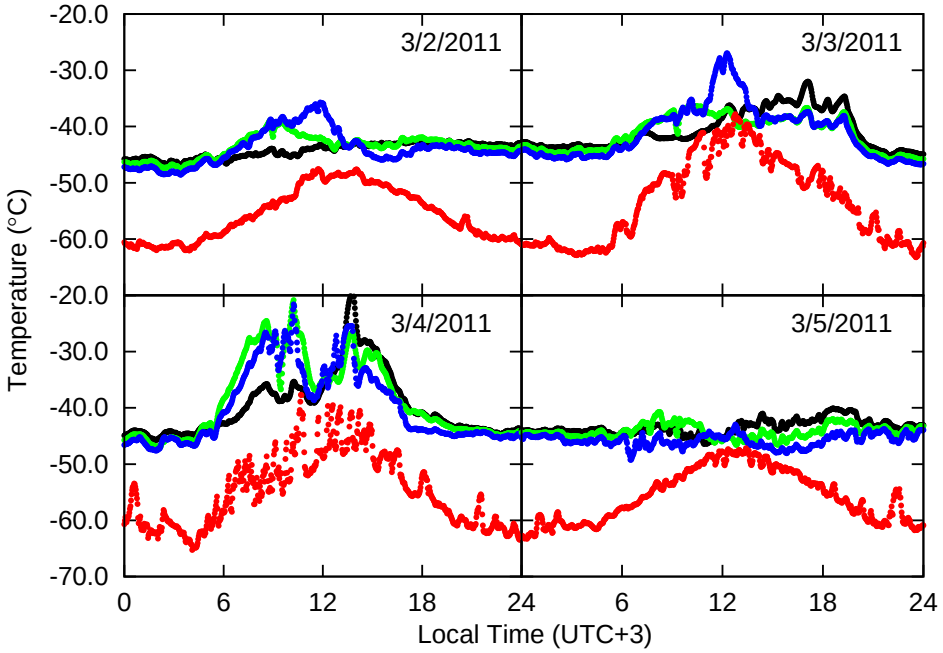

Figure C.11: Same as Fig. C.1, but for the period from March 2 00:00 (UTC+3) to March 5 24:00, 2011.

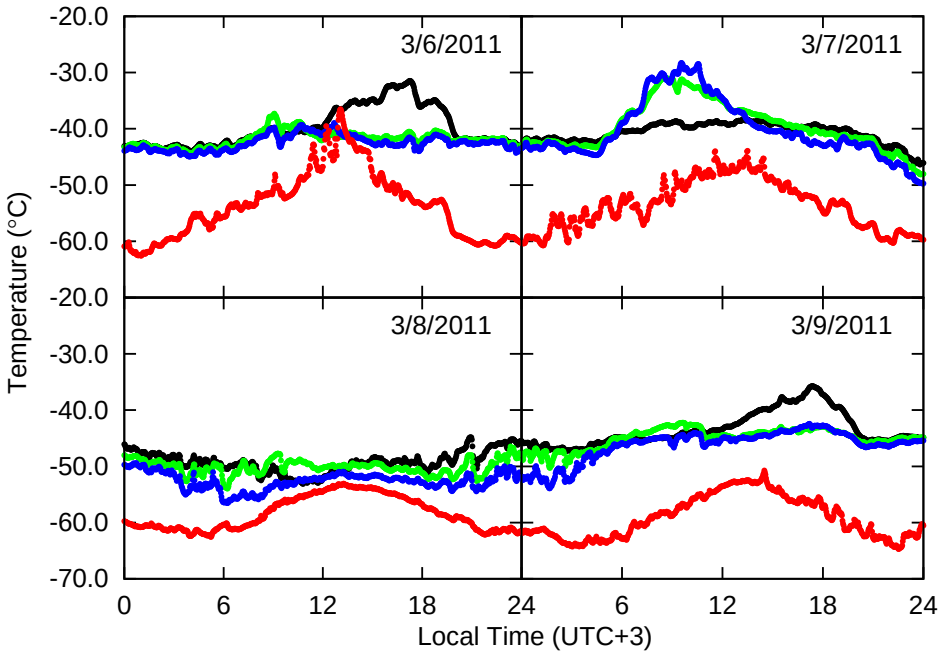

Figure C.12: Same as Fig. C.1, but for the period from March 6 00:00 (UTC+3) to March 9 24:00, 2011.

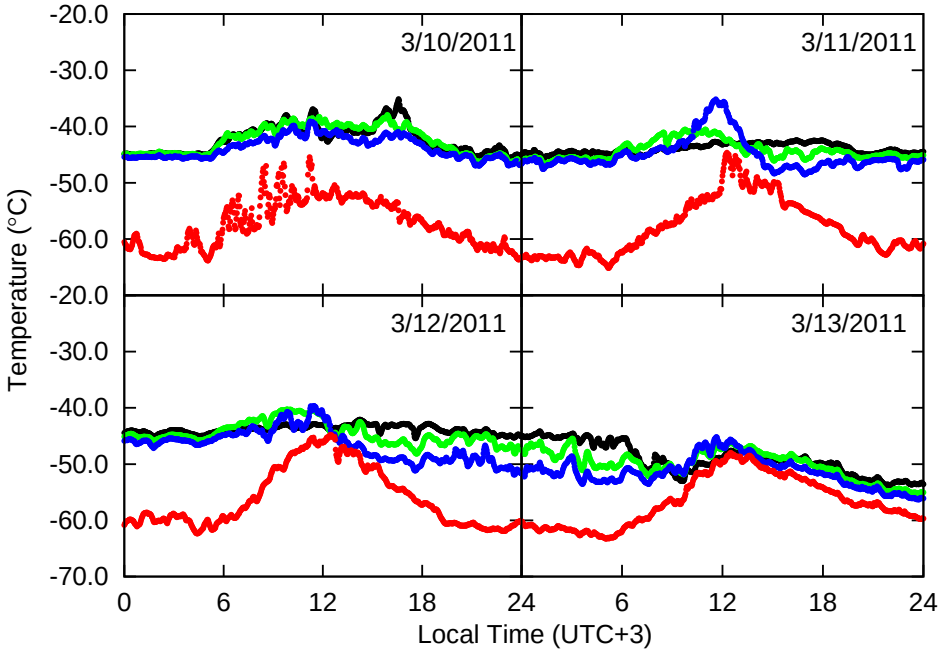

Figure C.13: Same as Fig. C.1, but for the period from March 10 00:00 (UTC+3) to March 13 24:00, 2011.

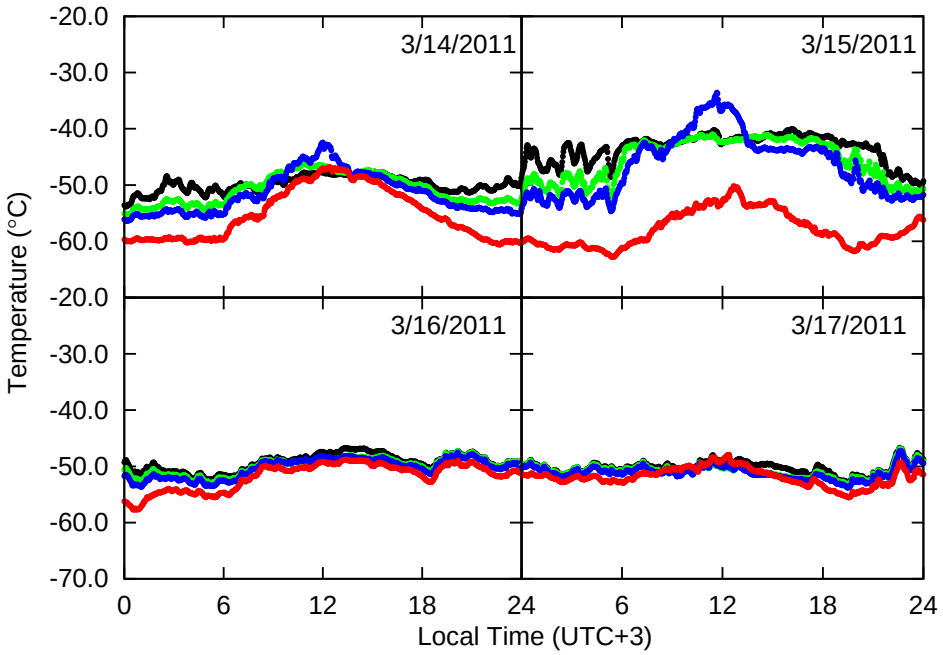

Figure C.14: Same as Fig. C.1, but for the period from March 14 00:00 (UTC+3) to March 17 24:00, 2011.

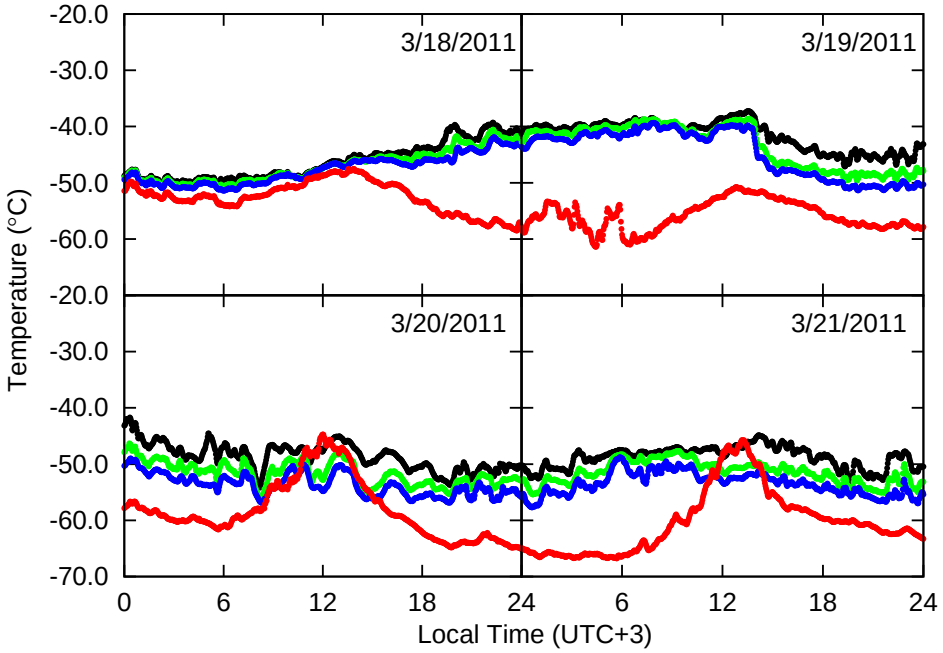

Figure C.15: Same as Fig. C.1, but for the period from March 18 00:00 (UTC+3) to March 21 24:00, 2011.

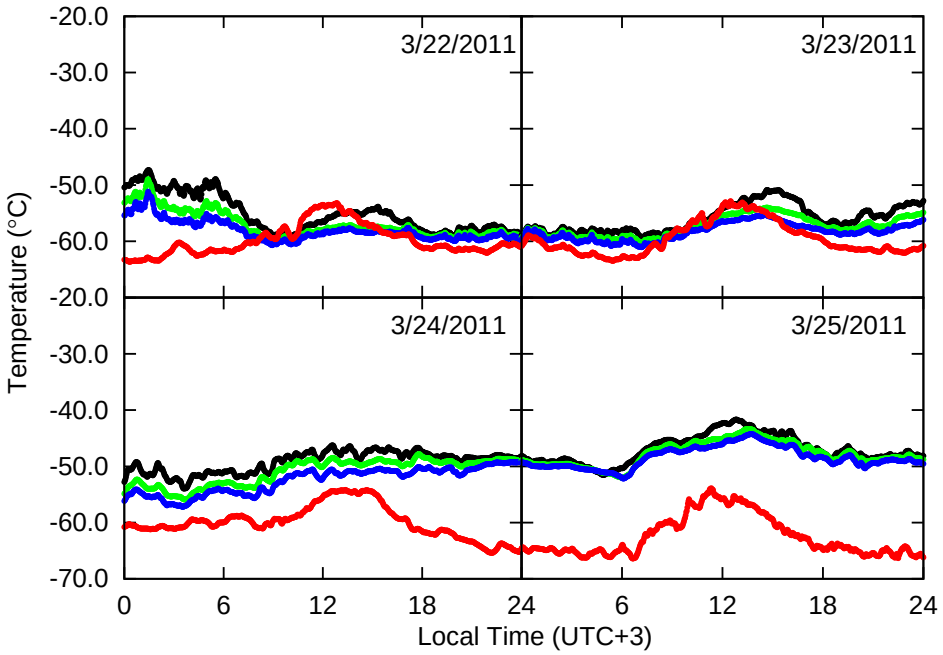

Figure C.16: Same as Fig. C.1, but for the period from March 22 00:00 (UTC+3) to March 25 24:00, 2011.

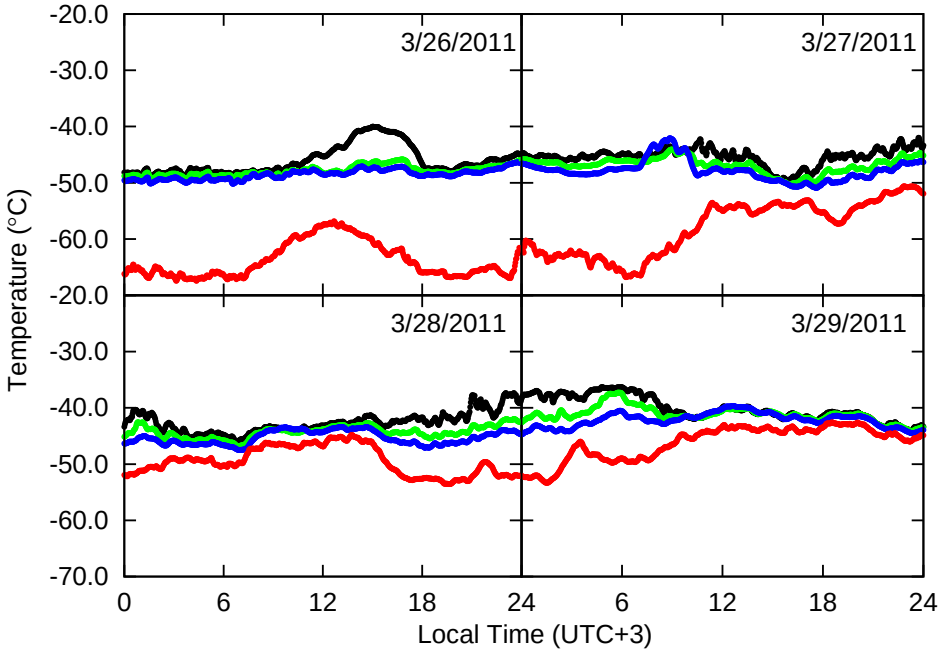

Figure C.17: Same as Fig. C.1, but for the period from March 26 00:00 (UTC+3) to March 29 24:00, 2011.

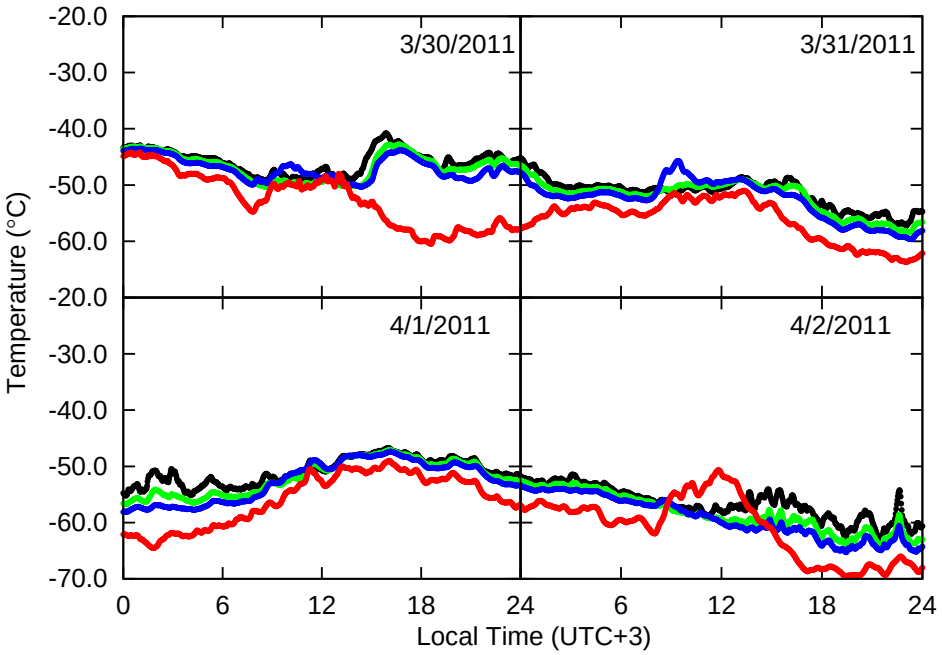

Figure C.18: Same as Fig. C.1, but for the period from March 30 00:00 (UTC+3) to April 2 24:00, 2011.

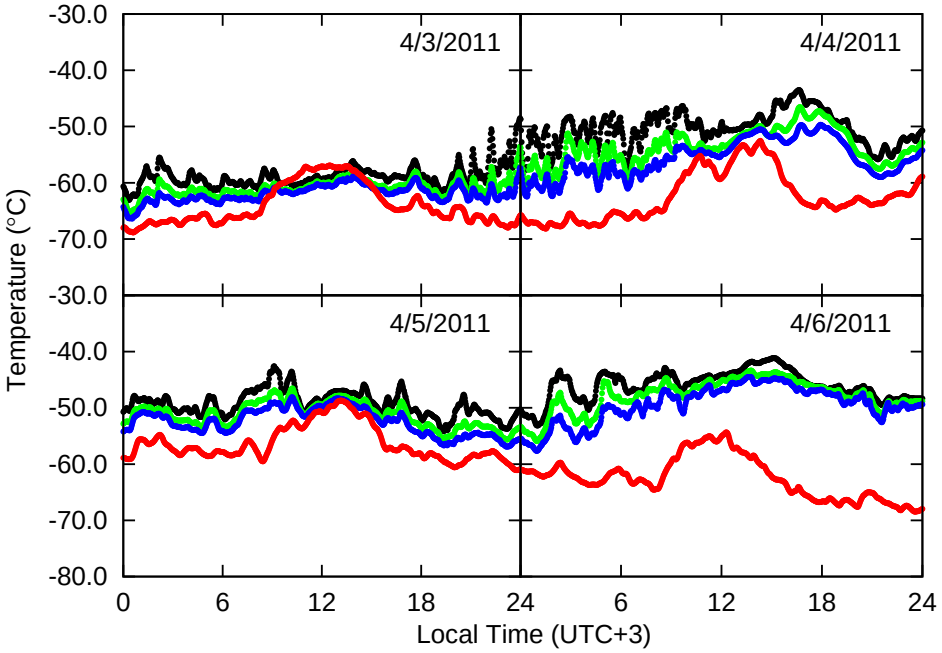

Figure C.19: Same as Fig. C.1, but for the period from April 3 00:00 (UTC+3) to April 6 24:00, 2011.

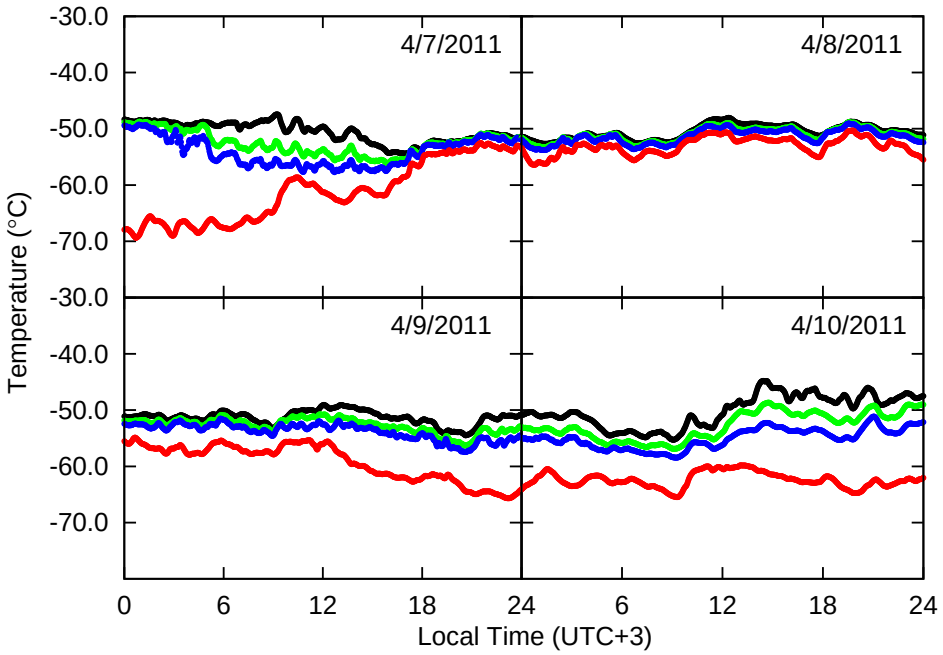

Figure C.20: Same as Fig. C.1, but for the period from April 7 00:00 (UTC+3) to April 10 24:00, 2011.

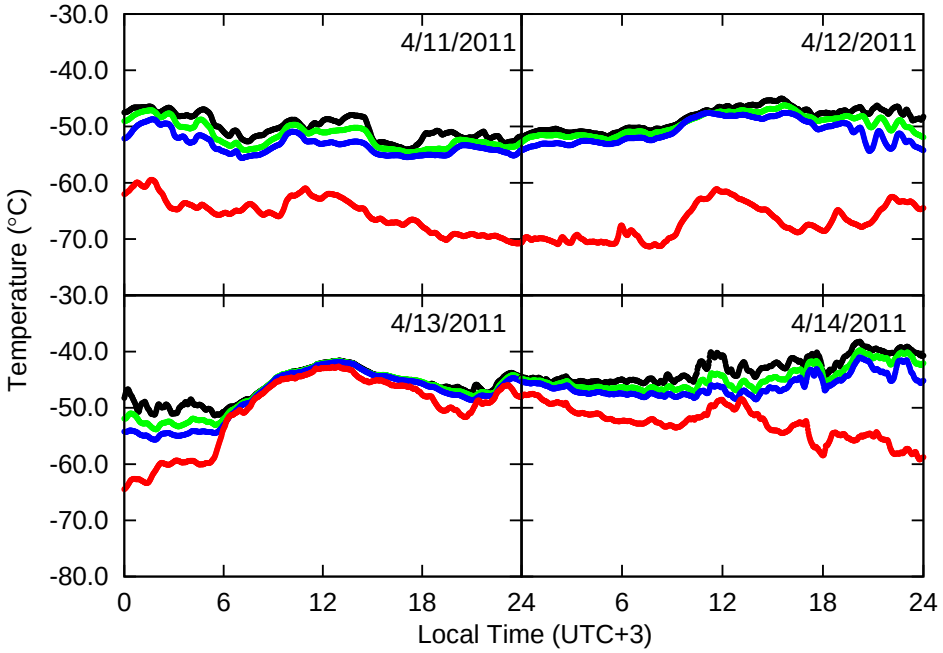

Figure C.21: Same as Fig. C.1, but for the period from April 11 00:00 (UTC+3) to April 14 24:00, 2011.

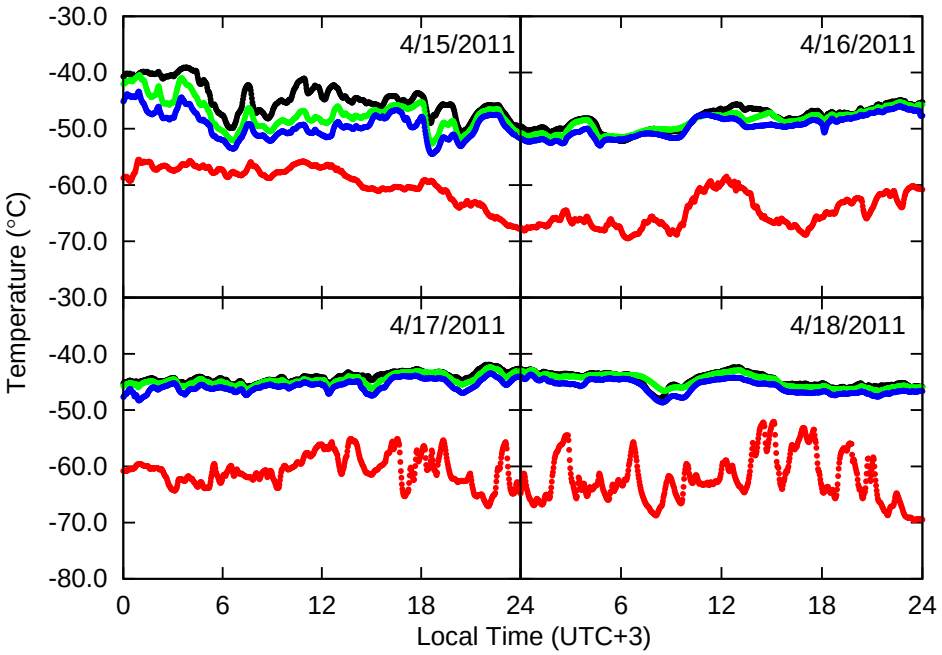

Figure C.22: Same as Fig. C.1, but for the period from April 15 00:00 (UTC+3) to April 18 24:00, 2011.

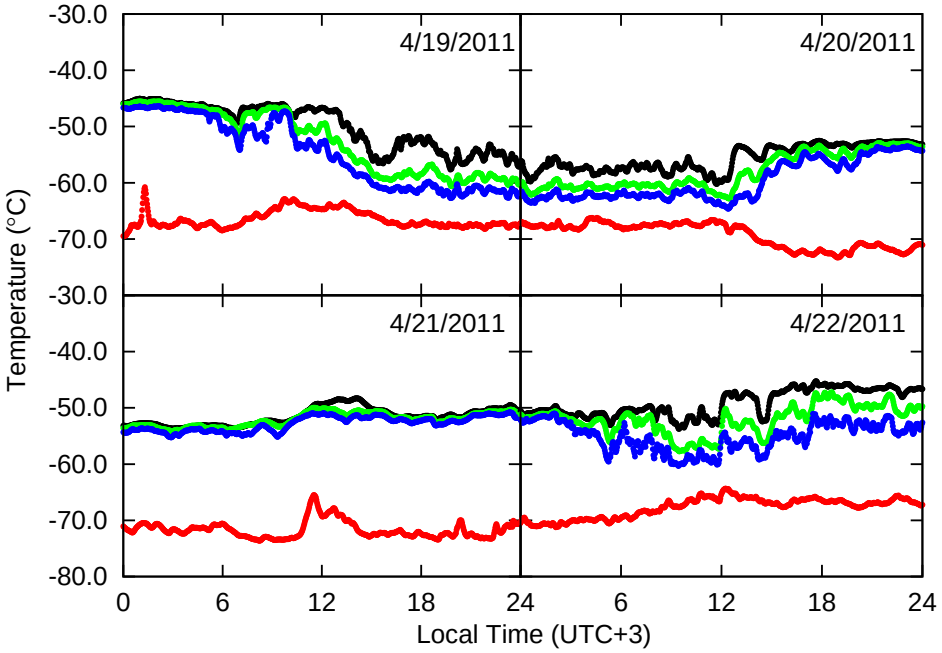

Figure C.23: Same as Fig. C.1, but for the period from April 19 00:00 (UTC+3) to April 22 24:00, 2011.

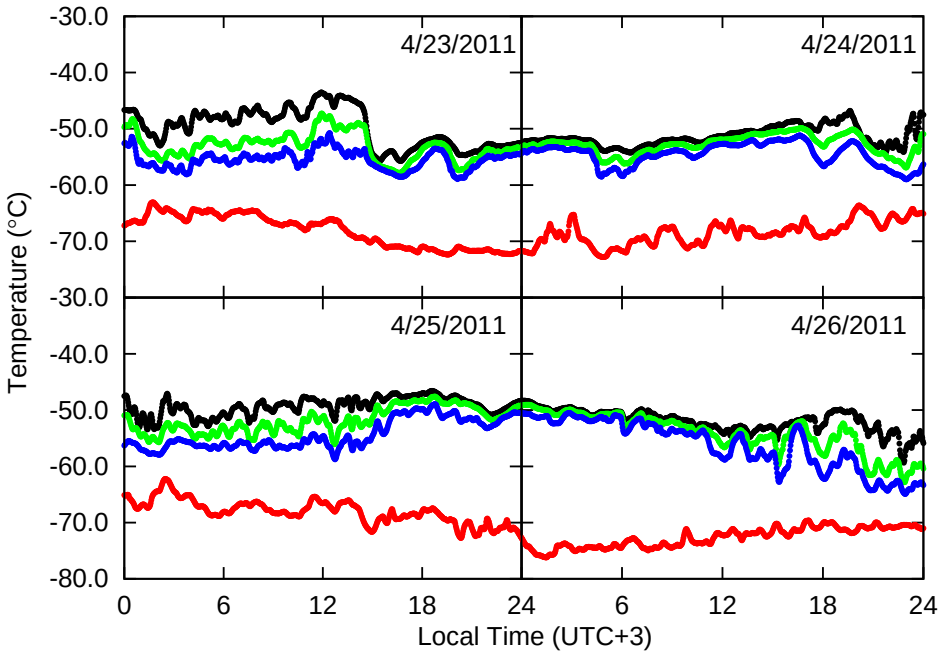

Figure C.24: Same as Fig. C.1, but for the period from April 23 00:00 (UTC+3) to April 26 24:00, 2011.

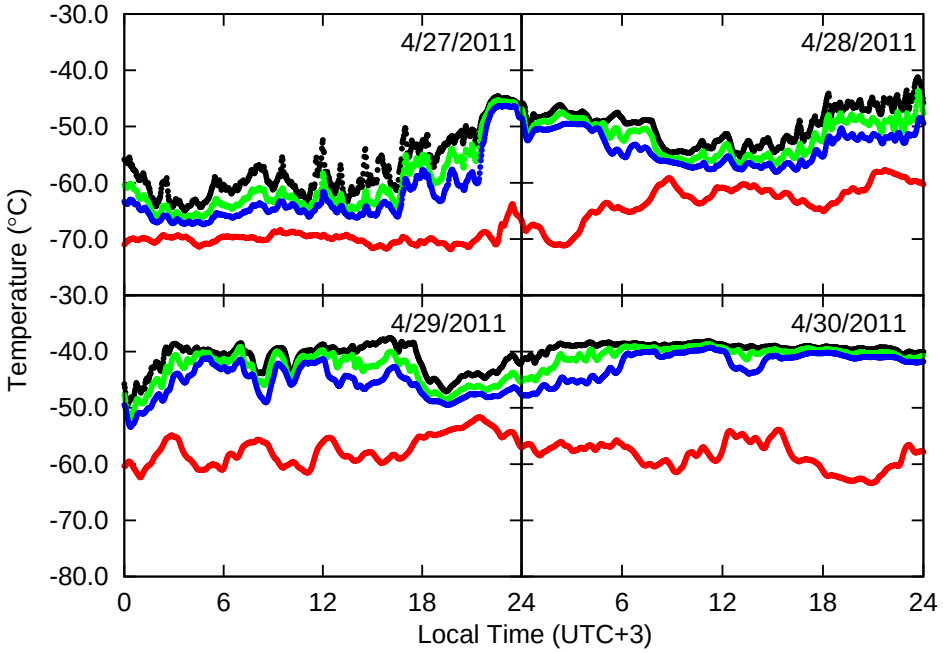

Figure C.25: Same as Fig. C.1, but for the period from April 27 00:00 (UTC+3) to April 30 24:00, 2011.

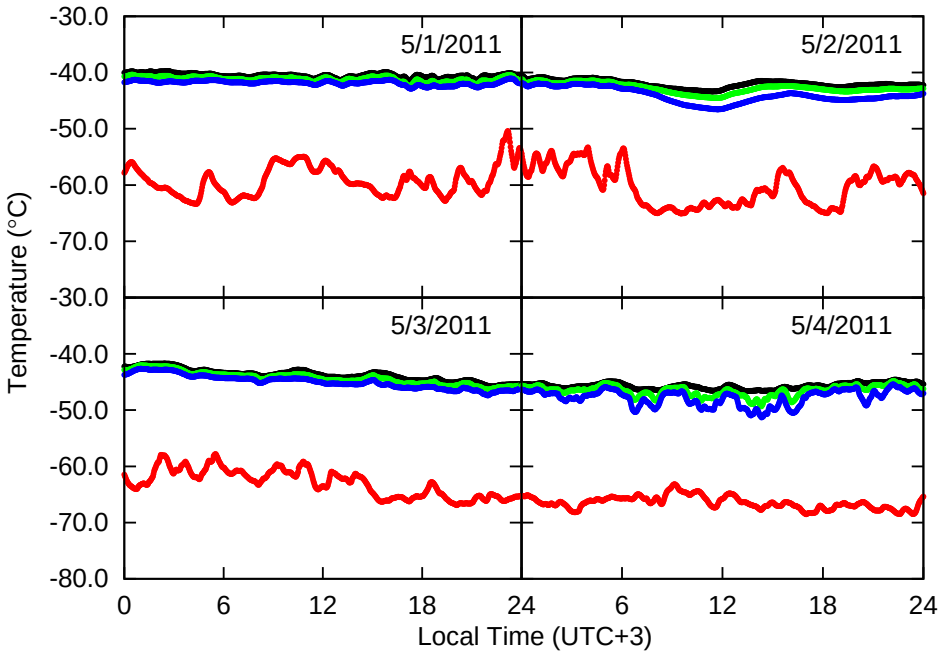

Figure C.26: Same as Fig. C.1, but for the period from May 1 00:00 (UTC+3) to May 4 24:00, 2011.

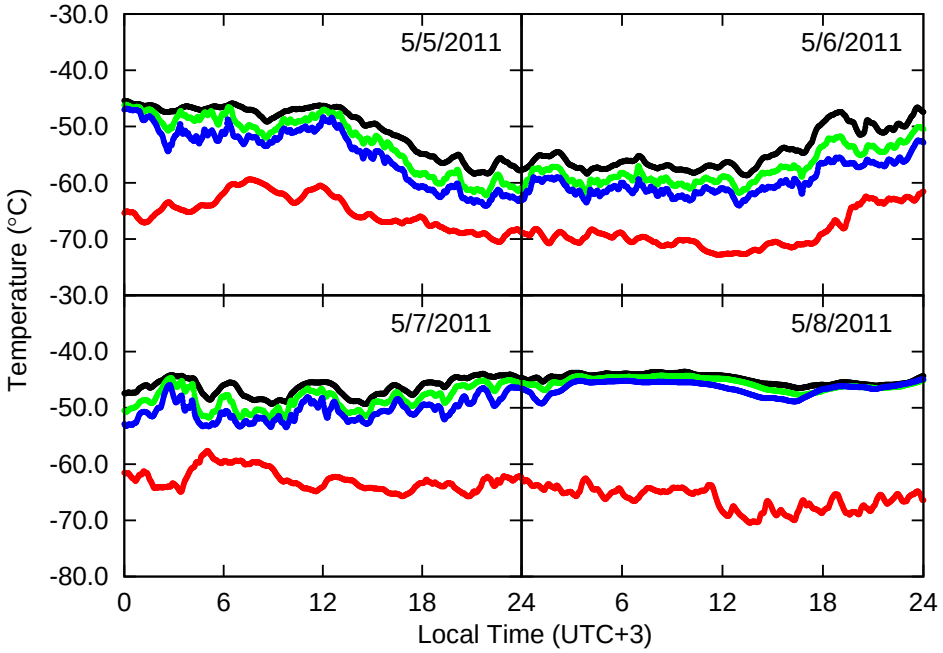

Figure C.27: Same as Fig. C.1, but for the period from May 5 00:00 (UTC+3) to May 8 24:00, 2011.

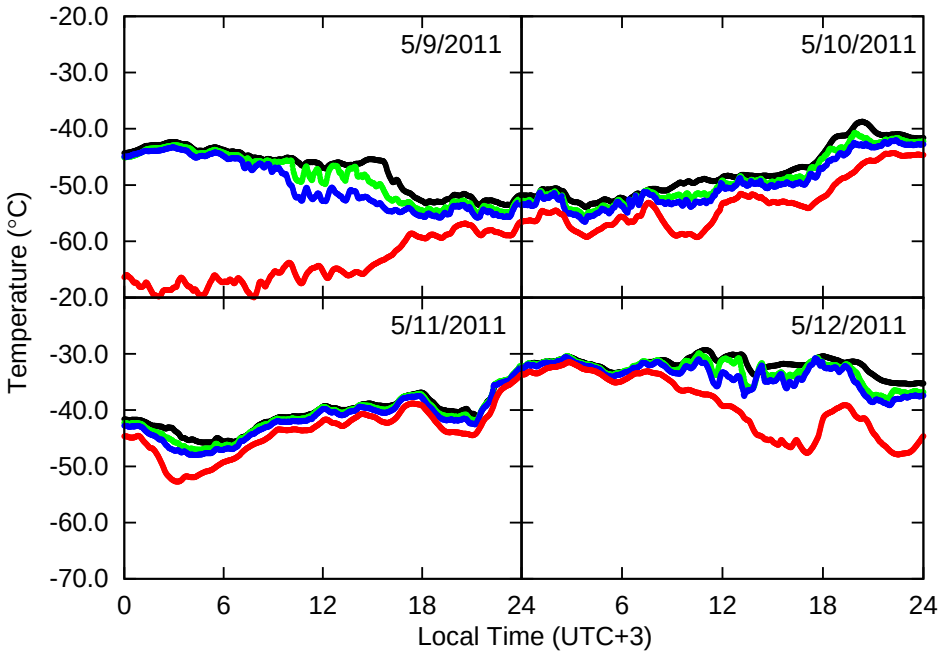

Figure C.28: Same as Fig. C.1, but for the period from May 9 00:00 (UTC+3) to May 12 24:00, 2011.

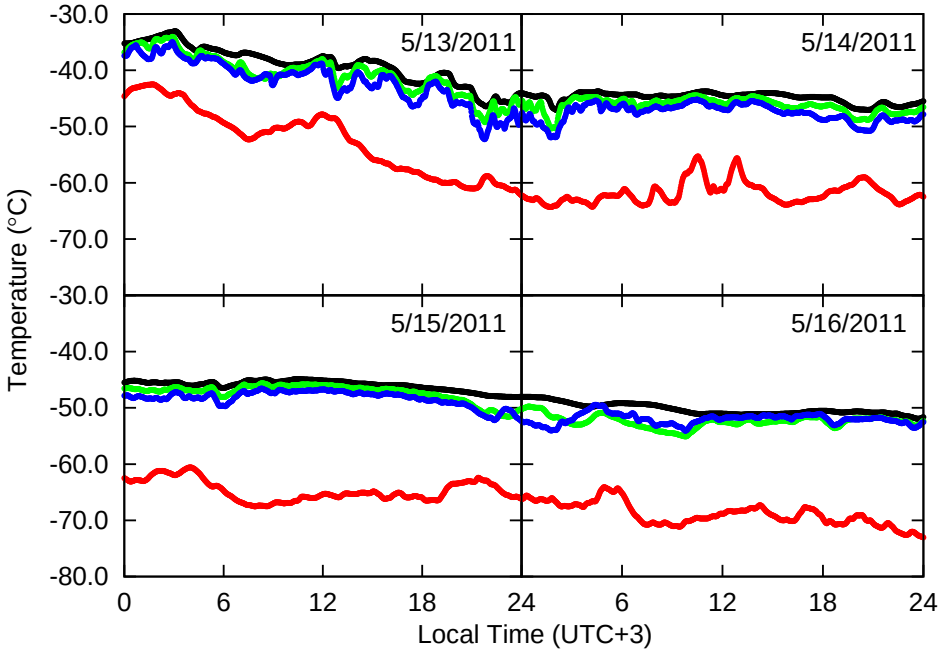

Figure C.29: Same as Fig. C.1, but for the period from May 13 00:00 (UTC+3) to May 16 24:00, 2011.

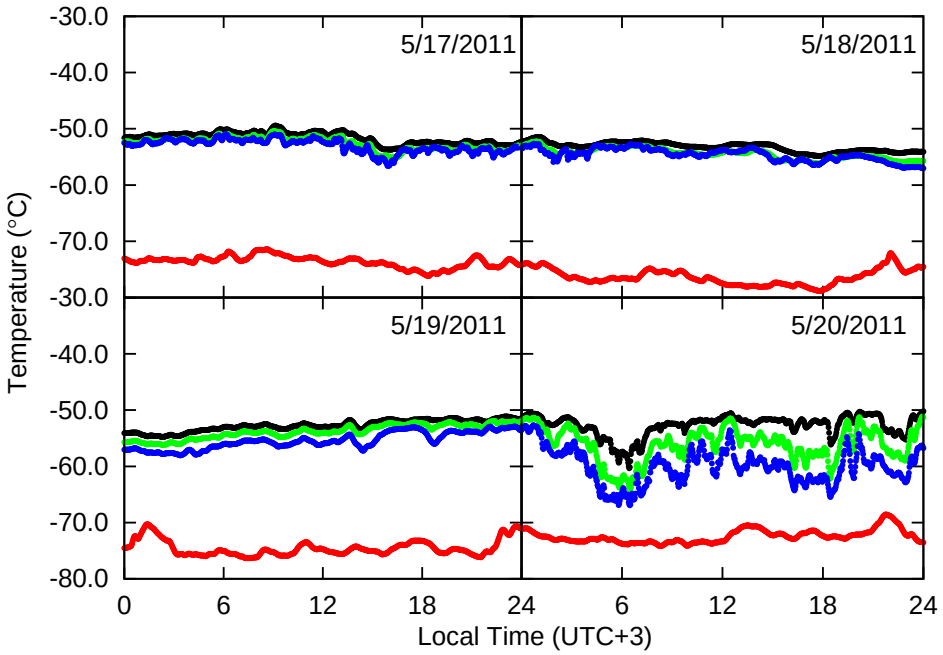

Figure C.30: Same as Fig. C.1, but for the period from May 17 00:00 (UTC+3) to May 20 24:00, 2011.

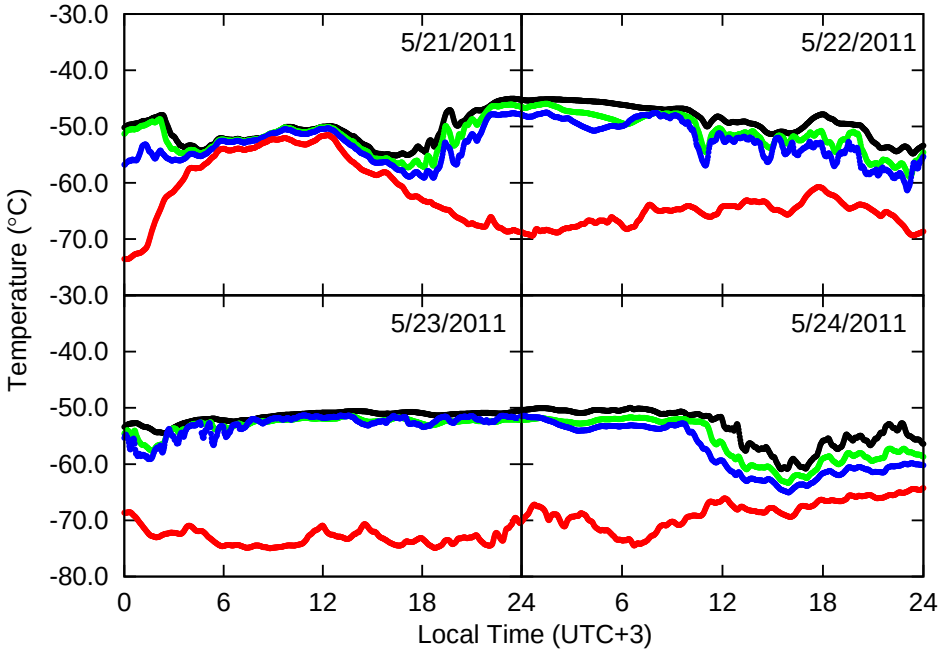

Figure C.31: Same as Fig. C.1, but for the period from May 21 00:00 (UTC+3) to May 24 24:00, 2011.

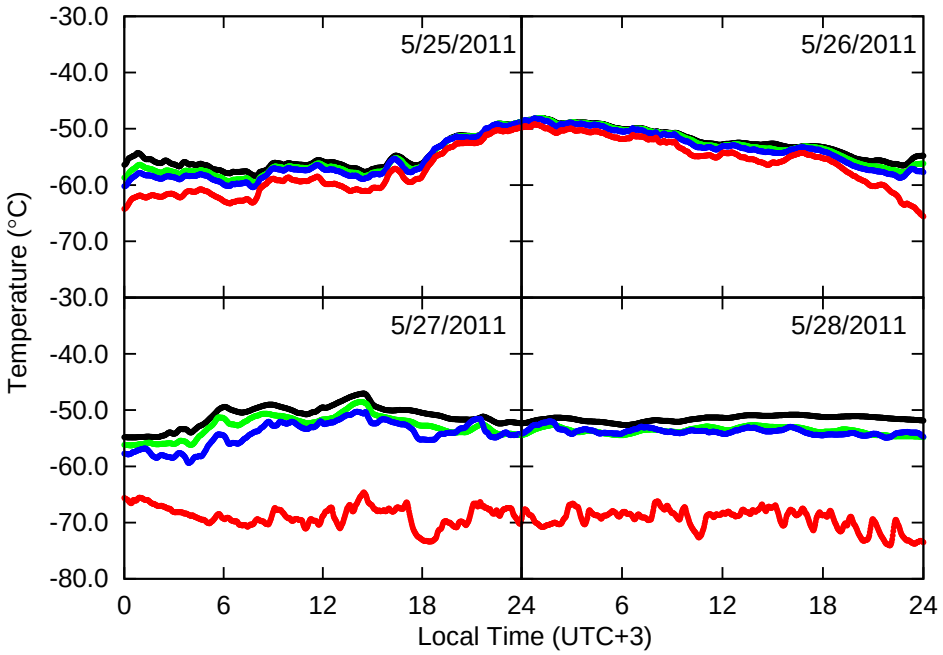

Figure C.32: Same as Fig. C.1, but for the period from May 25 00:00 (UTC+3) to May 28 24:00, 2011.

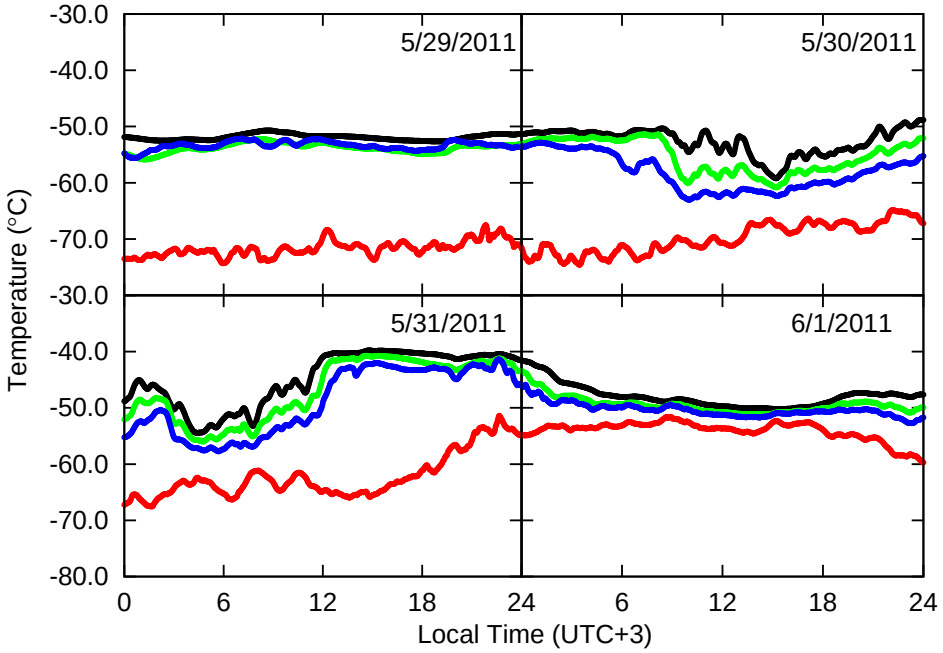

Figure C.33: Same as Fig. C.1, but for the period from May 29 00:00 (UTC+3) to June 1 24:00, 2011.

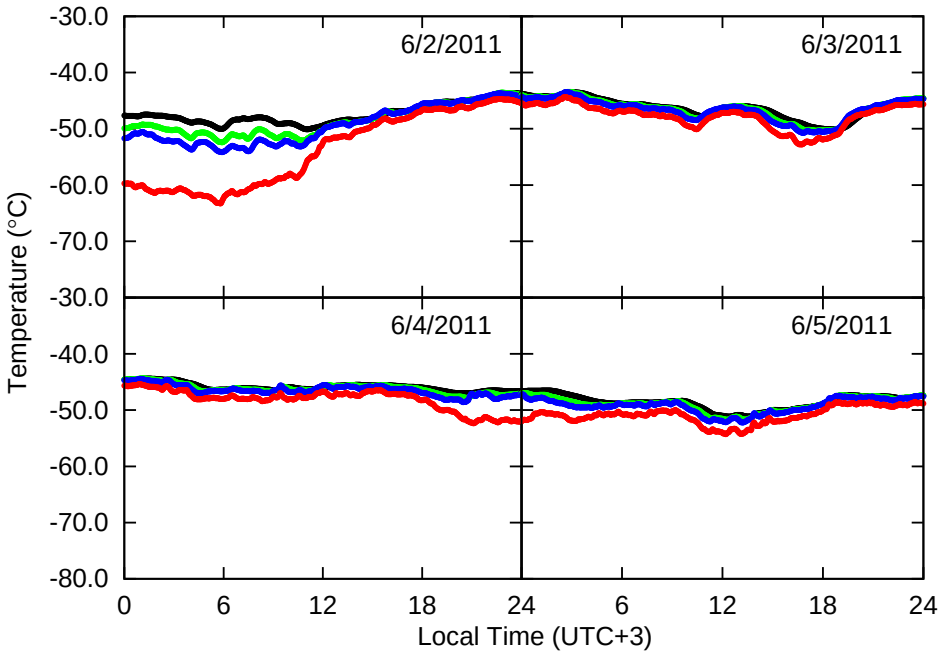

Figure C.34: Same as Fig. C.1, but for the period from June 2 00:00 (UTC+3) to June 5 24:00, 2011.

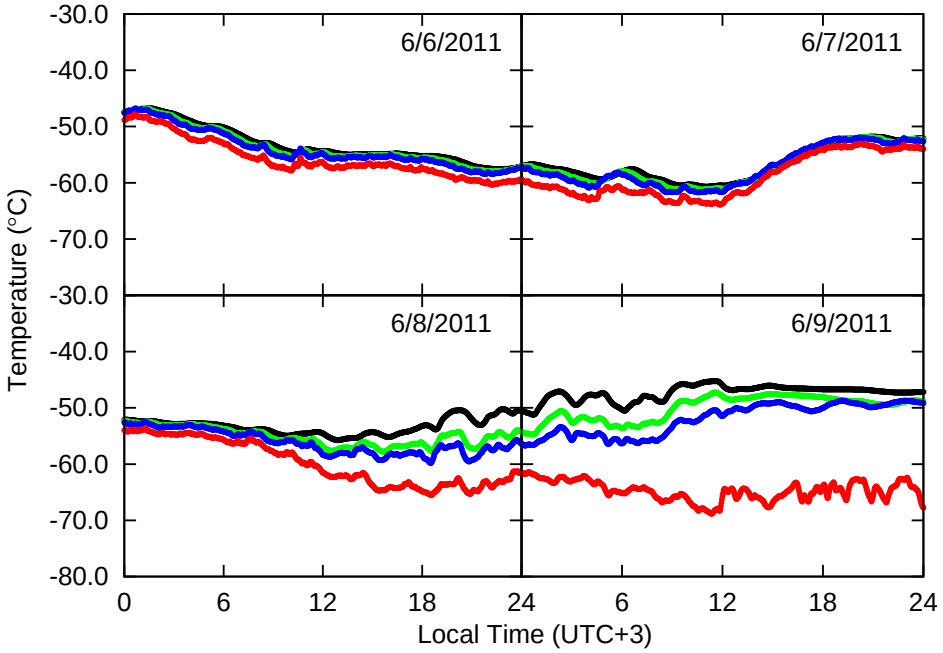

Figure C.35: Same as Fig. C.1, but for the period from June 6 00:00 (UTC+3) to June 9 24:00, 2011.

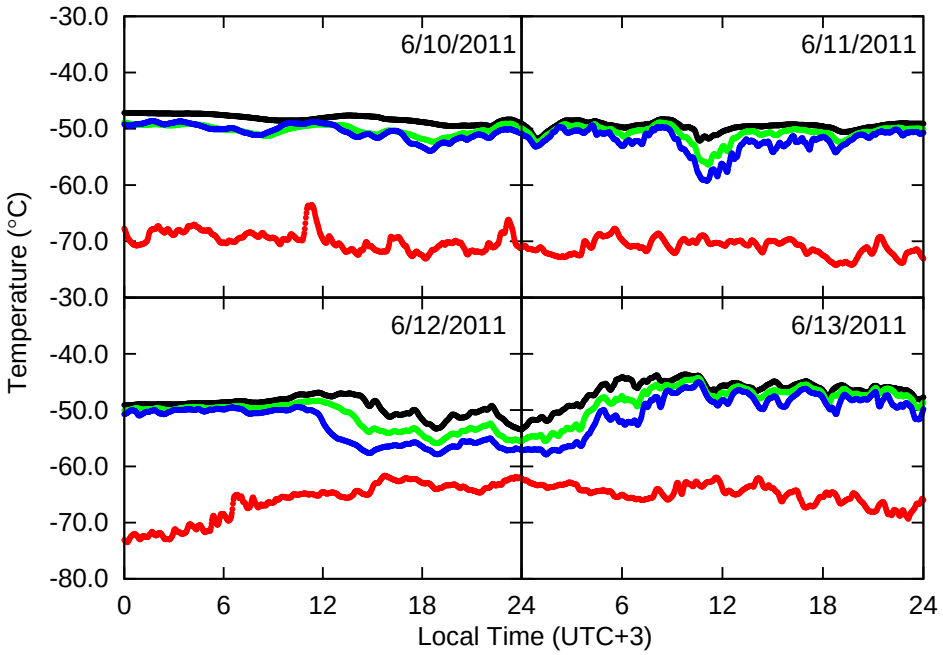

Figure C.36: Same as Fig. C.1, but for the period from June 10 00:00 (UTC+3) to June 13 24:00, 2011.

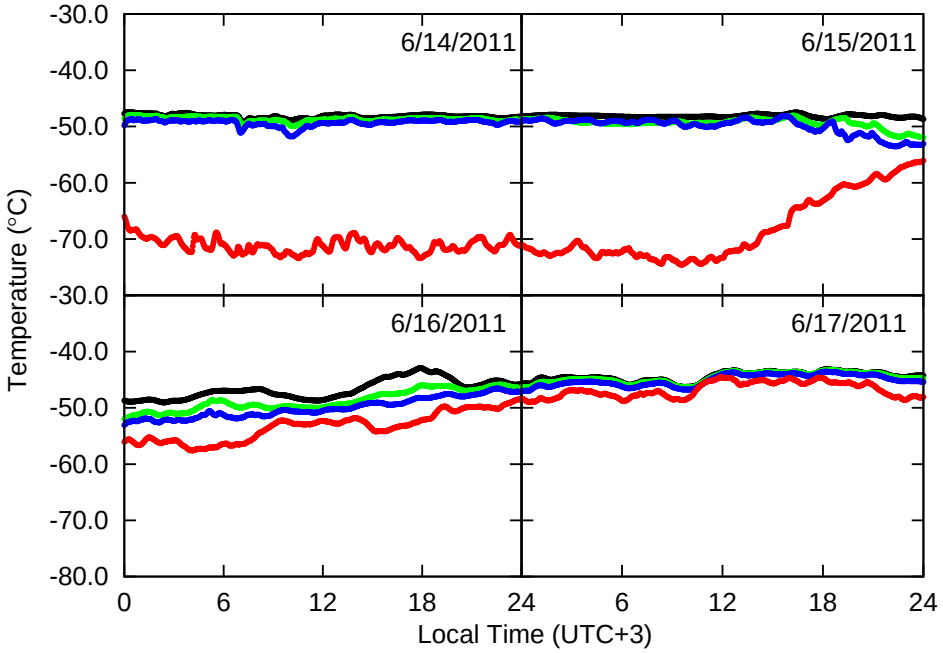

Figure C.37: Same as Fig. C.1, but for the period from June 14 00:00 (UTC+3) to June 17 24:00, 2011.

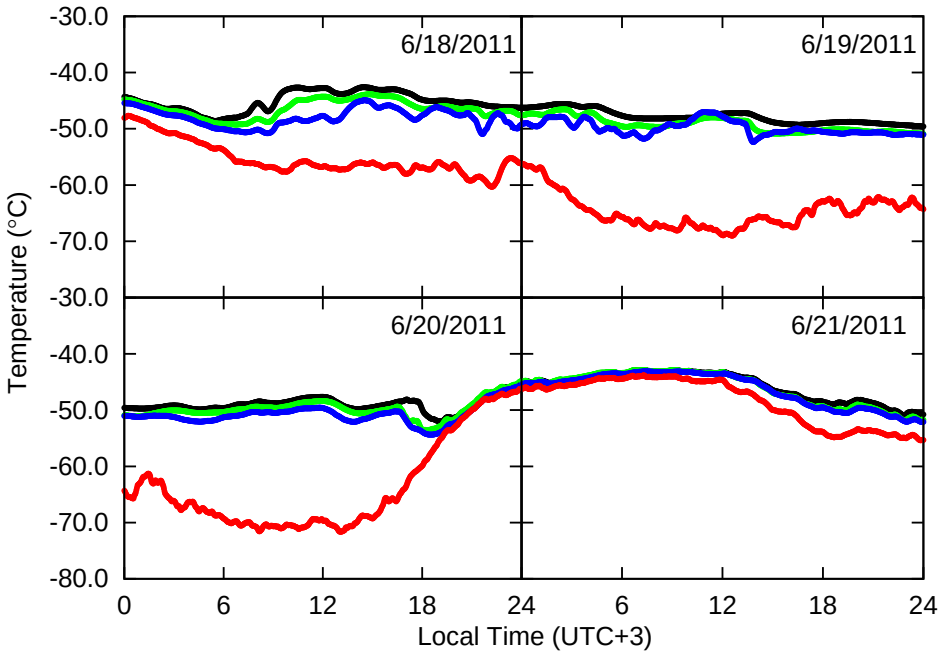

Figure C.38: Same as Fig. C.1, but for the period from June 18 00:00 (UTC+3) to June 21 24:00, 2011.

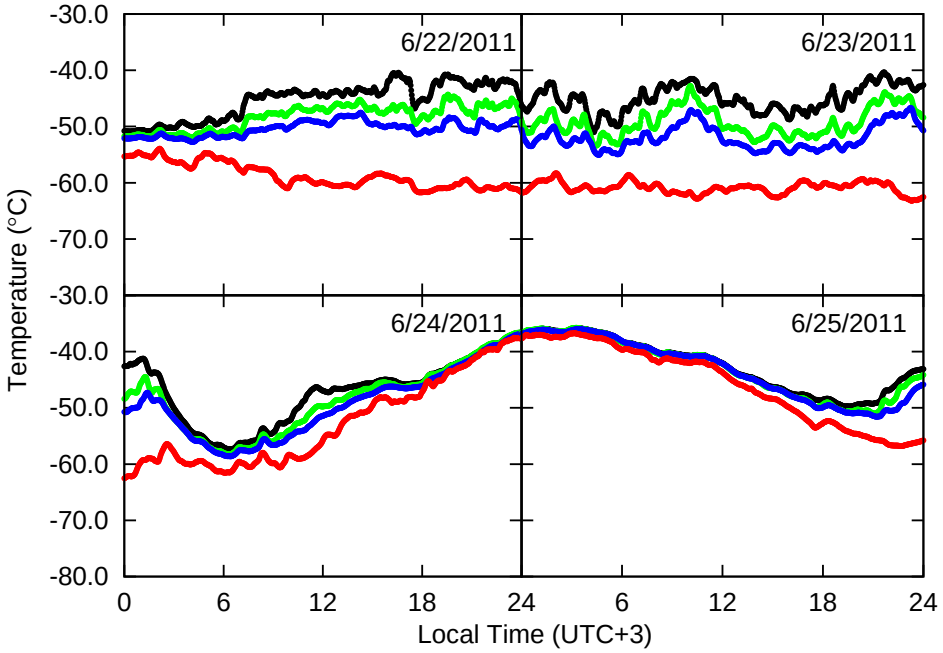

Figure C.39: Same as Fig. C.1, but for the period from June 22 00:00 (UTC+3) to June 25 24:00, 2011.

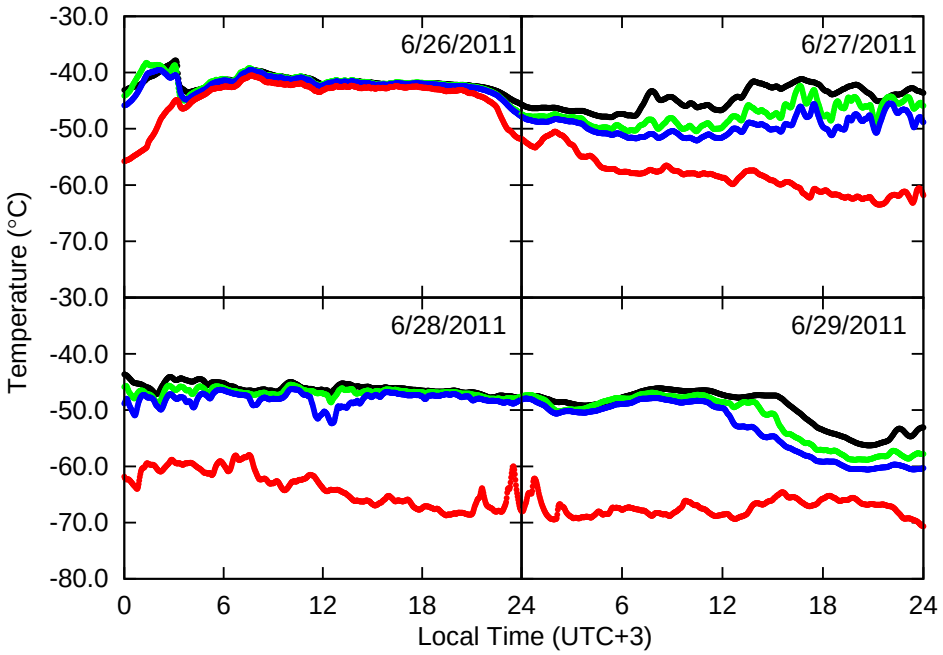

Figure C.40: Same as Fig. C.1, but for the period from June 26 00:00 (UTC+3) to June 29 24:00, 2011.

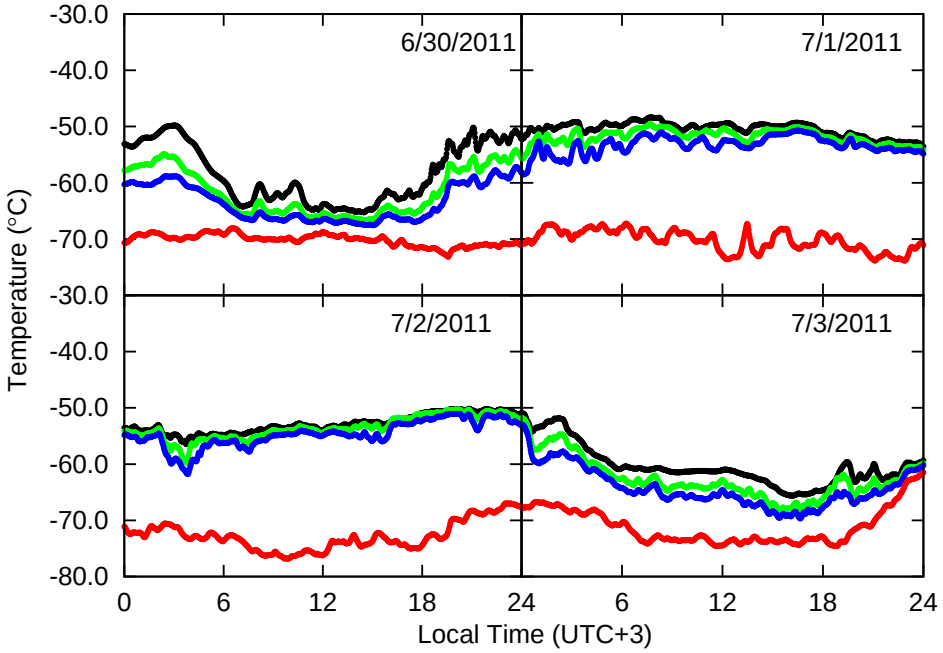

Figure C.41: Same as Fig. C.1, but for the period from June 30 00:00 (UTC+3) to July 3 24:00, 2011.

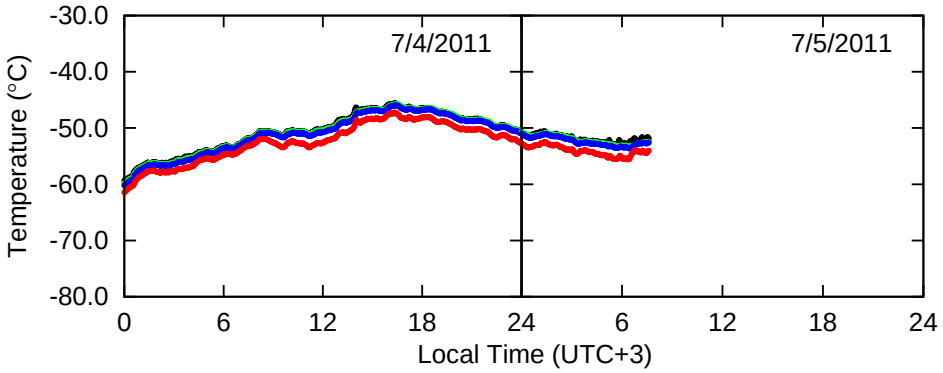

Figure C.42: Same as Fig. C.1, but for the period from July 4 00:00 (UTC+3) to July 5 24:00, 2011.

C.2 Temperature gradients

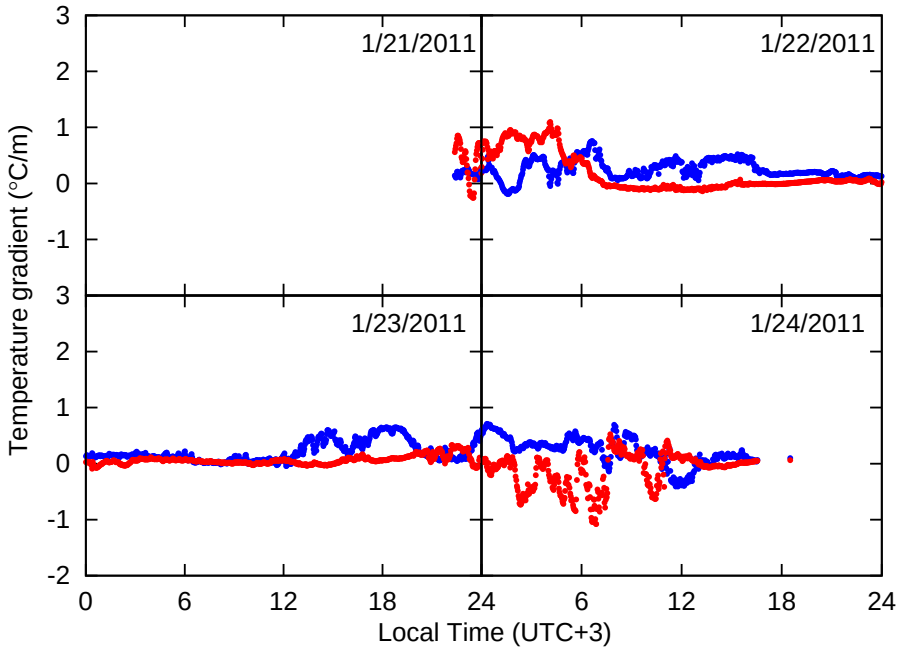

Figure C.43: Time series of the temperature gradients (°C/m) from 0.3 m to 9.5 m (red) and from 9.5 m to 15.8 m (blue) with two minute time resolution for the period from January 21 00:00 (UTC+3) to January 24 24:00, 2011.

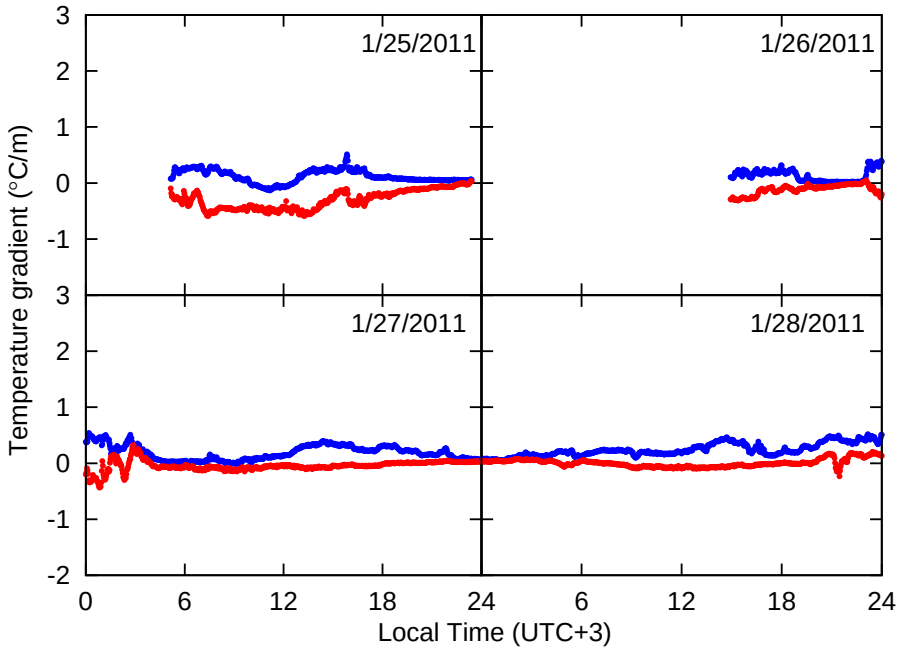

Figure C.44: Same as Fig. C.43, but for the period from January 25 00:00 (UTC+3) to January 28 24:00, 2011.

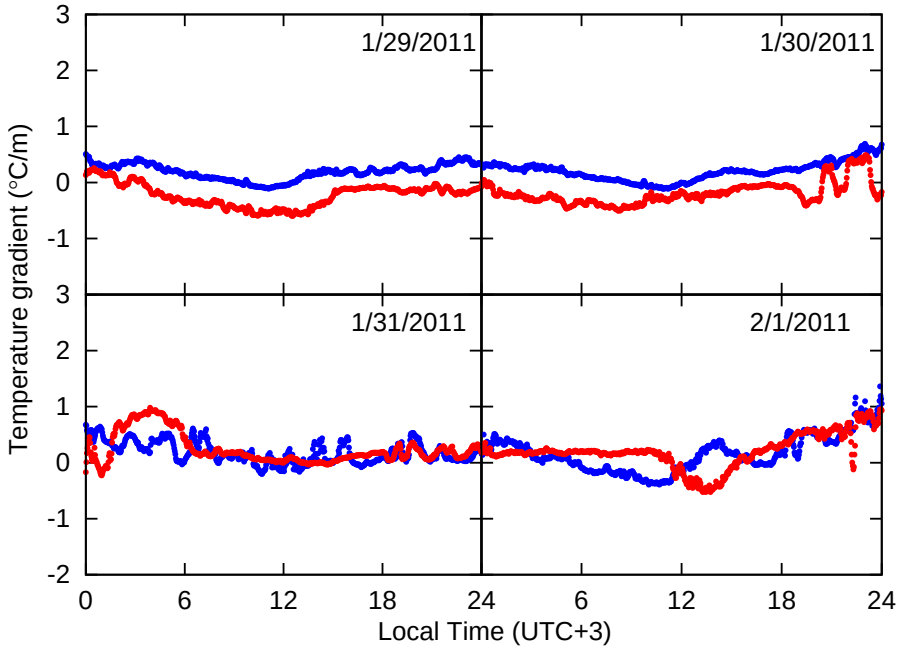

Figure C.45: Same as Fig. C.43, but for the period from January 29 00:00 (UTC+3) to February 1 24:00, 2011.

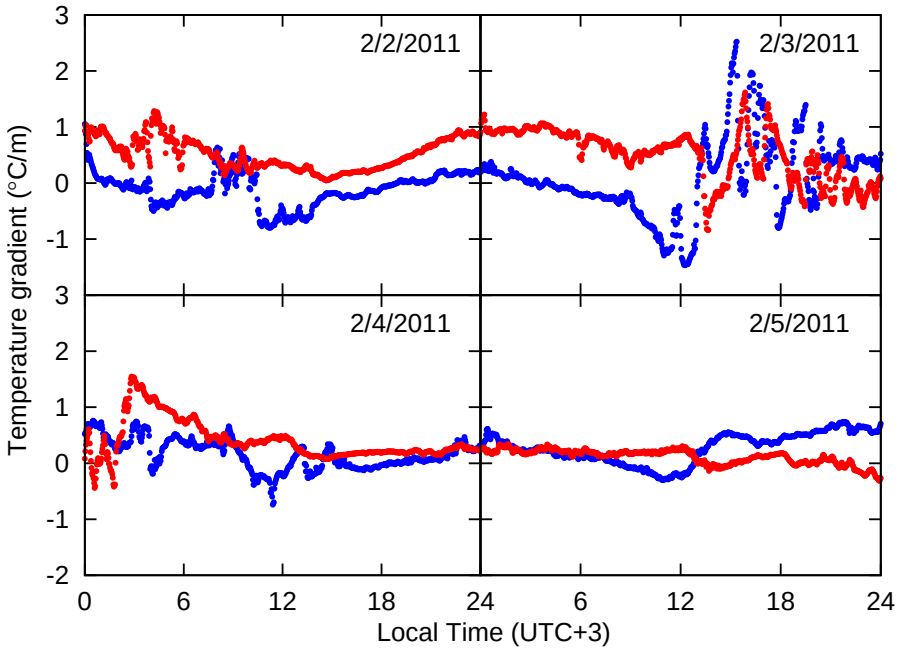

Figure C.46: Same as Fig. C.43, but for the period from February 2 00:00 (UTC+3) to February 5 24:00, 2011.

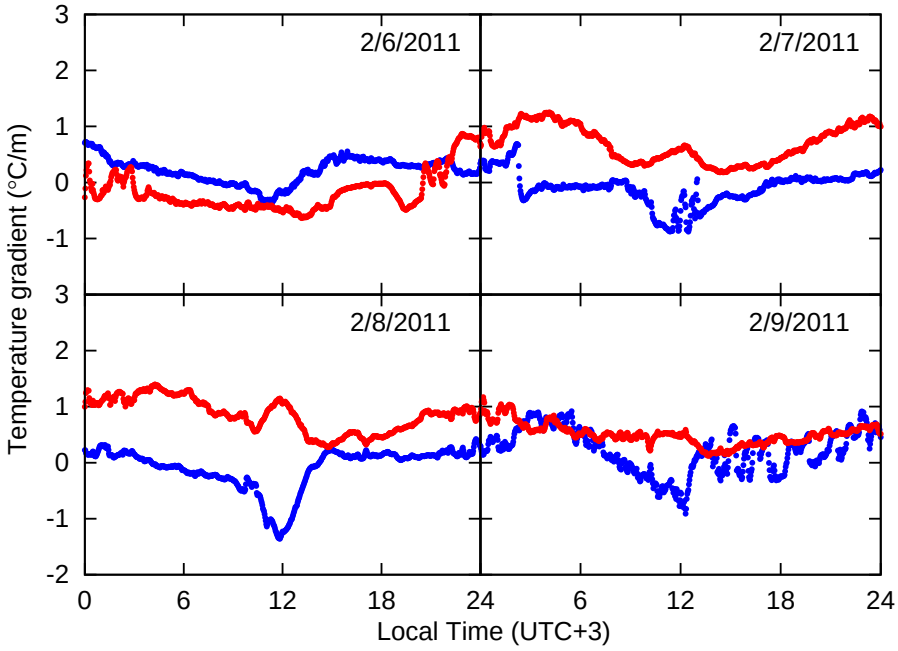

Figure C.47: Same as Fig. C.43, but for the period from February 6 00:00 (UTC+3) to February 9 24:00, 2011.

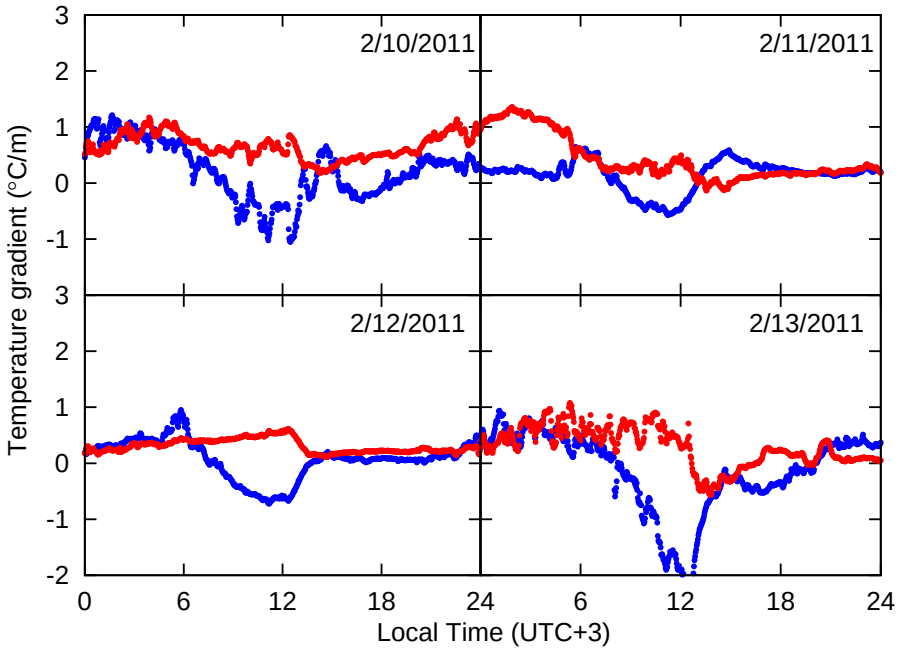

Figure C.48: Same as Fig. C.43, but for the period from February 10 00:00 (UTC+3) to February 13 24:00, 2011.

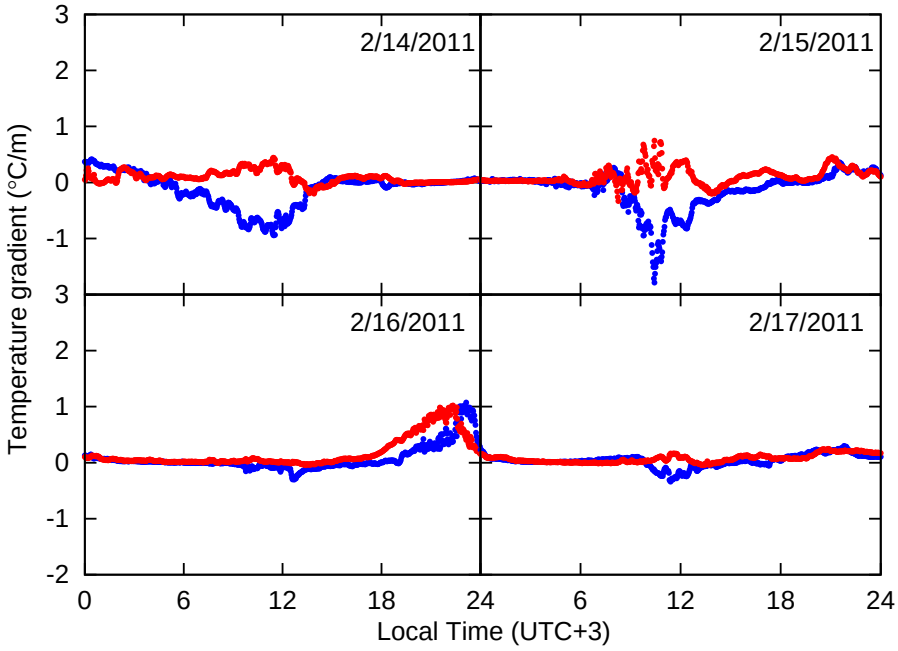

Figure C.49: Same as Fig. C.43, but for the period from February 14 00:00 (UTC+3) to February 17 24:00, 2011.

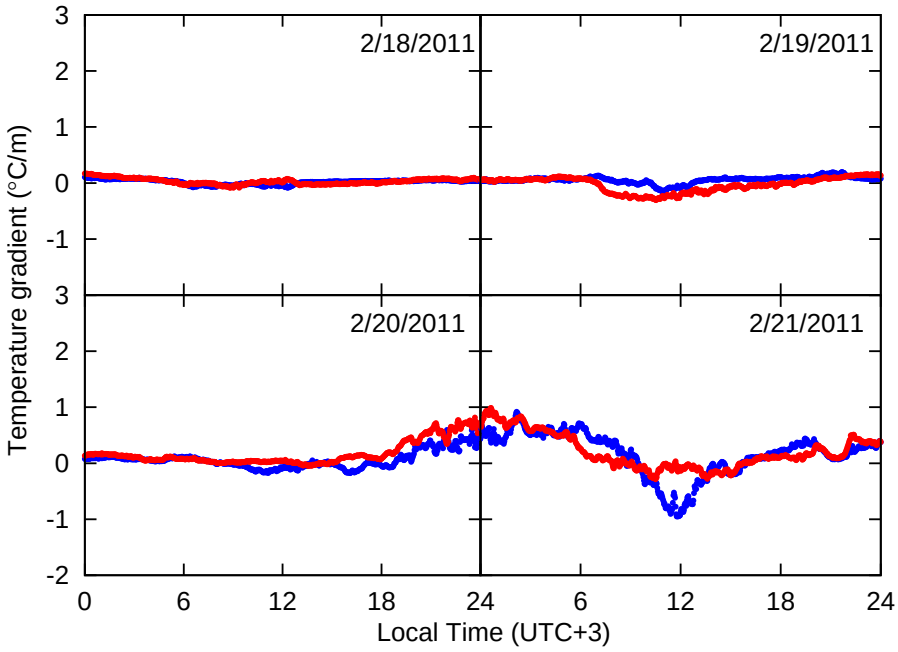

Figure C.50: Same as Fig. C.43, but for the period from February 18 00:00 (UTC+3) to February 21 24:00, 2011.

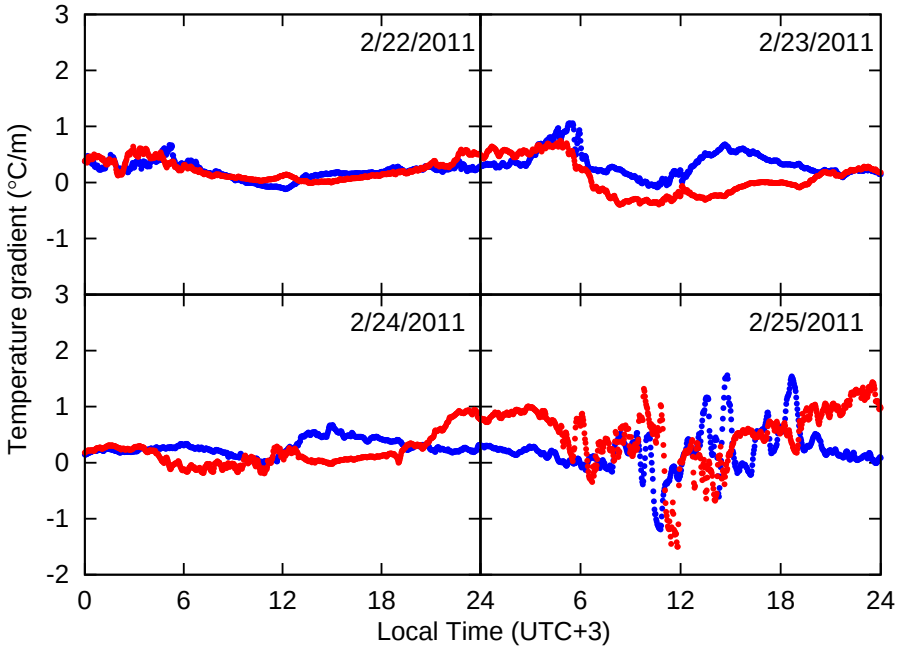

Figure C.51: Same as Fig. C.43, but for the period from February 22 00:00 (UTC+3) to February 25 24:00, 2011.

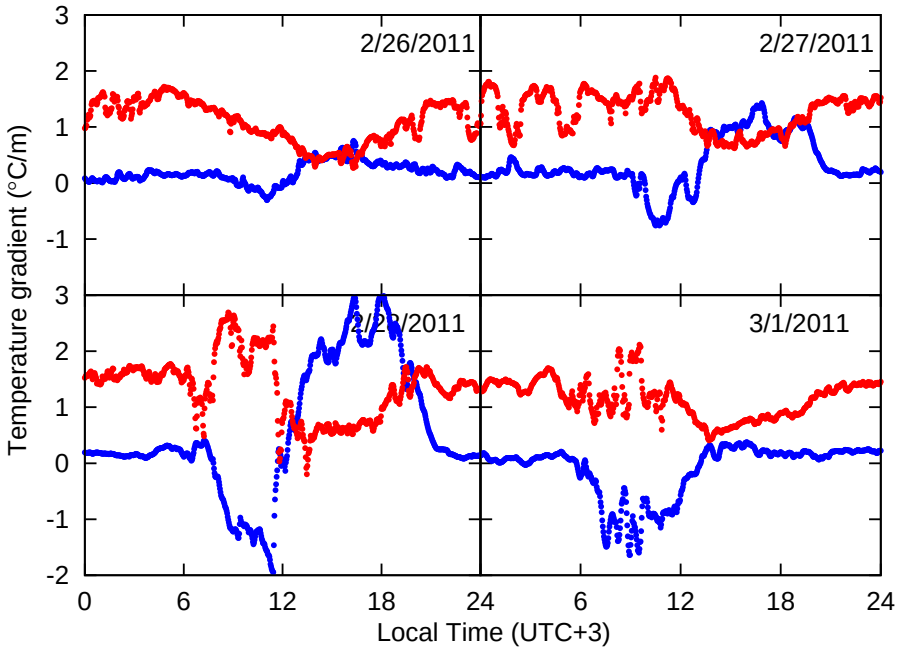

Figure C.52: Same as Fig. C.43, but for the period from February 26 00:00 (UTC+3) to March 1 24:00, 2011.

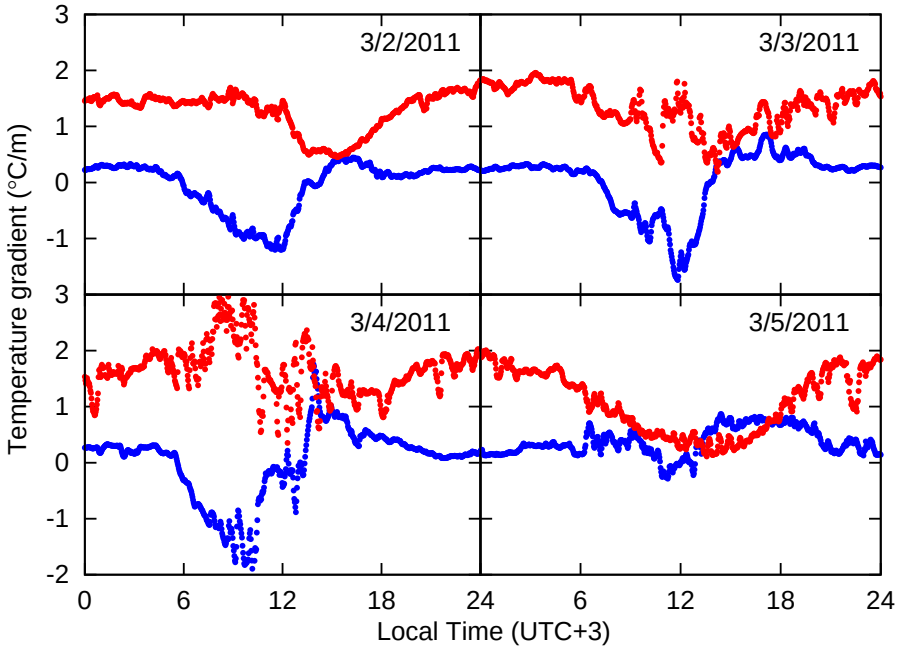

Figure C.53: Same as Fig. C.43, but for the period from March 2 00:00 (UTC+3) to March 5 24:00, 2011.

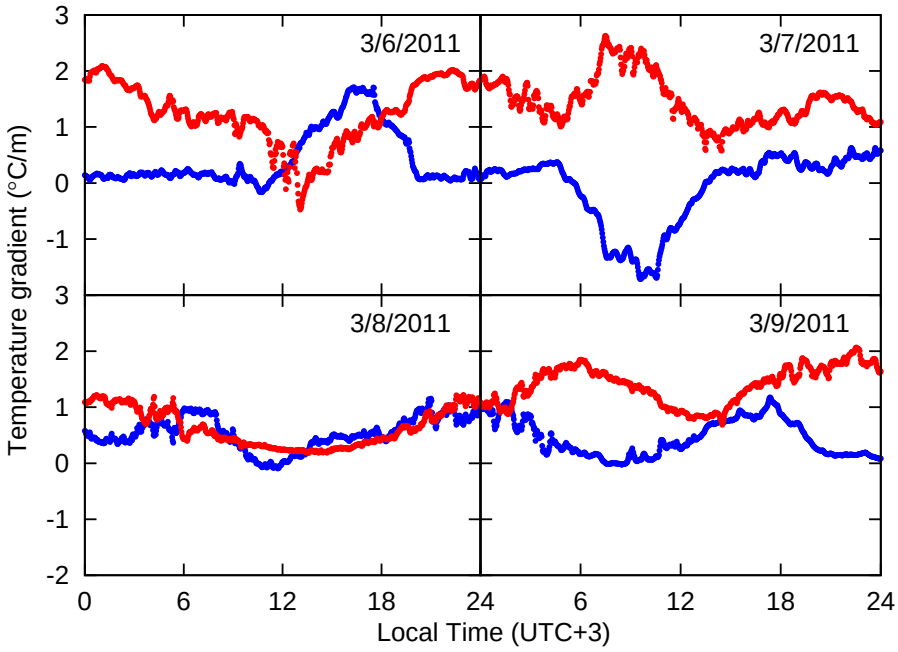

Figure C.54: Same as Fig. C.43, but for the period from March 6 00:00 (UTC+3) to March 9 24:00, 2011.

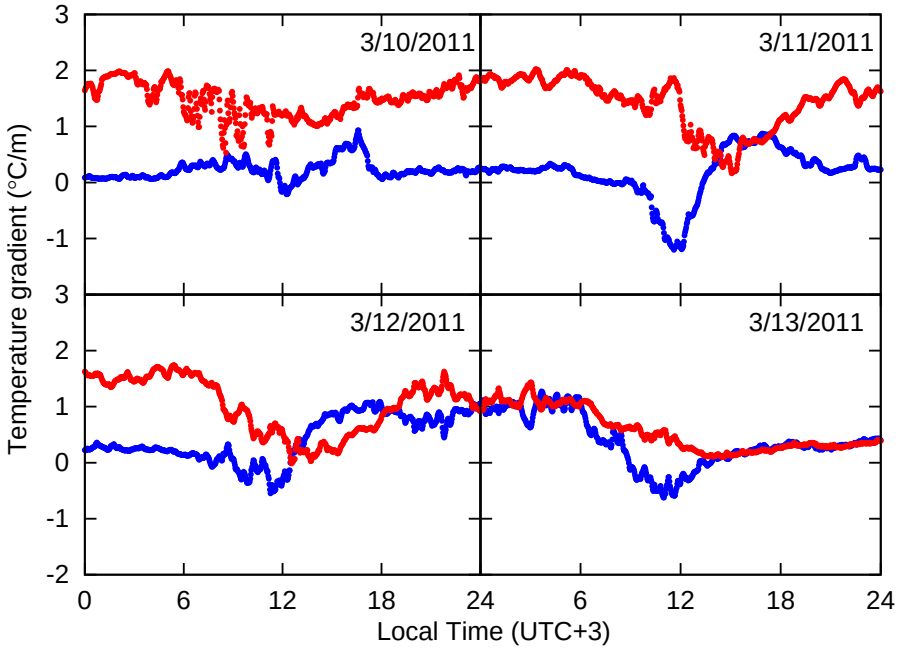

Figure C.55: Same as Fig. C.43, but for the period from March 10 00:00 (UTC+3) to March 13 24:00, 2011.

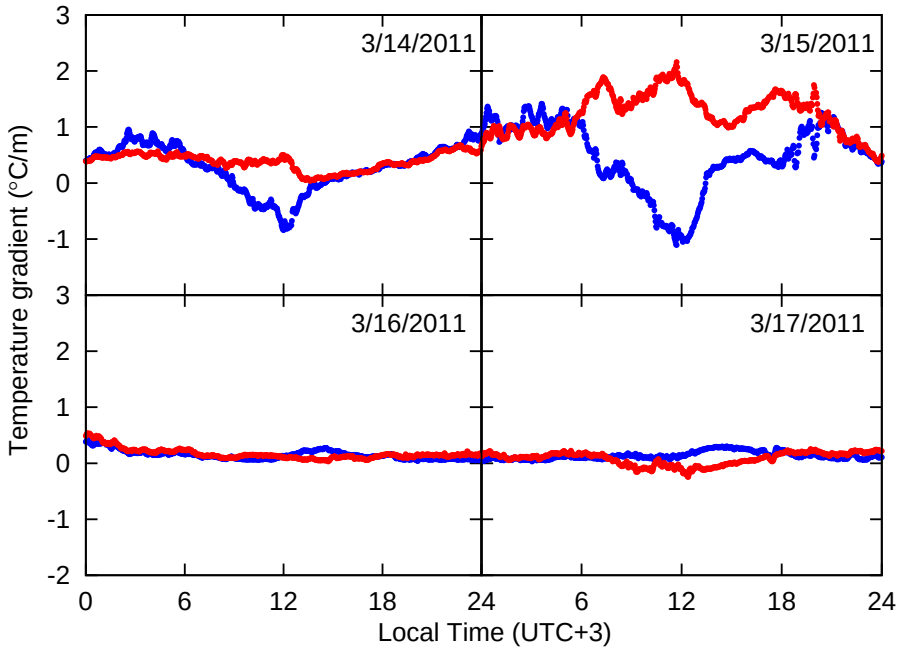

Figure C.56: Same as Fig. C.43, but for the period from March 14 00:00 (UTC+3) to March 17 24:00, 2011.

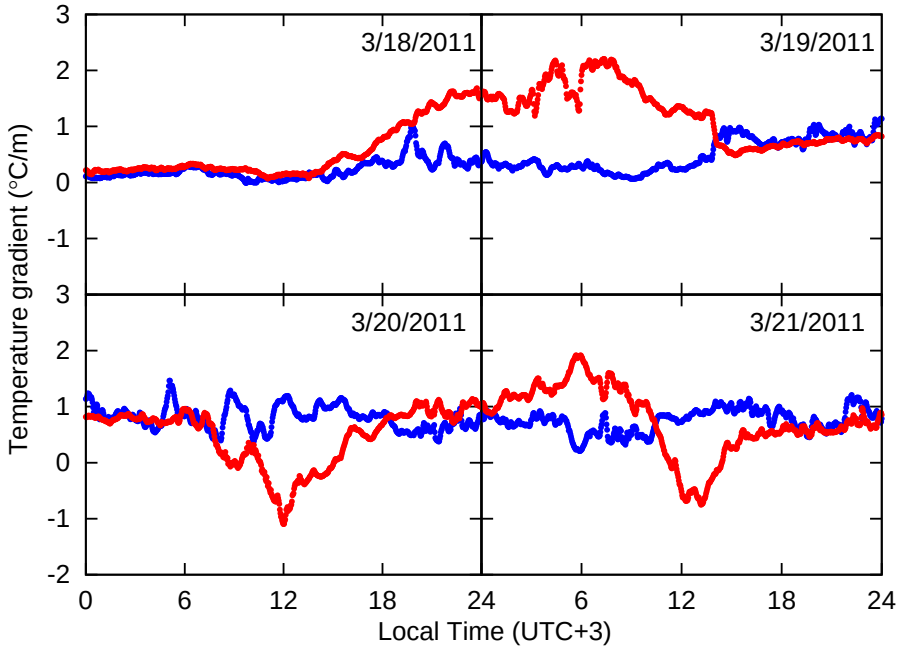

Figure C.57: Same as Fig. C.43, but for the period from March 18 00:00 (UTC+3) to March 21 24:00, 2011.

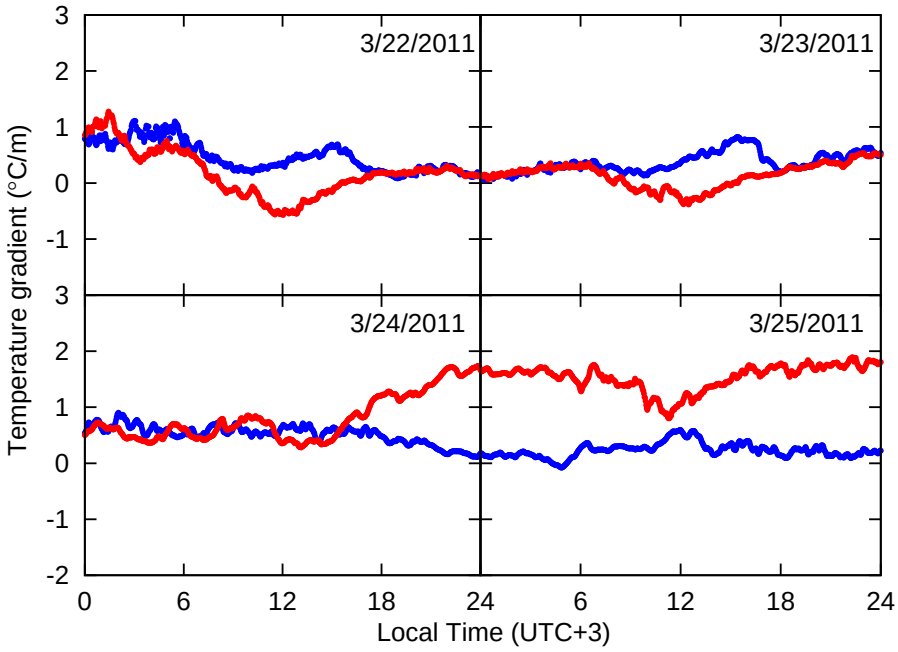

Figure C.58: Same as Fig. C.43, but for the period from March 22 00:00 (UTC+3) to March 25 24:00, 2011.

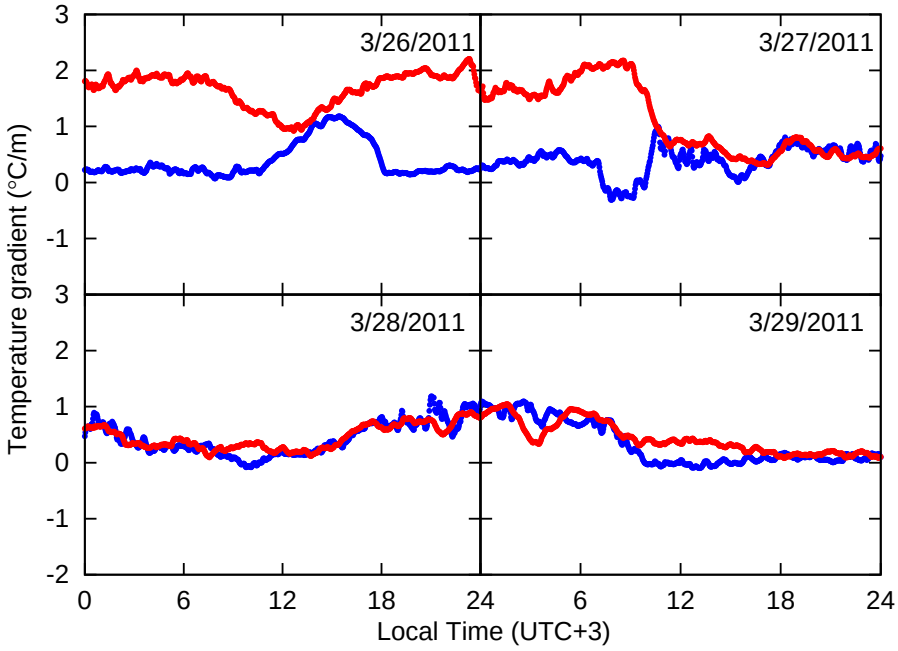

Figure C.59: Same as Fig. C.43, but for the period from March 26 00:00 (UTC+3) to March 29 24:00, 2011.

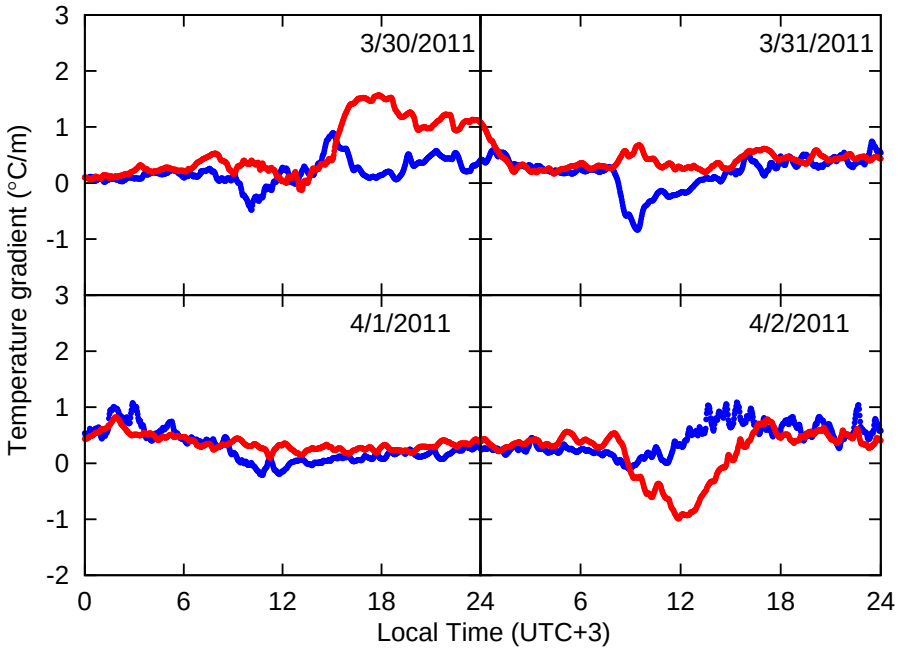

Figure C.60: Same as Fig. C.43, but for the period from March 30 00:00 (UTC+3) to April 2 24:00, 2011.

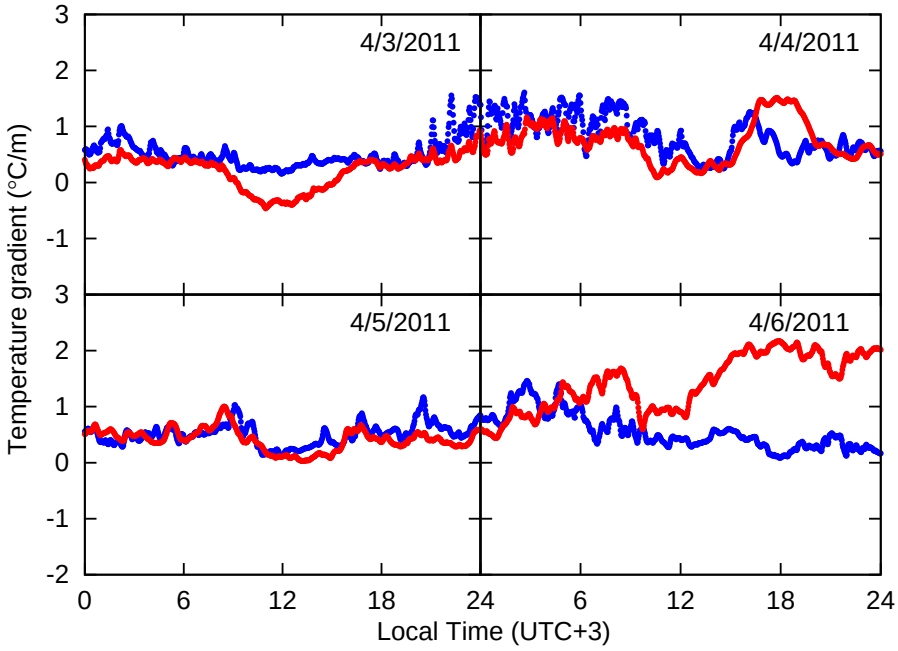

Figure C.61: Same as Fig. C.43, but for the period from April 3 00:00 (UTC+3) to April 6 24:00, 2011.

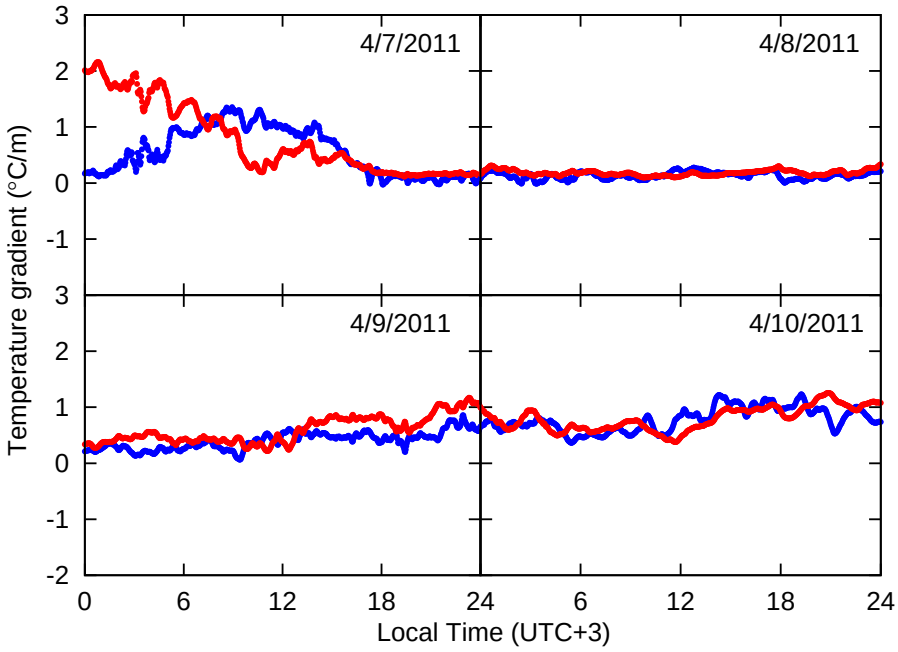

Figure C.62: Same as Fig. C.43, but for the period from April 7 00:00 (UTC+3) to April 10 24:00, 2011.

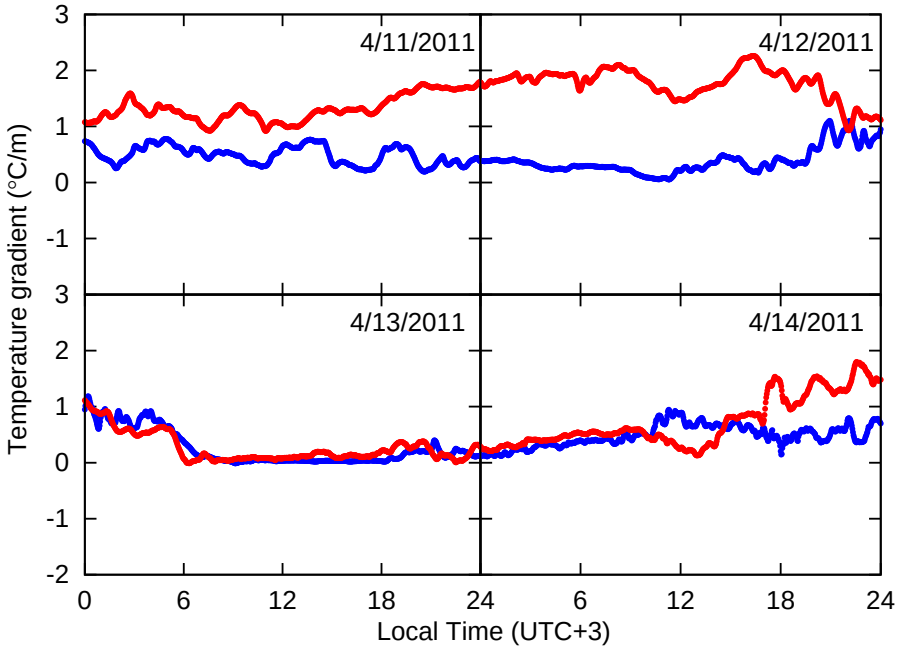

Figure C.63: Same as Fig. C.43, but for the period from April 11 00:00 (UTC+3) to April 14 24:00, 2011.

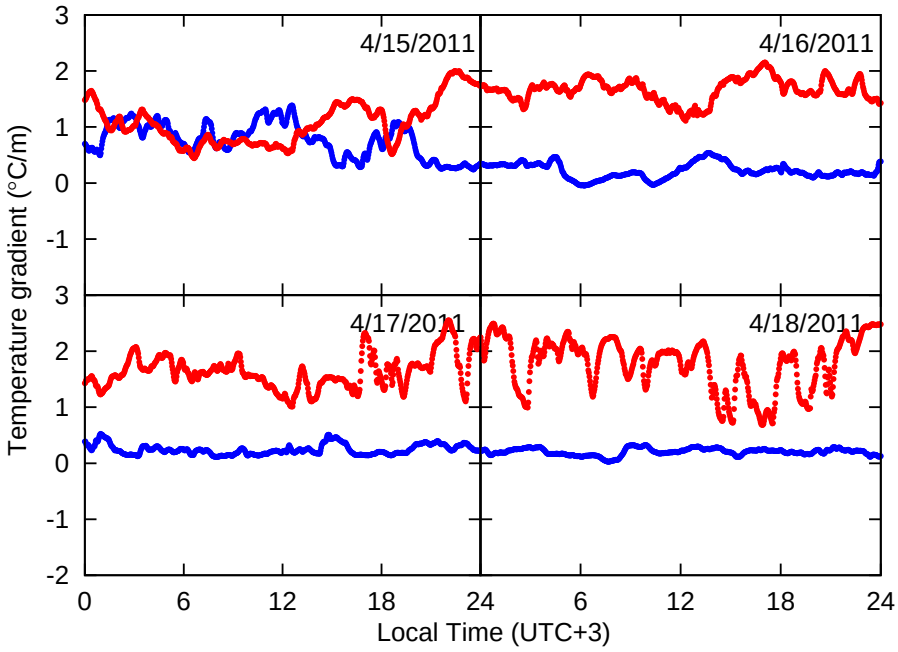

Figure C.64: Same as Fig. C.43, but for the period from April 15 00:00 (UTC+3) to April 18 24:00, 2011.

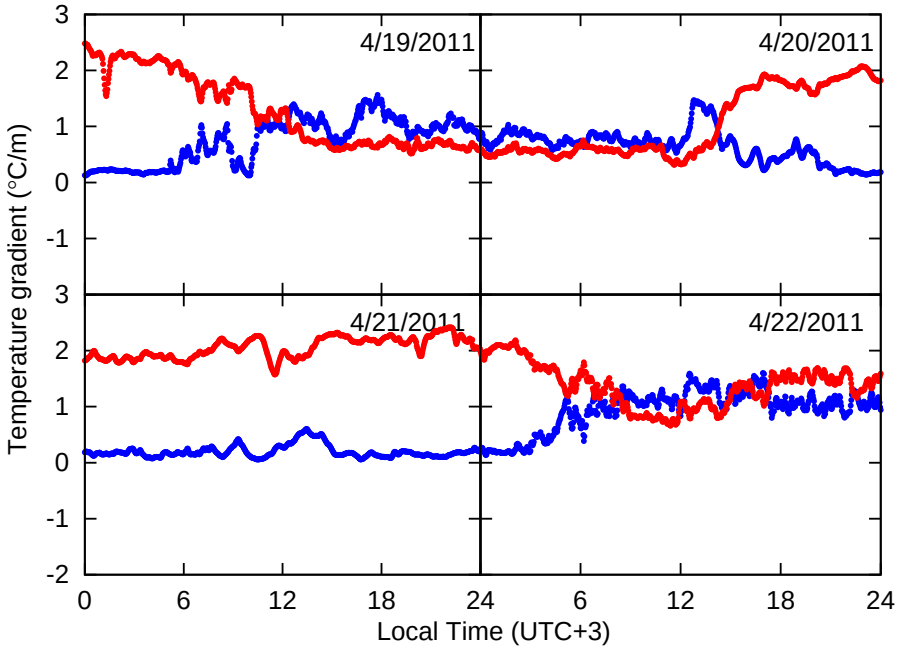

Figure C.65: Same as Fig. C.43, but for the period from April 19 00:00 (UTC+3) to April 22 24:00, 2011.

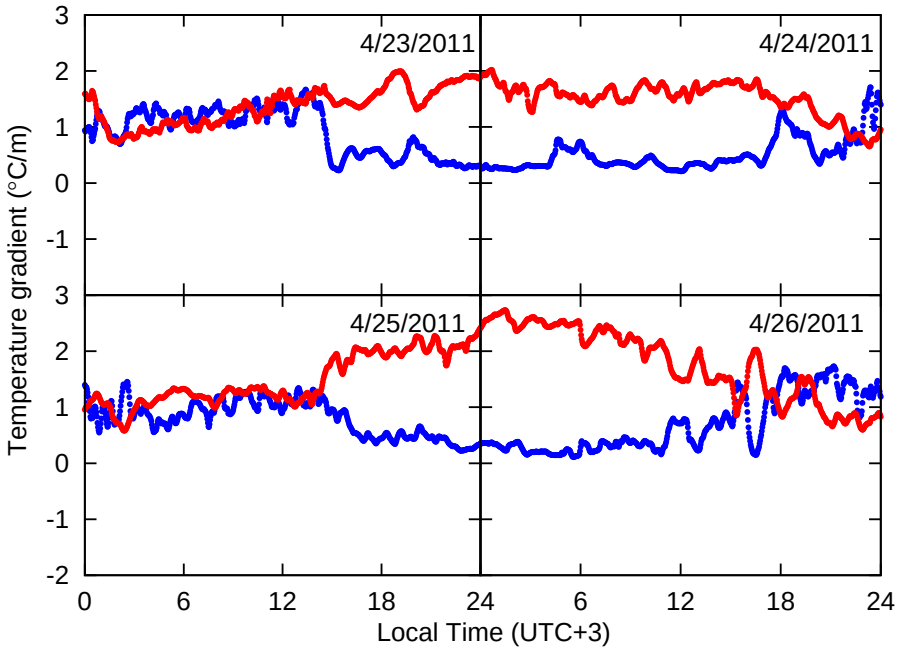

Figure C.66: Same as Fig. C.43, but for the period from April 23 00:00 (UTC+3) to April 26 24:00, 2011.

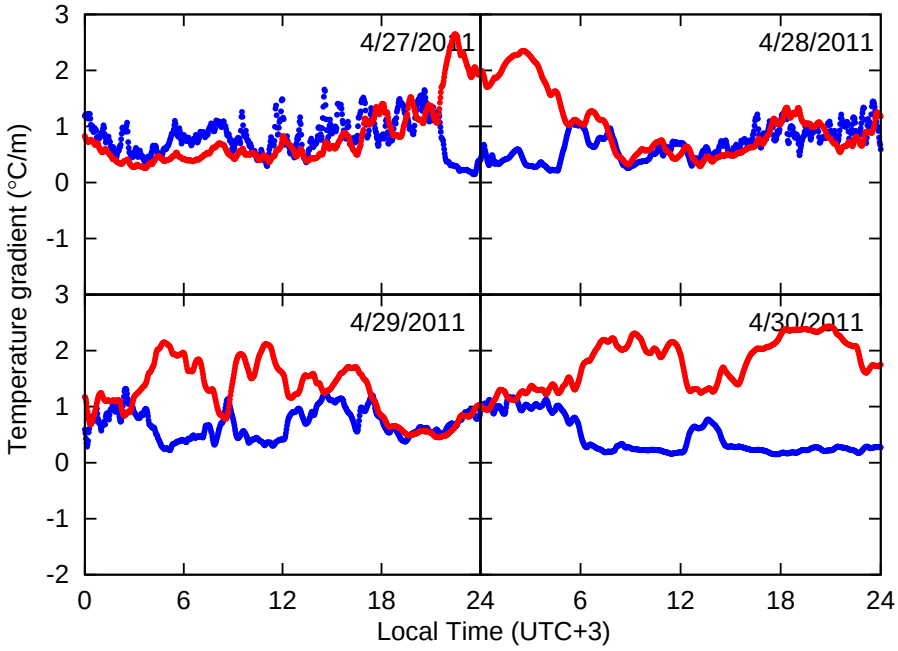

Figure C.67: Same as Fig. C.43, but for the period from April 27 00:00 (UTC+3) to April 30 24:00, 2011.

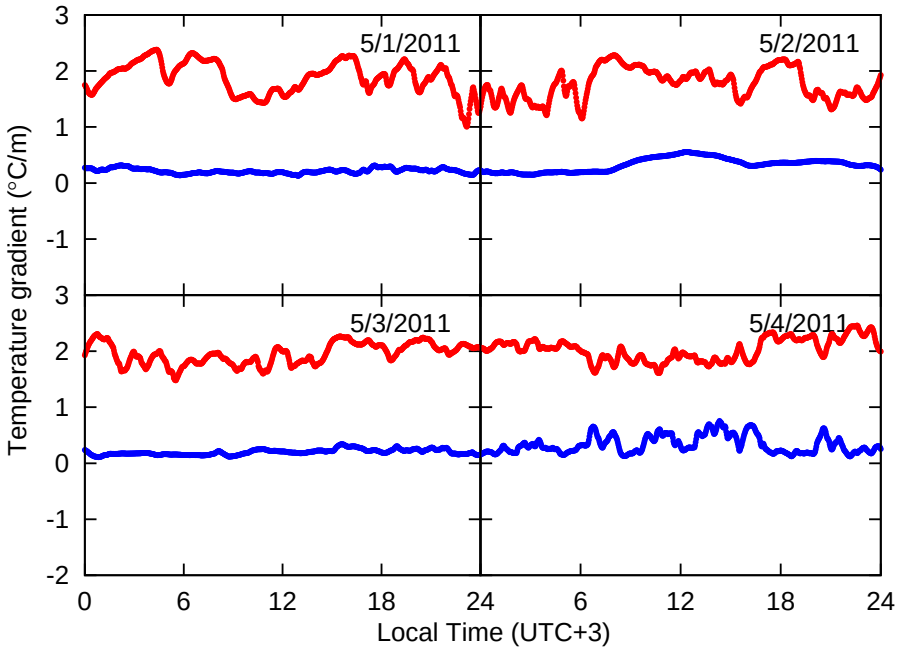

Figure C.68: Same as Fig. C.43, but for the period from May 1 00:00 (UTC+3) to May 4 24:00, 2011.

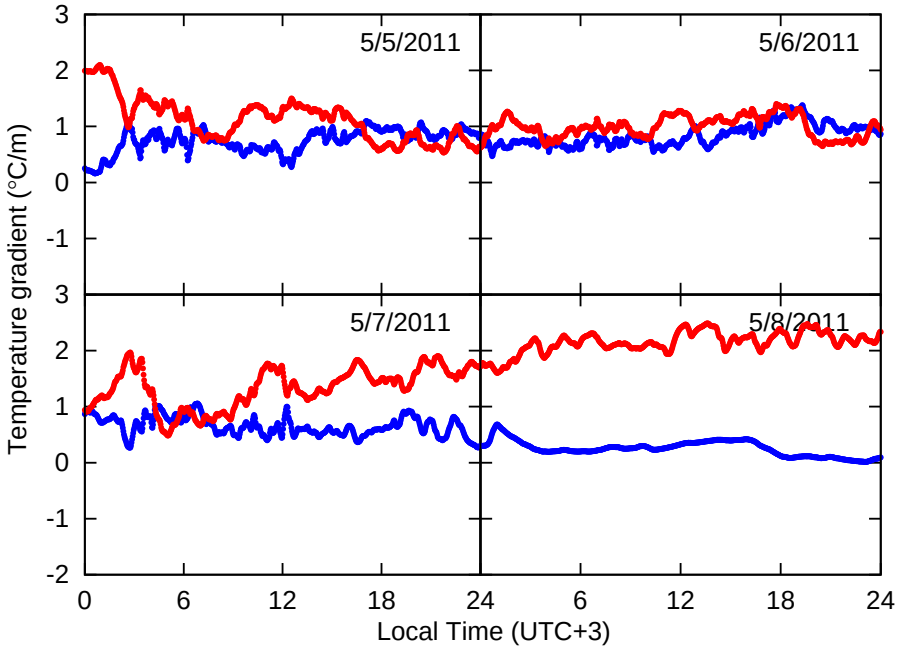

Figure C.69: Same as Fig. C.43, but for the period from May 5 00:00 (UTC+3) to May 8 24:00, 2011.

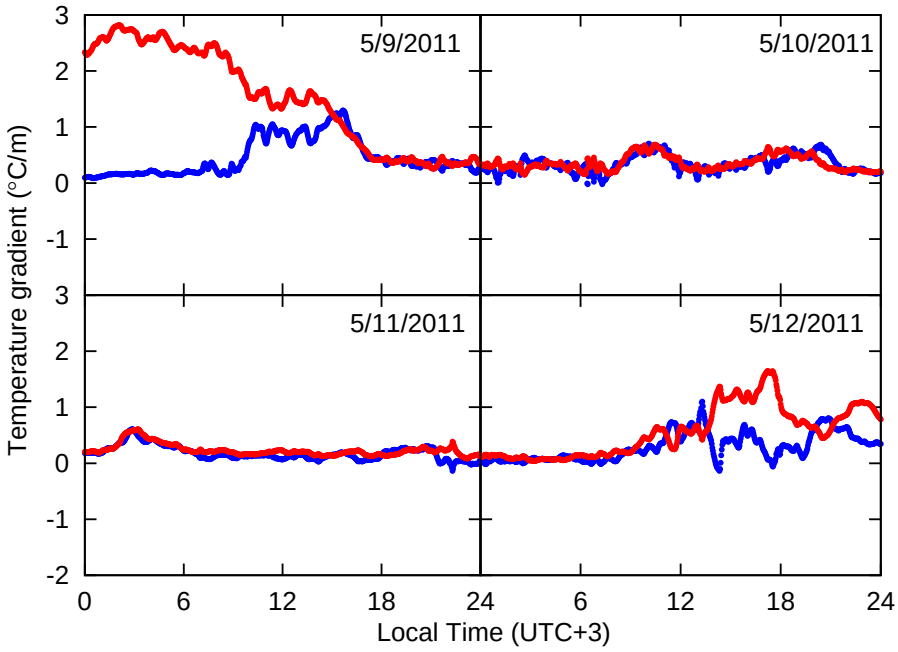

Figure C.70: Same as Fig. C.43, but for the period from May 9 00:00 (UTC+3) to May 12 24:00, 2011.

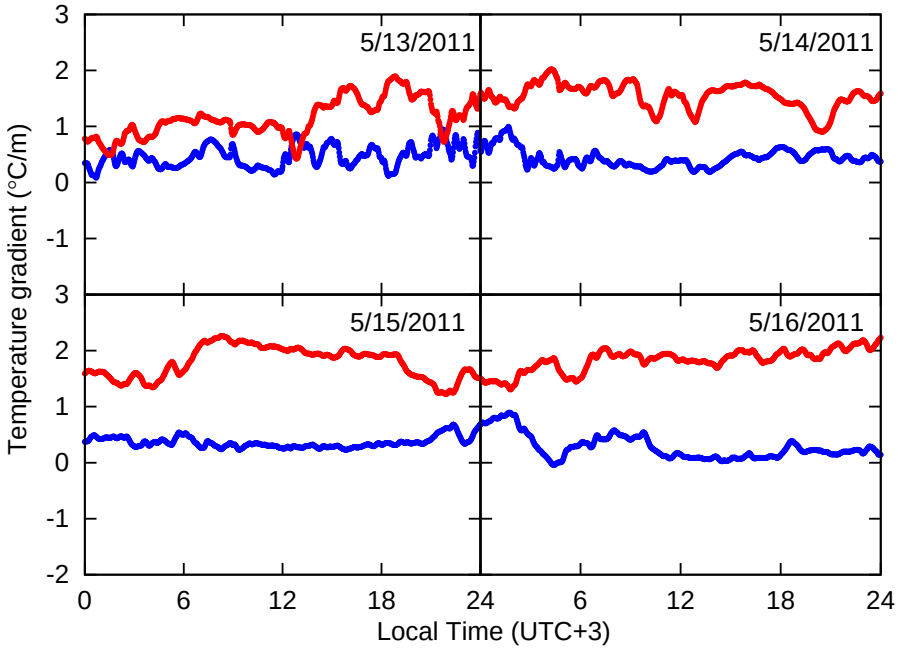

Figure C.71: Same as Fig. C.43, but for the period from May 13 00:00 (UTC+3) to May 16 24:00, 2011.

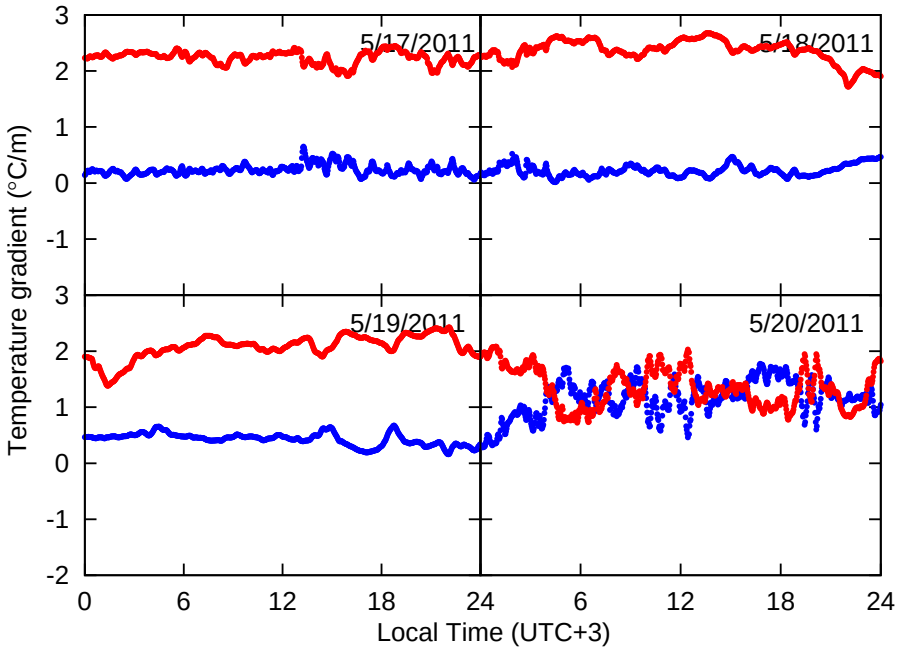

Figure C.72: Same as Fig. C.43, but for the period from May 17 00:00 (UTC+3) to May 20 24:00, 2011.

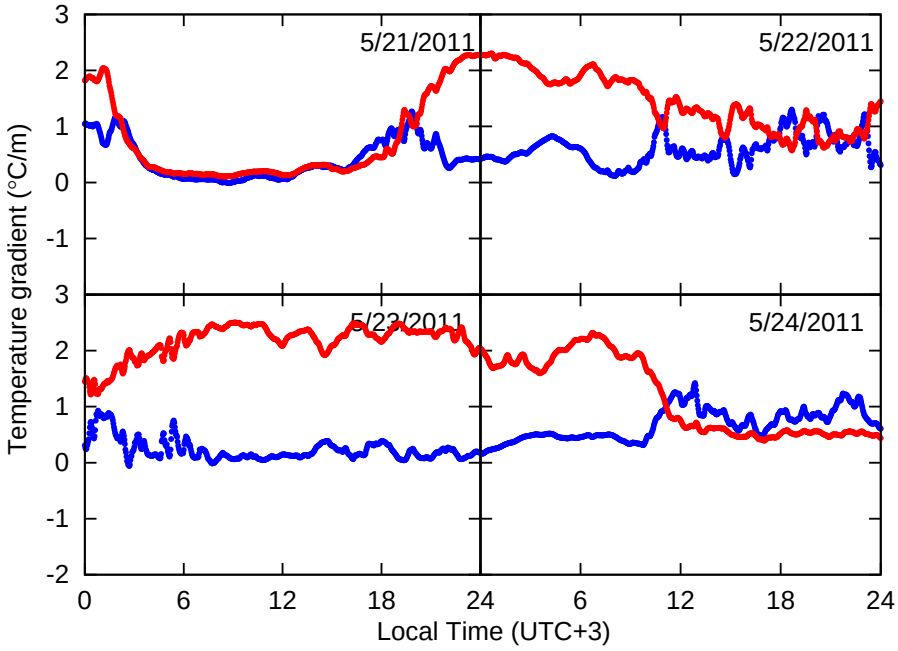

Figure C.73: Same as Fig. C.43, but for the period from May 21 00:00 (UTC+3) to May 24 24:00, 2011.

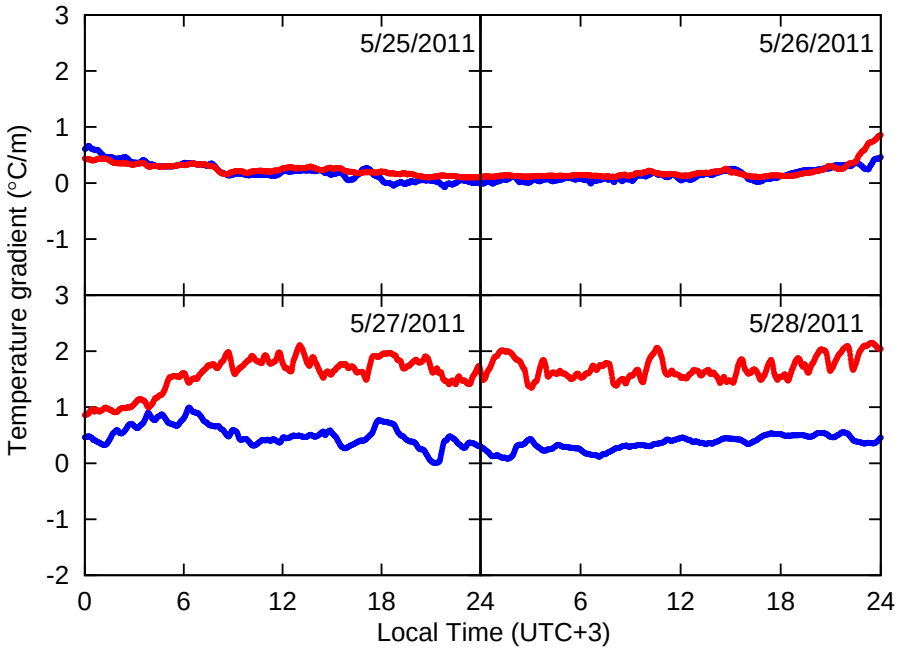

Figure C.74: Same as Fig. C.43, but for the period from May 25 00:00 (UTC+3) to May 28 24:00, 2011.

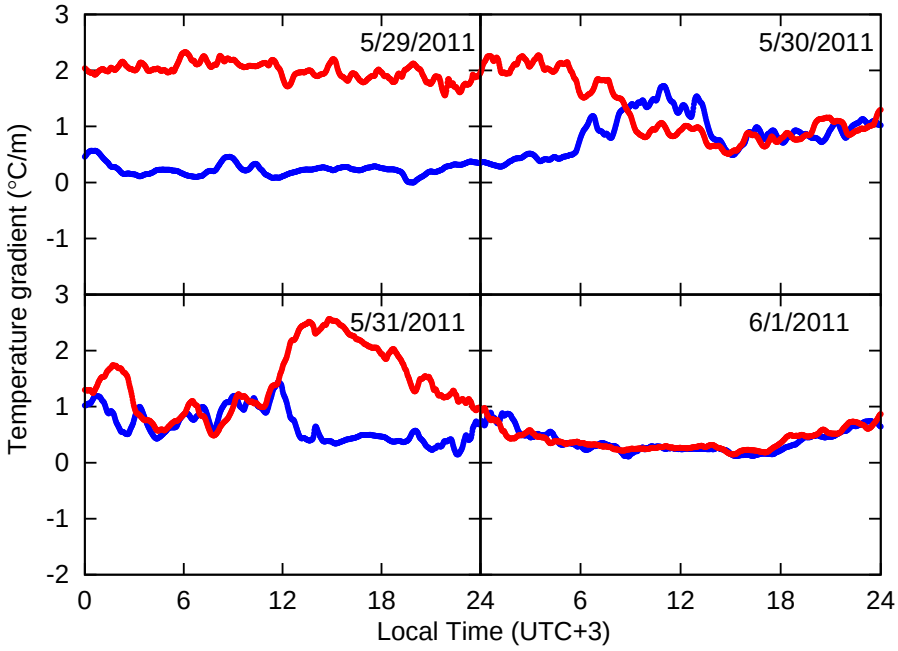

Figure C.75: Same as Fig. C.43, but for the period from May 29 00:00 (UTC+3) to June 1 24:00, 2011.

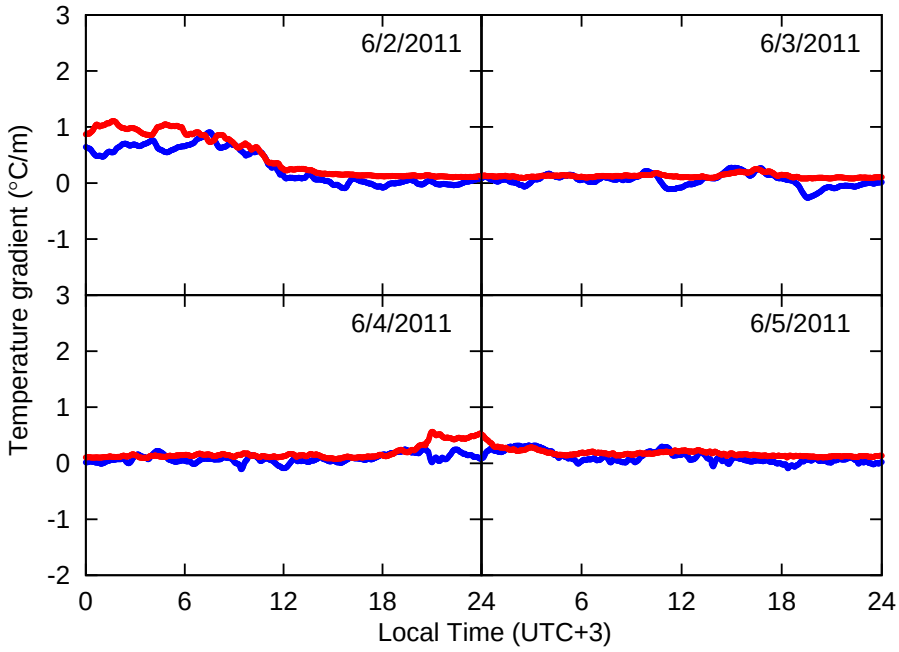

Figure C.76: Same as Fig. C.43, but for the period from June 2 00:00 (UTC+3) to June 5 24:00, 2011.

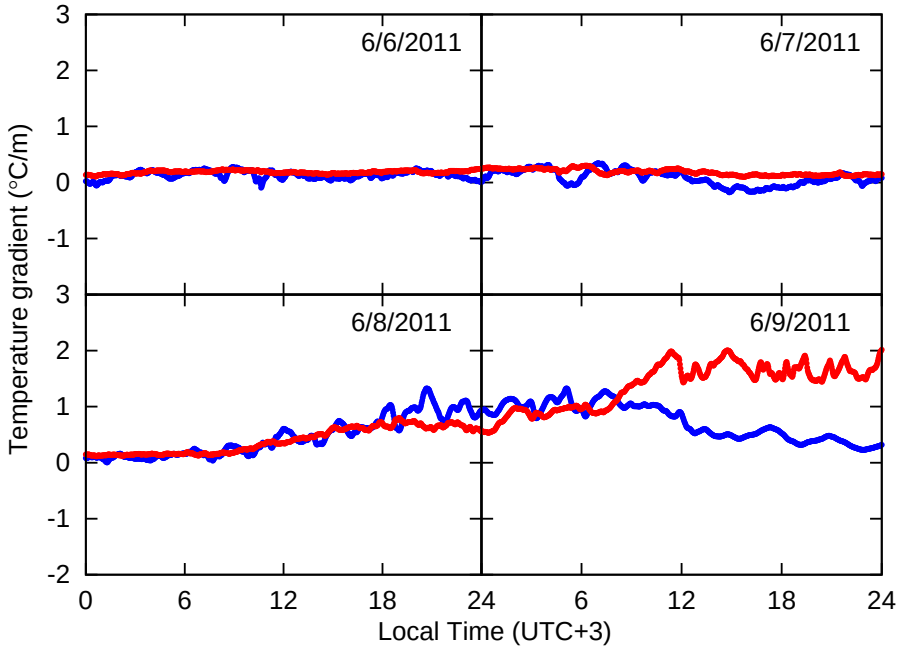

Figure C.77: Same as Fig. C.43, but for the period from June 6 00:00 (UTC+3) to June 9 24:00, 2011.

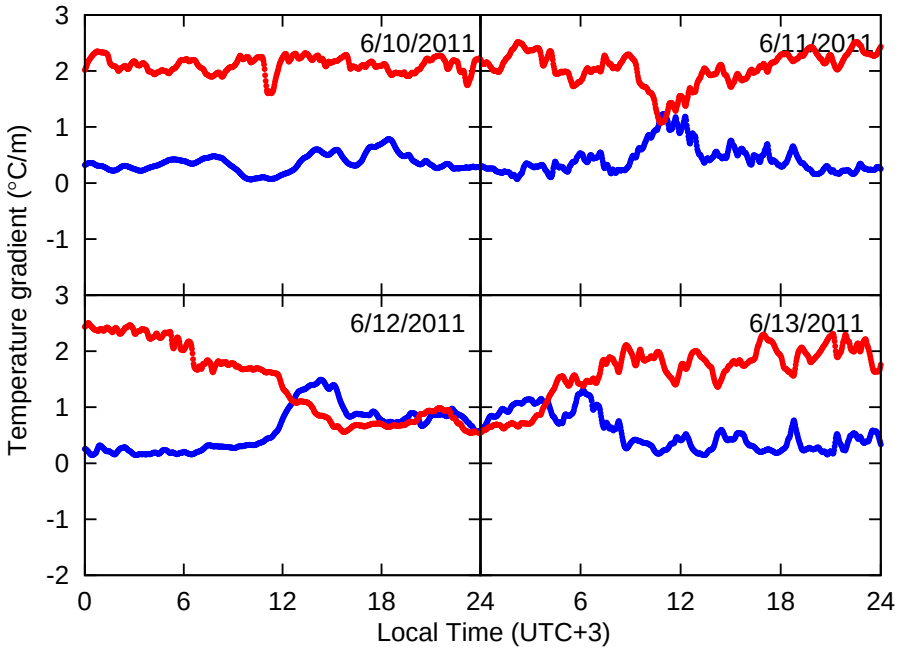

Figure C.78: Same as Fig. C.43, but for the period from June 10 00:00 (UTC+3) to June 13 24:00, 2011.

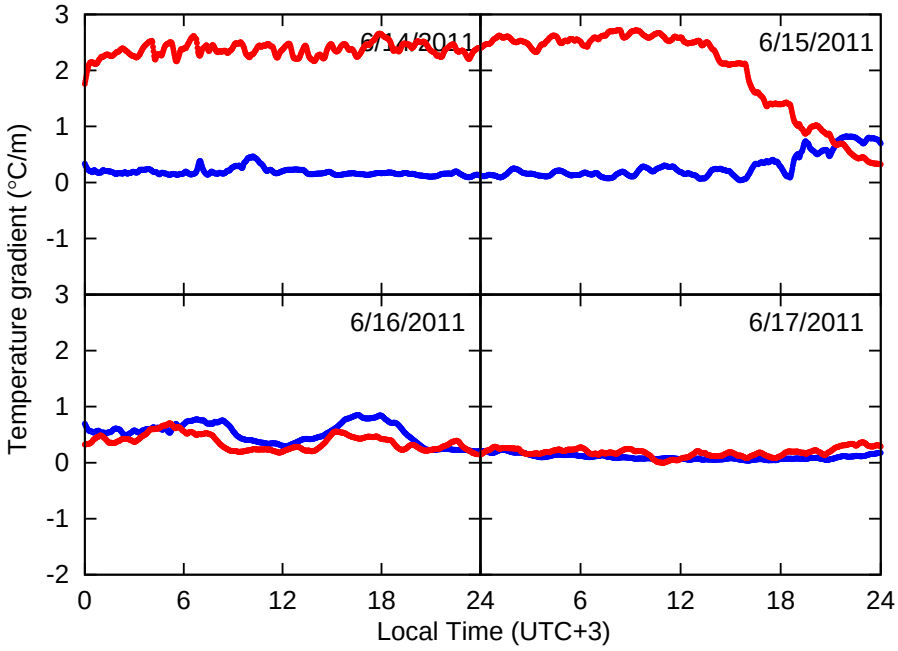

Figure C.79: Same as Fig. C.43, but for the period from June 14 00:00 (UTC+3) to June 17 24:00, 2011.

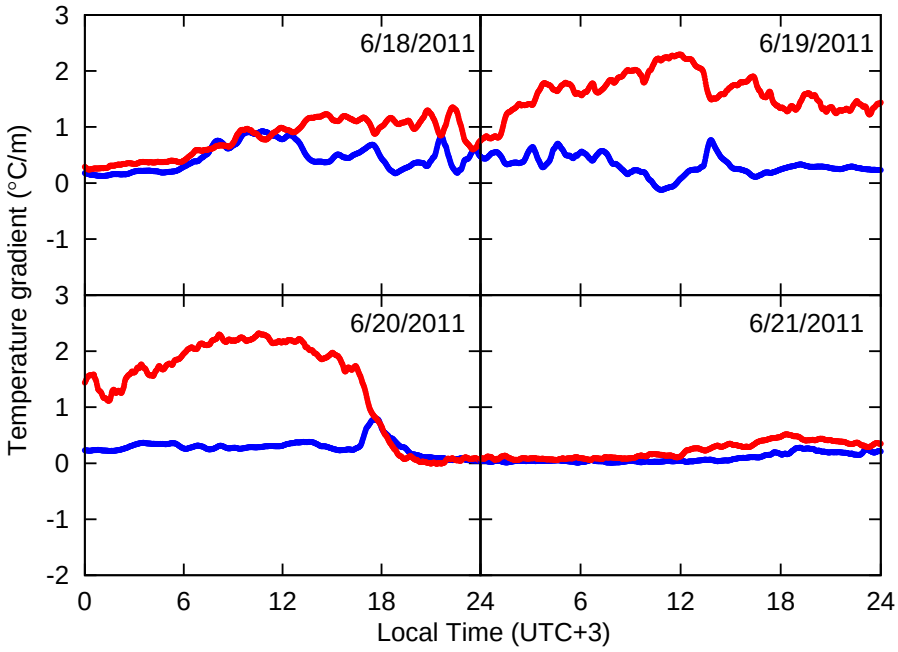

Figure C.80: Same as Fig. C.43, but for the period from June 18 00:00 (UTC+3) to June 21 24:00, 2011.

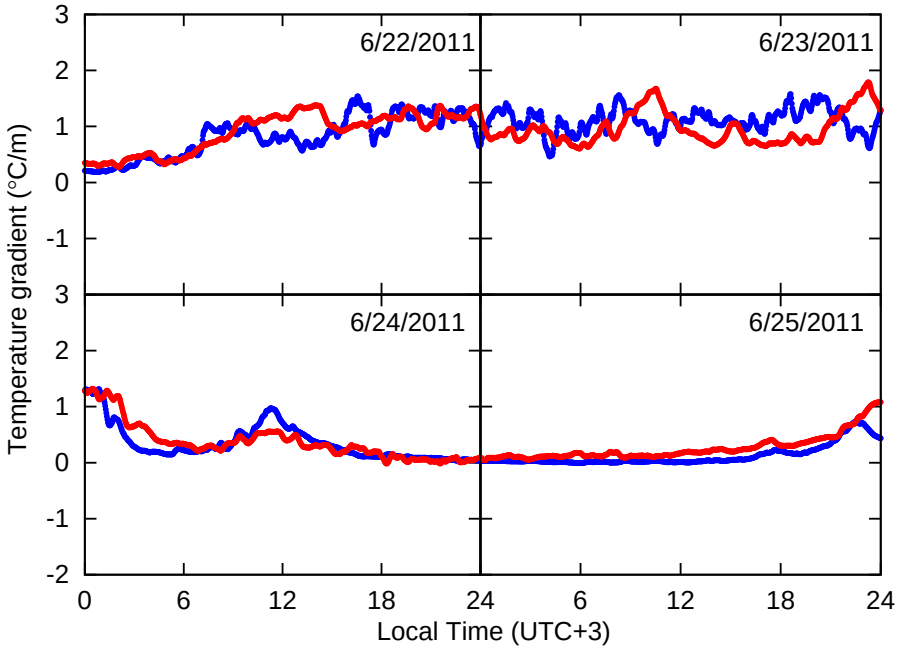

Figure C.81: Same as Fig. C.43, but for the period from June 22 00:00 (UTC+3) to June 25 24:00, 2011.

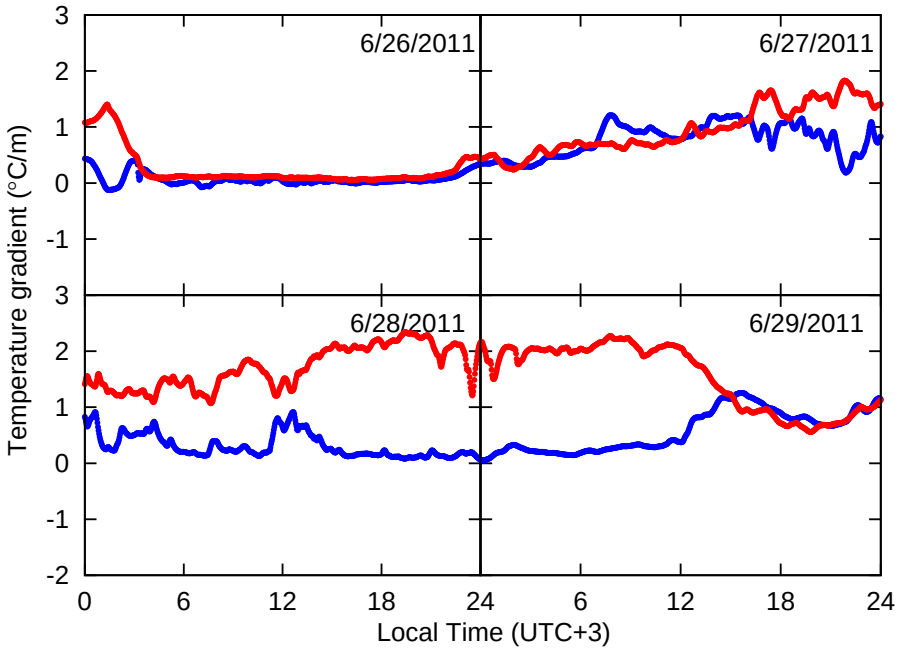

Figure C.82: Same as Fig. C.43, but for the period from June 26 00:00 (UTC+3) to June 29 24:00, 2011.

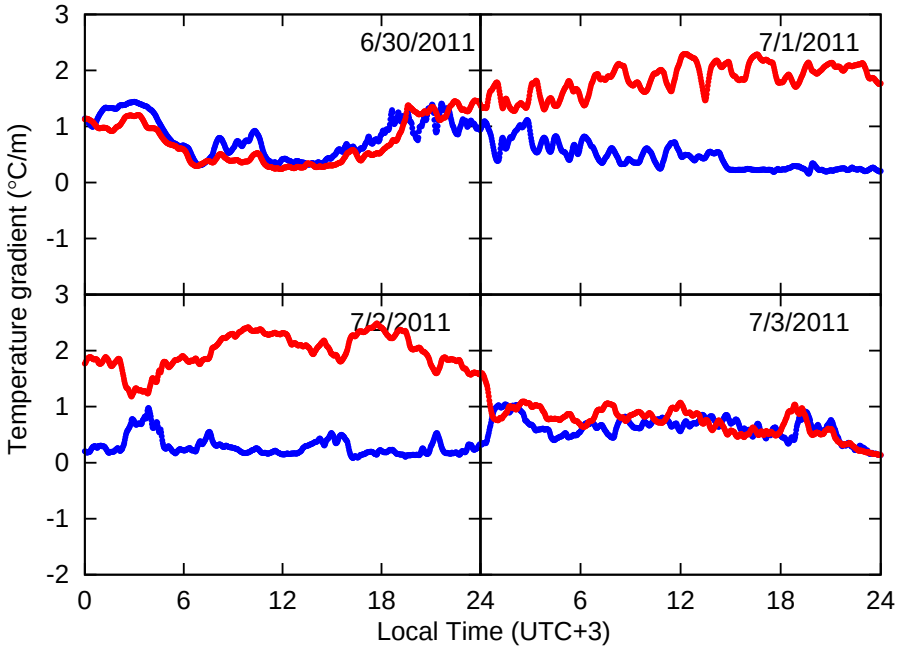

Figure C.83: Same as Fig. C.43, but for the period from June 30 00:00 (UTC+3) to July 3 24:00, 2011.

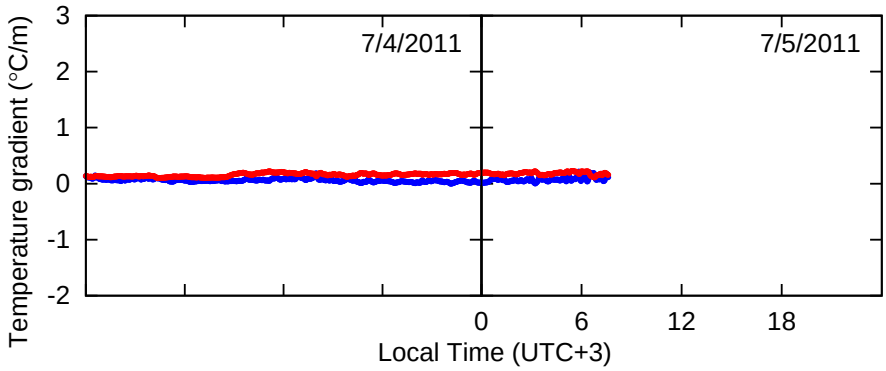

Figure C.84: Same as Fig. C.43, but for the period from July 4 00:00 (UTC+3) to July 5 24:00, 2011.

Appendix D

Barometer results

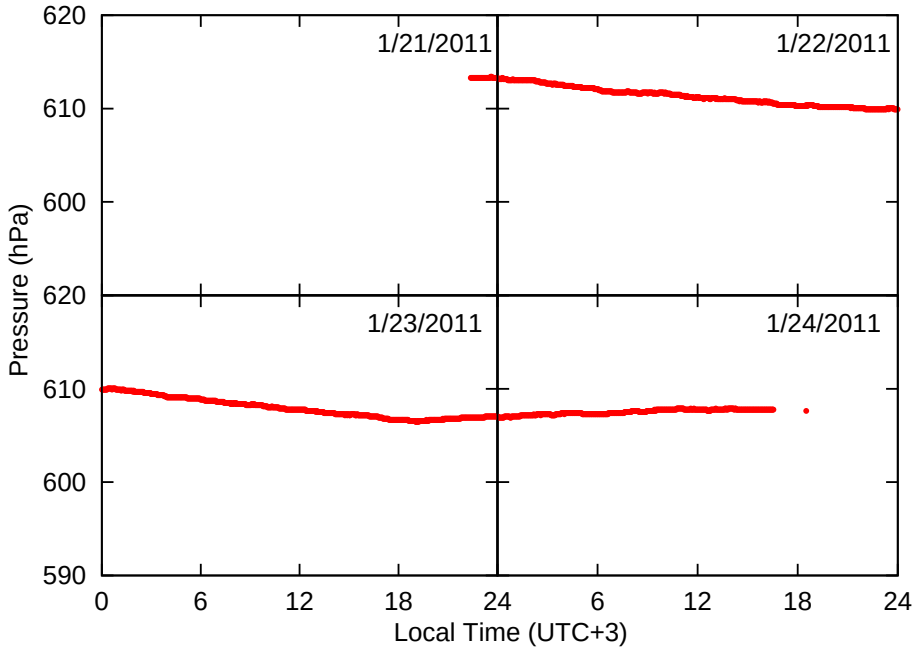

Figure D.1: Time series of the atmospheric pressure (hPa) with two minute time resolution for the period from January 21 00:00 (UTC+3) to January 24 24:00, 2011. We note that we could not measure the pressure under 596 hPa due to the wrong setting of the data logger.

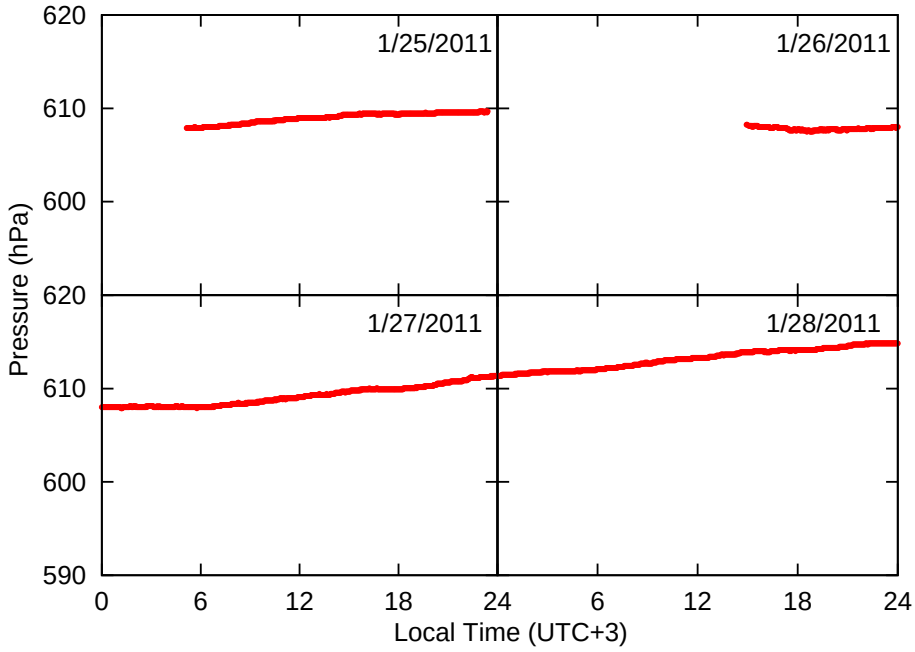

Figure D.2: Same as Fig. D.1, but for the period from January 25 00:00 (UTC+3) to January 28 24:00, 2011.

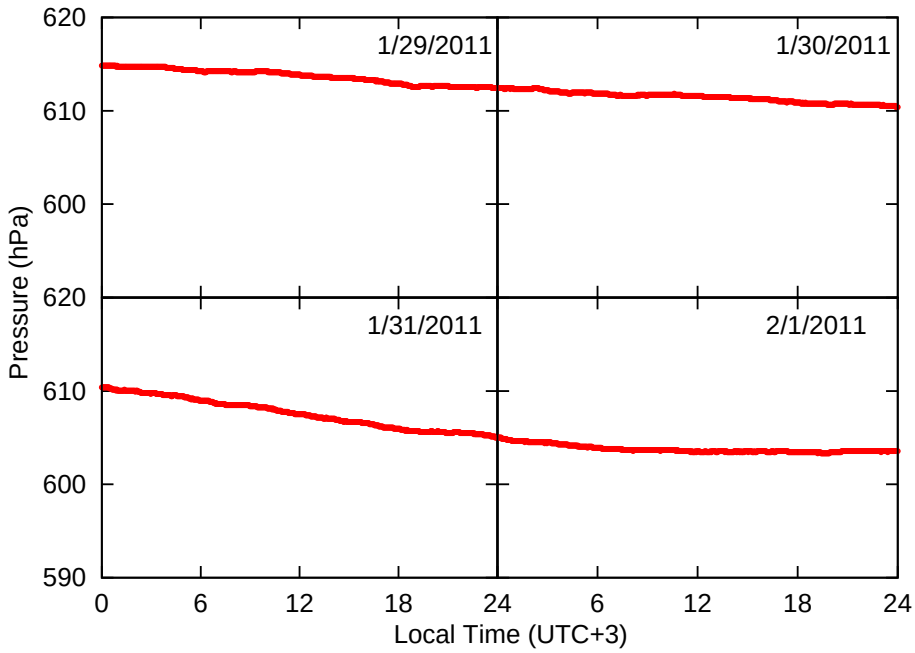

Figure D.3: Same as Fig. D.1, but for the period from January 29 00:00 (UTC+3) to February 1 24:00, 2011.

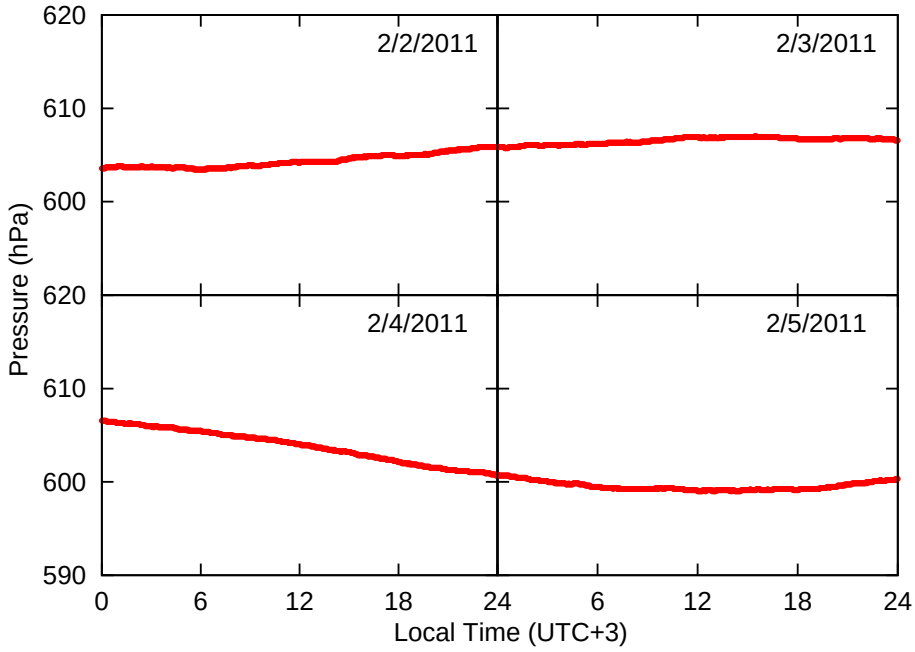

Figure D.4: Same as Fig. D.1, but for the period from February 2 00:00 (UTC+3) to February 5 24:00, 2011.

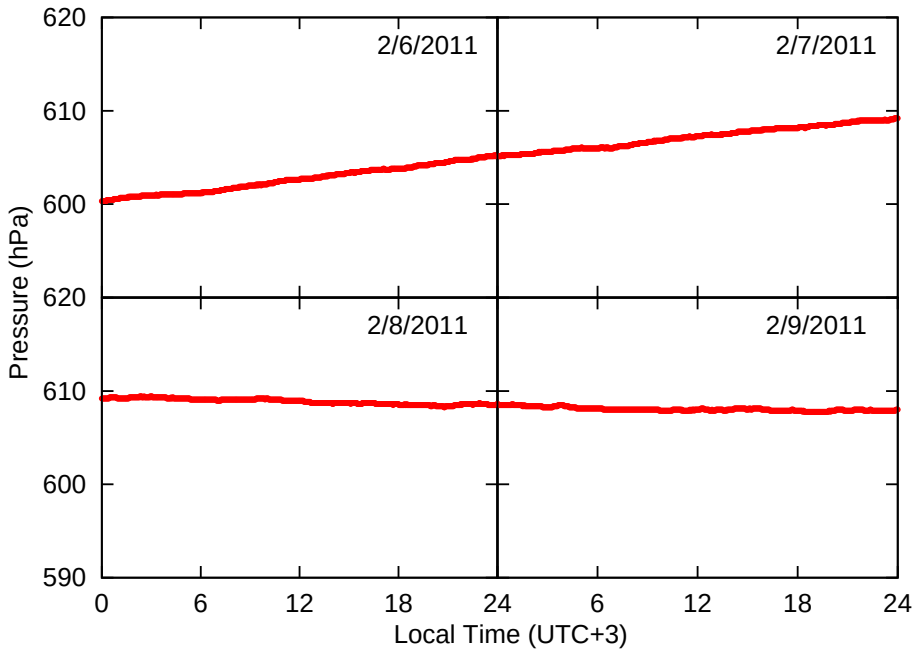

Figure D.5: Same as Fig. D.1, but for the period from February 6 00:00 (UTC+3) to February 9 24:00, 2011.

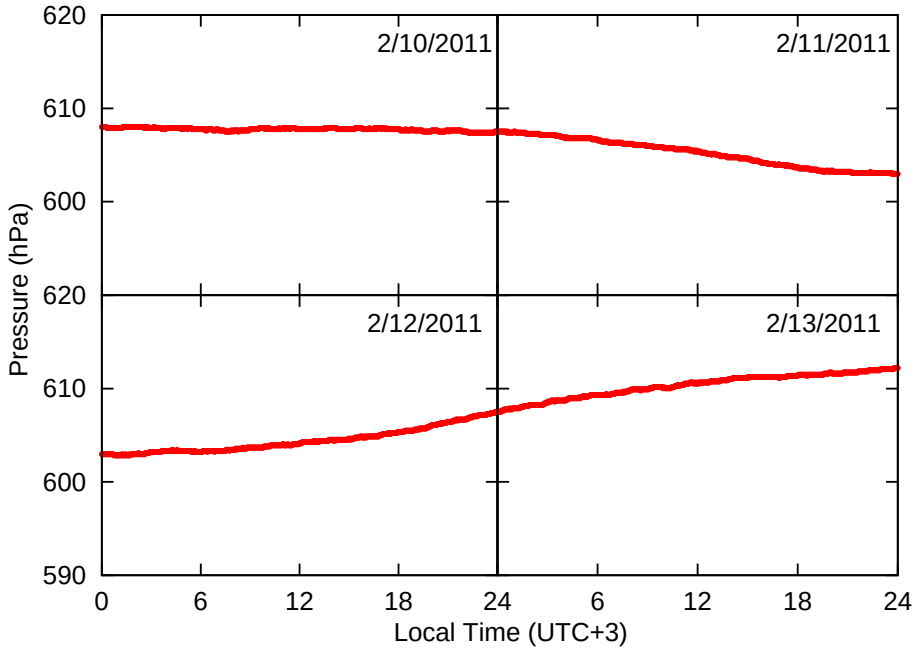

Figure D.6: Same as Fig. D.1, but for the period from February 10 00:00 (UTC+3) to February 13 24:00, 2011.

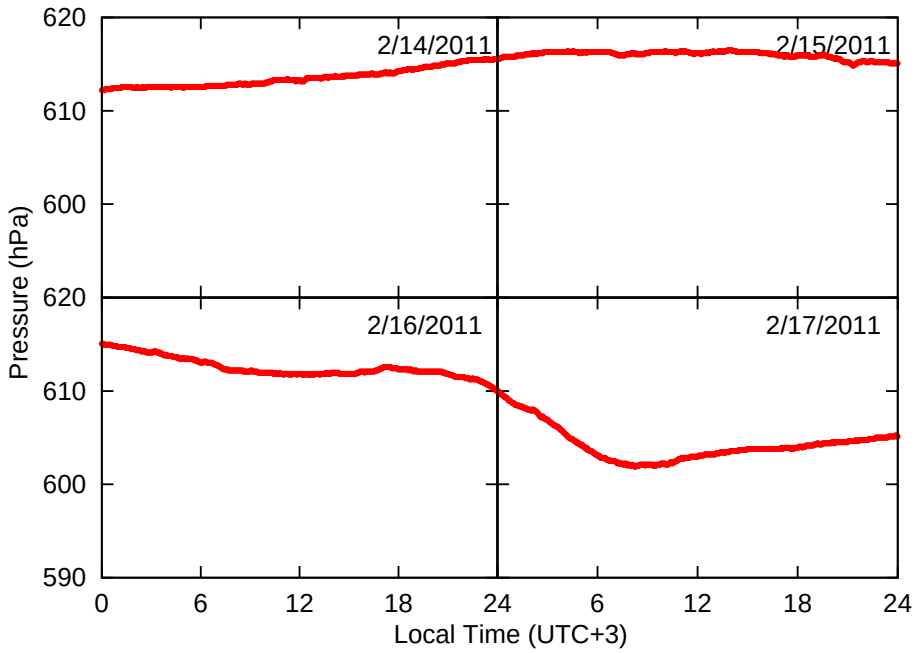

Figure D.7: Same as Fig. D.1, but for the period from February 14 00:00 (UTC+3) to February 17 24:00, 2011.

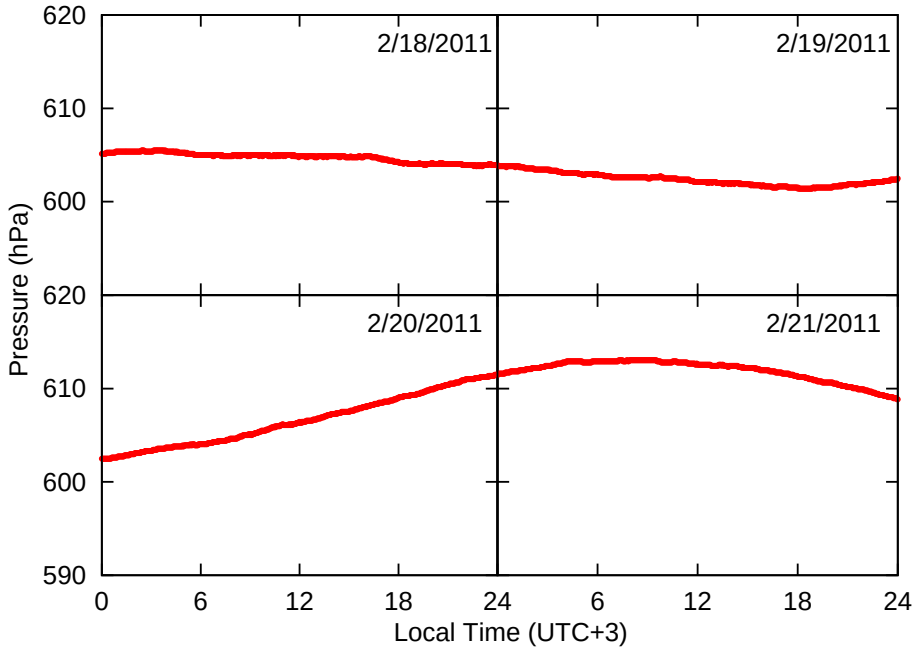

Figure D.8: Same as Fig. D.1, but for the period from February 18 00:00 (UTC+3) to February 21 24:00, 2011.

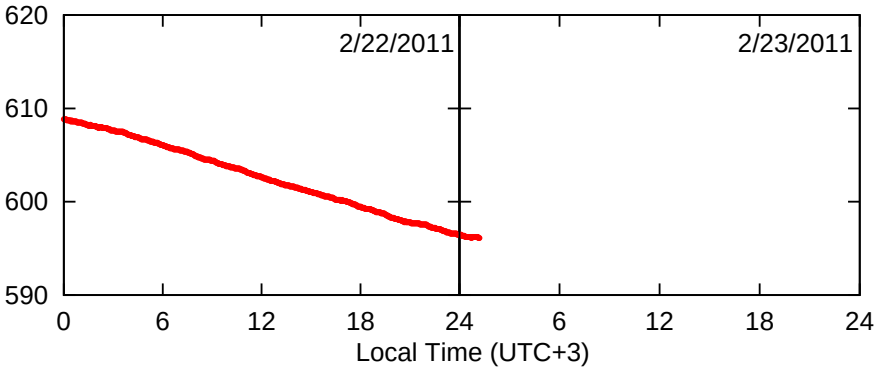

Figure D.9: Same as Fig. D.1, but for the period from February 22 00:00 (UTC+3) to February 23 24:00, 2011.

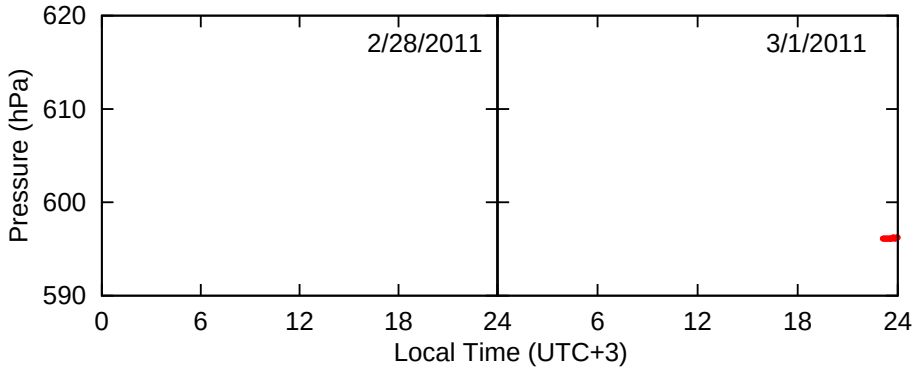

Figure D.10: Same as Fig. D.1, but for the period from February 28 00:00 (UTC+3) to March 1 24:00, 2011.

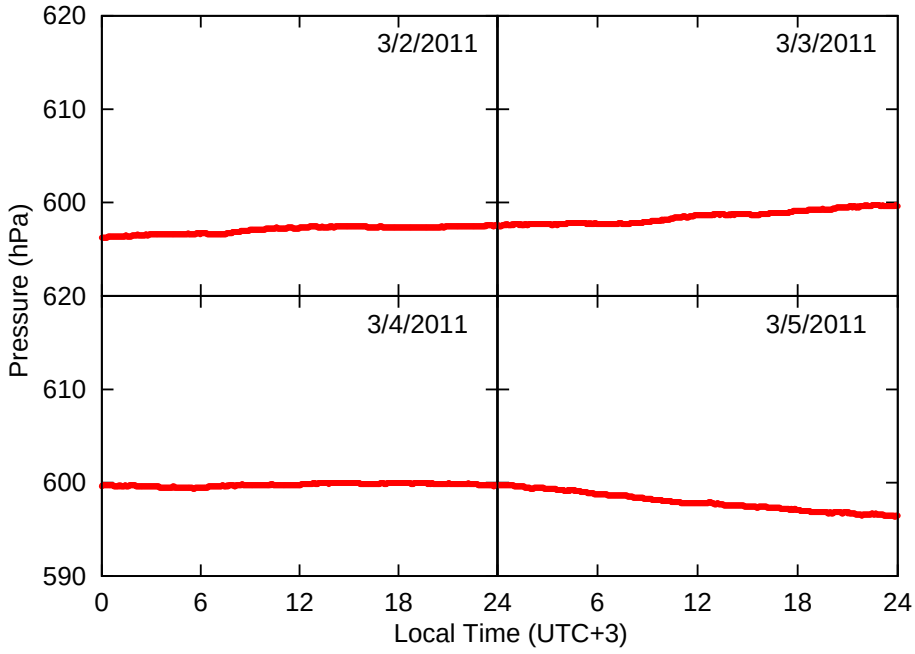

Figure D.11: Same as Fig. D.1, but for the period from March 2 00:00 (UTC+3) to March 5 24:00, 2011.

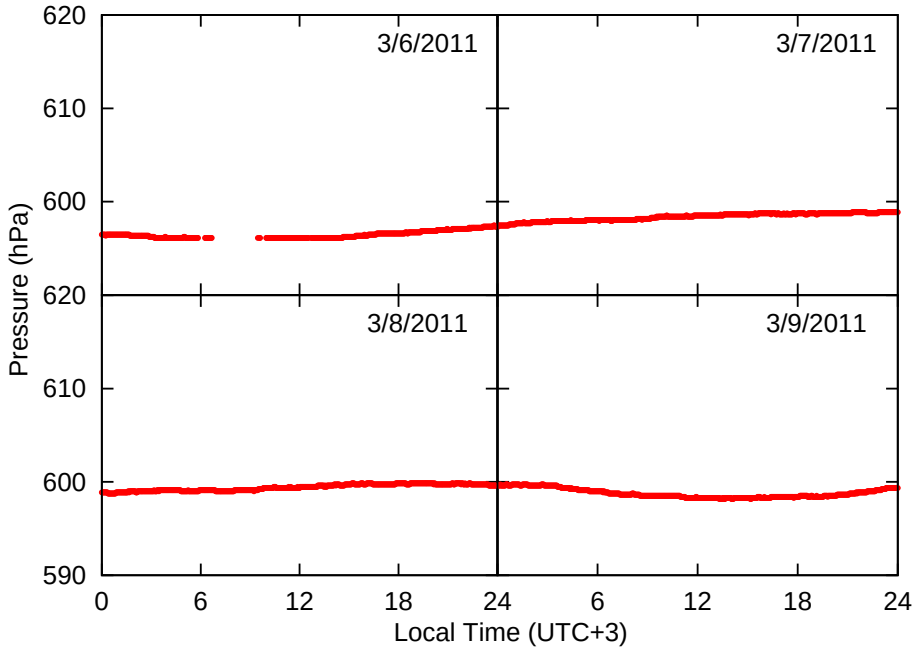

Figure D.12: Same as Fig. D.1, but for the period from March 6 00:00 (UTC+3) to March 9 24:00, 2011.

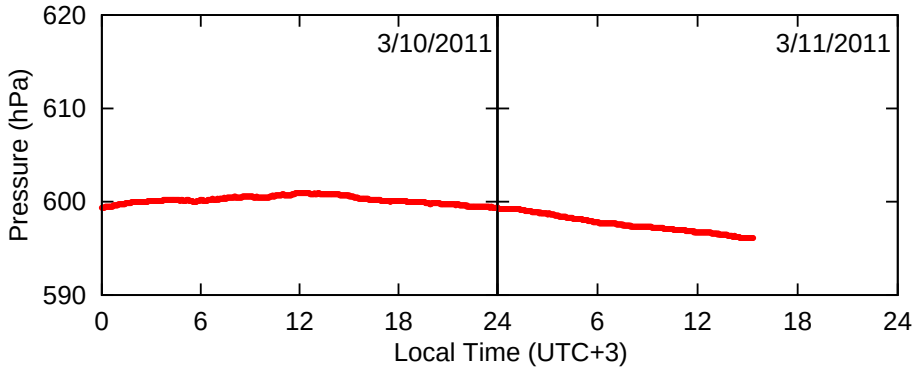

Figure D.13: Same as Fig. D.1, but for the period from March 10 00:00 (UTC+3) to March 11 24:00, 2011.

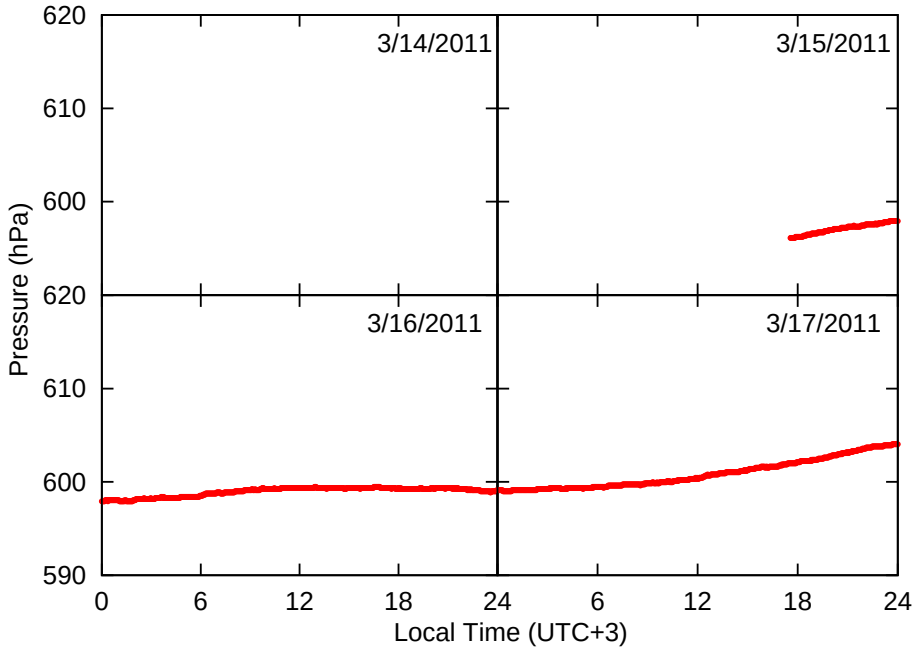

Figure D.14: Same as Fig. D.1, but for the period from March 14 00:00 (UTC+3) to March 17 24:00, 2011.

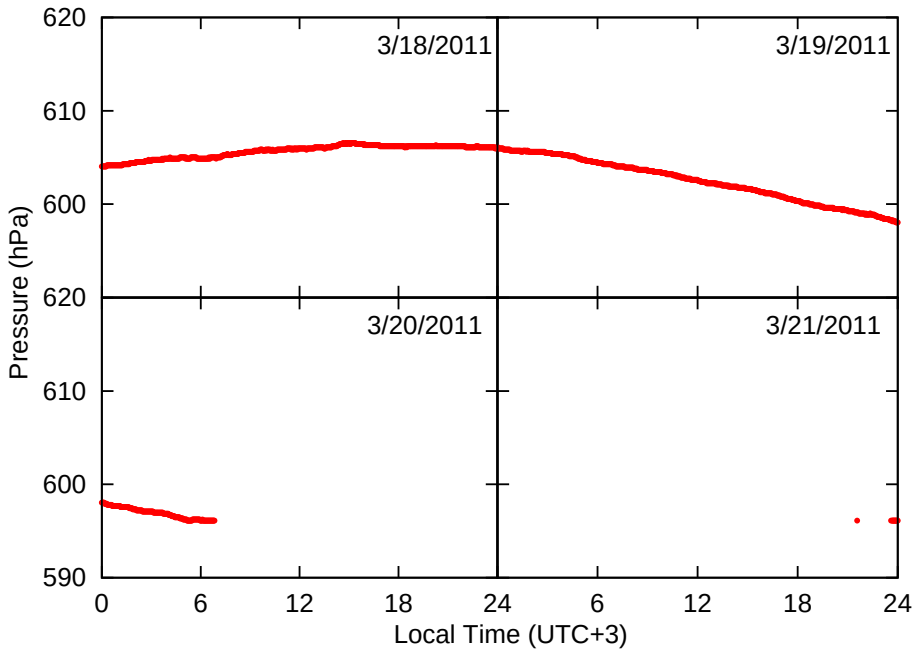

Figure D.15: Same as Fig. D.1, but for the period from March 18 00:00 (UTC+3) to March 21 24:00, 2011.

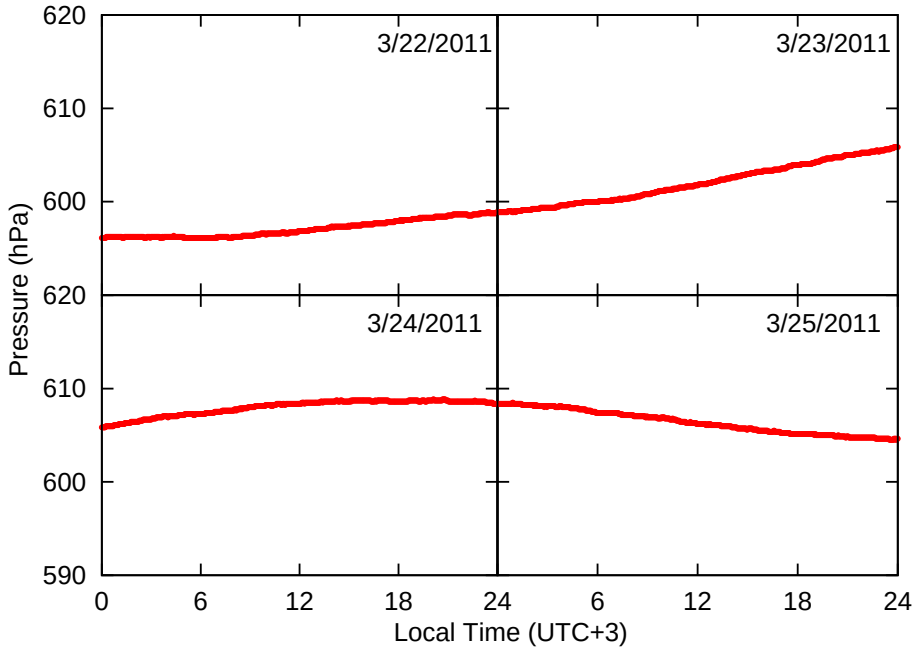

Figure D.16: Same as Fig. D.1, but for the period from March 22 00:00 (UTC+3) to March 25 24:00, 2011.

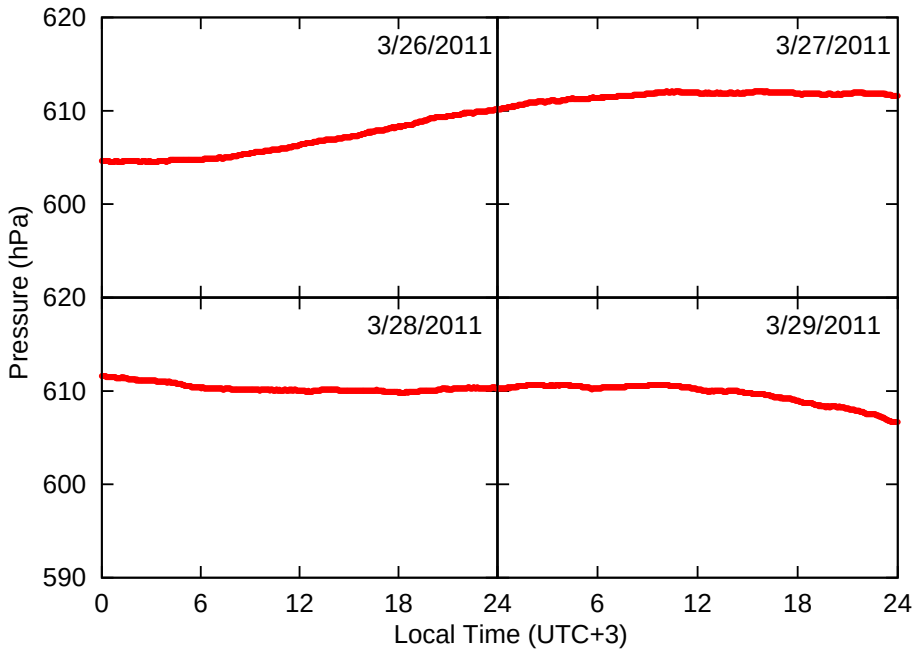

Figure D.17: Same as Fig. D.1, but for the period from March 26 00:00 (UTC+3) to March 29 24:00, 2011.

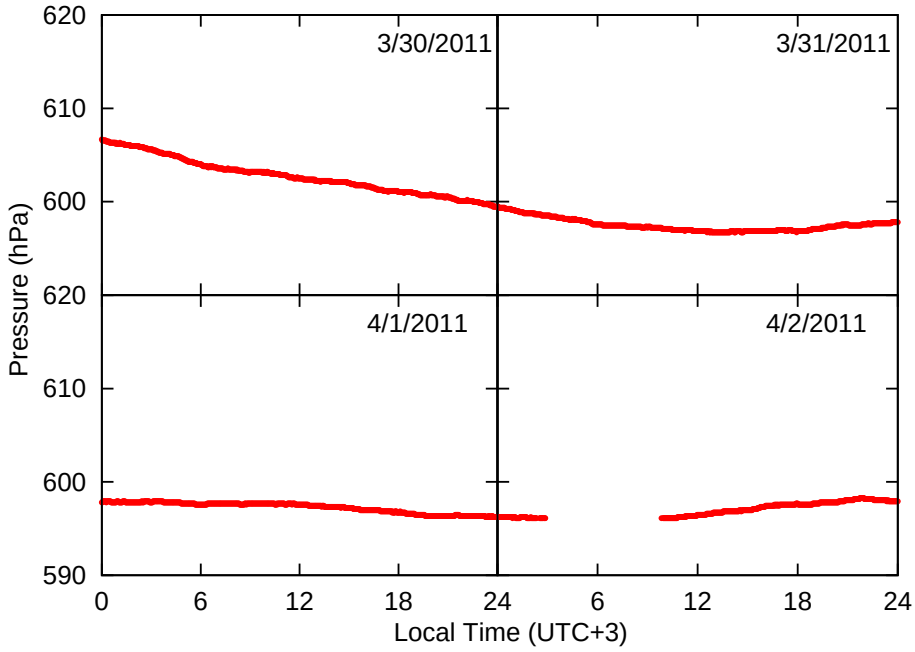

Figure D.18: Same as Fig. D.1, but for the period from March 30 00:00 (UTC+3) to April 2 24:00, 2011.

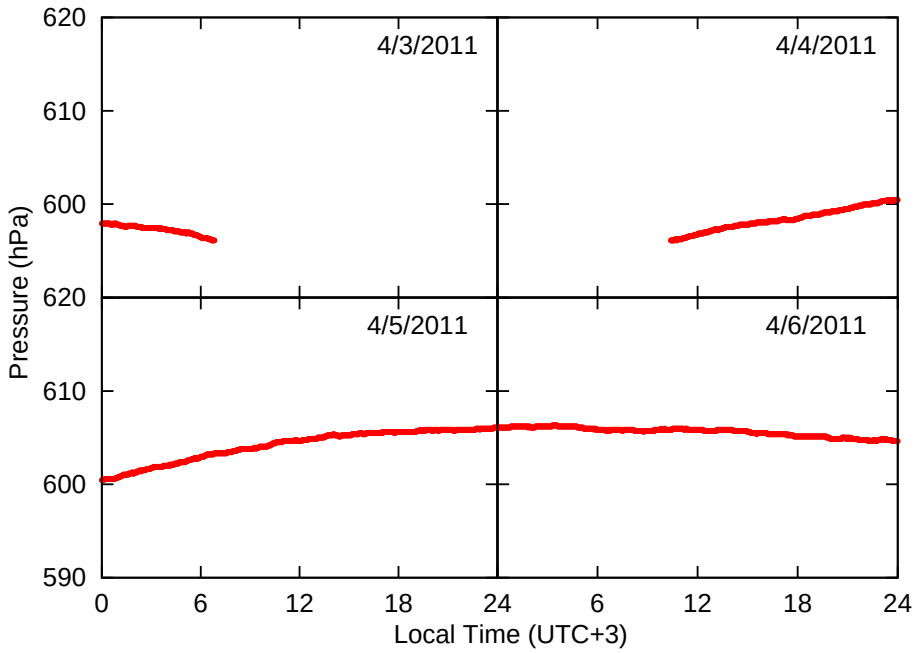

Figure D.19: Same as Fig. D.1, but for the period from April 3 00:00 (UTC+3) to April 6 24:00, 2011.

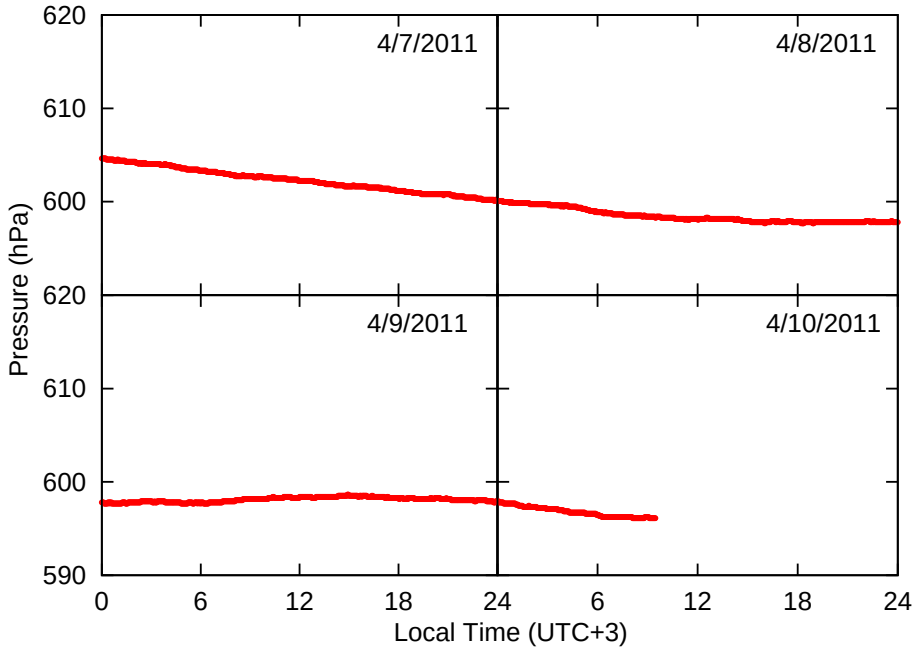

Figure D.20: Same as Fig. D.1, but for the period from April 7 00:00 (UTC+3) to April 10 24:00, 2011.

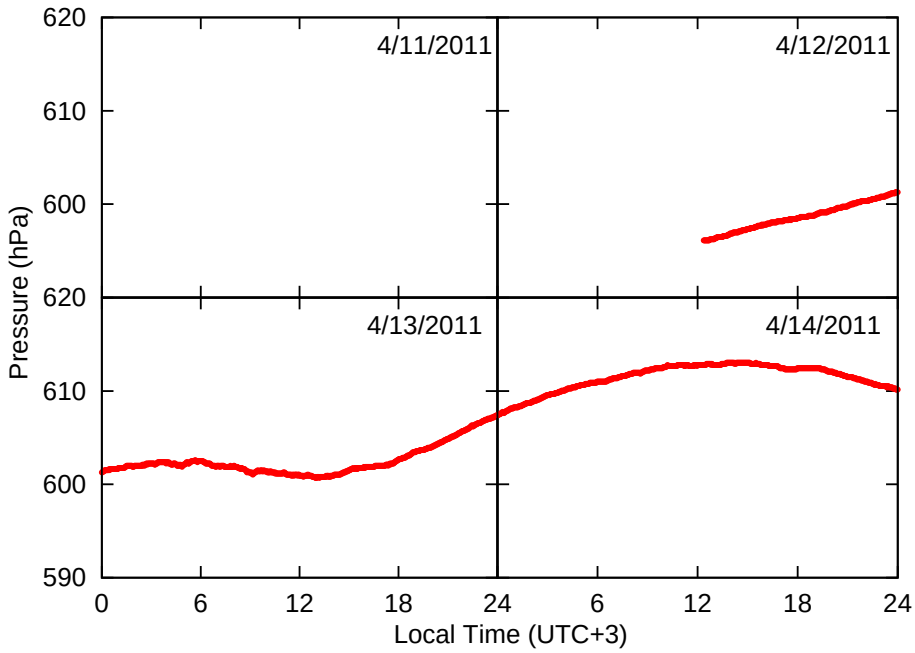

Figure D.21: Same as Fig. D.1, but for the period from April 11 00:00 (UTC+3) to April 14 24:00, 2011.

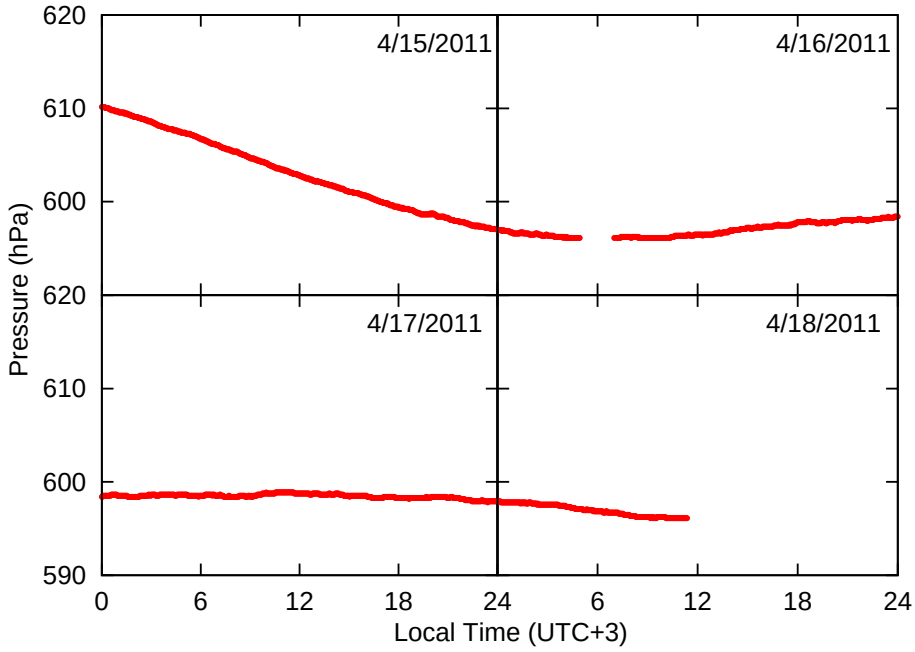

Figure D.22: Same as Fig. D.1, but for the period from April 15 00:00 (UTC+3) to April 18 24:00, 2011.

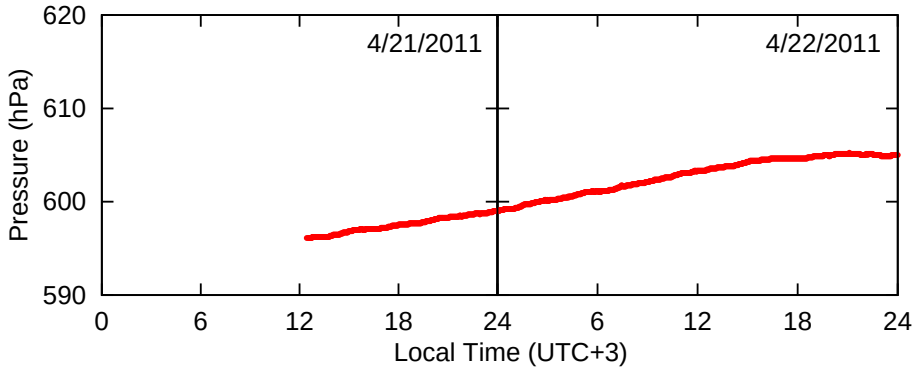

Figure D.23: Same as Fig. D.1, but for the period from April 21 00:00 (UTC+3) to April 22 24:00, 2011.

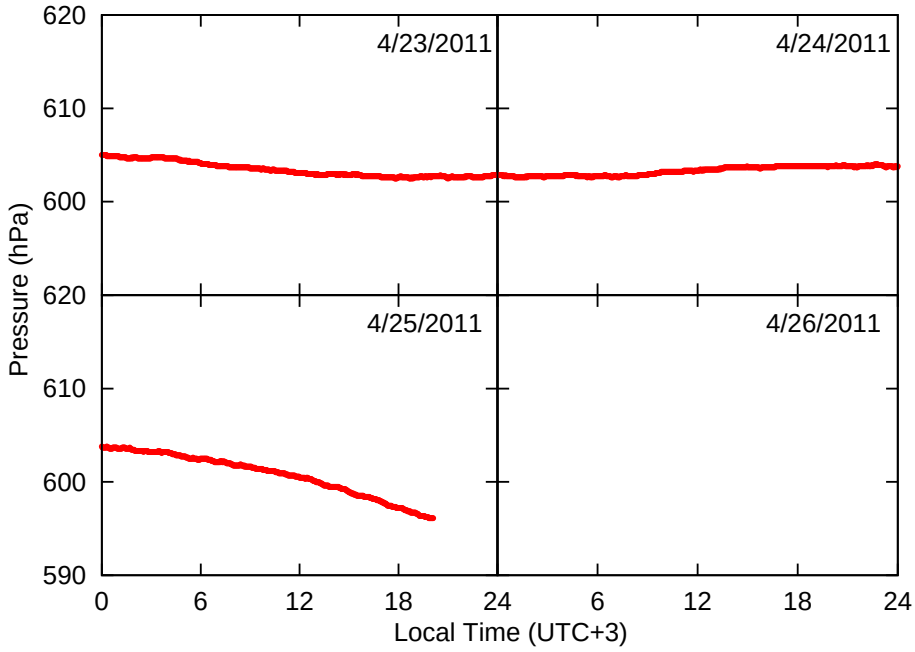

Figure D.24: Same as Fig. D.1, but for the period from April 23 00:00 (UTC+3) to April 26 24:00, 2011.

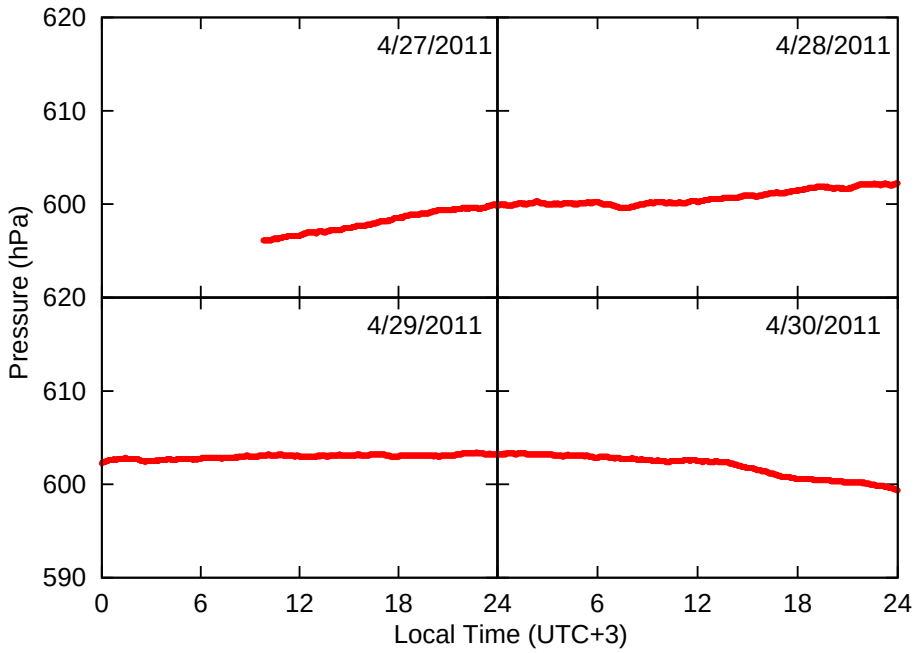

Figure D.25: Same as Fig. D.1, but for the period from April 27 00:00 (UTC+3) to April 30 24:00, 2011.

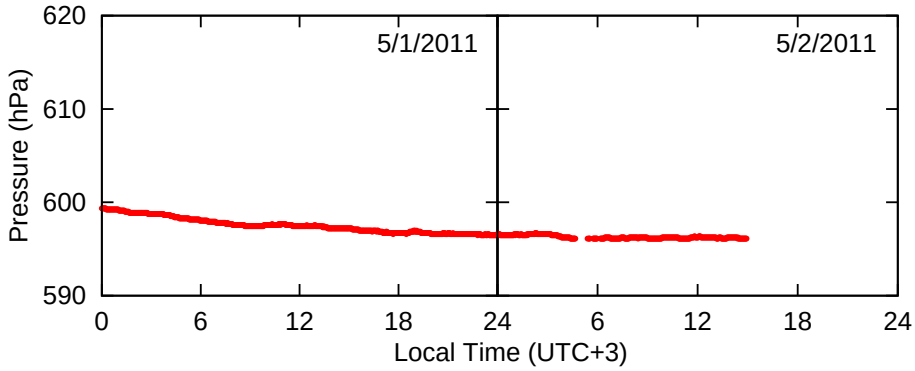

Figure D.26: Same as Fig. D.1, but for the period from May 1 00:00 (UTC+3) to May 2 24:00, 2011.

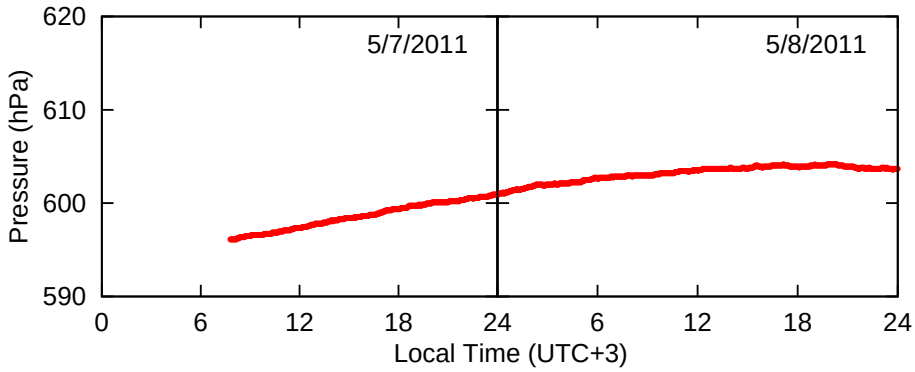

Figure D.27: Same as Fig. D.1, but for the period from May 7 00:00 (UTC+3) to May 8 24:00, 2011.

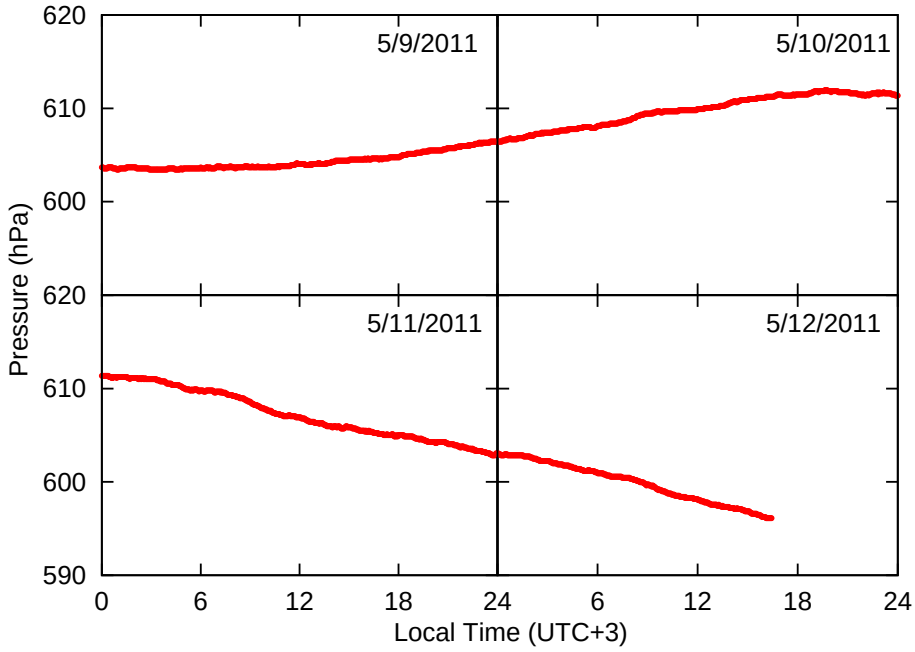

Figure D.28: Same as Fig. D.1, but for the period from May 9 00:00 (UTC+3) to May 12 24:00, 2011.

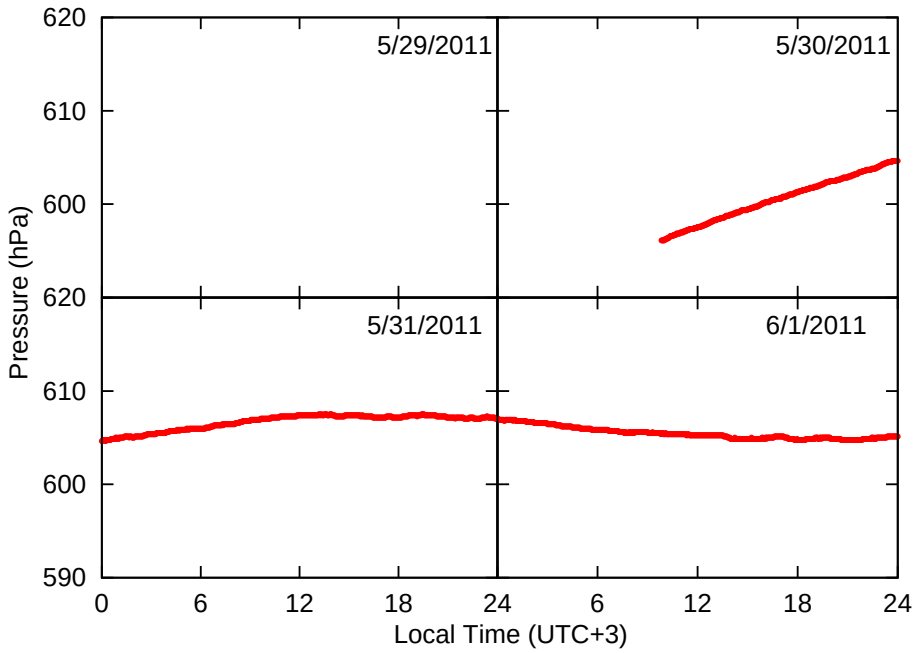

Figure D.29: Same as Fig. D.1, but for the period from May 29 00:00 (UTC+3) to June 1 24:00, 2011.

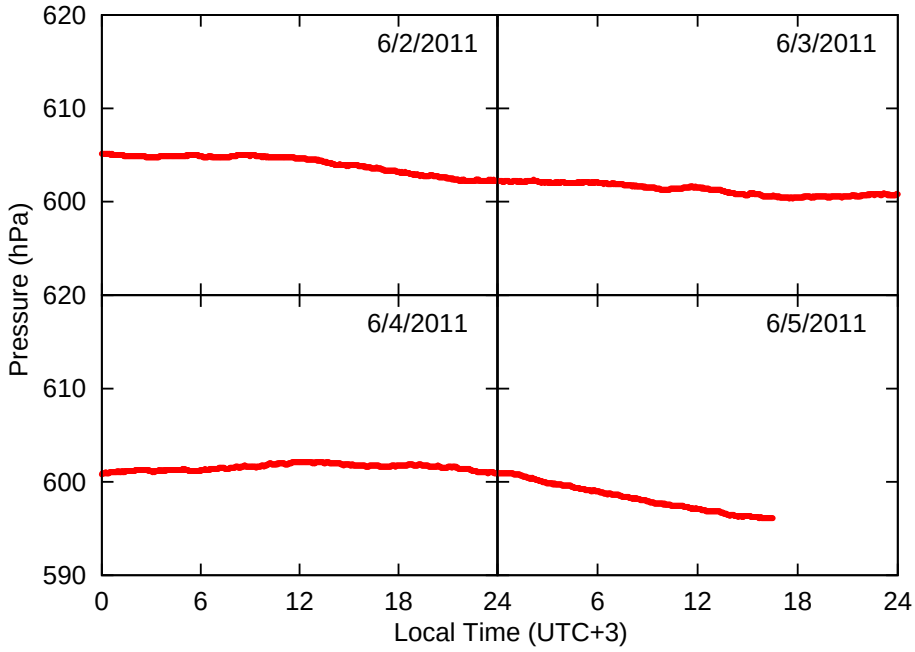

Figure D.30: Same as Fig. D.1, but for the period from June 2 00:00 (UTC+3) to June 5 24:00, 2011.

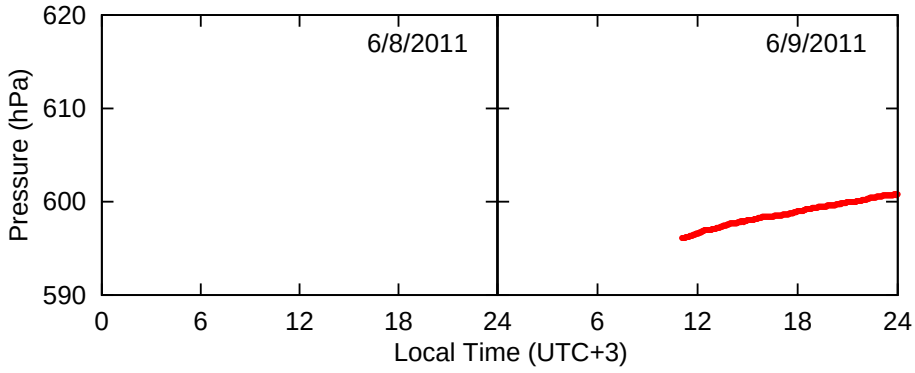

Figure D.31: Same as Fig. D.1, but for the period from June 8 00:00 (UTC+3) to June 9 24:00, 2011.

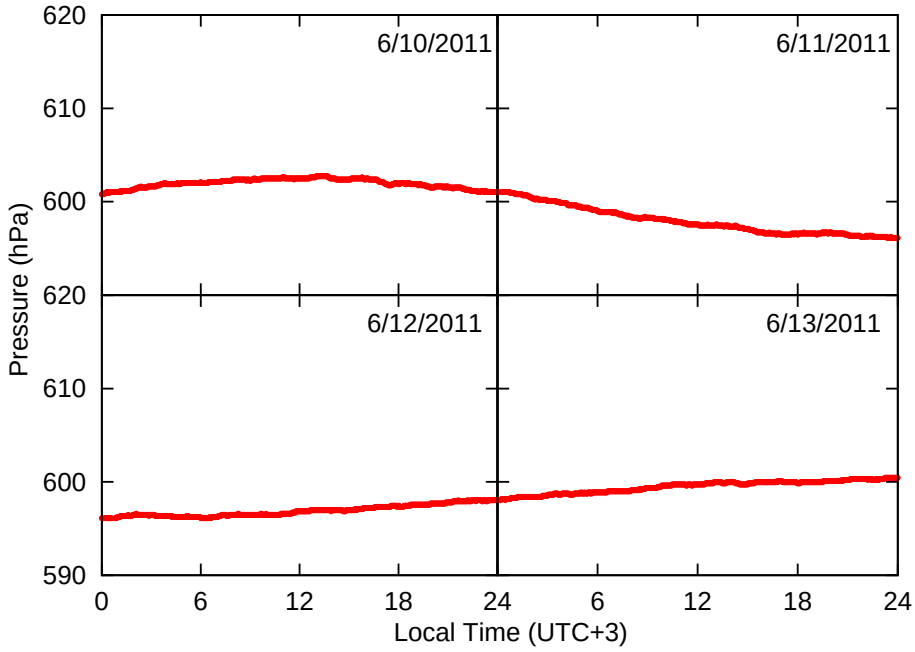

Figure D.32: Same as Fig. D.1, but for the period from June 10 00:00 (UTC+3) to June 13 24:00, 2011.

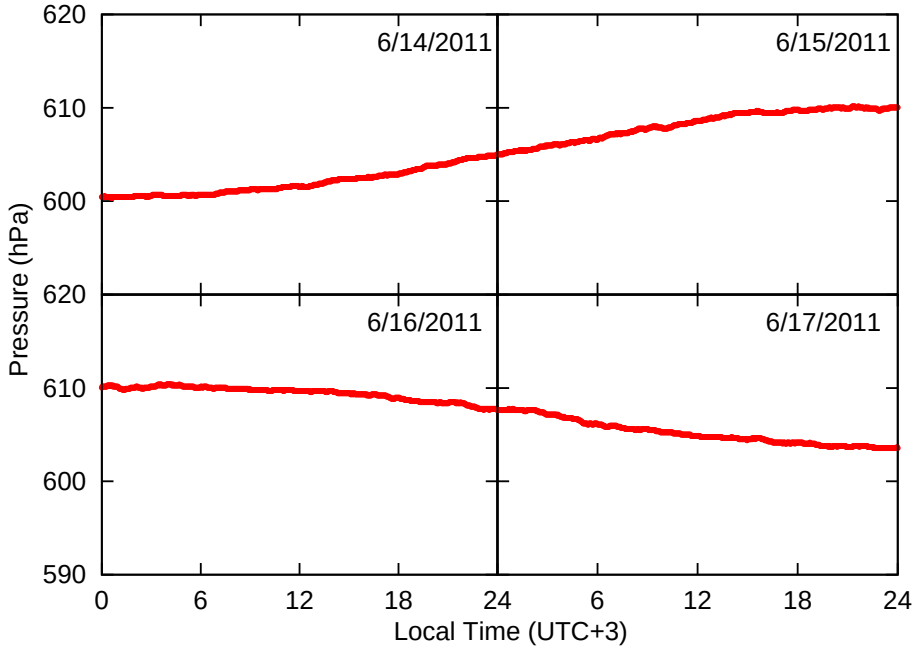

Figure D.33: Same as Fig. D.1, but for the period from June 14 00:00 (UTC+3) to June 17 24:00, 2011.

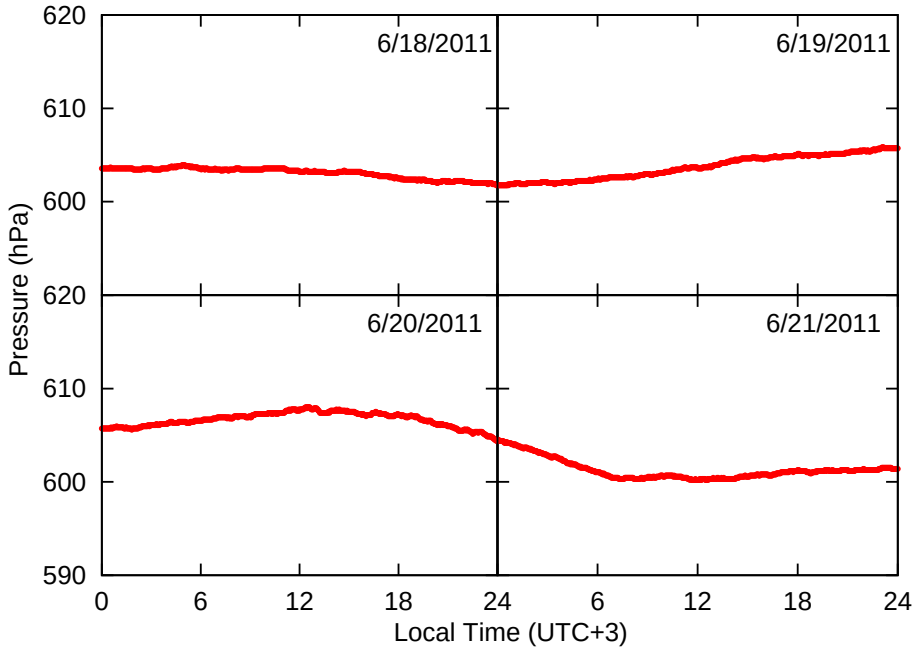

Figure D.34: Same as Fig. D.1, but for the period from June 18 00:00 (UTC+3) to June 21 24:00, 2011.

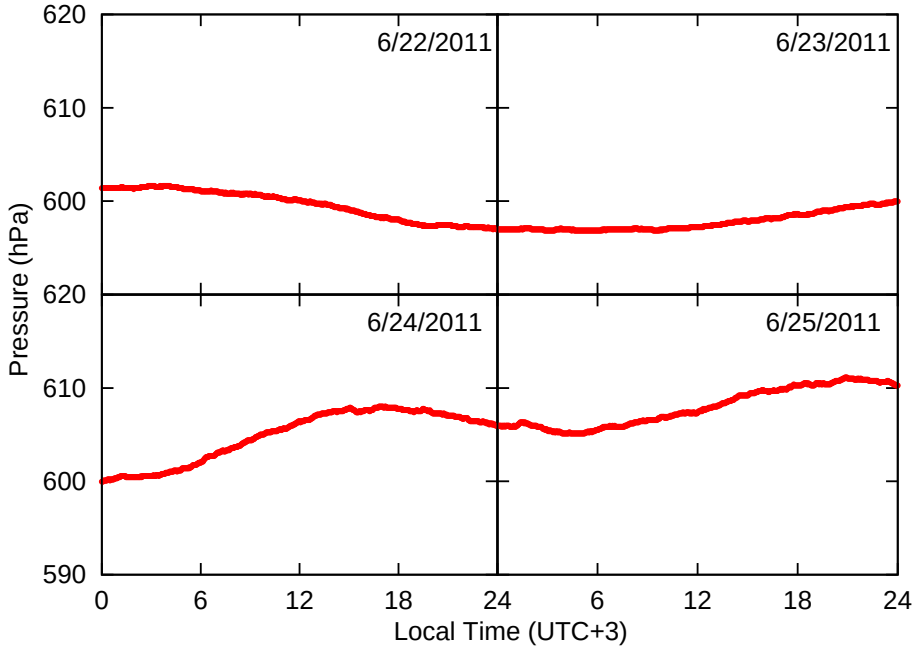

Figure D.35: Same as Fig. D.1, but for the period from June 22 00:00 (UTC+3) to June 25 24:00, 2011.

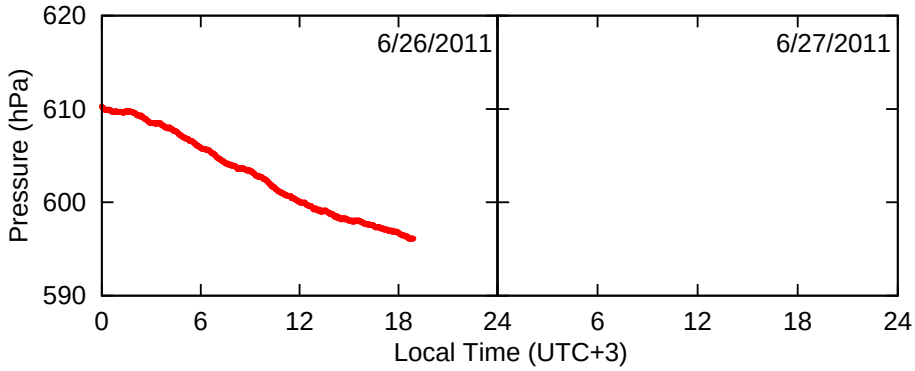

Figure D.36: Same as Fig. D.1, but for the period from June 26 00:00 (UTC+3) to June 27 24:00, 2011.